

ATOMIC FORCE MICROSCOPY STUDIES OF NANOTRIBOLOGY AND NANOMECHANICS

THÈSE N° 3905 (2007)

PRÉSENTÉE LE 8 OCTOBRE 2007

À LA FACULTÉ DES SCIENCES DE BASE
LABORATOIRE DE NANOSTRUCTURES SUPERFICIELLES
PROGRAMME DOCTORAL EN PHYSIQUE

ÉCOLE POLYTECHNIQUE FÉDÉRALE DE LAUSANNE

POUR L'OBTENTION DU GRADE DE DOCTEUR ÈS SCIENCES

PAR

Ismaël PALACI

ingénieur physicien diplômé EPF
de nationalité suisse et originaire de Cheiry (FR)

acceptée sur proposition du jury:

Prof. R. Schaller, président du jury
Prof. H. Brune, directeur de thèse
Prof. J. Frenken, rapporteur
Prof. K. Kern, rapporteur
Prof. E. Meyer, rapporteur



ÉCOLE POLYTECHNIQUE
FÉDÉRALE DE LAUSANNE

Suisse
2007

Résumé

CETTE THÈSE s'inscrit dans le cadre des études de la tribologie à l'échelle nanoscopique. Les techniques expérimentales utilisées dans ce travail reposent sur la microscopie à force atomique. Cette dernière donne un accès direct à la topographie du système observé, mais aussi aux forces en présence. Deux aspects principaux nous ont intéressés dans le domaine de la nanotribologie, ce sont la nanofriction et la nanomécanique. Ces deux domaines divisent cette thèse en deux grandes parties, qui restent toutefois intimement liées.

La première partie expérimentale de la thèse traite du phénomène de la friction entre une pointe nanoscopique et des surfaces hydrophiles. La dépendance de la force de friction avec la vitesse de glissement de la pointe sur la surface est étudiée en fonction de différentes forces normales appliquées à la surface par la pointe, ainsi que pour différentes humidités relatives. Il en résulte une dépendance logarithmique de la force de friction avec la vitesse de glissement et l'humidité relative. De plus, en jouant sur l'humidité relative, nous avons observé, pour la première fois, la transition entre une pente positive et une pente négative de la force de friction en fonction du logarithme de la vitesse de glissement, et cela pour le même contact entre la pointe et la surface. L'effet de l'humidité relative sur la force de friction a ensuite été étudié plus en profondeur, permettant de mettre en évidence une loi en puissance deux-tiers régissant le comportement de la force capillaire en fonction de la force normale. Finalement, des expressions analytiques du phénomène de friction et de la formation de capillaires entre les aspérités de la pointe et de la surface ont été développées afin d'expliquer les comportements phénoménologiques observés.

La seconde partie expérimentale de la thèse s'est intéressée à la mécanique des nanotubes de carbone multi-feuillets et du virus mosaïque du tabac. Afin de rester dans le régime de déformation élastique, de petites amplitudes d'indentations ont été appliquées dans la direction radiale des nanotubes de carbone adsorbés sur une surface d'oxyde de silicium. En se basant sur une théorie développée par Hertz, leur rigidité radiale a été évaluée et comparée à des simulations de dynamique moléculaire. Nous avons obtenu un module d'Young radial fortement décroissant avec l'augmentation du rayon du tube, et atteignant une valeur asymptotique de 30 ± 10 GPa. Le virus mosaïque du tabac a, quant à lui, été adsorbé sur une surface poreuse de polyimide. La mollesse et la flexibilité caractérisant ces virus ont été mises en évidence au moyen de la microscopie à force atomique en mode non-contact. Des virus suspendus tel des cordes au-dessus des pores de la surface ont servi de base dans la détermination d'un module d'Young longitudinal caractérisant leur élasticité en flexion. Un modèle de poutre encastrée, chargée par un gradient discret de forces de van der Waals, a permis d'évaluer un module d'Young de 3.1 ± 0.1 MPa.

Mots-clés: nanotribologie, microscopie à force atomique, friction, force capillaire, nanomé-

canique, nanotube de carbone, virus mosaïque du tabac.

Abstract

THIS THESIS comes within the scope of tribology studies at the nanometer scale. The experimental techniques used in this work are essentially related to atomic force microscopy, which gives a direct access to the topography and forces of the studied systems. Two principal aspects of the nanotribology have kept our attention. They are the nanofriction and the nanomechanics. These two domains divide the thesis in two main parts that remain however intimately bound.

The first experimental part of the thesis describes the friction of a nanoscopic tip sliding on hydrophilic surfaces. The dependence of the friction force on the sliding velocity is studied for various applied normal loads and surrounding relative humidity levels. We found a logarithmic dependence of the friction force on both the scanning velocity and the relative humidity. For the first time, a transition from a positive to a negative slope of the friction force versus the logarithm of the sliding velocity has been observed for the very same tip-surface contact, by varying the relative humidity. The role of the relative humidity on the friction force has then been studied more deeply, leading to a two-thirds power law dependence of the capillary force on the normal load. Finally, analytical expressions for the friction phenomenon and the capillary condensation between the asperities of the tip and the surface have been developed to explain the phenomenological behaviors.

The second experimental part describes the mechanics of carbon nanotubes and tobacco mosaic viruses. In order to stay in the linear elasticity regime, small indentation amplitudes have been applied in the radial direction of multiwalled carbon nanotubes adsorbed on a silicon oxide surface. Using a theory based on the Hertz model, the radial stiffness has been evaluated and compared to molecular dynamics simulations. We found a radial Young modulus strongly decreasing with increasing radius and reaching an asymptotic value of 30 ± 10 GPa. The tobacco mosaic viruses have been adsorbed on a polyimide porous membrane. Evidence for the softness of the viruses has been obtained by imaging the tubes with the atomic force microscope in non-contact mode. Viruses hanging like ropes over the pores of the surface served as basis to measure their bending Young modulus. Using a model of a clamped beam loaded by a discrete gradient of van der Waals forces, we found a bending Young modulus of 3.1 ± 0.1 MPa.

Keywords: nanotribology, atomic force microscopy, friction, capillary force, nanomechanics, carbon nanotube, tobacco mosaic virus.

Contents

Abstract	V
Introduction	1
1 Surface interactions	3
1.1 From ideal surface to real surfaces	3
1.2 Atomic and intermolecular forces	5
1.2.1 Ionic bond	5
1.2.2 Covalent bond	6
1.2.3 Metallic bond	6
1.2.4 Van der Waals forces	6
1.2.5 Hydrogen bonding	8
1.2.6 Capillary forces	9
1.3 Continuum mechanics	12
1.3.1 Generalized Hooke's law	12
1.3.2 Contact mechanics	15
1.3.3 Experimental contact area	19
1.3.4 Notion of compliance	20
2 Experimental techniques	23
2.1 Atomic Force Microscopy	23
2.1.1 History	23
2.1.2 Working principle of the AFM	24
2.1.3 AFM spectroscopy: the force-distance curve	28
2.1.4 AFM modes	29
2.1.5 Cantilevers	33
2.1.6 Calibration	37
2.2 Other microscopy techniques: TEM and SEM	45
2.2.1 Electron-surface interactions	45
2.2.2 SEM and TEM working principles	47
2.3 Contact angle measurements	48
3 Friction at the nanoscale	51
3.1 History of the friction	52
3.2 Thermally activated phenomena in nanofriction	54

3.2.1	An atomistic view of the Amontons-Coulomb laws: the Tomlinson model	55
3.2.2	The concept of superlubricity in friction	59
3.2.3	Recent experimental results on friction and evolution of the Tomlinson model	61
3.3	Presentation and motivation of our theoretical model	64
3.3.1	Theoretical model	65
3.3.2	Experimental results on the effects of the sliding velocity on the nanofriction of hydrophilic surfaces	69
3.4	Capillary effects	75
3.4.1	From water molecules to capillary bridges	75
3.4.2	Thermally activated condensation of capillary bridges	77
3.4.3	2/3 power law dependence of the capillary force on the normal load	78
3.4.4	Experimental results on capillary condensation	80
3.5	Conclusion	86
4	Nanomechanics	87
4.1	Introduction to nanostructured materials	88
4.1.1	Inorganic nanostructures	89
4.1.2	Organic nanostructures	90
4.2	Mechanics of nanostructures	91
4.2.1	The modulated nanoindentation AFM method	92
4.2.2	Classical elastic beam in the nanoworld	95
4.3	The mutliwalled carbon nanotube	97
4.3.1	Description and characteristics	98
4.3.2	CNTs chirality	98
4.3.3	Synthesis of CNTs	99
4.3.4	CNTs properties	100
4.4	Experimental results on radial elasticity of CNTs	101
4.4.1	Experimental details	102
4.4.2	Molecular dynamics simulations	104
4.4.3	Results and discussion	105
4.5	The tobacco mosaic virus	109
4.5.1	Description and characteristics	109
4.5.2	Possible applications	110
4.5.3	Experiments on TMV mechanics	110
4.6	Experimental results on longitudinal elasticity of TMVs	112
4.6.1	Experimental details	112
4.6.2	Results and discussion	114
4.7	Conclusion	123
	General conclusions	125
	A CNTs elasticity: an overview	127
	Bibliography	135

Introduction

ONE NANOMETER (nm) is equal to one-billionth of a meter. It is approximately the width of 10 water molecules and a human hair is about 80'000 nm wide. This dimension became relevant with the increasing development of the miniaturization of many technological devices, such as micro-electromechanical systems (MEMS) and hard disks, but also in the fields of the biotechnology and medicine, where nanometer sized molecules are studied and used, for example, in the treatment of diseases. Consequently, it has become of primary importance to study the forces occurring at the small scales, as well as the chemical and physical behaviors of nanosystems in function of their surrounding environment.

Unfortunately, the balance of forces reigning in the well-known macroscopic scale is somewhat disrupted as one goes down to the nanoscopic level. Effectively, if we consider a solid parallelepiped body whose dimensions are a , b and c , and if we reduce each of its dimensions by a factor 100, then its volume decreases by a factor 100^3 , whereas its surfaces are reduced by a factor 100^2 . Therefore, the changes for the forces proportional to the surface and for the forces related to the bulk, like inertial forces, are quite dissimilar. As result, the concepts established from a macroscopic point of view are not always valid on a smaller length scale. In theses conditions, it is necessary to be able to measure the forces, to test the properties and the behaviors related to the world of the infinitely small.

In this framework, this thesis proposes to study surface forces and mechanics at the nanometer scale, to which are referred the words "nanotribology"¹ and "nanomechanics" in the thesis title. We will develop in particular the cases of the sliding friction and the mechanics of nano-tubular structures. The fundamental understanding of sliding friction is crucial in fields as widespread as earthquake dynamics and preplanetary dust aggregation, where friction and adhesion are strongly related. It has also an economical impact, as it is the cause of energy loss in many moving components. As for the mechanics of tubular nano-objects, it takes its importance from the development of semiconductor or metal nanostructures at surfaces, where the tubular structures are used as template for hybrid organic/inorganic nanostructures. These challenging structures open the way to complex functional devices based for example on the self-assembly.

The first chapter of this thesis introduces the surface interactions, starting from the forces arising from the proximity of two objects, to the surface deformations occurring with the contact of the objects. The second chapter presents the experimental techniques used in this thesis. It is mainly based on atomic force microscopy, which serves to image the nano-objects and to measure their deformations. The experimental results figure in the third and fourth chapters. The first one deals with sliding friction as function of the relative humidity, the scanning velocity and the applied normal load. The second one is related to the mechan-

¹ The nanotribology is basically the study of friction, adhesion and wear at the nanoscale.

ics of nano-tubular objects adsorbed on surfaces. The experimental results are accompanied with theoretical models that explain the phenomenology and serve as basis to extract physical parameters. In particular, we will measure the Young modulus of the tubular objects. Finally, a conclusion will close this work by reminding the essential points of the thesis.

Chapter 1

Surface interactions

This chapter provides a theoretical basis on surface science. It is divided in two main parts. The first one introduces the concept of surface and presents the case of surfaces in close proximity. The resulting interactions are treated in terms of forces that might be attractive or repulsive. The second part takes the point of view of continuum mechanics to study the case of two surfaces in direct contact. The phenomenology is related to the surface geometry and material elastic properties, which are expressed in a general tensorial form. Special attention will be carried on the question of mechanical properties of transverse isotropic materials.

WHAT DO WE CALL "SURFACES"? By convention, we will define the surface as the separation between a gaseous and a condensed phase (liquid or solid). From a macroscopic point of view, the surface of an object is a well-defined limit corresponding to its outer covering and characterized by the same properties as its body. From a microscopic point of view, the surface is not a well-defined frontier. It corresponds in fact to the spatial extension of an object, related to the transition from the object itself to its surrounding medium. It is a favorable area for chemical and physical interactions, modifying in that way the material properties of the object.

The recurrent order of magnitude which will interest us in this work is the nanoscopic size. It corresponds to 10^{-9} times the usual units of the International System of Units (SI). It is, for example, the size of small molecular objects like viruses or nano-objects of few hundreds of nanometers that will be presented later in Chapter 4. At this length scale, the surfaces have to be thinking in terms of atomic arrangements and the interactions between atoms of adjacent surfaces play a non negligible role. To fix the ideas, we introduce now the concept of ideal surface and then, we gently move to the case of real surfaces by taking the crystalline solid as illustration and keeping the microscopic point of view in mind.

1.1 From ideal surface to real surfaces

We consider a crystal at zero Kelvin, composed of perfectly arranged atoms represented by small spheres. If we split it along a plane (hkl) forming a small angle with one of its dense planes such as (001), (111) or (110), we obtain terraces composed by portions of dense plane

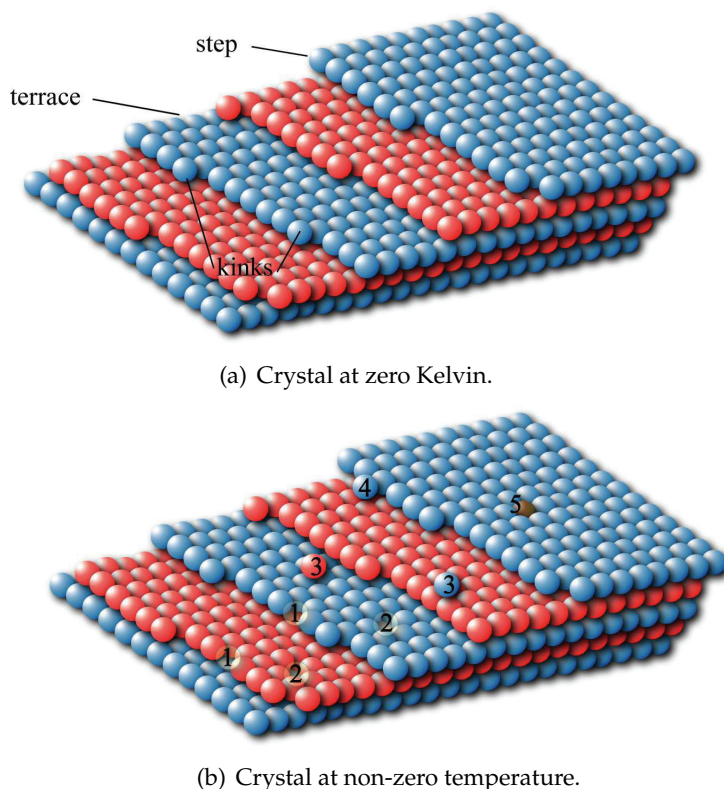


Figure 1.1: Illustration of the transition from the ideal crystal at zero Kelvin (a) to the real case of a surface at non-zero temperature (b).

and separated by steps showing some kinks as presented in Fig. 1.1(a). By increasing the temperature of the surface, the atoms diffuse on the surface due to the energy of thermal activation. The consequence of the new position of the atoms is a roughening of the surface. Figure 1.1(b) illustrates the case of a crystalline solid at non-zero temperature. Some gaps in the edge of the steps (1) and in the terraces (2) are possible. Adatoms diffuse on the terraces (3) or stay against a step (4). Finally, foreign atoms may adsorb on the surface (5). The disorder of the surface follows the increase of temperature until surface melting.

The previous paragraph still concerns model surfaces rarely encountered in engineering science, but rather in semi-conducting science. In fact, a certain roughness of the surface with some alterations appears each time an object is split. If we go from the bulk material to its external surface, we progressively find, first, the intact matter of the object having its own defects, then, an area of structural modification due to the splitting, and finally, a mixture of impurities and deteriorated matter. This last area is generally covered by a thin layer of native oxide with a thickness varying in function of the material and the kinetic of the oxidation. Typical values of 2 nm are found for the silicon oxide, but the thickness of these layers may rise up to hundreds of nanometers in the case of aluminum or titanium oxides. A last modification takes place at the top of the surface. It concerns physical and chemical adsorptions of organic or inorganic molecules. Each time surfaces are used in nanoscale research, the complexity reigning at the extreme part of the objects has to be taken into account.

1.2 Atomic and intermolecular forces

The origin of the surface forces has to be found at the atomic level. Molecular or even macro-molecular forces are generally not due to gravity, but arise from atomic interactions. Let us consider for a first approach a di-atomic molecule formed by two atoms A and B of respective mass m_A and m_B . The frequency of vibration ν of the molecule gives access to an estimation of the force between the two atoms. Indeed, in the case of the harmonic oscillator approximation, the frequency of vibration of the molecular system is given by

$$\nu = \frac{1}{2\pi} \sqrt{k/m_r} \quad (1.1)$$

where k is the spring constant of the system and $m_r = \frac{m_A m_B}{m_A + m_B}$ is the reduced mass of the molecule. Wavenumbers W_n between $100 - 10'000 \text{ cm}^{-1}$ are usually associated to the vibrations of molecules in vibrational spectroscopy studies [1]. Corresponding frequencies are between $3 \cdot 10^{12} - 3 \cdot 10^{14} \text{ Hz}^1$. As result, if we take the case of the hydrogen molecule H_2 characterized by $m_A = m_B = 1.673 \cdot 10^{-27} \text{ kg}$ and $W_n \simeq 4400 \text{ cm}^{-1}$, we obtain $k \simeq 580 \text{ N/m}$. Then, for small vibrations Δx close to the equilibrium state ($\Delta x \sim 10^{-12} \text{ m}$), the force is roughly given by $F = k \cdot \Delta x \sim 6 \cdot 10^{-10} \text{ N}$. This force is an approximation of the order of magnitude characterizing the force between two atoms. In the case of a surface, the atom is generally an integral part of the crystal lattice and it is bound to its neighboring atoms. Those bonds maintain the atom more rigidly to the surface and increase the total spring constant, as well as the final force.

In the next section, we introduce the different interatomic bonds at the origin of many macroscopic properties such as electrical, mechanical and thermal properties. The general idea is that the type of bond depends on the arrangement of the valence electrons when two objects are put the one next to the other one (together). As basic criterium, the total energy of the system in the bound state shall be inferior to the previous total energy, when the bodies were separated. The result is cohesive or adhesive forces that hold molecules or surfaces together.

1.2.1 Ionic bond

The ionic bond is a heteropolar bond related to the electrostatic attraction between electropositive (metallic) and electronegative (non metallic) elements. An example is the ionic salt KBr called potassium bromide. The potassium (K) has the configuration of the argon, a noble gas of the periodic table, plus one electron. If the bromine (Br) gets one electron, it reaches the stable configuration of the krypton. So, due to their difference in electronegativity, attraction occurs between the two ions to reach for each one the stable configuration of the closest noble gas. It results in the formation of the KBr salt for which the supplementary electron of the potassium left its external shell to saturate the last shell of the bromine. The potassium atom becomes negatively ionized and the bromine positively charged. The final result is an electrostatic attraction giving rise to the bonding. The high energy of the ionic bonds confers to ionic solids a high melting point. Moreover, a larger difference in the electronegativity between the atoms induces a stronger ionic bond.

¹ $W_n \cdot c = \nu$, with $c \simeq 3 \cdot 10^{10} \text{ cm/s}$ being the velocity of the electromagnetic radiation.

1.2.2 Covalent bond

Whereas the ionic bond is characterized by a donation of valence electrons, covalent bonding is subject to the sharing of valence electrons between neighboring atoms of equivalent electronegativity. As atoms are brought together, the atomic orbitals interact to form molecular orbitals. The shared electrons take up the area between the two bound atoms, screening the nucleus repulsion. Usually, bonds are defined by a mutual attraction that holds the resultant molecule together. An example of covalent bonding is the hydrogen molecule H_2 .

Covalent bonds may be stronger than ionic bonds, but in contrast to the latter, the strength of the covalent bond depends on the angular relation between the atoms in polyatomic molecules. Thus, covalent bonds have a specific direction, whereas ionic bonds have a non-directional spherical symmetry. From a mechanical point of view, covalent materials are hard and fragile, like the diamond which is hard to cleave due to a high charge density between the ions.

1.2.3 Metallic bond

In the metallic bonding, the valence electrons are not bound to specific atoms, but are shared among the whole atoms forming the metal lattice. They are delocalized and move freely in the crystal. One often speaks about a sea of electrons surrounding a lattice of positive ions to describe the case of the metallic bonds. From a simple point of view, the result of having free electrons in the solid is a high thermal and electrical conductivity. As the positive ions are not directly bound to each other, but owe their cohesion to their interactions with the valence electrons, the atoms or layers are allowed to slide past each other, resulting in the characteristic properties of malleability and ductility of metals. Finally, the strong attractive force between the electrons and the positive ions induces generally also a high melting or boiling point.

1.2.4 Van der Waals forces

Van der Waals bonds are due to electrostatic forces called van der Waals (vdW) forces. These forces are weaker than the previous one observed in the case of ionic, covalent or metallic bonds and are for example responsible for the condensation of noble gas at low temperature. The origin of vdW forces is generally attributed to electromagnetic forces and one distinguishes three different types of contributions: the electrostatic contributions, the induction contributions and the dispersion contributions.

The Coulomb force F is the basis for the understanding of intermolecular forces. This electrostatic force interacting between two charges Q_1 and Q_2 is given by the formula

$$F = \frac{Q_1 Q_2}{4\pi\epsilon\epsilon_0 d^2} \quad (1.2)$$

where d is the distance between the charges. The parameter ϵ is the dielectric permittivity of the medium and ϵ_0 is the vacuum permittivity. The corresponding potential energy W is obtained by the negative integration of the previous equation and results in

$$W = \frac{Q_1 Q_2}{4\pi\epsilon\epsilon_0 d} \quad (1.3)$$



Figure 1.2: Schematic representation of the interaction between charges and dipoles.

As consequence, opposite charges have a negative potential energy that is reduced when the charges get closer. Van der Waals forces are based on the same principle. Most of the molecules are not charged, but they present generally a non uniform repartition of the electric charge inducing a dipole² in the molecule. This dipole is schematically represented by a vector μ pointing from the negative to the positive side of the molecule and called the dipole moment. For two opposite charges Q and $-Q$ separated by a distance D , we have $\mu = Q \cdot D$. Two effects have an opposed contribution on the dipole. If the dipole is free to rotate, it will point its negative pole towards the positive charge at proximity, whereas thermal activation will drive it away from a perfect orientation. On average the preferential orientation chosen by the dipole is to point toward the monopole. As result, two freely rotating dipoles, given by μ_1 and μ_2 , attract each other through their opposite charge. Their potential energy, that corresponds in fact to the Helmholtz free energy of interaction³, is then given by [2]

$$W = -\frac{C_{orient}}{D^6} = -\frac{\mu_1^2 \mu_2^2}{3(4\pi\epsilon_0)^2 k_B T D^6} \quad (1.4)$$

where $D \gg d$ is the distance between the dipole and C_{orient} is a parameter independent of the distance between the monopoles. $k_B T$ represents the thermal energy, k_B being the Boltzmann constant and T the temperature. This randomly oriented electrostatic dipole interaction is generally referred to as the **Keesom** contribution to the van der Waals forces.

Another contribution involves the effect of a charge on a molecule having no static dipole moment. In fact, even if the molecule has a homogeneous distribution of the charges, the presence of a monopole induces a charge shift and creates a polar molecule. The induced dipole μ_{ind} interacts then with the charge. In the case of freely rotating dipoles, a molecule with a static dipole moment interacts with a different, but polarisable molecule, giving rise to the Helmholtz free energy expressed as [2]

$$W = -\frac{C_{ind}}{D^6} = -\frac{\mu^2 \alpha}{(4\pi\epsilon_0)^2 D^6} \quad (1.5)$$

with α being the polarizability in $C^2 m^2 J^{-1}$ and defined by the relation $\mu_{ind} = \alpha \cdot E$, where E is the electric field strength. C_{ind} is a term independent of the distance. This effect is called the **Debye** interaction and corresponds to the randomly oriented induced dipole contribution to the van der Waals forces.

² A dipole is induced by the presence of a negative and a positive side in the molecule.

³ The Helmholtz free energy is a thermodynamic potential which measures the *useful* work obtainable from a closed thermodynamic system at a constant temperature. It has to be distinguished from the Gibbs free energy that applies to systems evolving at constant temperature and pressure. The expression of energy given in Equ. 1.4 is derived under constant volume conditions.

The last contribution concerns dispersion interactions. In fact, the two previous explanations fail to explain the attraction between non polar molecules that is experienced in gas condensation at some temperature. To explain such a behavior, we have to refer to quantum mechanical perturbation theory. An illustration is given by considering an atom having its electrons circulating at high frequency around its positive nucleus. If we freeze the atom at a time t , it will show a polarity due to the spatial repartition of its electrons, i.e. we might find more electrons in an area, than in another one. As result, the direction of the atom polarity changes at high frequency following the rapid movement of its electrons around the nucleus. Now, if one approaches two atoms, referred to as atom 1 and atom 2, they will start to influence each other, and, on average, attractive orientations will dominate. The result is an attractive force, called dispersion or **London force**, characterized in the case of molecules by the Helmholtz free energy [2]

$$W = -\frac{C_{disp}}{D^6} = -\frac{3}{2} \cdot \frac{\alpha_1 \alpha_2}{(4\pi\epsilon_0)^2 D^6} \cdot \frac{h\nu_1 \nu_2}{\nu_1 + \nu_2} \quad (1.6)$$

where the suffixes refer to the corresponding atoms. $h\nu_1$ and $h\nu_2$ are the ionization energies of the molecules, h being the Planck's constant and ν , the respective frequency. Again, the parameter C_{disp} regroups the terms independent of the distance.

The vdW forces are the sum of the Keesom, Debye and London interactions, with generally a domination of the London contribution based on the dispersion forces. Thus, we can add all the terms independent of the distance by writing $C_{vdW} = C_{orient} + C_{ind} + C_{disp}$, with the final potential energy decreasing in accordance with $1/D^6$. From a general point of view, the polarization of the electronic cloud and the presence of dipoles are at the origin of van der Waals forces. Contrary to the previous strong bonds, there is no charge transfer between molecules in the case of van der Waals bonding. Resulting solids are generally soft with bad mechanical properties, as solid noble gas.

1.2.5 Hydrogen bonding

Hydrogen bonding is a particular bond in chemistry. If one considers a water molecule H_2O , two hydrogen atoms are bound to one oxygen with a sharing of their electrons. It may be shown that the electron of the hydrogen has a higher probability to be found in the proximity of the oxygen atom. Practically, it amounts to say that the hydrogen atom has lost one electron to the favor of the oxygen, which one becomes negatively charged. It explains why water molecules attract each other, as the positively charged hydrogen is attracted by the oxygen of the other water molecule. So, the hydrogen atom divides up its bond between the water molecule it belongs, and an adjacent molecule. Generally, when a molecule has at its periphery a group OH or NH, the electron of the hydrogen is transferred to the O or N atoms which are deeply electronegative. It results in a positive charge ending, the proton, which can easily polarize a neighboring oxygen atom. The hydrogen atoms bind for example two O, N or F atoms, which is contrary to elementary valence laws (O-H..O): it is an electrostatic bond where the hydrogen atom is not symmetrically placed between the atoms. The hydrogen bond is generally stronger than vdW forces, but weaker than covalent or ionic bonds and it often intervenes in organic molecules bonding.

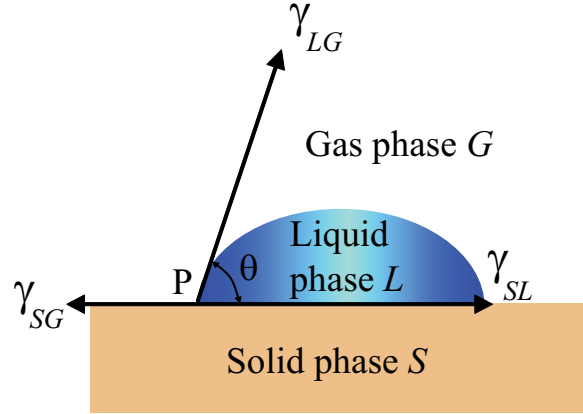


Figure 1.3: Liquid phase on a solid phase and its corresponding contact angle.

1.2.6 Capillary forces

Another force relevant at the molecular level is the capillary force. Under ambient conditions, a surface might be covered by a thin layer of water coming from the condensation of the humidity. The adsorbed water molecules influence then the contact between two solids, modifying their adhesion and friction. The configuration of the adsorbed water molecules on a surface depends on its wetting properties. From a general point of view, the phenomenon of wetting corresponds to the equilibrium between a solid phase S on which are deposited atoms or molecules of a liquid phase L , and the whole surrounded by atoms or molecules of a gaseous phase G (See Fig. 1.3). The intersection between the three phases is called the contact line. The angle between the flat solid surface and the tangent to the gas/liquid interface, measured from the liquid side of the contact line, is called the contact angle θ . It is representative of the wetting properties of the system and it depends on the interfacial tensions between the solid and the liquid (γ_{SL}), between the solid and the gas (γ_{SG}), and between the liquid and the gas (γ_{LG}). The surface tension is measured in Nm^{-1} and is defined, for example in the case of a liquid surface in equilibrium, as the force per unit length along a line perpendicular to the surface, necessary to cause the extension of this surface. In the case of a solid-liquid interface, the wetting of the surface is defined by the wetting coefficient K_W following the equation

$$K_W = \cos(\theta) = \frac{\gamma_{SG} - \gamma_{SL}}{\gamma_{LG}} \quad (1.7)$$

This last equation is often referred to as Young's equation in memory of the first person who derived an expression for the contact angle [3]. The wetting is considered as perfect if $K_W = 1$, whereas there will be no wetting when $K_W = -1$. Then, depending on the surface species, different situations take place in terms of surface and interfacial tensions. If K_W is strictly inferior to minus one, the liquid gathers in droplets and there is no wetting of the surface (example: mercury-glass). If $-1 < K_W < 1$, a contact angle θ is measured. In the case of water, for θ greater than 90° , one speaks about hydrophobic surface, whereas for θ smaller than 90° , the surface has a hydrophilic behavior, which means that the water

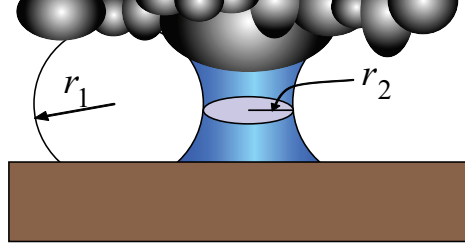


Figure 1.4: Kelvin radii for a capillary bridge between two surfaces.

molecules are more attracted to the surface than to themselves⁴. Finally, if K_W is strictly superior to one, there is no more equilibrium, the liquid spreads out on the surface and forms a layer.

For a working environment with a non-zero percentage of relative humidity, two surfaces at a near contact position present a potentially suitable geometry for the formation of water bridges. The water will spontaneously condensed from vapor into bulk on the surfaces with which it has a small contact angle. The molecules of water arrange themselves in the gaps and small cavities. They form capillaries that bind the neighboring surfaces. For constant environmental conditions, the size of the capillary depends on the geometry and chemistry of the surfaces. Lord Kelvin gave one of the first classical views of a capillary bridge. Referring to the Fig. 1.4, the principal radii of curvature of the meniscus formed between the surface asperities are r_1 and r_2 . The Kelvin radius R_K of the meniscus is then determined by the relation [4]

$$R_K = \left(\frac{1}{r_1} + \frac{1}{r_2} \right)^{-1} \quad (1.8)$$

At equilibrium, the relation between the Kelvin radius and the relative vapor pressure of water P/P_S is [4]

$$R_K = \frac{\gamma V_M}{k_B T \ln(P/P_S)} \quad (1.9)$$

where P and P_S are respectively the effective and saturation water vapor pressure⁵. γ is the surface tension of the liquid, V_M the molar volume, k_B the Boltzmann constant and T the temperature. The additional force on adhesion arising from the condensation of a capillary between a flat surface and a sphere finds its root in the work of Young, Laplace and Kelvin. For a capillary, the Laplace pressure P_L under the condition $r_1 \ll r_2$ becomes [5]

$$P_L = \gamma \left(\frac{1}{r_1} + \frac{1}{r_2} \right) \approx \frac{\gamma}{r_1} \quad (1.10)$$

⁴ The relation between the contact angle and the property of hydrophilic behavior or hydrophobicity is still not well defined. Generally contact angles to water $\theta \ll 10^\circ$ refer to super-hydrophilic surfaces by opposition to super-hydrophobic surfaces ($\theta > 120^\circ$). Then for $10^\circ < \theta < 80^\circ$ the surface is normal-hydrophilic and for $\theta \approx 80 - 120^\circ$ the surface is called normal-hydrophobic.

⁵ P/P_S corresponds to the relative humidity RH in the case of water.

Nature of bond	Type of force	Distance [\AA]	Energy [kcal/mol]
Ionic bond	Coulombic force	2.8	180 (NaCl)
		2	240 (LiF)
Covalent bond	Electrostatic force (wave function overlap)	N/A	170 (Diamond) 283 (SiC)
Metallic bond	free valency electron sea interaction	2.9	96 (Fe)
		3.1	210 (W)
Hydrogen bond	directional dipole-dipole interaction	N/A	7 (HF)
Van der Waals	dipole-dipole dipole-induced dipole dispersion force	few \AA to hundreds of \AA	2.4 (CH_4)

Table 1.1: Overview of the type of surface forces.

Referring to Fig. 1.5, the Laplace pressure acts on an area equals to $\pi x^2 \approx 2\pi R d$. The resulting adhesion force is then $F \approx 2\pi R d(\gamma/r_1)$. This adhesion force is called the capillary force F_C and in a more general case, it is given by the equation [4]

$$F_C = \frac{2\pi R \gamma (\cos(\theta_T) + \cos(\theta_S))}{1 + D/d} \quad (1.11)$$

where D is the separation between the sphere and the plane, θ_T and θ_S are respectively the contact angles of the flat surface and the sphere. The stronger capillary force arises from the condition of separation $D = 0$.

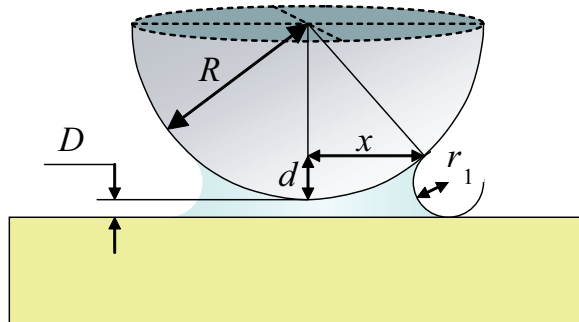


Figure 1.5: Geometric representation of a capillary bridge between a flat surface and a sphere.

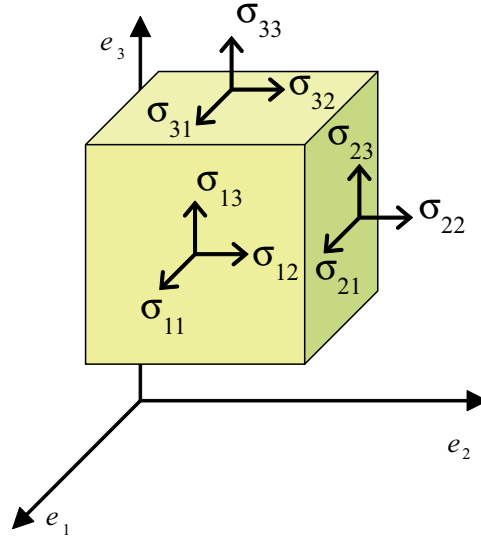


Figure 1.6: Stress formalism for a loaded small cube.

1.3 Continuum mechanics

In this section, we introduce the phenomenology related to surfaces in direct contact. We give a general idea of the main theories governing the contact between elastic homogeneous isotropic bodies. We start from the pioneering work of Heinrich Hertz written in 1881 [6] and follow its gradual improvements related to the evolution of the experimental results in the field of elastic deformations. Contact mechanics deals with bulk material properties like classical mechanics, but on the contrary to the latter, it considers also the surface and geometrical constraints acting on the matter. The elastic behavior of a body is based on Newton's laws of motion, Euclidian geometry and Hooke's law.

1.3.1 Generalized Hooke's law

When two solids are in contact, they undergo deformations going from the elastic to the plastic range. The constitutive equations governing the elastic deformations are given by the generalized Hooke's law. The behavior of the solids under stress is approximated on the basis of the following assumptions:

1. the relation between the applied stress and the deformation is linear;
2. the deformation is very small and disappears completely upon removal of the initial stress;
3. the rate of stress application does not affect the behavior of the material upon time;

The second condition corresponds in fact to the definition of an elastic solid, by opposition to non-elastic solids, which show a hysteresis for the deformation versus stress relation. From these assumptions, it is possible to establish the constitutive equations of an ideal

material, called the *Hookean* elastic solid.

Specific notations are generally used to express the Hooke's relations. The stress components are denoted by the symbol σ_{ij} with the suffix j indicating the direction of the stress component, and i , the direction of the outward normal to the surface upon which the stress acts. An illustration in the Cartesian coordinate system $(\mathbf{e}_1, \mathbf{e}_2, \mathbf{e}_3)$ is given in Fig. 1.6. As consequence, normal stresses have both suffixes the same, whereas shear stresses have two different suffixes⁶. From the equilibrium of moments acting on the cube of Fig. 1.6, we find the relations $\sigma_{ij} = \sigma_{ji}$ for $i, j = 1, 2, 3$. Strain components are denoted by the symbol ε_{ij} with the appropriate i, j suffixes. Each of the stress components is a linear function of the components of the strain tensor. The general elastic body is finally represented by a 6×6 stiffness matrix of coefficients C_{ij} called the elastic coefficients [7]:

$$\begin{pmatrix} \sigma_{11} \\ \sigma_{22} \\ \sigma_{33} \\ \sigma_{12} \\ \sigma_{13} \\ \sigma_{23} \end{pmatrix} = \begin{pmatrix} C_{11} & C_{12} & C_{13} & C_{14} & C_{15} & C_{16} \\ C_{21} & C_{22} & C_{23} & C_{24} & C_{25} & C_{26} \\ C_{31} & C_{32} & C_{33} & C_{34} & C_{35} & C_{36} \\ C_{41} & C_{42} & C_{43} & C_{44} & C_{45} & C_{46} \\ C_{51} & C_{52} & C_{53} & C_{54} & C_{55} & C_{56} \\ C_{61} & C_{62} & C_{63} & C_{64} & C_{65} & C_{66} \end{pmatrix} \begin{pmatrix} \varepsilon_{11} \\ \varepsilon_{22} \\ \varepsilon_{33} \\ \varepsilon_{12} \\ \varepsilon_{13} \\ \varepsilon_{23} \end{pmatrix} \quad (1.12)$$

The elastic coefficients depend on the time, the temperature and the location in the body if it is inhomogeneous. In fact, the relations given by the system of Equations 1.12 are an approximation for small strains, since any continuous function is approximately linear in a small range of its variables. For a given time, temperature and location in the body, the coefficients C_{ij} are constant and characteristic of the body material. Moreover, it can be shown that the matrix \mathbf{C} is symmetric [7], and thus, the general anisotropic linear elastic material is characterized by 21 elastic coefficients C_{ij} governing its elastic behavior. More details on the general theory of elasticity might be found in reference [7].

We are now interested to develop the constitutive relationships in the special case of the transversely isotropic material. This property of transverse isotropy is usually found in rod-shaped structures like cylindrical beams or reinforced fibers going from the macroscopic to nanoscopic range of scale [8, 9]. For such structures, each plane perpendicular to their long axis is a plane of material symmetry. The planes in which their long axis lies are called planes of isotropy. If we consider the case of a cylinder with its long axis along x_1 and its plane of isotropy described by the coordinates x_2 and x_3 according to an orthonormal coordinate system (See Fig. 1.7), its transverse isotropy is defined by five independent elastic coefficients: C_{11} , C_{12} , C_{13} , C_{33} and C_{44} . Thus, due to the isotropy and the symmetries of the solid, the stress-strain laws become:

⁶ Shear components are often represented by the symbol τ , while σ is retained for normal stress.

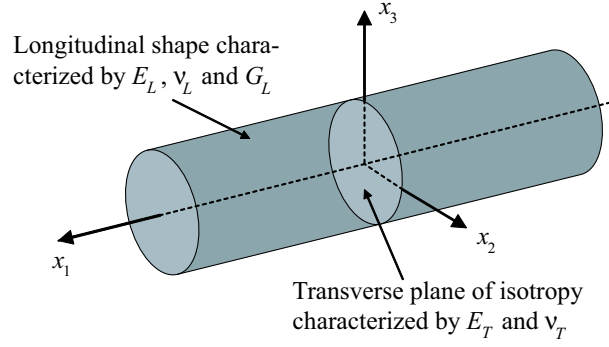


Figure 1.7: Characteristic planes and their corresponding elastic constants for a transverse isotropic tubular structure.

$$\begin{pmatrix} \sigma_{11} \\ \sigma_{22} \\ \sigma_{33} \\ \sigma_{2,3} \\ \sigma_{31} \\ \sigma_{12} \end{pmatrix} = \begin{pmatrix} C_{11} & C_{12} & C_{13} & 0 & 0 & 0 \\ C_{12} & C_{11} & C_{13} & 0 & 0 & 0 \\ C_{13} & C_{13} & C_{33} & 0 & 0 & 0 \\ 0 & 0 & 0 & C_{44} & 0 & 0 \\ 0 & 0 & 0 & 0 & C_{44} & 0 \\ 0 & 0 & 0 & 0 & 0 & (1/2)(C_{11} - C_{12}) \end{pmatrix} \begin{pmatrix} \varepsilon_{11} \\ \varepsilon_{22} \\ \varepsilon_{33} \\ 2\varepsilon_{23} \\ 2\varepsilon_{31} \\ 2\varepsilon_{12} \end{pmatrix} \quad (1.13)$$

In the transverse isotropic plane of the solid, only two elastic parameters are required to describe its mechanical properties. A more conventional form of the stiffness matrix is the compliance matrix \mathbf{S} given by $\mathbf{S} = \mathbf{C}^{-1}$. This matrix is also symmetric and gives a direct access to the engineering constants for the transversely isotropic elastic solid. Considering cylindrical coordinates (r, θ, z) to describe a tubular structure having its long axis along z in the plane of isotropy, the compliance stress-strain relations might be written in the following form:

$$\begin{pmatrix} \varepsilon_{rr} \\ \varepsilon_{\theta\theta} \\ \varepsilon_{zz} \\ \varepsilon_{\theta z} \\ \varepsilon_{rz} \\ \varepsilon_{r\theta} \end{pmatrix} = \begin{pmatrix} \frac{1}{E_T} & \frac{-\nu_T}{E_T} & \frac{-\nu_L}{E_L} & 0 & 0 & 0 \\ \frac{-\nu_T}{E_T} & \frac{1}{E_T} & \frac{-\nu_L}{E_L} & 0 & 0 & 0 \\ \frac{-\nu_L}{E_L} & \frac{-\nu_L}{E_L} & \frac{1}{E_L} & 0 & 0 & 0 \\ 0 & 0 & 0 & \frac{1}{G_L} & 0 & 0 \\ 0 & 0 & 0 & 0 & \frac{1}{G_L} & 0 \\ 0 & 0 & 0 & 0 & 0 & \frac{1}{G_T} \end{pmatrix} \begin{pmatrix} \sigma_{rr} \\ \sigma_{\theta\theta} \\ \sigma_{zz} \\ \sigma_{\theta z} \\ \sigma_{rz} \\ \sigma_{r\theta} \end{pmatrix} \quad (1.14)$$

Five constants describe the phenomenology of the transverse isotropic body: ν_T , E_T , ν_L , E_L and G_L . The constants ν_T and E_T are respectively the Poisson ratio and the Young modulus of the planes perpendicular to the z -axis. In these planes, the relation between ν_T , E_T and the transverse shear modulus G_T is given by

$$G_T = \frac{E_T}{2(1 + \nu_T)} \quad (1.15)$$

ν_L , E_L and G_L are the elastic constants in the longitudinal plane, i.e. the plane of isotropy. They are respectively the Poisson ratio, and the Young and shear moduli. Whereas only two constants are necessary to describe the behavior of an isotropic material, five elastic constants define the elastic properties of transversely isotropic bodies.

1.3.2 Contact mechanics

Hertz theory

When two elastic solid bodies are pressed together, the pressure acting on the limited contact area generates local stresses. The initial problem related to this contact of two elastic bodies was to determine, on the one hand, the contact area, and, on the other hand, the maximum stress on and beneath the contact area. One must wait the end of the 19th century to find the first theories in good agreement with the experiments. One of these theories is due to H. Hertz [6]. He was the first to obtain a satisfactory solution for the compressive stresses in the contact area between two ideal elastic bodies having curved surfaces. His theoretical concepts have served as basis for numerous further developments. Note that his theory of continuum elasticity does not take into account the surface forces that may be acting between the two bodies in contact.

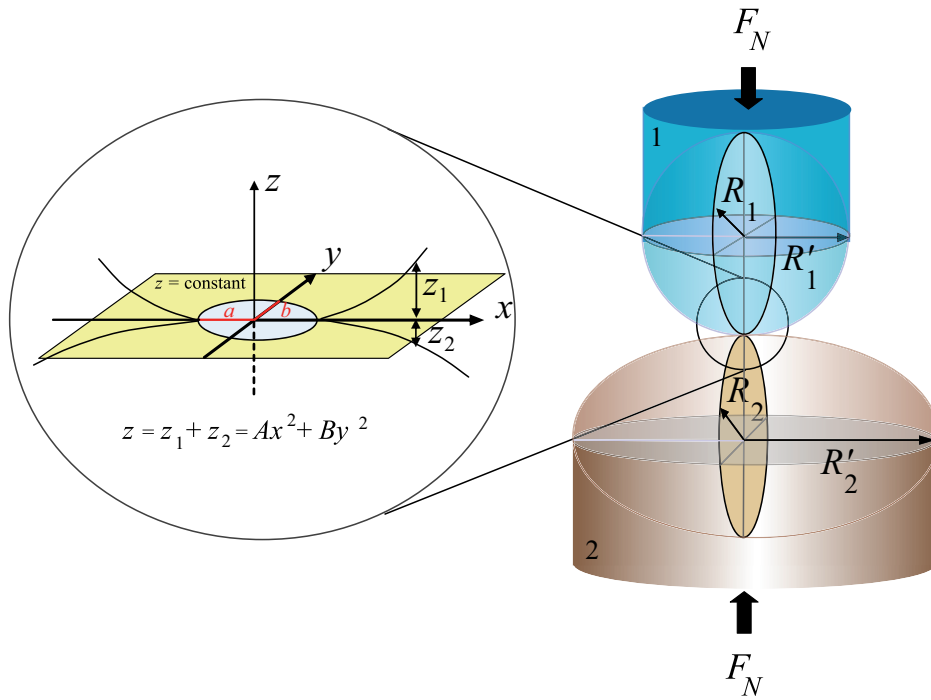


Figure 1.8: Illustration of the contact of two egg-shaped bodies in the model of Hertz.

The geometry of the initial problem of contact mechanics is illustrated in Fig. 1.8. Two egg-shaped bodies, denoted by the suffixes 1 and 2, are initially in contact at a single point. They are made of homogeneous, isotropic and elastic material satisfying Hooke's law. Their respective principal radii of curvature are R_1, R'_1 and R_2, R'_2 , and their curved surfaces are smooth near the contact point. The radii are positive when the centers of curvature are

located inside the respective bodies. A system of normal forces F_N presses one body against the other one in their elastic range of deformation. The action line of F_N lies along the axis that passes through the initial contact point and the centers of curvature of the bodies. Due to F_N , the surfaces of the solid bodies are elastically deformed over an area surrounding the initial contact point. These deformations allow the bodies to contact over a small area neighboring the initial contact point and being part of their common tangent plane. The distance z separating two neighboring points⁷ is given by the equation

$$z = Ax^2 + By^2 \quad (1.16)$$

where A and B are positive constants that depend upon the principal radii of curvature of the bodies at the contact point, and on the angle between the corresponding planes of the principal curvatures. x and y are Cartesian coordinates in the tangent plane. The origin of the x - and y -axes is fixed at the contact point as shown in Fig. 1.8. It is assumed that under the action of F_N on the bodies, points which were originally at an equal distance of the tangent plane come into contact. Hence, through Equ. 1.16, those contacting points form an elliptic contact area characterized by the equation

$$\frac{x^2}{a^2} + \frac{y^2}{b^2} = 1 \quad (1.17)$$

in which a and b correspond respectively to the semi-major and semi-minor axes of the ellipse as presented in the enlargement of the contact area in Fig. 1.8. As result, Hertz obtained the following equations describing the mechanics of contact:

$$\delta = \frac{3kF_N K(k')(A+B)\Delta}{2\pi b} \quad (1.18)$$

$$b = \sqrt[3]{\frac{3kE(k')}{2\pi} F_N \Delta} = ka \quad (1.19)$$

The variable $\delta = \delta_1 + \delta_2$ corresponds to the relative displacement of the body centers toward each other by amounts δ_1 and δ_2 for body 1 and 2 respectively. Actually, the relation between δ and z is $\delta - (w_1 + w_2) = z$, where w_i ($i \in \{1,2\}$) is the displacement due to local compression of a point of the body i . w_i is defined positive in the direction away from the tangent plane. The different variables involved in these equations are defined as follows:

⁷ A point M_1 of the body 1 is a neighboring point for a point M_2 of body 2 if they lie on the same perpendicular line of the tangent plane.

$$k = \frac{b}{a} = \sqrt{1 - k'^2} \quad (1.20)$$

$$K(k') = \int_0^{\pi/2} \frac{d\theta}{\sqrt{1 - k'^2 \sin^2 \theta}} \quad (1.21)$$

$$E(k') = \int_0^{\pi/2} \sqrt{1 - k'^2 \sin^2 \theta} d\theta \quad (1.22)$$

$$B = \frac{1}{4} \left(\frac{1}{R_1} + \frac{1}{R_2} + \frac{1}{R'_1} + \frac{1}{R'_2} \right) \quad (1.23)$$

$$A = \frac{1}{4} \left(\frac{1}{R_1} + \frac{1}{R_2} + \frac{1}{R'_1} + \frac{1}{R'_2} \right) + \frac{1}{4} \sqrt{\left[\left(\frac{1}{R_1} - \frac{1}{R'_1} \right) + \left(\frac{1}{R_2} - \frac{1}{R'_2} \right) \right]^2 - 4 \left(\frac{1}{R_1} - \frac{1}{R'_1} \right) \left(\frac{1}{R_2} - \frac{1}{R'_2} \right) \sin^2(\alpha)} \quad (1.24)$$

$$\frac{B}{A} = \frac{(1/k^2)E(k') - K(k')}{K(k') - E(k')} \quad (1.25)$$

$$\Delta = \frac{1}{A + B} \left(\frac{1 - \nu_1^2}{E_1} + \frac{1 - \nu_2^2}{E_2} \right) = \frac{1}{E^*(A + B)} \quad (1.26)$$

k is the ratio of the ellipse semi-axes. K and E are complete elliptic integrals of the second kind. α corresponds to the angle between the planes of principal curvatures at the contact point. E_i and ν_i are respectively the normal Young modulus of elasticity and the Poisson ratio of the corresponding bodies ($i \in \{1, 2\}$) that are written in a more general form using the term of reduced elastic modulus E^* . The parameters A , B , k' , k are strictly related to the geometry of the contact area, whereas E_i and ν_i describe the material properties of the contacting bodies. More details on solving the Hertz problem are found in Ref. [10]. Since the Hertz model does not consider the adhesion between the contacting solids, then, if the normal force $F_N = 0$, the indentation and the contact radius are also zero. Two interesting cases of the Hertz theory are the contact between a sphere and a plane, and the contact of a sphere with a cylinder. The first case is a usual model for the indentation of a flat surface with a hard ball to measure its normal mechanical properties. The second case will interest us more specifically when deforming small cylindrical structures with a round shaped tip. Those two cases are based on the general equations described above and the particularity of their geometry is reported in the table 1.2.

JKR theory

In the Hertz theory, the surface interactions, such as near contact van der Waals interactions, or contact adhesive interactions, are neglected. Thus, the Hertz model describes accurately the contact between elastic bodies in the absence of adhesion, but it is not reliable as soon as significant attractive surface forces are no more negligible. Actually, the development

Variables	sphere-plane	sphere-cylinder
curvatures	sphere: $R_1 = R'_1$ plane: $R_2 = R'_2 = \infty$	sphere: $R_1 = R'_1$ cylinder: R_2 and $R'_2 = \infty$
material properties	sphere: E_1, ν_1 plane: E_2, ν_2	sphere: E_1, ν_1 cylinder: E_2, ν_2
A and B constants	$A = B = \frac{1}{2R_1}$	$A = \frac{1}{2R_1}, B = \frac{1}{2} \left(\frac{1}{R_1} + \frac{1}{R_2} \right)$
contact radius	$a = b = \sqrt[3]{\frac{3F_N R_1}{4E^*}}$	$b = \sqrt[3]{\frac{3kE(k')}{2\pi E^*} F_N \left(\frac{2R_2 + R_1}{2R_1 R_2} \right)} = ka$
relative indentation	$\delta = \left(\frac{3F_N}{4E^*} \right)^{2/3} R_1^{-1/3} = a^2/R_1$	$\delta = \frac{K(k')}{E(k')^{1/3}} \left(\frac{3kF_N}{2\pi E^*} \right)^{2/3} \left(\frac{2R_2 + R_1}{2R_1 R_2} \right)^{1/3}$

Table 1.2: Hertz theory in the case of a sphere-plane contact and sphere-cylinder contact.

of nanoscale sciences showed that the contact area as calculated with the Hertz model is generally underestimated, especially when the load F_N decreases to zero. In fact, the case $a = \delta = 0$ never occurs in experiments. It proves that the surface forces do play an important role at the nanometer scale, even at zero load. The first successful model taking account of surface forces was elaborated by Johnson, Kendall and Roberts in 1971 and is called the JKR model [11]. In this model, the adhesion due to short-range forces inside the contact area is taken into consideration. In the case of a sphere of radius R contacting a compliant elastic half space, this adhesion force is $F_{adh} = 3\pi\gamma R = 3/2\pi W R$, where γ is the effective surface energy of adhesion of both surfaces and W the corresponding work of cohesion per unit area gained when two identical solid materials come into contact [12]. For $\gamma = 0$ (or $W = 0$), one recovers the Hertz model with no adhesion force. The contact radius a and the relative indentation δ predicted by the JKR theory for the contact between the sphere and the half plane is given by the equations

$$a = \left(\frac{3R}{4E^*} \right)^{1/3} \left(F_N + 3\pi\gamma R + \sqrt{6\pi\gamma R F_N + (3\pi\gamma R)^2} \right)^{1/3} \quad (1.27)$$

$$\delta = \frac{a^2}{R} - \left(\frac{2\pi\gamma a}{E^*} \right)^{1/2} \quad (1.28)$$

By adding an adhesive force to the Hertz model, the JKR theory is able to explain why contacts can be formed during the unloading cycle, also in the negative loading of one body against another one. However, the JKR approach of the contact of two elastic bodies is not right in every case, since it neglects the forces acting outside the contact area. Generally, this model gives a good description in the case of large, soft solids. In fact, the assumption that the system gains energy only when materials are in direct contact is reasonable only for relatively compliant materials showing a strong short-range adhesion. The case of stiff materials characterized by a weak long-range adhesion force needs therefore another theory, which will be the Derjaguin-Müller-Toporov (DMT) theory.

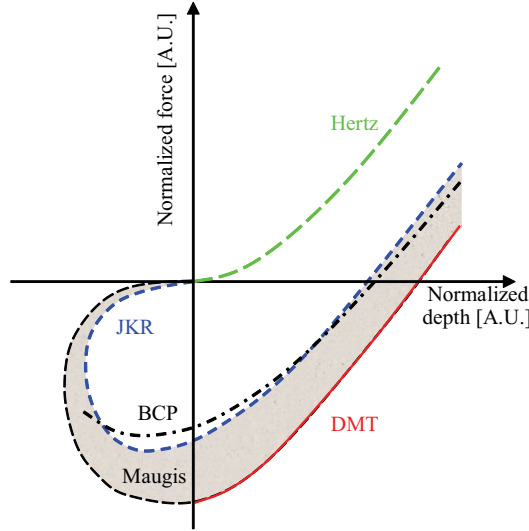


Figure 1.9: Comparison of the different contact theories: the initial Hertz theory and its two extreme developments corresponding to the JKR and DMT models, with, in between, the Maugis-Dugdale theory allowing different values of forces as function of the body material. The figure has been adapted from Ref. [14], where more details on the force and depth normalisation might be found.

DMT theory

The DMT model of elastic contact involves the calculation of the attractive forces acting in the periphery of the contact area [13]. Sometimes, this attraction is represented by a kind of meniscus formed along the contact line. This model assumes that the deformed profile given by the Hertz model does not change for a spherical body of radius R interacting with a plane. Thus, the normal force F_N is simply completed by a supplementary long-range adhesion force, $F_{adh} = 4\pi\gamma R$, acting outside the contact zone. This model is appropriate for small, hard solids and the equations for the contact radius and the relative indentation in the case of a sphere indenting a plane become

$$a = \left(\frac{3R}{4E^*} \right)^{1/3} (F_N + 4\pi\gamma R)^{1/3} \quad (1.29)$$

$$\delta = \frac{a^2}{R} \quad (1.30)$$

1.3.3 Experimental contact area

From the point of view of the nanoscale sciences, determining the contact area is crucial when measuring friction forces, mechanical properties or performing material indentations. The Hertz model, while describing accurately the behavior of contact mechanics in the case of large loads, is not sufficient when dealing with weak normal forces that become comparable to the adhesion force. It has to be completed by an appropriate estimation of the surface forces. The aim of the DMT or JKR theories was to complete the Hertz model of the interaction between two contacting surfaces by adding the surface forces. The limitations of

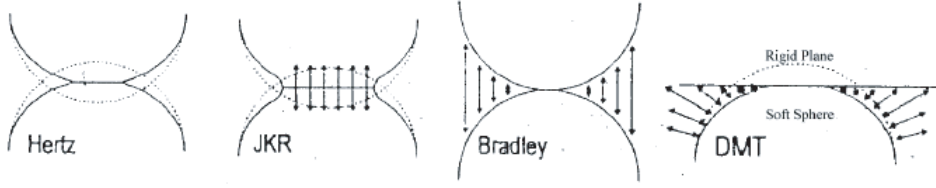


Figure 1.10: Schematic illustration of the contact areas for different contact models (From Ref. [17]).

the DMT and JKR theories are respectively the underestimation of the contact area due to a restrictive contact geometry and the underestimation of the loading force due to the surface forces. The DMT and JKR theories represent two extreme models of the real situation. In between, some other interesting theories, like the Burnham-Colton-Pollock (BCP) [15] theory, or more specifically the Maugis-Dugdale theory [16], propose more accurate descriptions of a sphere contacting a flat plane. Unfortunately, they cannot be expressed as useful analytical expressions due to complex parametric equations or surface parameters determination, and thus, they are less convenient to apply to experimental data. Figure 1.9 shows graphically the difference between the mechanics of contact of these models.

A usual way to describe contact mechanics in experimental studies is to define an effective normal force $F = F_N + F_{adh}$, where the adhesion force F_{adh} is the offset force required to break the contact at zero load and thus, represents all the surface forces. By implementing this modified normal force in the Hertz theory, we obtain a good approximation of the contact mechanics, convenient for theoretical developments and fitting well the experimental data for low loads. The main equations of Hertz theory become then

$$\delta = \frac{3k(F_N + F_{adh})K(k')}{2\pi} \left(\frac{A + B}{b/\Delta} \right) \quad (1.31)$$

$$b = \sqrt[3]{\frac{3kE(k')}{2\pi}(F_N + F_{adh})\Delta} \quad (1.32)$$

1.3.4 Notion of compliance

The compliance C is by definition a measure of the stiffness of a material, i.e. the amount of force per unit displacement required to compress an elastic contact in a particular direction. It corresponds to the inverse of the elastic spring constant of the material and is also defined as $C_i = d\delta_i/dF_i$, where δ_i and F_i are respectively the relative approach of two bodies and the contacting system of forces parallel to the i -axis. In the case of the contact of two egg-shaped bodies as illustrated in Fig. 1.8, there exist three different compliances: the torsional, the tangential and the normal compliance. The main paper describing the compliance of elastic bodies in such a configuration was written in 1949 by R. D. Mindlin [18]. If we consider two homogeneous elastic isotropic bodies in contact at a point O , the Hertz theory leads to the normal compliance C_z through Equ. 1.18 and we can write

$$C_z = \frac{\delta_z}{F_N} = \frac{3kK(k')}{2\pi bE^*} \quad (1.33)$$

Referring to Fig. 1.8, we suppose now that the elliptic contact area is in the plane (x, y) perpendicular to O_z and with its major-axis along x . We add a supplementary system of tangential forces $F_{T,x}$ and $F_{T,y}$ such that $F_{T,x}$ (respectively $F_{T,y}$) applied to the bodies induces a small force perpendicular to O_z and parallel to O_x (respectively O_y) of one body on the other one. We consider the case where no slip occurs at the contact. In general, the compliance will be greater in the direction of the major-axis of the elliptic contact and normal compliance is usually smaller than the tangential one. If the ellipse axes verify the condition $a > b$ (or $k = b/a < 1$), Mindlin's solution for tangential compliance is given by

$$\begin{aligned}
 C_x &= C_{1,x} + C_{2,x} \\
 &= \frac{\delta_{1,x}}{2F_{T,x}} + \frac{\delta_{2,x}}{2F_{T,x}} \\
 &= \frac{2 - \nu_1}{8aG_1} \left[\frac{2K(e_x)}{\pi} - \frac{\nu_1}{2\pi^2(2 - \nu_1)} \frac{N_x(e_x)}{e_x} \right] \\
 &\quad + \frac{2 - \nu_2}{8aG_2} \left[\frac{2K(e_x)}{\pi} - \frac{\nu_2}{2\pi^2(2 - \nu_2)} \frac{N_x(e_x)}{e_x} \right]
 \end{aligned} \tag{1.34}$$

with G_1, G_2 being the shear moduli of the corresponding bodies, $e_x = (1 - k^2)^{1/2}$ and $N_x(e_x) = [-4\pi(\frac{2}{e_x} - e_x)K(e_x) + \frac{2}{e_x}E(e_x)]$. Then, for the tangential compliance along y , corresponding to the case $a < b$ and $k > 1$, we consider the tangential force along y with $e_y = (1 - 1/k^2)^{1/2}$ and $N_y(e_y) = [4\pi(\frac{2}{e_y} - e_y)K(e_y) - \frac{2}{e_y}E(e_y)]$. Mindlin's solution is then given by

$$\begin{aligned}
 C_y &= C_{1,y} + C_{2,y} \\
 &= \frac{\delta_{1,y}}{2F_{T,y}} + \frac{\delta_{2,y}}{2F_{T,y}} \\
 &= \frac{2 - \nu_1}{8bG_1} \left[\frac{2K(e_y)}{\pi} - \frac{\nu_1}{2\pi^2(2 - \nu_1)} \frac{N_y(e_y)}{e_y} \right] \\
 &\quad + \frac{2 - \nu_2}{8bG_2} \left[\frac{2K(e_y)}{\pi} - \frac{\nu_2}{2\pi^2(2 - \nu_2)} \frac{N_y(e_y)}{e_y} \right]
 \end{aligned} \tag{1.35}$$

$K(e_i)$ and $E(e_i)$ ($i \in \{x, y\}$) are the complete elliptic integrals as defined in the Hertz model. Details of the solutions are given in the original work of Mindlin in Ref. [18].

The experimental study of the compliance of a body is a way to define its mechanical properties. While it is easy to characterize an isotropic material defined by only two elastic coefficients, it becomes less trivial to measure the mechanical properties of transversely isotropic materials characterized by five independent elastic coefficients. In the case of transversely isotropic tubular structures, the bending properties are often deduced from beam mechanics, and thus, their bending Young modulus and the corresponding Poisson ratio are experimentally measured using beam theory. Mindlin's theory gives then access to the three last elastic coefficients through the Equ. 1.33, 1.34 and 1.35. It allows by this way to determine the complete elastic properties of a transverse isotropic body.

Chapter 2

Experimental techniques

This chapter presents the experimental techniques used to study the tribology and mechanics at the nanometer scale. We introduce simple models and methods useful to understand what are the real data measured in the different experiments, and how the acquiring devices work. A specific emphasis is dedicated to the atomic force microscope, as it is the central pillar for data acquisition in this work. Other tools for probing or imaging the surfaces will be reviewed, such as the electron beam methods.

OUR EXPERIMENTAL TECHNIQUES are strongly related to the field of tribology. This word was introduced in 1966 by Peter Jost. It comes from the Greek $\tau\rho\iota\beta\omicron\varsigma$ and means to rub. The tribology is thus the study of rubbing, but more precisely, it popularly refers to the study of friction, wear, lubrication and contact mechanics. Tribological problems are not recent. In fact, as soon as men began to work the matter, they encountered tribological problems, such as the wear of their cutting tools, or the resistance of motion, also called friction, when they were pulling large loads. Solving these problems was of great interest as it often allows to save energy or time. For example, Egyptians already used frictional devices and lubricants, such as water-lubricated sleds, to transport large stone blocks (3500 BC). However, the understanding of the whole tribology is up to date incomplete. The explanations of abnormal experimental results, in particular in the field of the mechanisms of energy dissipation in friction, are found little by little [19], and some lacks are still present [20]. The actual technological development allowed to study the tribology from the macroscopic to the atomistic point of view. Observing what is going on at the atomic level is of crucial importance to understand, then, what occurs at the macroscopic level for sliding, rolling or indenting surfaces. One familiar tool to explore the surface interactions at the small scales is the atomic force microscope (AFM).

2.1 Atomic Force Microscopy

2.1.1 History

The AFM belongs to the great family of surface force apparatus (SFA). Those devices have been developed at the beginning of the 20th century to study tribology of modern ma-

chinery. They gained more and more precision as the industry and the computer sciences evolved, to reach nowadays the atomic resolution and measure forces down to the nano Newton. The AFM is in fact strongly related to the invention in 1981 of the first scanning tunneling microscope (STM) capable of imaging a solid surface with atomic resolution in three dimensions [21, 22]. The scientific community acknowledged this invention by awarding the Nobel prize to its inventors, Binnig and Rohrer, in 1986. This instrument, based on electron tunneling between a small tip and a surface, was limited to the study of electrically conductive samples. Indeed, insulators have the particularity to rapidly charge to the same potential as the tip, and thus stop the tunneling. Few years later, in 1985, Binnig and Rohrer developed an atomic force microscope based on the same design as their STM. It had the properties of surface imaging and surface force measuring down to the nano-scale, but this time, contrary to the STM, the instrument was not restricted to one type of surface. It could be used in different environments going from the ultra high vacuum to the liquids, to study any kinds of surfaces, including biological samples. This faculty soon propelled the AFM as popular tool for probing surfaces and commercial AFM are now available with a great variety of characteristics. In this work, we used four different AFMs: an AutoprobeTM M5 from Park Scientific Instruments, a PicoPlus from Molecular Imaging, and finally, a multimode Nanoscope IV and a CP-II, both from Veeco.

2.1.2 Working principle of the AFM

The working principle of an AFM is rather simple. It consists essentially of three systems working together: a force-sensing system, a detection system and a positioning system, the whole managed by control electronics and feedback systems, which are usually realized with the help of a computer. A sketch of the AFM setup is shown in Fig. 2.1.

The force-sensing system

The force-sensing system is the AFM part in direct interaction with the sample surface. Usually, a flexible leaf spring, called cantilever and ended by a small sharp tip located at its free end, is used as sensor. The AFM tip is the component in contact or in near contact with the surface. The shape of the tip is generally either a pyramid or a cone, but can also be a ball. Forces acting between the AFM tip and the sample surface result in deflections of the cantilever. Depending on the forces, you will have a torsion and/or a bending of the cantilever while scanning a sample. Microfabricated cantilevers with integrated tip are commercially available in a wide range of dimensions and spring constants. The final radius of the AFM tip is decisive for the characteristics of the interactions with the surface. This radius might reach few nanometers for a tip height of typically a couple of microns long. The length of a cantilever is usually hundreds of micrometers for 0.5 to 5 micrometers of thickness and tenth of micrometers width. There are two classical shapes of cantilevers, one-beam cantilever and two-beam V-shaped (triangular) cantilever (See Fig. 2.2). They are mainly characterized by their normal, longitudinal, and torsional (or lateral) spring constants. Their coating, geometry and material are also important factors in AFM studies. Cantilever mechanics and forces are described later in this chapter (See Section 2.1.5). The choice of the cantilever depends on the nature of the measurements that are performed. In some cases, you might be interested in just imaging a sample, and another time, in measur-

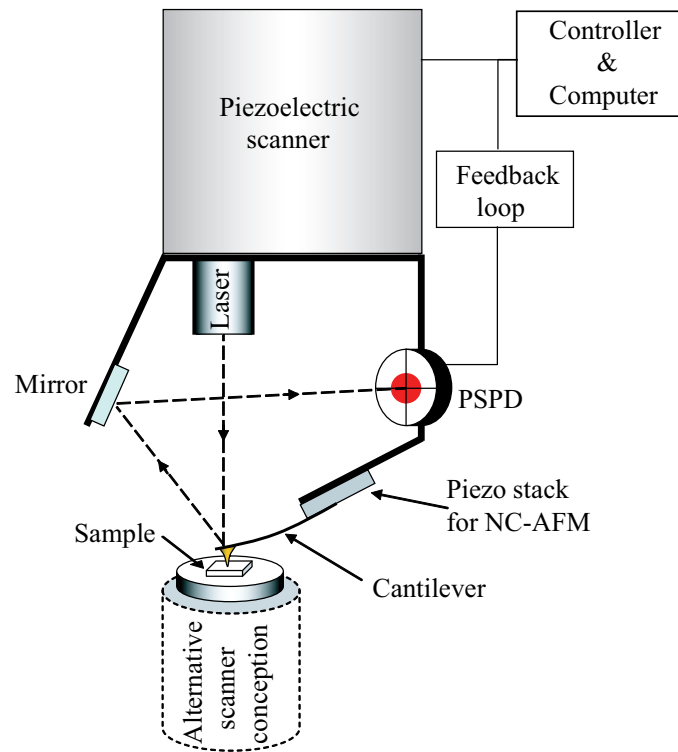


Figure 2.1: Illustration of the working principle of the AFM. A laser beam is reflected on the back side of a cantilever and then on a mirror, to finally interact with a PSPD. The displacements of the AFM tip on the surface induce variations in the output voltage of the PSPD. It results, via a feedback loop, in an extension or contraction of the piezoelectric scanner, which moves the whole system (laser-cantilever-mirror-PSPD). Sometimes, in other AFM conceptions, the piezoelectric scanner does not move the whole system, but only the sample.

ing physical properties such as friction, elastic moduli or surface conductivity. Static charge and magnetic fields measurements figure also among the possible studies with an AFM. In each case, cantilevers specifically designed for a particular experiment allow notable improvements of the measurements.

The detection system

The tip-sample interaction is detected by monitoring the deflection of the cantilever. An easy method that is actually the most used in commercial AFM is the laser-beam deflection system. A laser beam is focused on the rear end of the cantilever and reflected into a four-quadrant position sensitive photodetector (PSPD). Bendings and torsions of the cantilever result in the motion of the laser spot on the photodetector and thus, in changes in the output voltage of the photo diode. The amount of bending or torsion of the cantilever is magnified since the distance between the cantilever and the photodetector measures thousand of times the length of the cantilever. Small variations in the position of the cantilever result in large displacements of the laser spot. By this way, tip displacements smaller than 1 nm are easily detectable [23]. One major property of the detection system is its ability to record the deflection of the cantilever in the three dimensions separately and simultane-

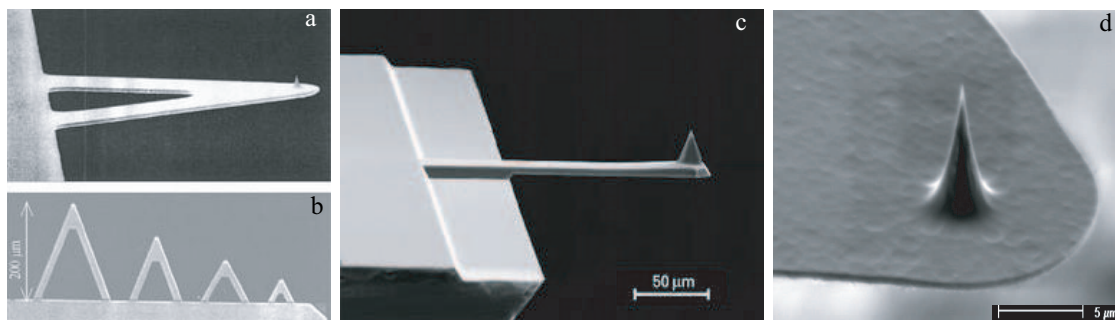


Figure 2.2: The two main shapes of commercially available cantilevers: pictures (a) and (b) are the so-called V-shaped cantilevers and picture (c) is a beam cantilever. Picture (d) gives an idea of the dimension and shape of a conical AFM tip.

ously. Thus, the AFM has the potential to measure the three components of the force vector describing the interaction of the tip with the surface. The cantilever displacements or the forces acting on the cantilever are then deduced from the measurement of the PSPD output voltage, provided that the photo diode sensitivity and the cantilever spring constants are known.

The other main detection systems involve piezoresistive cantilever (piezoresistors are integrated to the cantilever whose bending is measured through resistance change using a Wheatstone bridge) or interferometry (the laser beam reflected to the back side of the cantilever interferes with the original beam and produces an interference pattern whose intensity is related to the deflection).

Positioning system

The positioning and the fine displacement of the AFM tip relatively to the surface are done via piezoelectric scanners, whereas coarse displacements use stepper motors when available. Piezoelectric materials are ceramics that change dimensions in response to an applied voltage. Conversely, a mechanical strain of the piezoelectric material causes an electrical potential. The relative position of the tip over the sample is thus controlled by the application of voltage to the electric contacts of the piezo, resulting in extension, squeezing or bending of the piezoelectric material. Piezoelectric scanners can be designed to move in the three dimensions by expanding in some directions and contracting in others. Actually, two designs are available in commercial AFMs. Either the cantilever is attached to a piezo system and the sample is held at a fixed position, or the cantilever is fixed and the sample is moved in the three dimensions through a piezoelectric support. However, new generations of AFMs separate the displacement normal to the surface from the in-plane displacement to limit piezo material artifacts. This is done by dividing the task between one piezo for the displacements normal to the surface and to which is attached the cantilever, and a sample support made of two other piezo elements for the in-plane displacements.

The working principle of the AFM¹ is illustrated in Fig. 2.3. The AFM tip is driven by a

¹ The description given here is based on the working principle of the AFM AutoprobeTM M5. Differences with the working principle of other AFMs may exist.

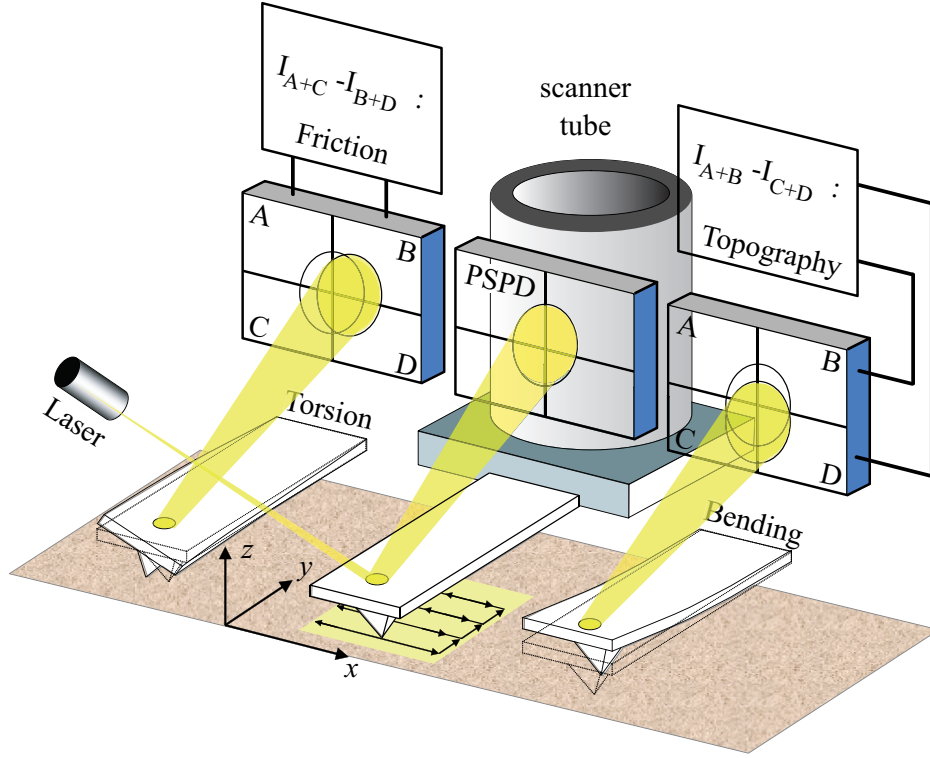


Figure 2.3: Schematic description of the working principle of the AFM. Friction measurements are obtained via the torsion of the cantilever, whereas topography results from normal deflection.

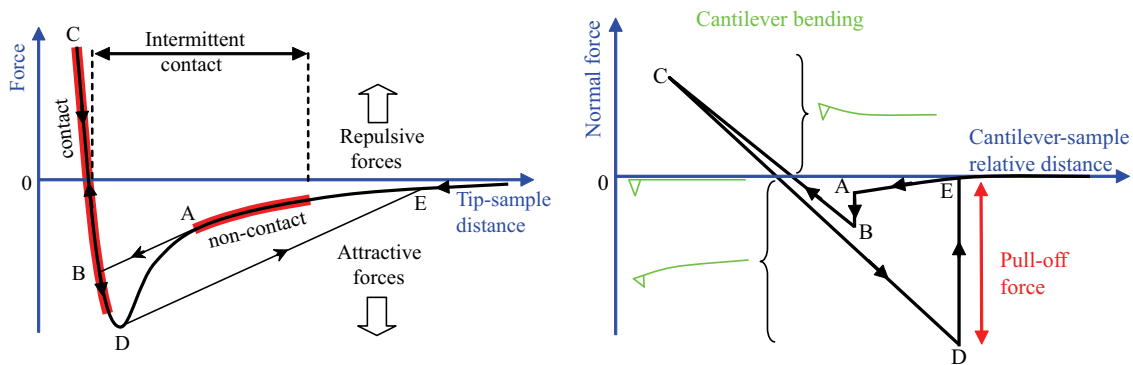
piezoelectric tube and horizontally scans the surface in a regular way over a square area. In this case, the horizontal scan (along x) is the fast-scan direction, whereas the vertical scan (along y) corresponds to the slow scan direction. A sketch of the scanner motion during data acquisition figures in Fig. 2.3. It can be divided in two main steps. First, the scanner moves across the first scan line and back. Data are collected according to the number of data points allocated per line of the scan². At this point, the lateral resolution of the AFM is given by the scan size divided by the number of data points per scan line, which could be a limiting factor in the lateral resolution. Second, it steps in the perpendicular direction to the second scan line. The steps in the perpendicular direction of the fast-scan motion are related to the number of data points constructing the image. Note that no data are collected in the perpendicular direction to minimize line-to-line registration errors coming from scanner hysteresis. These repetitions of horizontal scan lines and vertical steps are the basic cycles of image construction. They are done as many times as the image contains data points. It differs from a traditional raster pattern in that the alternating lines of data are not taken in opposite directions. Then, if we move back to the general working principle, the laser beam is reflected on the back side of the cantilever into the four-quadrant photodetector. The intensity difference between the upper and lower segments of the four-quadrant photodetector is proportional to the normal deflection ($I_{A+B} - I_{C+D}$: topography) and corresponds to a change ΔV_N of the output voltage of the PSPD, whereas the intensity difference between the left and right segments is proportional to the torsion of the cantilever ($I_{A+C} - I_{B+D}$:

² The possible values for the number of data points are usually 256, 512 or 1024 with recent AFMs.

torsion or lateral force) and is related to a PSPD output voltage variation ΔV_L .

2.1.3 AFM spectroscopy: the force-distance curve

A cantilever, also called AFM probe, experiences attractive and repulsive forces as the AFM tip is brought close to the sample surface and then pulled away. These forces define two domains where an AFM may operate: the contact mode and the non-contact mode. In between, it is possible to have an intermittent contact mode. The force most commonly associated with the cantilever deflection is the van der Waals force, already studied in Section 1.2.4. The dependence of this force as function of the separation distance between the tip and the surface is illustrated in Fig. 2.4(a). The corresponding experimental record of the amount of force felt by the cantilever at a single location on a sample surface is depicted in Fig. 2.4(b). This so-called force-distance (FD) curve is important to determine the optimum settings for the interaction between the studied surface and the AFM probe. It gives effectively information about the long-range attractive or repulsive forces acting between the AFM tip and the sample surface, as well as mechanical and chemical local properties. Looking at the typical FD curve presented in Fig. 2.4(b), the approach and withdraw of the tip might be divided in four steps.



(a) Potential experienced by an AFM tip approaching the surface. (b) Typical force-distance curve observed experimentally.

Figure 2.4: Schematic representation of attractive and repulsive forces experienced by the AFM-tip as a function of the tip-sample distance 2.4(a) and corresponding force distance curve giving information about the deflection of the front end of the cantilever 2.4(b).

In the first step, the piezoelectric scanner extends, letting the cantilever slowly approach the surface. At the beginning of this process, the AFM tip does not yet interact with the surface. There is neither a deflection of the cantilever, nor measurable force due to the large distance of separation between the tip and the surface. Then, while approaching progressively, attractive forces result in a small downward deflection of the cantilever until the gradient of the attractive forces exceeds the elastic constant of the cantilever. At this point (A), the tip reaches an unstable position, resulting in a snap-into-contact of the tip on the surface (B). For the second step, the piezoelectric scanner continues with its expansion and the cantilever bends from a concave shape (attractive regime) to a convex shape (repulsive regime) with its tip in contact with the surface. The cantilever deflection is proportional to

the movement of the piezo element assuming that the tip and the surface are rigid bodies. In fact, deformations are generally negligible compared to the cantilever deflection. This is of crucial importance to perform an accurate force calibration of the AFM, as we will see later. For the third step, the expansion of the piezoelectric scanner is stopped (C) while being in the elastic domain of deformation of the cantilever. And then, by contracting the piezo element, the withdraw of the tip begins. The tip stays into contact with the surface until the pulling force coming from the contraction of the piezoelectric scanner overcomes the tip-surface adhesion and results in the jump out of contact of the tip ($D \rightarrow E$). The difference between the zero normal force and the force preceding the jump out of contact is called the pull-off force. The FD curve for the retracting process differs slightly from the approach part, on the one hand due to piezo hysteresis and, on the other hand, due to the tip-surface adhesion. The capillary forces, the increase of the contact area and short-range forces are the principal causes of the tip-surface adhesion.

2.1.4 AFM modes

The AFM may work in different modes depending on what kinds of measurements are expected or simply depending on the surface you are analyzing. For example, sensitive surfaces require low normal forces or even no contact between the tip and the surface, whereas hard surfaces tolerate high normal loads without damaging the surface. In this section, we present the main AFM modes that are commonly used.

Contact mode

As indicated by its name, the contact mode (C-AFM) corresponds to the case where the AFM tip is held in contact with surface. A feedback loop allows two basic contact modes. The AFM may operate in the constant force mode or constant height mode. In the constant force mode, the force between the tip and the surface is simultaneously measured and kept constant via a feedback loop controlling the vertical position of the sample relatively to the tip. Thus, the scanner responds instantaneously to topographical changes by keeping the cantilever deflection constant. By this way, the topography is deduced from the voltage applied to the z -piezo and the scanning speed is limited by the time response of the feedback loop. For the constant height mode, the measured data are the cantilever deflection, whereas the relative distance between the tip and the surface is kept constant via the feedback loop. The deflection of the cantilever is thus directly used to reconstruct the topography of the sample. This mode is restricted to flat surfaces to avoid tip crashes on the surface.

Non-contact mode and intermittent contact mode

In the non-contact mode (NC-AFM) and intermittent contact mode (IC-AFM) also called tapping mode, the cantilever is oscillated sufficiently close to the surface to interact with it via long-range attractive forces. Generally, a stiff cantilever is attached to a small piezoceramic system (See the piezo stack in Fig. 2.1), which vibrates perpendicularly to the surface at a frequency close to the cantilever free-space resonance frequency. The tip is then scanned over the surface and each surface pixel represents an average of hundreds of oscillations. The distance between the sample and the AFM tip is controlled by tracking the changes in the oscillating frequency, amplitude or phase. The resonance frequency or the oscillating

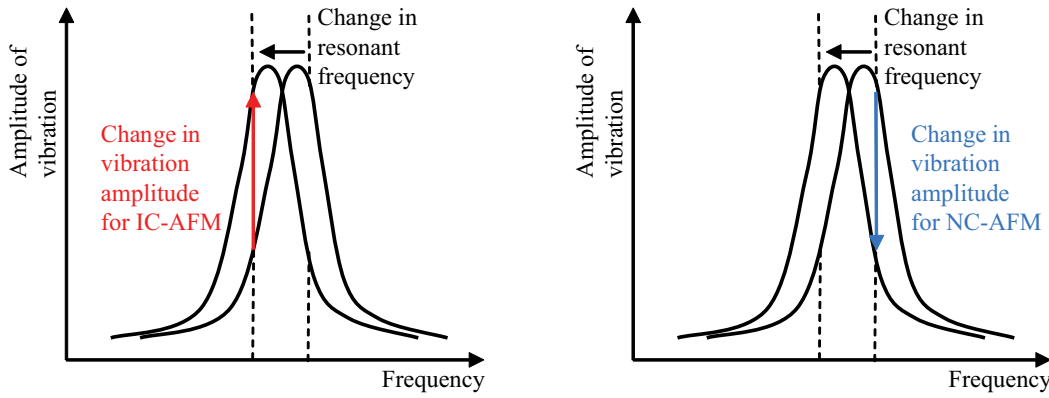


Figure 2.5: Response curves for a cantilever vibrating close to the surface. A decrease in cantilever resonance frequency induces an increase of the vibrational amplitude in IC-AFM and at the opposite a decrease in vibration amplitude in NC-AFM.

amplitude is kept constant by a feedback loop, which controls the cantilever displacement normal to the surface. Thus, the resonance frequency of the cantilever is indirectly used to measure the surface topography.

In NC-AFM, the oscillation frequency is chosen close to, but greater than the free-space resonance frequency, whereas for IC-AFM, the frequency is also close to, but smaller than the cantilever resonance frequency. By this way, the vibration amplitude decreases significantly as the cantilever is brought closer to the surface in the NC-AFM mode, whereas it increases for the IC-AFM mode, allowing intermittent contact. Fig. 2.5 illustrates the changes in amplitude related to the shift in frequency arising from variations of the force gradient acting on the cantilever. These variations are notably related to the tip-sample separation. In the non-contact regime, tens to hundreds of angstroms separate the AFM-tip from the sample surface. This explains why stiff cantilevers are for example preferable for non-contact measurements, as soft cantilevers might be pulled into contact with the surface while imaging the sample.

Force Modulation Microscopy

The force modulation microscopy (FMM) is an AFM-based technique which opens the field to qualitative and quantitative measurements of the local elastic properties of the surface. This technique was first described in 1991 by P. Maivald *et al.* [24]. The principle is based on C-AFM. While scanning the surface in an x - y pattern, the cantilever is moved with a small vertical oscillation Δz which is far away from any resonance frequencies of the cantilever and significantly faster than the raster scan rate. The average normal force on the sample equals that one in traditional contact AFM. Hard areas deform less than soft areas when submitted to the same normal strain. As consequence, the cantilever bends more when scanning a hard than a soft area. The resistance to the cantilever normal oscillations is at the basis of the determination of the surface elastic properties. This technique allows to collect simultaneously data of topography and surface elasticity, as illustrated in Fig. 2.6. It is also possible to modulate the cantilever tangentially to the surface so that in-plane compliance is measured.

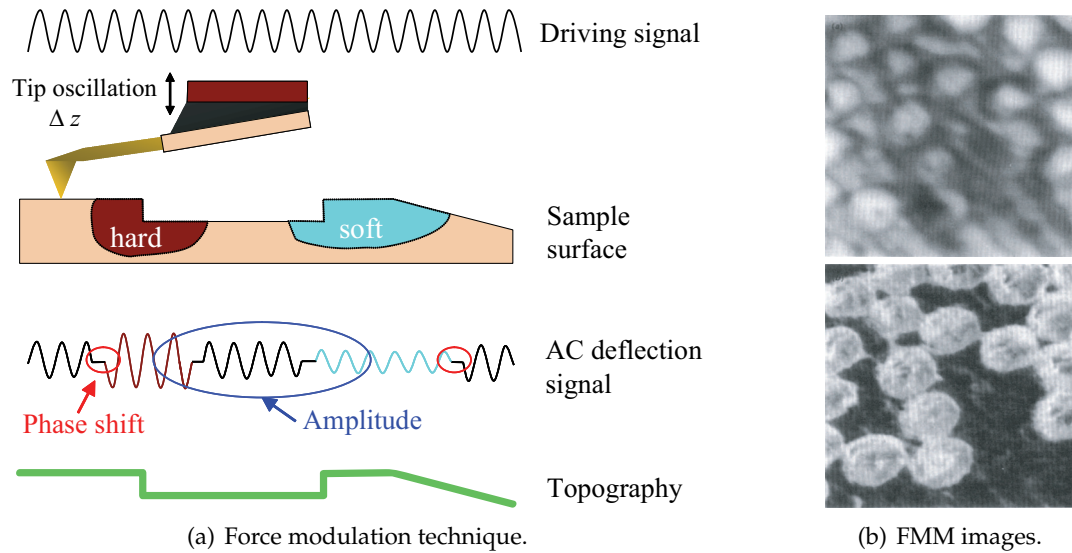


Figure 2.6: (a) Illustrations of the working principle of the FMM: a driving signal vibrates the AFM cantilever while it scans the surface in contact mode. The changes in topography and in vibration amplitude are recorded simultaneously to construct a map of the topography and elastic properties of the surface. (b) Images of carbon fiber and epoxy composite in air obtained by Maivald *et al.* [24] at the beginning of the FMM technique in 1991. The intensity corresponds to height in the topographic image (top image) and stiffness in the force modulation (bottom image). The image width is $32 \mu\text{m}$.

Lateral Force Microscopy

In lateral force microscopy (LFM), the AFM operates in contact mode, keeping the normal force constant and recording the torsion of the cantilever. Thus vertical and lateral bending of the cantilever are simultaneously measured. The lateral bending (or twisting) arises from forces parallel to the plane of the sample surface and acting on the AFM-tip. This lateral force has actually two main origins: first of all, the friction force, that is opposed to the tip displacement, and secondly, the changes in the topography. The figure 2.7 illustrates by two schemes the lateral force generated by a change in local slope and by a change in the friction coefficient.

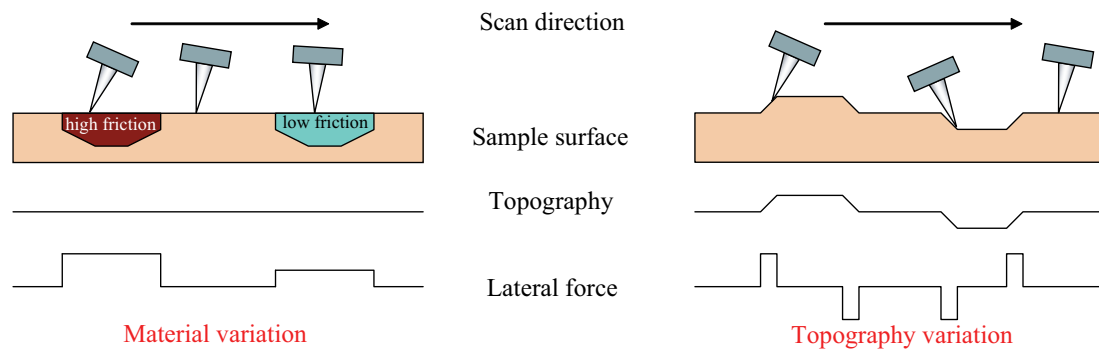


Figure 2.7: Sketch of the lateral deflection of the cantilever induced by local changes of the friction due to a different type of material (on the left), or coming from topography variations (on the right).

The sign of the friction force signal depends on the scan direction. The friction force signal changes its sign when the scanning direction is reversed, while the normal force remains unchanged. In fact, one scan line in the forward and reverse direction forms a loop called a friction loop (See Fig. 2.8). The total energy dissipated while the AFM-tip is dragged along the surface during one friction loop is given by the area enclosed by the loop. At the beginning of a scan, the friction loop shows a linear increase of the lateral force as function of the support position (I). It corresponds to the static friction, the tip stick to the surface but does not move, whereas the cantilever twists due to the displacement of the cantilever support. Then the lateral displacement of the piezo overcomes the potential well characterizing the cantilever-tip-surface system. At this point, the tip begins to slip (II) until the scan direction is reversed and the process repeated (III \rightarrow IV). The difference between the mean lateral force for the forward and backward directions corresponds to twice the mean friction force.

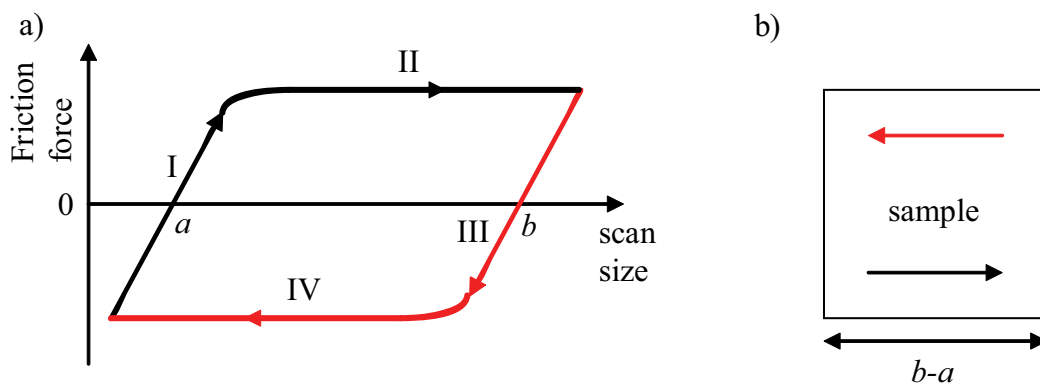


Figure 2.8: (a) Theoretical friction loop and (b) its corresponding scanning direction on the sample. The size of the sample is given by $b - a$. Parts (II) and (IV) of the friction loop correspond to the sliding of the AFM tip on the surface, whereas part (I) and (III) characterize the adhesion (sticking part) of the tip to the surface.

Other modes

Magnetic force microscopy (MFM) consists in taking a NC-AFM image of a surface using a magnetized tip. Magnetic materials have some domains that can exert an attractive or repulsive force on the magnetized tip, resulting in changes in the oscillating amplitude of the cantilever. These local changes of magnetization are recorded while taking an image of the surface and thus, a cartography of the magnetic properties of the sample is created. MFM requires a ferromagnetic coating of the cantilever. The magnetic force decreases less than vdW forces when the tip-surface distance increases. It becomes then possible to image only the magnetic domains of a sample by keeping the tip far away from the surface, where vdW forces are negligible.

Most of the atomic force microscopes might be used as scanning tunneling microscopes (STM). For this mode of operation, the cantilever is replaced by a sharp conductive tip. A bias voltage on the order of 1 V is applied between the tip and the conductive sample, so that electrons can tunnel between the tip and the sample when these last ones are close

enough. While scanning the surface, the tunneling current changes due to variations in the local topography and in the electronic properties of the sample. Two modes are possible. First, the constant height mode records the tunneling current variation while scanning in a horizontal plane. And second, the constant-current mode uses a negative feedback loop to maintain the tunneling current constant by adjusting the relative distance between the STM-tip and the surface. Depending on the sample, atomic resolution was reached using STM in air, but usually, STM is used in a close chamber under vacuum.

2.1.5 Cantilevers

The characterization of the cantilever properties is of crucial importance in atomic force microscopy. This versatile element determines on the one hand the interaction with the surface, and, on the other hand, the reading and the transmission of the corresponding information. Its geometrical, optical, chemical and mechanical properties are at the basis of the interpretation of AFM results, and strongly related to the applied forces to the surface, the intensity of the reflected beam or the imaging resolution. Therefore, cantilevers are chosen in function of the experiment that has to be performed. The optical and chemical properties of a cantilever are generally managed via special coatings or functionalization of its outer surface and might be specifically adapted to a particular experiment. Numerous designs are commercially available for cantilevers. They are generally build in silicon oxide or silicon nitride through different processes of fabrication, like lithography, bulk silicon micromachining or thin film deposition and etching.

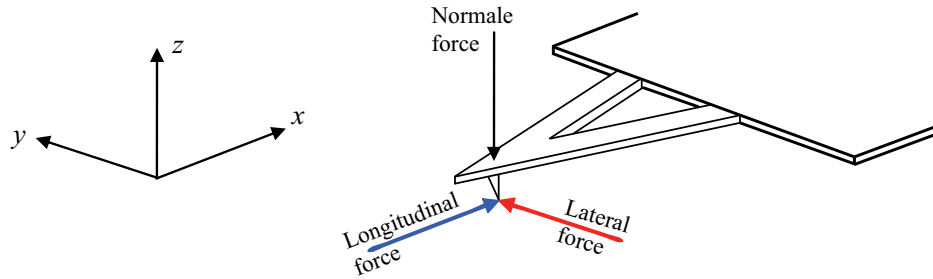


Figure 2.9: Sketch of the forces experienced by an AFM tip.

Cantilevers mechanics and forces

The normal, torsional and lateral spring constants of the cantilever, respectively k_N , k_T and k_L , are used in the force calibration of the AFM. Finite element methods (FEM) and continuum mechanics are generally used to calculate the spring constants of the cantilever, in contrast with experimental techniques that probe the cantilever on or with calibrated samples or loads to determine its mechanical properties. Referring to Fig. 2.9, the normal force F_N is applied on the top of the conical AFM tip, perpendicularly to the cantilever plane. The lateral force F_L acts at the end of the pyramidal tip, perpendicularly to the plane of symmetry of the cantilever. It causes a torque T that twists the cantilever. Note that another force makes the cantilever bend. It is the longitudinal force F_{Long} acting also at

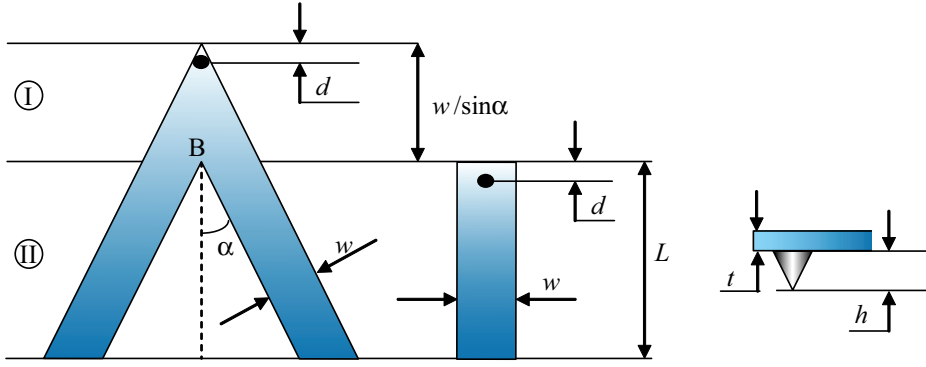


Figure 2.10: Geometry of a V-shaped and a beam cantilever.

the end of the pyramidal tip with a direction parallel to the cantilever length. F_N and F_{Long} result both in the bending of the cantilever, but the related stiffnesses are not the same [25].

We consider now the mechanics of a beam and a V-shaped cantilever submitted to F_N or F_L , in a Cartesian coordinate system as shown in Fig. 2.9. The theory presented here is based on simple continuum mechanics of beam theory and gives access to the relations between the force and the deformation. In the case of the V-shaped cantilever, we present only the interesting results and the details of the method might be found in Ref. [25]. Referring to Fig. 2.10, both cantilevers have a tip of height h positioned at a distance d from the cantilever free end. Their thickness is t for a width w that corresponds, in the case of the triangular cantilever, to the width of one of its arms. L is a parameter describing the cantilever length. For the beam cantilever, it is equal to its exact length, whereas it represents, in the case of the triangular cantilever, the distance between the cantilever support and the point B where the two arms of the V-shaped cantilever join forming an angle 2α .

For the rectangular beam cantilever, the relations between the force and the cantilever spring constants are given by [26, 27]

$$F_N = k_N \Delta z = \frac{3EI}{(L-d)^3} \Delta z = \frac{Et^3w}{4(L-d)^3} \Delta z \quad (2.1)$$

$$F_L = k_L \Delta y = \frac{Gt^3w}{3(L-d)h^2} \Delta y \quad (2.2)$$

where E and G are respectively the Young and shear moduli. $I = wt^3/12$ is the moment of inertia of the beam respective to its long axis. Δz and Δy are respectively the normal and lateral deflection of the free end of the beam. Moreover, the change in angular orientation of the cantilever free end when submitted to small vertical displacements is given by

$$\theta = \frac{6(L-d)^2}{Ewt^3} F_N = \frac{3\Delta z}{2(L-d)} \quad (2.3)$$

Equ. 2.1 highlights the importance of the cantilever thickness measurement in the calculation of its mechanical properties as the thickness appears to the power three. An easy way to measure the cantilever thickness is to measure its resonance frequency f . The relation between f and k_N is then given by [28]

$$f = \frac{1}{2\pi} \sqrt{\frac{k_N}{m}} \simeq \frac{t}{2\pi L^2} \sqrt{\frac{E}{\rho}} \quad (2.4)$$

where m is the cantilever mass and ρ the material density. By this way, it becomes possible to extract the thickness value from resonance frequency measurements.

One method to determine the normal, lateral or torsional spring constants of a V-shaped cantilever is to subdivide it into two parts: a triangular plate (I) and two prismatic beams (II) for which the deformations are accessible under elastic beam theory. Adopting this configuration, the deformation of a clamped triangular plate (I) loaded with the normal force F_N is given by

$$\Delta_I = \frac{3N}{Et^3 \tan(\alpha)} \left[\left(\frac{w}{\sin(\alpha)} - 2d \right)^2 - d^2 \left(2 \log \frac{w}{d \sin(\alpha)} + 1 \right) \right] \quad (2.5)$$

$$\theta_I = \frac{6N}{Et^3 \tan(\alpha)} \left(\frac{w}{\sin(\alpha)} - d - d \log \frac{w}{d \sin(\alpha)} \right) \quad (2.6)$$

where Δ_I is the normal deflection relatively to its free position and θ_I is the corresponding angle of rotation occurring at the tip basis. Then, this triangular plate exercises forces and moments on each of the beams (II) resulting again in a normal deformation Δ_{II} and a rotation θ_{II} expressed by the relations

$$\Delta_{II} = \frac{NL^2}{Ewt^3 \cos^2(\alpha)} \left[\frac{2L}{\cos(\alpha)} + 3(w \cot(\alpha) - d \cos(\alpha) - r \sin(\alpha)) \right] \quad (2.7)$$

$$\theta_{II} = \frac{3NL(1+\nu)}{Ewt^3 \cos(\alpha)} \left(\frac{w}{\sin(\alpha)} - d + r \cot(\alpha) \right) \quad (2.8)$$

with the length r defined by

$$r = \frac{L \tan(\alpha) + (w - d \sin(\alpha))(1 - \nu) \cos(\alpha)}{2 - (1 - \nu) \cos^2(\alpha)} \quad (2.9)$$

The total normal deflection Δz and rotation θ under F_N relatively to its unloaded position is given by

$$\Delta z = \Delta_I + \Delta_{II} + \theta_{II} \left(\frac{w}{\sin(\alpha)} - d \right) \equiv \frac{F_N}{k_N} \quad (2.10)$$

$$\theta = \theta_I + \theta_{II} \quad (2.11)$$

Equ. 2.10 defines the normal stiffness $k_N = F_N/\Delta z$. Then for the lateral or torsional stiffnesses, we consider a torque $T = F_L h$ acting in the x -direction on the tip basis and resulting in a total torsion $\phi = \phi_I + \phi_{II}$, where ϕ_I and ϕ_{II} are the rotation of the triangular plate (I) and the beams (II). The twist formulas are expressed as

$$\phi = \phi_I + \phi_{II} = T \frac{3(1+\nu)}{ET^3} \left(\frac{1}{\tan(\alpha)} \log \frac{w}{d \sin(\alpha)} + \frac{L \cos(\alpha)}{w} - \frac{3 \sin(2\alpha)}{8} \right) \quad (2.12)$$

The torsional stiffness k_ϕ and the lateral stiffness k_L are related to their corresponding forces T and F_L through the relations

$$\phi = \frac{T}{k_\phi} = \frac{T}{k_L h^2} = \frac{F_L h}{k_L h^2} \quad (2.13)$$

For small angles, we have the approximation $\phi \cong \Delta y/h$ and Equ. 2.13 becomes

$$k_L = \frac{k_\phi}{h^2} = \frac{F_L}{\Delta y} \quad (2.14)$$

Tip-surface convolution

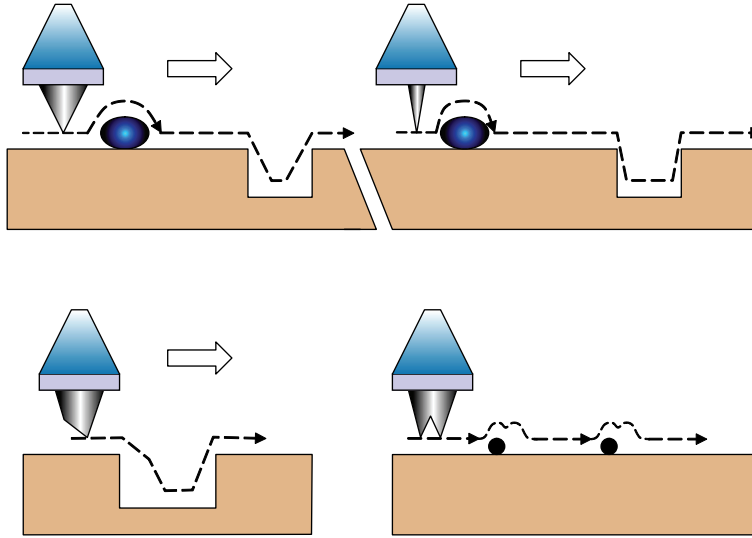


Figure 2.11: Illustration of the tip-surface convolution. The top images compare the resolution difference obtained with a large and a sharp tip. The bottom left image illustrates the case of a non symmetric tip. The bottom right image schematically highlights the artifacts arising from a double tip.

Another critical parameter of the cantilever is the shape of the tip. It can be a cone, a pyramid, a ball, or sometimes, an integrated needle like a carbon nanotube. The extreme part of the tip interacts directly with the surface and is characterized by a radius of curvature R_T . The size of this radius is important for quantitative experimental studies of forces and mechanics at surface, but also simply for the image construction of the surface. The tip sharpness is a limiting factor of the AFM image resolution. In fact, we do not see the real surface with an AFM, but only the result of the convolution between the tip and the surface geometry. Features with sharp edges or high aspect ratio (e.g. wide and very deep) will not be properly resolved by the AFM tip. This phenomenon is generally more significant in the lateral resolution than in the vertical one. Actually, very sharp tip with a nanometer size radius ($R_T \sim 1 - 2$ nm) are commercially available. They are generally used for non-contact mode since any contact with the surface might blunt the tip and decrease the resolution. Fig. 2.11 presents few classical examples of the spatial convolution of the tip with surface features, giving rise to the so-called probe artifacts. The dashed lines correspond to the

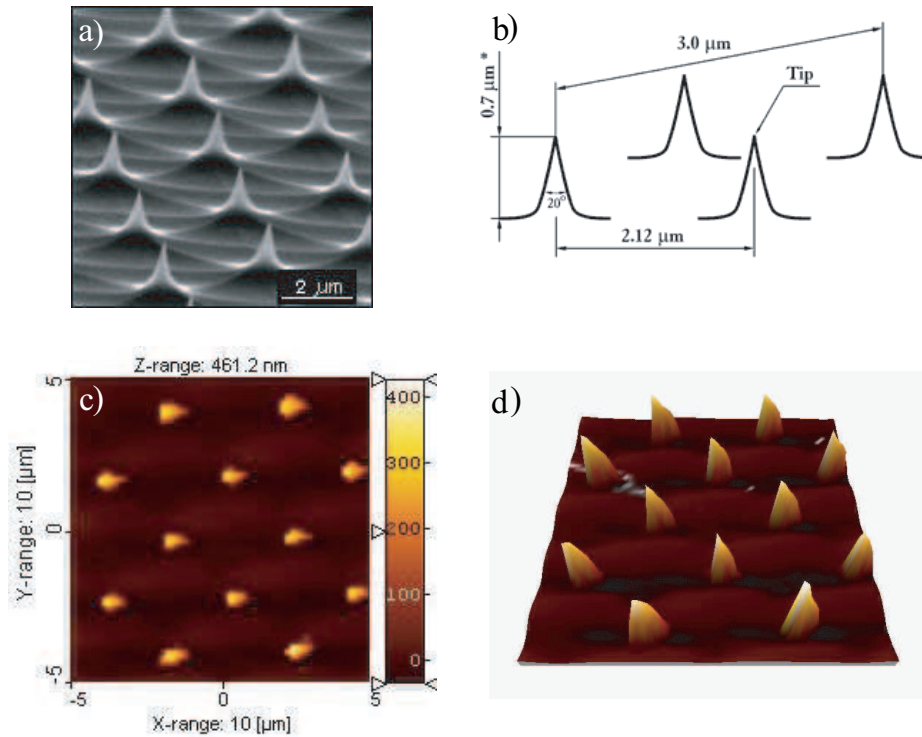


Figure 2.12: Illustration of a grating used for the deduction of the tip shape. The grating consists in sharp Dirac peaks (a) and with a well-known morphology (b). The topographic images (c) and (d), obtained from the scan of the grating, are then used to deduce the tip radius and shape.

topographic images obtained for the different features as function of the tip shapes. The importance of a small tip radius is highlighted and effects due to a non symmetric tip or double tip are illustrated. The convolution is also used to determine the tip radius by using well-known surface features as presented in Fig. 2.12.

2.1.6 Calibration

Quantitative measurements with an AFM rely on an accurate calibration of the piezoelectric scanner in the three dimensions (3D) and a precise estimation of the relation between the 3D tip displacements and the corresponding forces that depend on the cantilever spring constants.

Scanner calibration and artifacts

The scanner system is generally formed of tubes, cylinders or stacked elements of piezoelectric ceramics (PZT). Its construction allows displacements in the 3D space (x, y, z) . A scanner calibration is needed in order to know the relation between the voltage applied to the scanner and the real displacement of the cantilever support attached to the piezo-system, but also, to correct the scanner artifacts that may perturb quantitative AFM measurements.

The main artifacts recurrent to PZT systems are the non-linearity, the drift, and the hysteresis. These artifacts are presented in Fig. 2.13. For a scanner, the non-linearities occur in

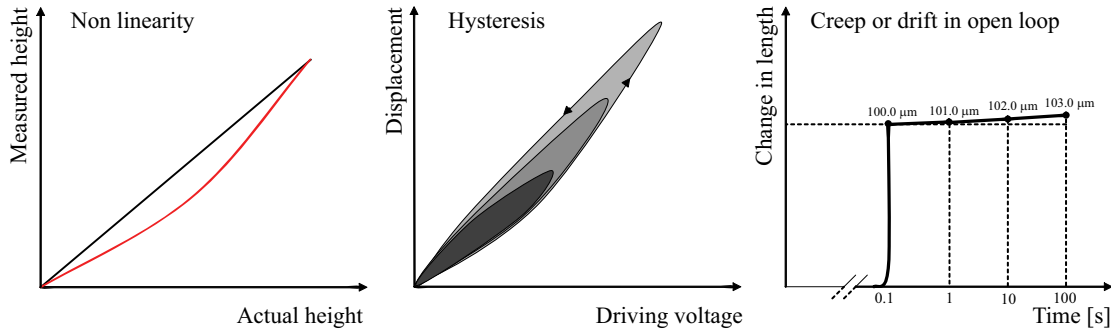


Figure 2.13: Illustration of the artifacts arising from the piezoceramic scanner. The non linear response induces errors in length measurements as the real length does not correspond to the expected length. The hysteresis is related to the applied voltage as shown in the second graph. The creep corresponds to an extra change in length after a commanded motion of the PZT. This change is on the order of 1% of the last motion.

the three directions of the space, but are generally louder in the $(x-y)$ plane of the surface due to greater scan dimensions. The real displacement is then no more equal to the measured displacement. The drift, also called creep, corresponds to the expansion of the PZT after that a voltage has been applied. It is time dependent and may vary with each PZT. It is a serious handicap when you want to scan a small area using scanner offsets, as the scanner will continue with its expansion because of the rapid change in voltage related to the offsets. The PZT hysteresis corresponds to the divergence between the scanner expansion while increasing and then decreasing the applied voltage. The amount of hysteresis is proportional to the amount of voltage applied to the scanner.

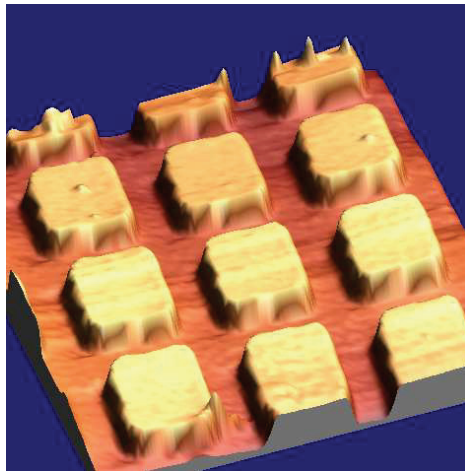


Figure 2.14: Typical topographic image of a calibration grating, showing the defects of the tip and the surface.

To overcome these problems, it is necessary to linearize the scanner and calibrate it. The general method is to take a topographic image of an object whose dimensions and shape are known and to find the parameters that make the topographic image matching the real dimensions of the object. From the complexity of the algorithms calculating these parame-

ters will depend the precision of the calibration. Nowadays, such objects with well defined shapes are available in a large panel of geometries and sizes via commercial calibration gratings that make easier the scanner calibration. Referring to Fig. 2.14, one grating allows the calibration for the three dimensions (x, y, z) and, due to its symmetry, it becomes also possible to correct the main artifacts at the same time. Moreover, the use of detectors for tracking the real movement of the scanner during data acquisition, and correcting it in time by a feedback-loop, as well as post-processing treatments of the obtained data may improve accurate calibrations. Nevertheless, it is always recommended to use calibration gratings providing the same scale as the studied objects. Note finally that other AFM artifacts are recurrent to the convolution of the AFM tip with the sample as illustrated in Fig. 2.11.

The true resolution of the scanner might also be a source of artifacts. In fact, a limiting factor of the resolution in AFM is related to the scanner motion controlled via the digital-to-analog converter (DAC). The voltage applied to the scanner is digitized in a number of values depending on the number of bits of the DAC. A 20-bit DAC expresses the voltage as a 20-bit number, and thus, a scan line is for example divided into 2^{20} digitized steps. This digitization has to be taken into account when imaging a large surface, while looking at small relevant features.

The next step after the scanner calibration is to find the relations between the cantilever torsion or bending and the corresponding forces. In fact, changes in the output voltage of the photodetector are proportional to angular changes of the lever resulting from bending, buckling and twisting. Thus, the change in angle can be directly related to the force required to induce such deflections.

Normal force calibration

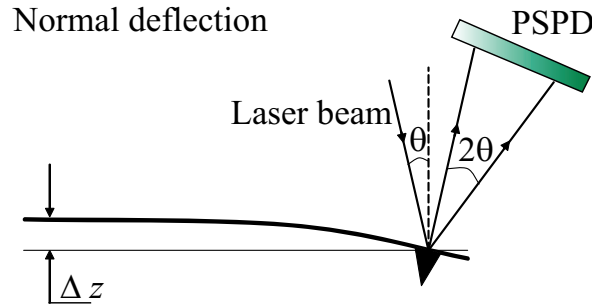


Figure 2.15: Cantilever normal deflection and associated change in angle of the reflected beam on the PSPD.

The normal force F_N acts on the tip end perpendicularly to the cantilever plane and leads to the cantilever bending (See Fig. 2.15). Its determination is a conventional procedure of calibration. Once the scanner is calibrated on standard samples, the relation between the change in voltage ΔV_N of the PSPD output and the applied normal force F_N is determined by the force-distance curve described in Section 2.1.3. The resulting relation is given by

$$F_N = k_N \Delta z = k_N S_z \Delta V_N \quad (2.15)$$

where S_z is the sensitivity (in nm/V) of the PSPD. The sensitivity S_z is directly measured via a linear fit of ΔV_N versus Δz on the part of the FD curve where the AFM tip is in direct contact with the surface. In Equ. 2.15, the normal force is calibrated to zero when the cantilever is not bent. This method supposes that the piezo movement and cantilever deflection are equal in the contact region and necessitates hard samples. Soft samples may induce an error in the calibration as their elastic deformation under the applied normal load might be non negligible. However, for the majority of the materials, Δz is greater than the surface deformation at least at one order of magnitude and therefore the FD curve is sufficient to calibrate accurately the normal force.

Lateral force calibration

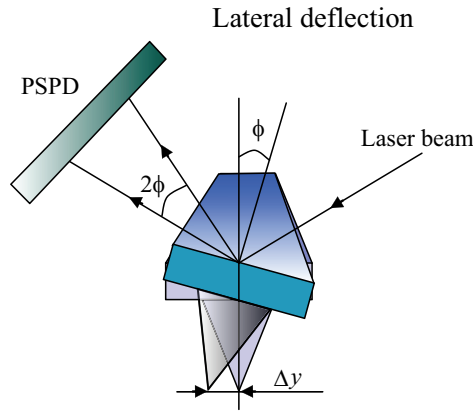


Figure 2.16: Torsion of the cantilever and change in angle of the reflected beam due to a lateral force.

The lateral force F_L induces a rotation of the end of the tip around its basis as illustrated in Fig. 2.16. This torsion of the cantilever results in a displacement Δy of the end of the tip. F_L acts at the contact of the tip with the surface, perpendicularly to the plane of symmetry of the cantilever. Referring to Fig. 2.16 and supposing small torsional angles ϕ , we have

$$F_L = k_L \Delta y = k_L S_y \Delta V_L = \frac{k_T}{h_{tip}^2} S_y \Delta V_L \quad (2.16)$$

where S_y is the sensitivity of the PSPD to a lateral displacement of the laser spot. While it was easy to determine S_z via a FD curve, there is unfortunately no simple methods for the measurement of S_y . Different methods have been suggested to calibrate the lateral force. One of the first interesting methods that has inspired further developments, is described by Fujisawa *et al.* in Ref. [29]. He performed a lateral force curve to calibrate the sensitivity of the PSPD. This curve is characterized by an initial sticking part where the tip adheres to the surface before it begins to slip. It is in fact the initial part of the friction loop presented in Fig. 2.8 and explained in Ref. [30]. The lateral force curve calibration consists in finding the relation between the initial sticking part and the output voltage of the PSPD. However, non-linearities in the lateral piezo movement, which can be of the order of 30%, and any slippage or deformation of the tip make this method inaccurate. The evolution of this method has

been done by combining lock-in techniques to lateral force curves measurements, as proposed by Piétrement *et al.* [31]. Their method uses a calibration based on modulated lateral force microscopy related to the exact knowledge of the sample lateral displacement. Other methods require special surfaces, like the wedge method described by Ogletree *et al.* [32], and for which the calibration is done via F_L measurements as function of the applied load on substrates with two different well-defined slopes. Finally, special AFM setups measure the torsion angle of the cantilever by pushing it against a protuberance offset from the cantilever axis [33, 34].

The calibration of the lateral force is necessary to perform quantitative measurements of the friction force that will interest us later. We adopted a method based on a lock-in technique whose working principle has been described in Ref. [31]. Shortly, using a lock-in amplifier³, a hard surface is modulated perpendicularly to the plane of symmetry of the cantilever with a known amplitude and a frequency far enough from any resonance peaks of the cantilever. The choice of diamond surface as calibration sample allows to neglect the lateral surface deformation. Then, the corresponding output signal of the PSPD is analyzed by the lock-in amplifier, keeping attention that no phase change occurs between the surface modulation signal and the PSPD output. An out of phase signal corresponds to the sliding of the tip on the surface, whereas a constant phase indicates that the tip sticks continuously to the surface. Then, assuming a surface infinitely stiff, the torsion angle of the cantilever is only due to the lateral motion of the surface. Thus, the relation between ΔV_L and the torsion angle, or its corresponding lateral displacement Δy , is determined through the linear fit of ΔV_L versus Δy as illustrated in Fig. 2.17.

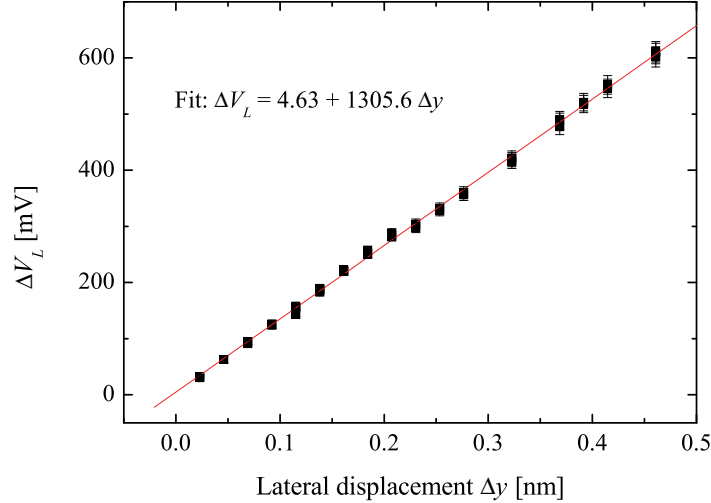


Figure 2.17: Linear variation of the voltage on the PSPD due to lateral displacement of the support of a V-shaped cantilever while the tip sticks to the surface.

Another method leads to the approximation of the lateral sensitivity S_y . For a same

³ Lock-in amplifier SR830, Stanford Research Systems.

motion up-and-down and right-to-left of the laser spot on the PSPD, the output signals ΔV_N and ΔV_L should a priori give the same quantity (homogeneous response of the PSPD). Thus, for a well constructed optical system, an angle θ of bending and an angle ϕ of torsion that are equal (i.e. $\theta = \phi$) result in a same variation of the output voltage of the PSPD. It means that it is possible to estimate the angular sensitivity S_{ang} of the PSPD and to use this value to find the lateral sensitivity from normal sensitivity measurements. More practically, the relation between the bending angle θ , the sensitivity S_z and the normal deflection Δz is given by

$$S_z = \frac{\Delta z}{\Delta V_N} = \frac{c_{shape} \cdot \theta}{\Delta V_N} = c_{shape} \cdot S_{ang} \quad (2.17)$$

where S_{ang} is expressed in [rad/V] and c_{shape} is a factor depending only on the geometry of the cantilever and has the dimension of meters. As example, if we take the case of the beam cantilever, the Equ. 2.3 and Equ. 2.15 relate S_z to S_{ang} via the following expressions

$$S_z = \frac{\Delta z}{\Delta V_N} = \frac{2(L-d)\theta}{3\Delta V_N} = c_{shape} \cdot S_{ang} \quad (2.18)$$

Then, the relation between S_y and S_z is given by

$$S_y = \frac{\Delta y}{\Delta V_L} = \frac{h\phi}{\Delta V_L} = h \frac{\phi}{V_L} = h S_{ang} = \frac{3h}{2(L-d)} S_z \quad (2.19)$$

In this last equation, the geometry of the cantilever and the measurement of S_z through the FD curve define completely S_y . The same approach might be applied to the case of the V-shaped cantilever. The main relation is given by

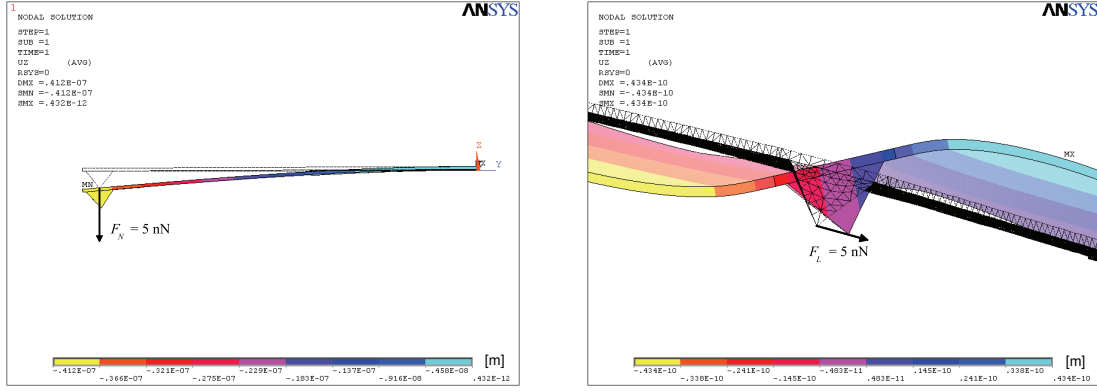
$$c_{shape} = \frac{\Delta z}{\theta} \quad (2.20)$$

where Δz and θ are defined respectively in Equ. 2.10 and 2.11. c_{shape} depends only on ν , α , w , d and L and is independent of the thickness t and the Young modulus E of the cantilever. To give an order of magnitude, for a cantilever with the following parameters, $\nu = 0.27$, $\alpha = 0.49$ radians, $w = 38 \mu\text{m}$, $d = 4 \mu\text{m}$ and $L = 90 \mu\text{m}$, one finds $c_{shape} = 6.5 \cdot 10^{-5} \text{ m}$.

Errors on force calibration and FEM as helping tool

Errors on force calibration are in the majority due to a bad estimation of the cantilever spring constants and/or the sensitivities. Cantilevers do not always have a suitable simple shape for which the approach given in Section 2.1.5 is possible. A helping tool for the estimate of the cantilever spring constants and the relations between the torsional and bending angles is the use of finite element method. Once the geometry and the material of the cantilever are known, it becomes then possible to simulate the cantilever under normal and lateral forces.

Figures 2.18(a) and 2.18(b) show a V-shaped cantilever submitted respectively to a normal force $F_N = 5 \text{ nN}$ and a lateral force $F_L = 5 \text{ nN}$. These simulations were performed using the software ANSYS from the ANSYS Inc. society. The structural deformation of the cantilever was solved under static loading conditions using a triangular mesh of structural



(a) V-shaped cantilever submitted to a normal force $F_N = 5 \text{ nN}$.

(b) V-shaped cantilever submitted to a lateral force $F_L = 5 \text{ nN}$.

Figure 2.18: Finite element method applied to a V-shaped cantilever under normal and lateral force.

solid element SOLID92⁴. Resulting spring constants were within 3% the same as obtained via the method described in Section 2.1.5 for simple shapes of cantilevers, whereas a discrepancy of 10% was found for more complex cantilever shapes. The comparison between the cantilever resonance frequency measured experimentally and the one obtained by simulation allows to validate the FEM calculation or to determine the effective cantilever thickness t when the latter was not precisely known. Moreover, FEM results highlight the influence of the laser spot position on the back side of the cantilever on the final sensitivity measurement as presented in Fig. 2.19. If the laser beam is not well centered on the free end of the cantilever, the previous assumption that $S_y = h \cdot S_z / c_{shape}$ is not more correct and results in significant errors.

Other difficulties in force calibration arise from the laser beam and the optical path conception. Among the causes of errors, we find the asymmetric gaussian beam produced by the laser diode. This asymmetry results in a different output voltage for a same vertical or horizontal displacement of the laser spot on the PSPD. In other words, $\Delta V_N \neq \Delta V_L$ and the approximation $S_y = h \cdot S_z / c_{shape}$ becomes inaccurate. Unfortunately, while the experimental measurement of S_z is a rapid and reliable process, the estimate of S_y is time consuming since it has to be done for each cantilever and each time the detection system is modified. This is one reason why the approximation $S_y = h \cdot S_z / c_{shape}$ done for lateral force measurements is so tempting, but it shall be used with precaution. Other difficulties encountered within the normal and lateral force calibrations are related to the alignment of the laser detection system itself. For example, errors due to diffraction effects might originate from a laser spot non carefully focused on the cantilever. In this case, the misaligned laser spot reflects on the edge of the cantilever and loses its symmetry. Similarly, the reflected beam on the PSPD should be perfectly centered to avoid the non linearities of the PSPD and so that variations of position result in linear variations of the output voltage, hoping of course for a circular shape of the laser spot. Finally, a misalignment of the system «laser-cantilever

⁴ SOLID92 has a quadratic displacement behavior and is well suited to model irregular meshes. The element is defined by ten nodes having three degrees of freedom at each node. The element also has plasticity, creep, swelling, stress stiffening, large deflection, and large strain capabilities.

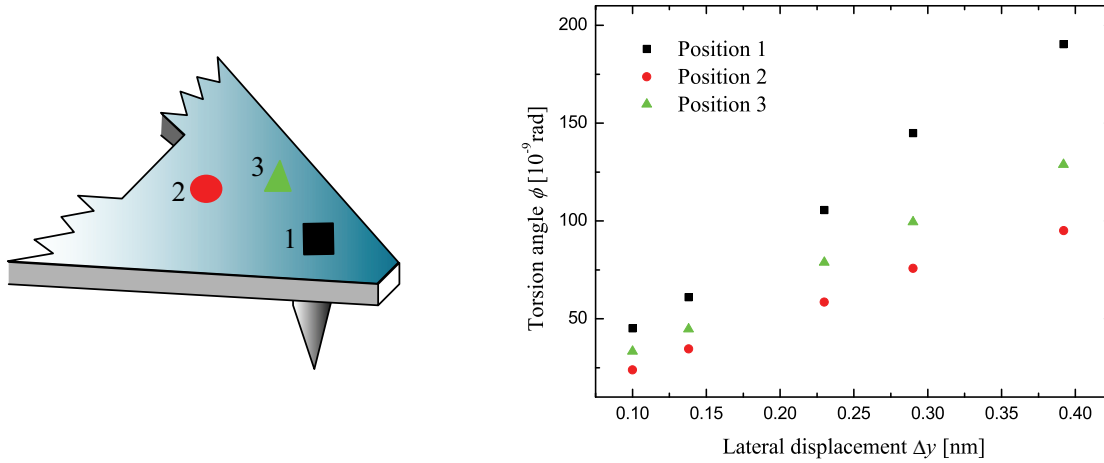


Figure 2.19: Torsion angle as function of the lateral displacement for different positions of the laser spot on the back side of the cantilever as schematically represented on the left picture. This schematic representation is based on FEM analysis.

main plane-PSPD» induces a coupling between the normal and lateral displacements of the laser spot on the PSPD. This coupling might be combined to mechanical crosstalk between torsional, lateral and normal displacements of the cantilever due to scanner geometry and movement.

A more detailed description of the recurrent errors occurring during the AFM calibration might be found in the papers of Schwarz [27], Feiler [34], Ogletree [32] and Liu [35]. To summarize, the main problem lies in the calibration of the lateral force, while the normal force is generally well calibrated using the FD curve. The lack of an accurate and generalized lateral force calibration explains the frequently poor reproducibility observed in the data obtained by different research groups on the same subject, sometimes even with the same AFM. In our case, we are more interested in the phenomenological behavior of the lateral force during friction experiments, than to perform precise quantitative lateral force measurements. Our results, based on relative comparison of data obtained on the same substrate, with the same cantilever, but with different environmental parameters, need the lateral force calibration only to fix an order of magnitude.

FMM calibration

The force modulation technique is based on extremely small displacements of few angstroms of the cantilever support while the AFM tip is scanning the surface in contact mode. The small displacements have to be accurately calibrated in order to obtain quantitative measurements of the surface elasticity. To achieve this goal, a lock-in technique is used. A lock-in amplifier⁴ modulates sinusoidally the voltage applied to a piezo system that moves the surface relatively to the cantilever support. The direction of the modulation is normal to the surface in the case of testing the normal compliance of a material, and tangential to the surface for shear elasticity measurements. To avoid any deformations of the surface, diamond samples are preferred as calibration reference. This modulation results in oscillations of the cantilever (torsion or bending) corresponding to small variations of the output voltage of

the PSPD. This last signal is then analyzed by the lock-in to check its amplitude and phase compared to the initial signal.

The calibration of the normal and lateral displacements of the FMM is based on the same procedures as the normal and lateral force calibrations. The method rests on two main assumptions, i.e. a linear response of the PSPD for small variations of the laser spot position and a linear behavior of the piezo-system governing the tip-surface relative motion. For the calibration of the displacement normal to the surface, we need the ratio of the vertical displacement of the scanner divided by the change in voltage ΔV_N of the PSPD. This ratio is in fact simply the normal sensitivity S_z obtained by performing FD curves with the piezo system previously calibrated on gratings. The value of the sensitivity S_z obtained in that way is defined for low frequencies of oscillations, since it is not possible to perform FD curves at few kHz. At the opposite, the FMM method uses oscillations at high frequencies (1kHz-100kHz) to obtain an average value of the elasticity while scanning the surface and to avoid noise problems. The frequency of the modulation signal is chosen far away from any resonance of the system surface-cantilever and the choice of its amplitude is determined by $S_z \cdot \Delta V_N < 0.5$ nm, so that surface deformations are small enough to stay in the elastic regime. The same approach is performed with the tangential modulation via the lateral sensitivity S_y . This sensitivity gives the ratio of the lateral displacement of the end of the tip, divided by the change in voltage ΔV_L of the PSPD. In this case, keeping no phase change is important to stay in the range of lateral motion where the tip sticks to the surface and does not slip. Once the normal or lateral modulation has been carefully calibrated using hard samples, it becomes then possible to test quantitatively the elasticity of surfaces or nano-objects.

2.2 Other microscopy techniques: TEM and SEM

Besides the scanning probe microscopies (SPM) that use physical probes to interact with the surface, other techniques use beam methods based on the interactions of photons, electrons, neutrons, or positrons with the surface. We briefly present here the scanning electron microscopy (SEM) and the transmission electron microscopy (TEM) that have been used to image surfaces, cantilevers and nano-objects in this work. Their basic principle is the same as optical microscopes except that instead of using light to image the surface, it uses electrons.

2.2.1 Electron-surface interactions

The response of the surface to an incident electron beam is composed of different particles and interactions as schematically represented in Fig. 2.20. When an incident electron passes near an atom, it can impart some of its energy to a lower energy electron belonging to an atom of the studied specimen. It results in an ionization of the low energy electron. Then, this ionized electron leaves the atom with a small kinetic energy (0-30 eV) and is picked up by a detector (See Fig. 2.21). These electrons are called secondary electrons (SE). Due to their low energy, only SE near the surface are measured, and thus, they are principally related to the surface topography. These SE let some vacancies in the shell of the atoms. Electrons of higher energies, belonging to the atom, may fall into the lower energy shell. This process goes with the emission of X-rays to balance the total energy of the atom. The

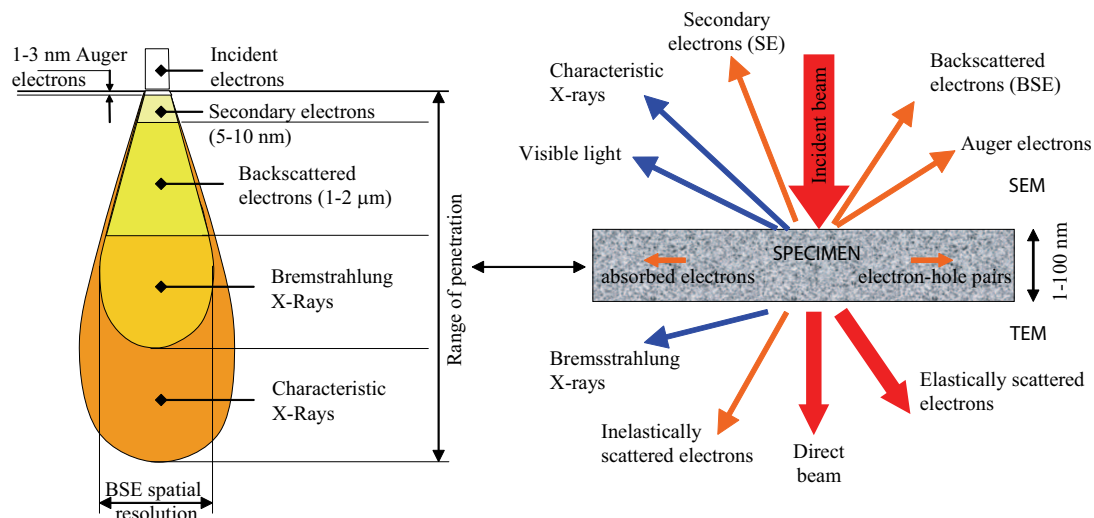


Figure 2.20: Interaction of an incident electron beam with a surface resulting in diverse particles depending on the intensity of the incident beam and its range of penetration.

X-rays are strongly related to the element from which they originated. Another possibility instead of the X-ray emission is that an electron of the outer shell leaves the atom. This electron is called an Auger electron. They are used for surface analysis and are generally not detected in SEM. Other electrons are scattered backward after colliding with an atom of the specimen. They are called backscattered electrons (BSE). The production of BSE is related to the material of the specimen and more precisely to the atomic number of its elements. Finally, some electrons of the incident beam are also absorbed in the material.

For a thin specimen, as it is the case in TEM, some electrons are unscattered and directly transmitted without any interactions. They form the direct beam. The intensity of the unscattered electron signal is inversely proportional to the thickness of the specimen. Another kind of electrons is the inelastically scattered electrons. These electrons have lost a part of their energy while interacting with the specimen atoms. This dissipation of energy might be due to phonons or plasmons, but also from intra- and inter-band transitions, ionizations and bond breaking. This loss of energy is specific to the elements composing the specimen. Thus, information about the composition of the specimen is deduced from inelastically scattered electrons and used for electron energy loss spectroscopy (EELS). At the opposite, other electrons are elastically scattered through the specimen. Their total kinetic energy and momentum are constant. In fact, the electron interacts with the electrical field in a heavy atom, but only little energy is transferred. The direction of the electron speed changes, whereas its amplitude remains almost constant.

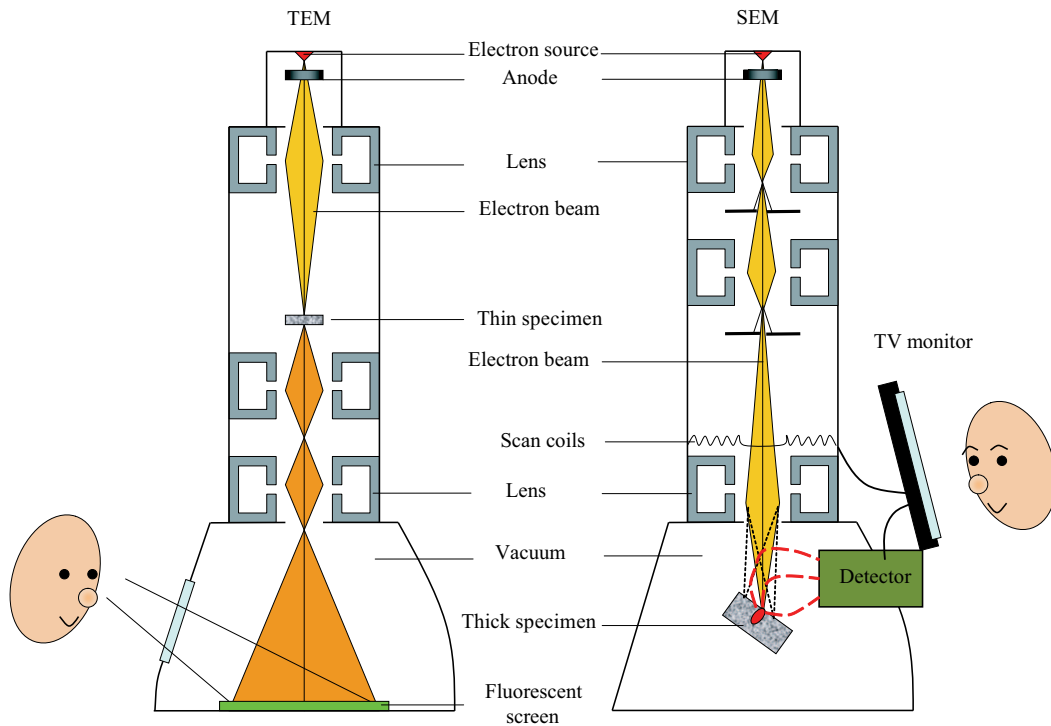


Figure 2.21: Comparison between the TEM and the SEM. The TEM is analog to a slide projector whereas the SEM is based on a TV principle.

2.2.2 SEM and TEM working principles

SEM and TEM principles are presented in Fig. 2.21. The TEM works like a slide projector, whereas the SEM is similar to a television where what you see is what the detector sees. For both microscopes, an electron gun produces a coherent monochromatic electron beam that is accelerated by a cathode. Field emission sources or thermionic sources are generally used for this purpose. Then, magnetic or electrostatic lenses focus the signal on the specimen. In TEM, the specimen is so thin that one observes directly the transmitted beam on a fluorescent screen. In SEM the signals have to pass through a detector, since the thickness of the specimen avoids any transmission of information and only particles emitted close to the surface are caught. This is in fact the main difference between TEM and SEM.

The TEM is used for chemistry analysis (X-rays, EELS), for atomic structure studies with a high resolution ~ 0.2 nm, or to have an insight into the microstructures and the defects. The SEM is more dedicated to topographic studies, but may also be related to chemistry analysis. The disadvantage of these techniques is the time allotted to the preparation of the samples to be imaged, due, for example, to the vacuum of their chamber or to the need of conductive samples to avoid charge effects.

2.3 Contact angle measurements

Information about the hydrophilic behavior of a surface might be deduced from contact angle measurements. We have to differentiate static from dynamic contact angle. A droplet lying on a flat solid surface allows to measure the static contact angle. We are in a configuration of minimum and stable energy and the contact angle is simply measured by drawing on an enlarged photograph a line tangent to the gas/liquid interface at the contact line. Other methods involve the shape of the sessile-drop to extract the contact angle via numerical algorithms based on the Laplace equation [36, 37]. Sometimes, instead of a drop, a flat plate or a needle is partially vertically submerged in the liquid and, again, contact angles are measured by means of low-power optics combined or not with numerical calculations. Measurements of static contact angle give a good approximation for the hydrophilic/phobic properties of a surface and are really convenient compared with dynamic contact angle measurements. Unfortunately, they are generally not enough precise in terms of surface tension measurements.

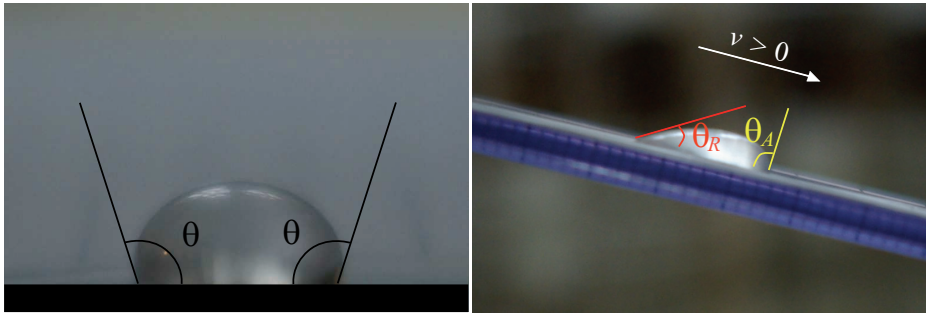


Figure 2.22: Illustration of the static and dynamic behavior of a droplet.

In the case of dynamic contact angle measurements, the three phases boundary (liquid/solid/gas) - in other words the contact line - is in motion. Thus, the contact angle depends on the spreading velocity v of the contact line [38]. If we consider the two-dimensional problem of a droplet moving straight forward from the left to the right along a line with a velocity $v > 0$, we will observe two different contact angles (See Fig. 2.22). One referring to the left part of the droplet, and that will be generally smaller than the other one, related to the right part of the droplet. The extrapolated value of the contact angle θ in the limit as $v \rightarrow 0$ with $v > 0$ (respectively $v < 0$) is called the advancing contact angle θ_A (respectively the receding contact angle θ_R). An illustration of experimental results on dynamic contact angle measurements is shown in Fig. 2.23. As consequence, for many material systems, there exists an interval $[\theta_R, \theta_A]$ characterized by a non-uniqueness static contact angle for a non-moving contact line. This difference between the maximum advancing and minimum receding contact angle values is often referred to as the contact angle hysteresis. Note finally that both dynamic and static contact angle measurements depend on the recent history of the surface-droplet interaction.

Measurements of dynamic contact angles are similar to those for static angles. They are based on the shape of the drop, but in addition, they are time dependent. Various techniques have been used to measure the dynamic contact angle. One is called the dynamic Wilhelmy method [5]. It consists in imaging the dynamic immersion and emersion of a fiber or a plate

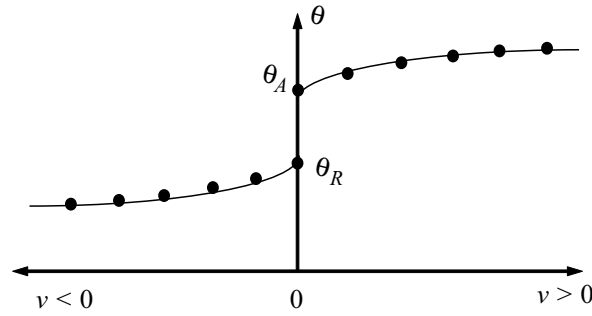


Figure 2.23: Illustration of experimental results on dynamic contact angle measurements as function of the velocity v of the droplet relatively to its solid support. The angles θ_A and θ_R correspond respectively to the advancing and receding contact angles.

into a liquid. The contact angle obtained from the immersion of the probe into the liquid is the advancing contact angle. The reverse process corresponding to the withdraw of the probe from the liquid gives rise to the receding contact angle. Another method starts from a conventional sessile-drop lying on a flat solid support. Then images of the drop are taken while the support is slowly tilted until the movement of the contact line occurs. Dynamic contact angles may be assayed at various rates of speed and, in theory, they should be equal to static contact angles when measured at low velocities provided that there is no hysteresis.

Chapter 3

Friction at the nanoscale

In this chapter, we are interested in the phenomenon of friction at the nanoscopic scale. We briefly review the historical background relative to the macroscopic friction before to focus on the recent theories explaining the friction at the molecular level. We present then our experimental results on the variation of the friction force as function of the AFM tip sliding velocities at different normal loads and relative humidity levels. Our results are accompanied with analytical relationships that explain the interplay between the characteristics of the contacting surfaces and the different environment variables like the applied load or the humidity.

WHEN TWO BODIES contact each other and one of the bodies begins to slide against the other one, a force opposed to the movement appears. This force is called the friction force F_F . It lies in the contact plane of the bodies and has to be perceived differently than the Newtonian approach of an independent external force that acts on a body. In fact, F_F is an internal force that opposes to the externally applied force inducing the motion [39]. It is a *reaction* force to an external solicitation, similar to the adhesion force that has to be overcome to break a body in two pieces. Thus, the friction force appears only when one tries to move one of the bodies relatively to the other one. Part of the energy used for the motion of the body is transferred to the friction phenomenon. This aspect plays a key role in the everyday life issue. On one hand, without friction force, we would effectively not be able to walk, cars to move or brake, but on the other hand, one third of the world energy resources is lost in unproductive friction phenomena [14], occurring for example in bearings or motors and necessitates then the use of lubricants to decrease the friction.

In some situations, the minimization or elimination of losses resulting from friction is desired, but at the opposite, in other situations, improvement of the friction is the final goal. Thus, the purpose of research in the field of friction is to understand its basic principles to better control the phenomenon. We will briefly review now the historical background related to the question of friction. As surprising as it may seem, many of the earliest ideas and models related to friction are still relevant today although they are 500 years old.

3.1 History of the friction

The first documentation related to a scientific approach of the phenomenon of friction was formulated by Leonardo da Vinci in the 15th century. His insights were unfortunately forgotten for years until the seventeenth century, when a French physicist, Guillaume Amontons, rediscovered da Vinci's laws of friction by studying the friction force F_F needed to slide a mass M across a flat surface. His first law predicts that the frictional force F_F is directly proportional to the applied normal force F_N . This law is also known as the Coulomb friction law. The parameter of proportionality, μ , is called the coefficient of friction. Furthermore, he observed that, counter intuitively, friction does not depend on the apparent contact area. This leads to the second Amontons law: the tribological friction coefficient μ is independent of the contact area of the sliding surfaces and the loading force. This law means that the friction force experienced by a small block on a flat surface is the same as the friction of a large block with the same mass! Finally, one century later, the French physicist Charles Augustin de Coulomb completed the empirical Amontons laws by a third one stipulating that the friction is independent of the relative velocity v of the bodies once the sliding movement begins. These three laws might be summarized by the equation

$$\mu = \frac{F_F}{F_N} = \text{constant} \quad (3.1)$$

where the constant is independent of the area of contact and the sliding velocity. From a theoretical point of view, there were some difficulties in explaining these laws. However, one starting point of explanation was based on geometrical aspects of the surface roughness of the bodies in contact. The description was as follows: the contact surface of the bodies sliding the one against the other one is made of numerous asperities. During the sliding process, each of the asperities has to "climb" the asperities of the other body in order that the body moves in the sliding direction (See Fig. 3.1). The force $dF_{F,i}$ needed to lift the i th asperity was given by

$$dF_{F,i} = dF_{N,i} \tan(\alpha_i) \quad (3.2)$$

where $dF_{N,i}$ is the corresponding load and α_i the maximum slope of the asperity junction. It results that for the whole area of contact, the friction force corresponds to the sum over all the asperities:

$$F_F = \sum_i dF_{N,i} \tan(\alpha_i) = F_N \langle \tan(\alpha_i) \rangle = \mu \cdot F_N \quad (3.3)$$

where it was assumed that μ was equal to the average of the local slopes and that there was no correlation between $\tan(\alpha_i)$ and $F_{N,i}$. In this model, the friction is explained in term of asperities mechanically locked against the normal load. No adhesion is considered and thus, it applies only to non adhering surfaces. At the end of the 18th century, this surface roughness model and the three laws of friction explained qualitatively and quantitatively the majority of rubbing surfaces. Then, in the case of adhering surfaces, the model was completed by adding a constant $F_{adh} = \mu \cdot F_0$ [13] so that

$$F_F = \mu \cdot (F_0 + F_N) = F_{adh} + \mu F_N \quad (3.4)$$

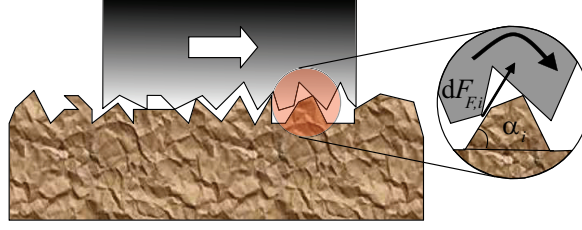


Figure 3.1: Schematic representation of the asperities at the microscopic scale. When one rough body moves on the top of the other one, each of its asperities has to climb the asperities of the other body in order to move in the sliding direction.

By this way, F_{adh} was the part of the friction force accounting for the intermolecular adhesive forces at the interface and the coefficient of friction was defined in a general form as $\mu = dF_F/dF_N$.

From a theoretical point of view, these models were able to explain the static friction, i.e. the initial force needed to initiate the motion, but they fail in explaining the dynamic (or kinetic) friction, i.e. why it was necessary to maintain this initial force once the motion started in order to have the relative motion of the bodies. This fact was pointed out by Leslie in 1804 [40]. Effectively, the energy expended to climb an asperity should be recovered when falling down to the other side of the asperity, since the normal load is a conservative force. And thus, no energy is ever lost, and once the relative motion of sliding starts, it should continue indefinitely rather than having to be continually maintained with a supplementary driving force. To overcome this problem, mechanisms of energy dissipation had to be included into the model.

Further progress in the comprehension of the friction arrived in parallel to the development of the surface investigation techniques. Another aspect on the friction phenomenology was brought up by Bowden and Tabor [41, 42]. They found that the electrical conductivity at a metal-metal interface was proportional to the load pressing the two surfaces together. The results showed that in general, the surface contact occurred only locally at the top of the microscopic asperities of the surfaces, so that the real contact area was very small and almost independent of the measured apparent contact area. In that way, the friction force should be independent of the apparent area of contact, but not of the real area of contact. At this point, another problem arises from the theory of elastic deformation of Hertz (See Section 1.3). Effectively, it was usually assumed that the real area of contact was proportional to the normal force to the power two-thirds and not as a first power as figured by the proportionality found by Bowden and Tabor. However, their experiments showed also that the surface deformations were mainly plastic, which explains the energy losses during the friction process and the disagreements with the Hertz theory. According to these last elements, the friction between unlubricated surfaces arises on the one hand from F_{adh} , i.e. the adhesions occurring at the region of real area of contact and that have to be sheared during the sliding process, and on the other hand, from F_{def} , i.e. the ploughing, grooving or cracking of one surface by the asperities on the other. The friction force was then written as [42]

$$F_F = F_{adh} + F_{def} = \tau A + F_{def} \quad (3.5)$$

where τ is the average shear strength of the junctions, i.e. the microscopic adhesions of the surfaces, and A is the real surface of contact. If we are strictly in an elastic domain, i.e. a reversible domain with no wear, the previous relation reduces to $F_F = \tau \cdot A$, where A depends on the surface geometry and is directly related to the normal load. Different models have been established for the dependence of the real area of contact on the normal force, and thus, the relation between the friction force and the normal force. In the case of a single asperity contact, a two-thirds power law is expected in accordance with the Hertz theory [17, 43, 44]. For multi-asperity contacts and self-affine surfaces [17, 43, 45], the linear dependence is more likely. The border between single and multi-asperity contact is not well defined, but, if we assume that the primary result of increasing the normal force is to cause the existing contact to grow and not to form new contacts inside the apparent area of contact, then we stay in the single asperity contact while increasing the normal force in a friction experiment [46].

Finally, it remains surprising that for several centuries, the general law described by Equ. 3.1 defied a satisfactory model-independent explanation, in the sense that contrary to other fields in physics where it is clearly possible to predict the solution of a complex problem like in solid state physics or astronomy, it is still not possible to find a coefficient of friction while all properties of the surfaces in contact are known (surface energy, elastic properties and loss properties) [14]. However, it is perhaps not so surprising. The interaction between two surfaces in contact is a really complex phenomenon for which a great variety of interactions occurs and has to be taken into account. Friction cannot be treated without thinking of wear and adhesion. All three are intimately related and, to understand what happens at the macroscopic level, we have to determine the non-equilibrium processes occurring at the molecular level. The development of apparatus looking down to the atomic scale and of sophisticated computer simulations of dynamic many-body systems started to bring an answer for a more fundamental representation of the friction.

3.2 Thermally activated phenomena in nanofriction

The actual course to the miniaturization of everyday life objects has lead to the study of friction from the macroscopic point of view to the nanoscopic one. In the nanoworld, forces or processes that were in a first approximation not relevant at larger length scale, such as capillary forces, become of crucial importance and have drastic effects. As result, behaviors of friction peculiar to the macroscale are not always valid at the nanoscale. An example is the dependence of the friction force on the scanning velocity. For macro-contacts, no changes in friction have been revealed by varying the scanning velocity, whereas the friction force presents numerous behaviors at the nanoscale when the sliding velocity is changed. Thus, the study of the friction phenomenon has to be done at scales relevant for its applications.

In this section, we study the dependence of the nanofriction on the velocity, while taking into account the normal force and the humidity. The complete understanding of the velocity dependence of the friction at the nanoscale is still under current reflection, motivated by its strong impact on our society. Indeed, we just have to think of the miniaturization of moving components, such as hard disk drives or nano-electromechanical systems, which requires a perfect comprehension of the forces at the surface and interface. Since almost ten years, different experiments have highlighted the phenomenological behaviors of the nanofriction.

Researchers have each time proposed a model to explain the results, sometimes, contradictory with the previous assumptions. However, no real consensus has been found until now. To begin, we propose here to have a look back to the Tomlinson model, one of the first friction models offering a satisfactory explanation of the friction at the molecular scale. Then, we will review shortly the main experimental results on the velocity dependence of the friction, having a look at the same time at the evolutions of the basic Tomlinson model to interpret the results.

But before going further, we have to discuss few experimental observations about the phenomenon of friction at the nanoscopic level. The first observation concerns the static and dynamic friction that might be seen as two distinct frictional phenomena. The static frictional force is defined as the minimal force needed to initiate the sliding. This force depends on the atomic structure of the sliding surfaces and the adhesion forces. The static frictional force has to be related to the breaking of bonds or the initiation of plastic flow occurring at the beginning of the motion of one body against the other one. The dynamic friction force is the force needed to keep two substrates sliding. In other words, it is the force necessary to balance the energy losses due to the motion of one body against the other one. It is directly related to energy dissipation. These losses might be caused by various excitations or deformations at the interface. The second and last observation is illustrated in Fig. 3.2. It is usual to observe a saw-tooth shape of the friction loop while scanning flat surfaces like HOPG or mica [47]. This shape is due to the atomic stick and slip of the tip sliding on the surface. It allows us to introduce the first theoretical model explaining these experimental observations from a molecular point of view. This theoretical work dates from 1929 and is due to Tomlinson. He proposed an atomistic picture of the origin of the frictional forces.

3.2.1 An atomistic view of the Amontons-Coulomb laws: the Tomlinson model

The Tomlinson model is a very simple and instructive mechanical model explaining already most of the phenomena occurring in friction, such as the atomic stick and slip, the static and the kinetic friction. It was introduced by G. A. Tomlinson in his paper entitled "*A molecular theory of friction*" [49] and his development has been successfully extended and modified to include thermal effects as in the Frenkel-Kontorova-Tomlinson model [50].

For the sake of simplicity, we consider the one-dimensional Tomlinson model at zero temperature ($T = 0$). In this model, the surface is described as a periodic arrangement of atoms whose potential of interaction with an AFM tip U_{ts} is usually approximated by a simple sine with a peak-to-peak amplitude U_0 and period a equal to the lattice periodicity:

$$U_{ts}(x) = -\frac{U_0}{2} \cos\left(\frac{2\pi x}{a}\right) \quad (3.6)$$

Then, the system of the AFM tip attached to the cantilever is schematically represented by a point-like tip of mass m , usually an atom, attached to a spring of elastic constant k fixed to a support moving at the velocity v . The point-like tip represents in fact the average of the real tip-surface contact where up to thousands of atoms may be involved. The spring is extended between the position of the tip (or atom) x and the position of the cantilever support $x_s = vt$, t being the time. The corresponding elastic potential, U_{el} , of the interaction between the tip and the support is then

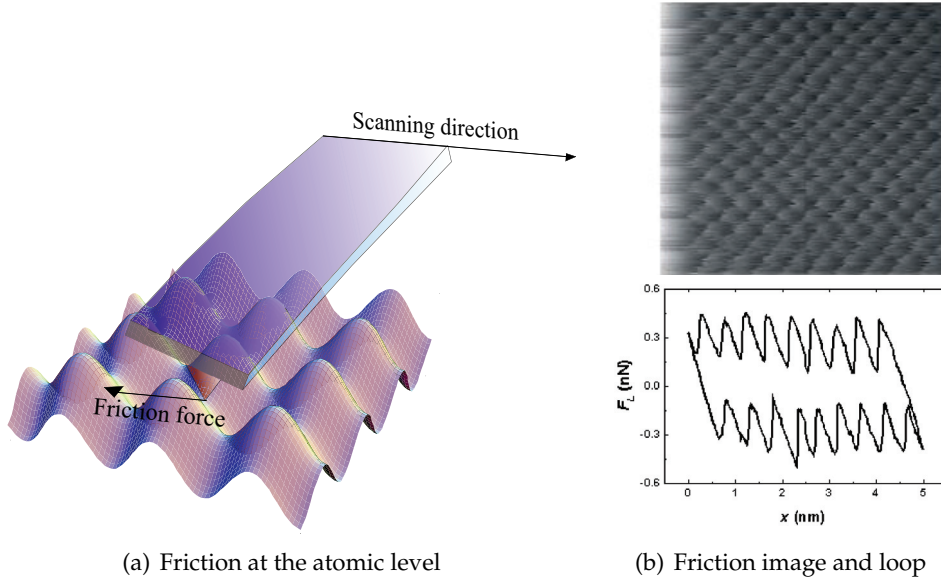


Figure 3.2: Illustration of the friction force at the atomic level. On the left (a), an AFM tip slides over an atomically flat surface represented by a sinusoidal potential of interaction. Corresponding experimental results are shown on the right (b): the top image is a map of the friction for which one loop is presented in the bottom image (from Ref. [48]). We clearly see the saw-tooth shape obtained for one loop over one line of scan.

$$U_{el} = \frac{k(x - x_s)^2}{2} \quad (3.7)$$

where the deformation of the spring is simply given by $(x - x_s)$. Note that the elastic constant k characterizing the in-plane deformations corresponds in fact to the spring constant of the system "surface-tip-cantilever" and not only the spring constant of the cantilever. Then the AFM tip is dragged over the sinusoidal potential and all atoms of the involved surfaces are assumed to interact with each other. The total energy of the system for a cantilever moving at a constant velocity v along x becomes

$$U_{tot}(x, t) = -\frac{U_0}{2} \cos\left(\frac{2\pi x}{a}\right) + \frac{k(x - vt)^2}{2} \quad (3.8)$$

Referring to Fig. 3.3, the cantilever support slowly moves along the x -direction and the AFM tip slides on the surface and passes from one minimum of energy to the next one. As long as the displacement of the cantilever support is small, the tip stays at its position in a local potential minimum of the surface and the energy is elastically stored in the spring. But beyond a certain distance and as a result of the movement of the support, this potential minimum vanishes and the tip prefers to move to the next minima. As we will see, the movement of the tip from one minimum to the next can be continuous or jumping depending on the relation between the corrugation U_0 and the elastic energy. Nevertheless, Tomlinson's model assumes that this change of position is done abruptly, meaning non-adiabatically. In other words, the elastic energy is transformed into vibrational or kinetic energy during the sliding process. The vibrational energy was considered to dissipate into

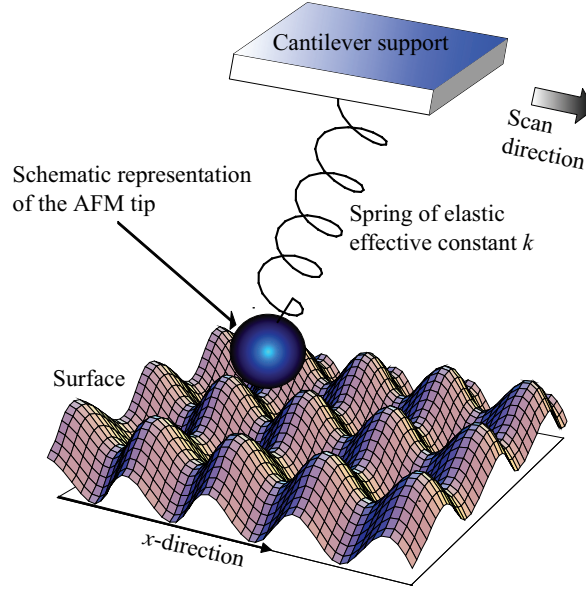


Figure 3.3: Sketch of the Tomlinson model. A point-tip (the sphere) is attached through a spring to the cantilever support, which moves slowly along the x -direction. The tip slides on the surface and passes from one minimum to the next one.

vibrational energies of the other atoms, i.e. into thermal energy, involving the irreversible process of friction. In the case the position does not change abruptly, i.e. in the assumption of slow displacement of the tip, then an adiabatical change from one minimum to the next one occurs and the Tomlinson model fails to explain the dissipation of energy during the sliding process [51].

To be more general, it is possible to add to the equation of motion of the tip a damping term $\eta\dot{x}$ proportional to the tip velocity to account for energy dissipation. In this case, the motion of the tip over the surface is described by

$$m\ddot{x} - \eta\dot{x} = \frac{\pi U_0}{a} \sin\left(\frac{2\pi x}{a}\right) + k(x - vt) \quad (3.9)$$

This last equation described the displacement of the point-tip over a surface from a phenomenological point of view. Sometimes, thermal fluctuations are taken into account by adding to Equ. 3.9 a stochastic force in the framework of the Langevin approach as described in Ref. [52].

During the sliding process, the position of the tip at a given time t is determined by equating to zero the first derivative of $U_{tot}(x, t)$ with respect to x :

$$\frac{\partial U_{tot}(x, t)}{\partial x} = \frac{\pi U_0}{a} \sin\left(\frac{2\pi x}{a}\right) + k(x - vt) = 0 \quad (3.10)$$

The critical position x_c at which the tip becomes unstable and gets ready to move to the next minimum takes place when the second derivative of Equ. 3.8 vanishes:

$$\frac{\partial^2 U_{tot}(x, t)}{\partial x^2} = 0 \implies x_c = \frac{a}{2\pi} \arccos\left(-\frac{ka^2}{2\pi^2 U_0}\right) \quad (3.11)$$

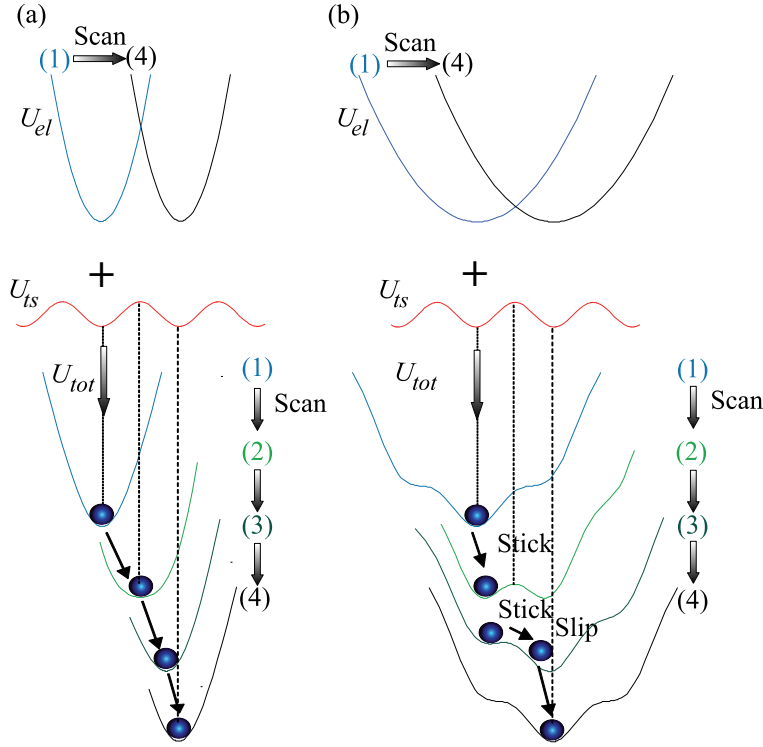


Figure 3.4: Illustration of the Tomlinson model (adapted from Ref. [53]). In this figure, the tip is schematically represented by the shaded circle always located at a minimum. (1)-(4) denote the time evolutions of the potential while scanning the surface. The total energy U_{tot} obtained by summing the elastic energy U_{el} stored in the spring with the tip-surface potential energy U_{ts} presents two cases: in (a), U_{tot} has only one minimum and the tip slides continuously over the surface. Such a case is peculiar to a stiff spring or cantilever. The sketch (b) illustrates the case of a soft cantilever. U_{tot} is characterized by several metastable minima whose result is a stick-slip behavior for the tip jumping from one minimum to the next.

As result, the stick-slip instability occurs only when $ka^2/2\pi^2U_0 < 1$, i.e. when the system is not too stiff or the tip-surface interaction strong enough to make the tip stick at its last position. In the other case, $ka^2/2\pi^2U_0 > 1$, uniform sliding occurs and the dissipation of energy arises only from the damping term $\eta\dot{x}$ which vanishes for $\dot{x} \rightarrow 0$ [52]. From Equ. 3.10 and Equ. 3.11, it is possible to evaluate the critical lateral force $F_{F,c}$ that induces the jump from one minimum to the next one:

$$F_{F,c} = -k(x_c - vt) = \frac{ka}{2\pi} \sqrt{\frac{2\pi^2U_0}{ka^2} - 1} \quad (3.12)$$

In this model, the static friction $F_{F,stat}$ is simply given by the force needed to overcome the energy barrier formed by the surface potential while the AFM tip is not yet in motion. And finally, the kinetic friction $F_{F,kin}$ corresponds to the average of the lateral force over a period of time [52]. Assuming a periodic motion of period na/v , n being an integer, we have

$$F_{F,stat} = \frac{\pi U_0}{a} \quad (3.13)$$

$$F_{F,kin} = \langle -k(x - vt) \rangle = \frac{v}{na} \int_0^{na/v} -k(x - vt) dt \quad (3.14)$$

$$\Delta W = - \int_0^{na/v} \eta \dot{x}^2 dt \quad (3.15)$$

where ΔW is the energy dissipated during one period. The relation between the kinetic friction and the energy dissipated during the same period is then [52]

$$F_{F,kin} = \frac{\Delta W}{na} \quad (3.16)$$

The figure 3.4 illustrates the Tomlinson model in the case of an AFM tip interacting with a surface. The parabolas in the top represent the elastic energy stored in the deformation of a stiff and a soft cantilever, whereas the sinusoidal potential below is the atomic potential corrugation of the interaction between the point-like tip and the surface lattice. As result, the total potential of interaction has only one minimum in the case of the stiff cantilever, while many minima characterize the interaction of the soft cantilever with the surface. The metastable positions of the AFM tip for these minima result in the stick-slip behavior.

3.2.2 The concept of superlubricity in friction

The superlubricity is defined as a sliding regime in which frictional forces vanish. It corresponds to a state of ultralow energy dissipation. However, friction is strongly reduced, but not entirely zero. Of course, it is a challenging regime for all mechanical devices where friction has to be avoided and different ways have been explored to reduce the dry friction. At the beginning, the term lubricity has been introduced to characterize the vanishing friction due to the mismatch of the lattice of two sliding surfaces. In 1990, Hirano and Shinjo presented a theoretical study that suggested the existence of two atomistic origins of the frictional force generated by the molecular constituent of the solids in contact: the *atomistic locking* and the *dynamic locking* [54]. By considering two flat surfaces in contact, one static and the other one sliding, the atomistic locking corresponds to a continuous change of the configuration of the whole atoms of the sliding surface due to dynamic processes, whereas the dynamic locking is the discontinuous change of this configuration occurring when the interatomic potential is stronger than a specific value. In other words, for the static locking, the atoms of the surface move continuously in a quasi-static way, changing their positions of equilibrium continuously, and thus, the system can slide without resistance. Another assumption behind this description is that the surfaces contact incommensurately¹ [51]. In fact, in the case of incommensurate lattices, the atoms experience the same forces, but with an out of phase variation. The result, from a simple point of view, is that at the same time some atoms will spend some energy to overcome an energy barrier, which will be compensated by the energy release of some other atoms sliding into a local minimum of energy. At the end, the energy dissipation may become so small that friction vanishes. In the other case, for the dynamic locking, the atoms change their equilibrium positions discontinuously in a non adiabatical manner leading to some energy dissipation. The transition from dynamic to

¹ The term incommensurate means that the ratio of the lattice constants of the surfaces along the sliding direction is irrational, whereas commensurate is used for a rational ratio. We speak of surface in registry for commensurate lattices and out of registry for incommensurate lattices.

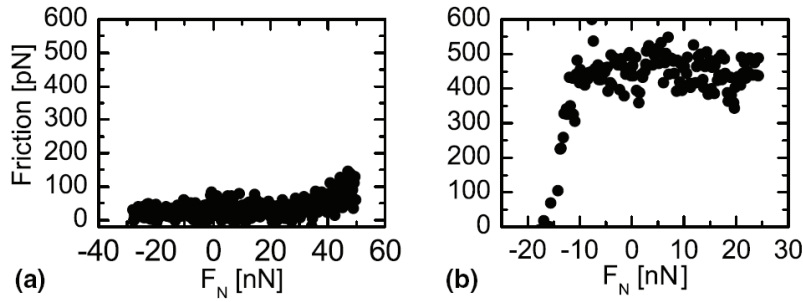


Figure 3.5: Experimental results on superlubricity obtained by twisting one graphite surface relative to the other one (from Ref. [56]). When the surfaces are twisted 20° out of registry, the friction is close to zero (a), whereas for a twist angle of 58° , friction is present and increases with the normal load (b).

static locking is experimentally obtained by twisting the sliding surface with respect to each other: when they are rotated out of registry, then the friction decreases. Recent experimental studies on this subject have highlighted the phenomenon for two flat graphite surfaces in contact [55, 56] and are illustrated in Fig. 3.5. For incommensurate lattices, the AFM tip finds equilibrium positions everywhere along the sliding direction, independently of the load. At the opposite, in the case of commensurate lattices, the tip finds stable positions at specific locations for which the corrugated surface potential depends on the tip-surface distance. As result, dynamic locking depends on the normal load. Notice finally that the main difference between the Tomlinson model and Hirano's theory lays in the fact that possible movements of the constituent atoms of the bodies are considered in the latter theory.

Another way to reach the superlubricity is achieved by reducing the normal load exerted by the tip on the surface [47]. The transition from the stick-slip motion to the superlubricated regime occurs in a continuous way. The theoretical explanation is based on a balance of negative and positive lateral forces whose sum vanishes in average with respect to the time (and not the space), provided there are no instabilities. Such an experiment has been carried out on ionic crystals in ultra high vacuum (UHV). The problem related to this technique is its application in industrial developments due to the need of vacuum and a load inferior to 1 nN. Another study decreased the scanning velocity below a critical value that increases with temperature in order to vanish the dry friction. This effect, called thermolubricity, has been related to thermally activated jumps occurring in the contact area [57].

Finally, a "dynamic" way has been used to reach the superlubricity regime on the atomic scale in UHV. The technique is based on normal modulation of either the surface or the AFM tip while they are in contact. A similar technique used by Riedo *et al.* [58] allowed previously to observe also a reduction of the friction when the contact between a tip and a mica surface in humid air was laterally excited (See Fig. 3.6). In fact, for well-defined frequencies corresponding to normal resonances of the combined tip-surface system, a systematic decrease of friction to negligible values is observed [59]. The cause of this behavior is probably related to an interplay between thermal activation and the fast variation of the tip-surface interaction.

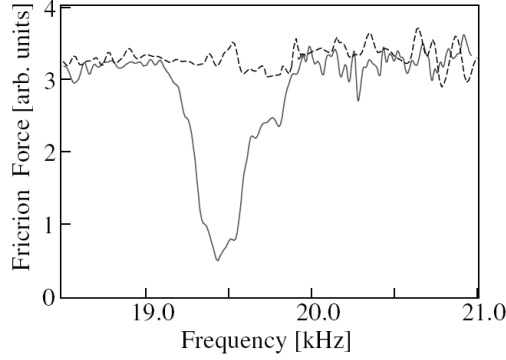


Figure 3.6: Experimental results on the dependence of the friction force on the external frequency of oscillations applied to the tip-surface system for two different velocities of the cantilever support (from Ref. [58]). The scanning velocities of the cantilever support are $8 \mu\text{m/s}$ and $150 \mu\text{m/s}$ for the continuous and the dashed lines respectively, for a same applied load $F_N = 15 \text{ nN}$.

3.2.3 Recent experimental results on friction and evolution of the Tomlinson model

The Tomlinson model has served as basis for the interpretation of the experimental results on friction, notably for the understanding of the dependence of friction on the velocity. As we will see, the relation between friction and scanning velocity has shown different and somewhat contradictory experimental results depending on the investigated surfaces and on the experimental conditions. To clarify the situation, we remind the most important results on velocity dependence of the friction and conclude by the two experimental studies that have shown the transition between a positive and a negative slope of the friction versus the velocity.

Independence of the friction versus the scanning velocity

In 1987, Mate *et al.* [60] observed for the first time atomic-scale features on the frictional force acting on a tungsten wire tip sliding on the basal plane of a graphite surface at loads inferior to 10^{-4} N . Measurements were performed in ambient conditions and revealed little velocity dependence of the friction for scanning velocities between $0.004 \mu\text{m/s}$ and $0.4 \mu\text{m/s}$. They interpreted their results using a phenomenological model based on the sum of a periodic tip-surface force and a spring force for the tip motion. Similarly, Zwörner *et al.* measured in 1998 a constant friction force over a wide range of velocities [61] for various carbon compounds (diamond, graphite, amorphous carbon) and under normal loads between 3.3 nN and 83.4 nN . In fact, they found that the friction force was independent of the scanning velocity for velocities up to $1 \mu\text{m/s}$, while a linear increase was numerically obtained with a theoretical model for higher velocities. They used an AFM working in air and equipped with a silicon cantilever which was moving at velocities between $0.02 \mu\text{m/s}$ and $24.4 \mu\text{m/s}$. Their results were explained using an athermal one-dimensional Tomlinson model.

Logarithmic increase of the friction versus the scanning velocity

In 1997, Bouhacina *et al.* [62] found a logarithmic increase of the friction force versus the scanning velocity (for $0.1 \mu\text{m/s} < v < 60 \mu\text{m/s}$), which was attributed to thermally activated processes. The surfaces were grafted layers on silica and the measurements were performed in a glove box in which the ppm of O_2 and H_2O was controlled. This choice was motivated by the fact that in ambient conditions, the measurements were not enough reproducible to extract a significant variation of the friction as function of the scanning velocity. Then, in 2000, Gnecco *et al.* [48] performed the first measurements related to the velocity dependence of atomic scale friction. Using a friction force microscope under UHV, they found a logarithmic dependence of the mean friction force on the velocity for a silicon tip sliding on a NaCl (100) surface at low velocity ($v \leq 1 \mu\text{m/s}$). A modified Tomlinson model was adopted to explain the experimental data. Finally, Riedo *et al.* [58, 63, 64] observed in addition that the logarithm increase of the friction force with the velocity leads to a critical velocity beyond which friction remains constant. This behavior was explained by the fact that thermal activation is more efficient at low velocity as it depends on the probability of transition between different equilibrium configurations. Notice that more recently, Sang *et al.* [65] proposed a $|\ln v|^{2/3}$ dependence of the friction on the velocity for higher scanning velocities, whereas the $|\ln v|$ dependence is still correct for low velocities.

Power-law increase of the friction versus the scanning velocity

In 1997, Gourdon *et al.* [66] reported a study of the friction on a mica surface covered by lipid films and with velocities ranging from $0.01 \mu\text{m/s}$ to $50 \mu\text{m/s}$. They observed a critical velocity of $3.5 \mu\text{m/s}$ over which the linear increase of friction changes for a constant regime of the friction versus the scanning velocity. Similarly, other experiments [67] showing an increase of the friction with the velocity do not display a logarithmic relation, but suggested an athermal power-law dependence of atomic friction in the form v^β with $\beta \simeq 1.6$ [52] for small scanning velocities inferior to $2 \mu\text{m/s}$. In Ref. [67], the authors found also a smooth non linear increase of the friction for lower velocities attributed to the predominance of stick forces, whereas the linear dependence observed at higher velocities is due to the predominance of viscous forces. For these last studies, the behaviors were explained using an athermal Tomlinson model.

Logarithmic increase and decrease of the friction versus the scanning velocity

In studies related to relative humidity (RH), Riedo *et al.* [63, 64] observed a decreasing friction with increasing the velocity on hydrophilic surfaces, whereas the contrary was observed on hydrophobic surfaces. These last results were interpreted considering thermally activated nucleation of water bridges between the tip and the surface asperities.

Transition from a positive to a negative slope of the friction versus the velocity

Recently, Opitz *et al.* studied the behavior of friction on hydrophilic silicon as a function of the applied load and the sliding velocity during pump-down in a vacuum chamber housing their scanning force microscope [68]. Three distinct regimes were found: first, capillary

Authors	Setup	F_F versus v	Model & note
Mate <i>et al.</i> [60]	tungsten wire tip graphite surface ambient conditions	\sim independence $0.004 \mu\text{m/s} < v < 0.4 \mu\text{m/s}$ $F_N < 10^{-4} \text{ N}$	similar to 1D Tomlinson model
Zwörner <i>et al.</i> [61]	silicon cantilever carbon compounds working in air	independence $0.02 \mu\text{m/s} < v < 24.4 \mu\text{m/s}$ $3.3 \text{ nN} < F_N < 83.4 \text{ nN}$	athermal 1D Tomlinson model
Bouhacina <i>et al.</i> [62]	nanotip grafted layers on silica gloves box	$F_F \nearrow \propto \ln v$ $0.1 \mu\text{m/s} < v < 60 \mu\text{m/s}$ $F_N = 0$	thermally activated processes
Gourdon <i>et al.</i> [66]	silicon tip lipid films on mica ambient conditions	$F_F \nearrow \propto v$ $0.01 \mu\text{m/s} < v < 3.5 \mu\text{m/s}$ $F_N = 1\text{-}15 \text{ nN}$	$F_F = \text{constant}$ for $v > 3.5 \mu\text{m/s}$
Gnecco <i>et al.</i> [48]	silicon tip NaCl(100) surface UHV	$F_F \nearrow \propto \ln v$ $v \leq 1 \mu\text{m/s}$ $F_N = 0.44 \text{ nN} ; F_N = 0.65 \text{ nN}$	thermal 1D Tomlinson model
Riedo <i>et al.</i> [64]	nanotip mica (hydrophobic) ambient conditions	$F_F \nearrow \propto \ln v$ $v = 0\text{-}20 \mu\text{m/s}$ $F_N = 4\text{-}12 \text{ nN}$	thermally activated processes
Riedo <i>et al.</i> [63]	nanotip CrN (hydrophilic) ambient conditions	$F_F \searrow \propto \ln v$ $v = 0\text{-}180 \mu\text{m/s}$ (hydrophilic) $F_N = 12 \text{ nN}$	thermally activated processes
Sang <i>et al.</i> [65]	theoretical study	$F_F \propto (\ln v)^{2/3}$ $v = 0.005\text{-}256 \mu\text{m/s}$	thermal 1D Tomlinson model
Prioli <i>et al.</i> [67]	silicon nitride H_3BO_3 ambient conditions constant RH	$F_F \nearrow \propto v^\beta$ $\beta \sim 1$ $v > 2 \mu\text{m/s}$ $F_N = 100 \text{ nN}$	athermal 2D Tomlinson model
Fusco <i>et al.</i> [52]	theoretical calculation graphite surface	$F_F \nearrow \propto v^{2/3}$ for $T = 0$ $0.001 \mu\text{m/s} < v < 2 \mu\text{m/s}$ $F_F \nearrow \propto \ln v$ for $T \neq 0$	athermal Tomlinson model

Table 3.1: Overview of the main results on the relation between the friction force and its dependence with the scanning velocity. Most of the theoretical explanations of the experimental results have at their origin the Tomlinson model. Notice that the symbols \nearrow and \searrow respectively means "increase" and "decrease".

forces dominate at ambient conditions, second, ordering effects grow up as the vacuum increases, and third, solid-solid contact governs the friction laws at ultra high vacuum. The first regime presents a negative slope of the friction versus the sliding velocity, as found before by Riedo *et al.* [69], and the second and third regimes show a positive slope of the friction as function of the sliding velocity as humidity is progressively removed. This last behavior is typical for hydrophobic surfaces [68, 69].

Another study realized in 2006 by Chen *et al.* [70] reported the transition between a negative and a positive slope for $F_F(v)$ and highlighted at the same time the relation between the dependence of the friction on the velocity and the chemical nature of the interface between the tip and the sample. In their study, surfaces having the potential of forming cross-linked structures (H-bond networks) at the interface with linkage energies that were easy to overcome at the applied loads presented a logarithmic decrease of the friction with the scanning velocity whereas the opposite behavior was observed for surfaces where no such networks were formed. This behavior was also observed in UHV so that capillary processes cannot be considered. The results have been explained in terms of disruption of the glassy H-bonds network domains at critical applied stress and leading to slippage.

To conclude this section, two main behaviors emerge from the review of the experimental results. We have, on the one hand, thermal activation involving vibrations that may excite the slipping from one equilibrium position to the next one. For this kind of thermal activation, the increase of the velocity reduces the probability of transition between the different equilibrium positions and thus it leads to a logarithmic increase of the friction with the sliding velocity. And on the other hand, we have time dependent processes involving intermolecular forces and leading to a logarithmic decrease of the friction force with the scanning velocity. It can be thermal activation of water bridges between the AFM tip and the surface, but also layers covering the surface and whose disorganization under the applied shear stress results in a decrease of the friction force once they do not have enough time to reorganize in a network. Most of the time, a logarithmic dependence has been found, but competition between the different thermal activated processes involving an increase or a decrease of the friction force with the sliding velocity may give rise to other slope trends. Athermal processes have been related to a variation of the friction proportional to v^β , with β equal to 1 or 2/3. However, only few experimental studies have reported such a dependence and most of the work on this subject has been done theoretically. Moreover, as all studies have been performed in environments without precise control of the involved parameters, such as the temperature, it becomes then difficult to judge which process, thermal or athermal, occurs in reality.

3.3 Presentation and motivation of our theoretical model

We present in this section the theoretical developments related to the phenomenological models used to describe our experimental results. Our friction measurements have been performed in an environment where the temperature was almost constant ($T \sim 24^\circ$) and the humidity continuously controlled. By this way, it has been possible to highlight thermally activated processes, and more precisely the balance between the activation of capillary bridges and thermal vibrations. For this purpose, we will show the transition from the hydrophilic to the hydrophobic regime of the friction, by scanning with the same AFM tip

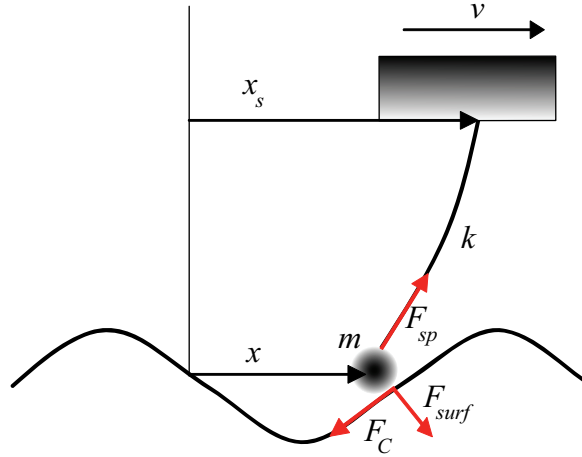


Figure 3.7: Sketch of a point-tip of mass m and coordinate x connected via a spring of constant stiffness k to a support moving at a constant velocity v . The point-tip moves in a corrugated substrate potential undergoing capillary forces F_C , surface forces F_{surf} and the spring force F_{sp} .

a single area of a CrN surface. The linear dependence of the friction on the logarithm of the sliding velocity for both hydrophobic and hydrophilic surfaces has already been explained in the works of Riedo and Gnecco [48, 69]. Until now, two different models were commonly used to explain either the increasing or the decreasing friction as function of the sliding velocity. Here we present a theoretical model including both, the increase and decrease of F_F with $\ln v$. A special behavior related to hydrophobic surfaces was the observation of apparent plateaux at sufficiently high sliding velocities for the curves of friction versus the logarithm of the sliding velocity [71]. Our experimental results reveal also a similar behavior for hydrophilic surfaces and is explained in our model by the analytical relationships between the humidity, the velocity and the normal load.

3.3.1 Theoretical model

Our theoretical model is based on recent developments of the relationships between the friction force F_F and the dynamic energy barrier ΔE which separates two stable positions of the AFM tip relative to the surface [48, 58, 65]. It can be described as a modified Tomlinson model, taking into account the effects of capillary forces and thermal activation. Considering the sliding system shown in Fig. 3.7, an AFM tip represented by a point-object of mass m moves on a surface and experiences the corrugated sinusoidal potential of interaction due to the tip-surface forces F_{surf} . The tip is coupled to a cantilever support by a spring of effective elastic constant k [N/m]. This effective spring constant is experimentally deduced from the slope of the friction force versus distance curves [30, 48, 72] performed on the studied sample. The cantilever support is moving at a velocity $v = \text{constant}$ and with its position described by $x_s = vt$. We take into account the thermally activated condensation of liquid bridges by introducing the capillary force F_C . This force is opposed to the tip displacement and its effect results in a non symmetric surface-tip energy barrier as illustrated in Fig. 3.8. From a simple point of view, the equation of motion is then given by

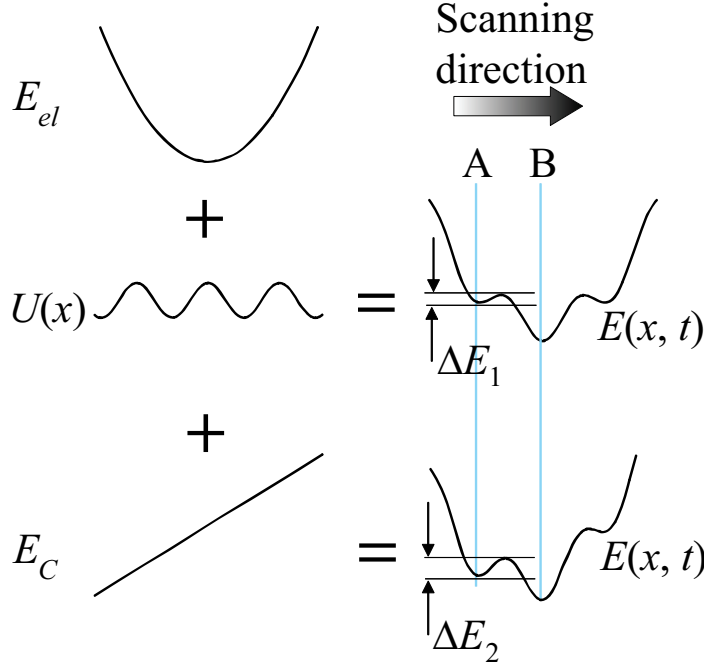


Figure 3.8: Effect of the capillary force on the total balance of energy $E_{x,t}$ of the system. E_{el} is related to the spring energy, $U(x)$ is the tip-surface corrugated energy and E_C is an approximation of the energy related to the capillary bridges meaning that it costs some energy to move in the sliding direction due to the presence of the capillary bridges. Without the capillary force, $E_{x,t}$ has a symmetric shape, whereas adding the energy E_C breaks the symmetry resulting in the increase of the energy barrier ΔE needed to go from A to B, such that $\Delta E_1 < \Delta E_2$.

$$\begin{aligned} m\ddot{x} &= F_{sp} + F_{surf} + F_C \\ &= k(vt - x) - U'(x) - F_C \end{aligned} \quad (3.17)$$

where x is the position of the tip and t the time. $U'(x) = dU(x)/dx$ is the first derivative of the corrugated substrate potential $U(x)$ experienced by the point-tip with respect to x , and F_{sp} is the conservative force resulting from the spring. We will not take into consideration other couplings of the point-tip to the sample surface. We consider now a line of motion along the x -axis and in the direction of $x > 0$, representing for example the movement of the AFM tip from a starting point $x = A$ to a position $x > A$ during a scanning process. Whereas F_{sp} and F_{surf} are conservative forces F^c that derive from a potential U^c following the relation $F^c = -\text{grad}(U^c)$, F_C is a non conservative force F^{nc} that is always opposed to the tip displacement. Thus, the potentials related to the conservative forces only depend on the starting and ending point of the line of motion, whereas the work done by F_C depends on the route along which the force acts. In our case, this route is a straight line going from the starting point A to some position x with $x > A$. Then, in the case of a sinusoidal surface potential $U(x)$, the energy describing the combined surface-tip-cantilever system can be approximated by

$$E(x, t) = \frac{1}{2}k(vt - x)^2 - \frac{E_0}{2} \cos(2\pi x/a) + F_C(x - x_c) \quad (3.18)$$

where x_c is a parameter related to a mean position of the bases of the capillary bridges on the static surface. It depends on the time and the velocity v of the tip support, with the assumption that $x_c < x$ for a displacement along the x direction. E_0 is half the surface barrier potential, a is the lattice constant of the sample surface. Compared to the Equ. 3.8 of the Tomlinson model, we only add the term $F_C(x - x_c)$ to take into account the activation of the capillary bridges². Referring to Fig. 3.8, the result of adding $E_C = F_C(x - x_c)$ to the potential defined by the Tomlinson model is to disrupt the symmetrical shape of the energy so that the energy barrier to slide from one minimum of energy (A) to the next one (B) is increased. In fact, for critical positions of the support, the AFM tip will overcome the energy barrier $\Delta E(t)$ between two consecutive extrema $E_{min}(x, t)$ and $E_{max}(x, t)$. The critical position is given by (i) $\partial E(x^*, t^*)/\partial x = 0$ and (ii) $\partial^2 E(x^*, t^*)/\partial x^2 = 0$, where x^* and t^* are respectively the critical position and the critical time for which the potential barrier vanishes. The condition (i) just states that the total forces acting on the point-tip should vanish and (ii) corresponds in fact to the equality between the slope of the substrate force curve ($\partial^2 U/\partial x^2$) and the slope k of the spring force line ($\partial F_{sp}/\partial x$). In our case, one critical point is given by the inflexion point $x^* = a/4$. At this point, $\partial E/\partial x$ is maximum and so, $\partial^2 E/\partial x^2 = 0$. Notice that condition (i) simply gives access to the position of the support (or the time) for the critical position of the point-tip. Thus, if we expand $\partial E(x, t)/\partial x$ around the critical point x^* , we find the positions of the minimum and maximum of the energy E :

$$\frac{\partial E(x, t)}{\partial x} \Big|_{x=\frac{a}{4}} = 0 \Leftrightarrow x_{1,2} = \frac{1}{4} \left(a \pm \frac{2\sqrt{2}}{E_0\pi^{3/2}} \sqrt{a^2 E_0 (E_0\pi - a k t v)} \right) \quad (3.19)$$

By taking $x_2 > x_1$, we finally obtain for the energy barrier

$$\begin{aligned} \Delta E(t) &= E_{max}(x, t) - E_{min}(x, t) = E(x_2, t) - E(x_1, t) \\ &= \frac{2^{3/2} E_0}{3} \left(1 + \frac{F_C}{F^*} - \frac{k t v}{F^*} \right)^{3/2} \end{aligned} \quad (3.20)$$

with

$$F^* = \frac{\pi E_0}{a} \quad (3.21)$$

In a more general form, without restricting the surface to a sinusoidal potential and by approximating the instantaneous lateral force f_f by $k v t$ [48]³, we have for the energy barrier related to the mean lateral force F_F :

$$\Delta E(F_F) = \frac{1}{\beta} \left(1 + \frac{F_C}{F^*} - \frac{F_F}{F^*} \right)^{3/2} \quad (3.22)$$

where β and F^* depend on the shape of the interaction potential between the tip and the surface. At zero temperature $T = 0$, the tip will move from a stable position to the following one when $\Delta E = 0$, leading to $F_F = F^*$. This result may explain the independence of the friction on the velocity in some works where thermal activation was not supposed. In

² Note that Equ. 3.18 contains an arbitrary constant coming from the integration over the line of motion. In our case, this arbitrary constant is $-A^2 k/2 + A(k v t - F_C) - k v t^2/2 + F_C x_c + E_0/2 \cos(2\pi A/a)$ and has been set to zero by an adequate choice of the starting point A .

³ It is based on the assumption that $\frac{dF_F}{dt} = \frac{dF_F}{dx} \frac{dx}{dt} = k v$.

the case of finite temperatures T , $\Delta E(t)$ is comparable to $k_B T$, k_B being the Boltzmann constant. Then, the master equation describing the probability $p(t)$ that the tip does not jump over the energy barrier takes the form [48]:

$$\frac{dp(t)}{dt} = -f_0 \exp\left(-\frac{\Delta E(t)}{k_B T}\right) p(t) \quad (3.23)$$

where f_0 is a characteristic attempt frequency of the system. The parameter f_0 has not yet revealed completely its physical meaning, but it has been found that the order of magnitude of f_0 corresponds to a vibration frequency whose effect on the system surface-tip-cantilever reduces drastically the friction independently of the applied load, as already illustrated in Fig. 3.6. Thus, the resonance frequency of the system plays probably a crucial role in activating the thermal jumps. The probability of jumping due to the thermal activation has its maximum at $d^2p/dt^2 = 0$. In our case, we are interested in the friction force maximizing the probability for overcoming the energy barrier. We have to exchange the temporal variable t by F_F in Equ. 3.23, so that

$$\frac{d^2p(F_F)}{dF_F^2} = 0 \quad (3.24)$$

which leads to

$$\ln\left(\frac{2f_0\beta k_B T F^*}{3kv}\right) - \frac{1}{2} \ln\left(1 + \frac{F_C}{F^*} - \frac{F_F}{F^*}\right) = \frac{1}{\beta k_B T} \left(1 + \frac{F_C}{F^*} - \frac{F_F}{F^*}\right)^{3/2} \quad (3.25)$$

Solving Equ. 3.25 for F_F leads to 6 roots among which only one has a physical signification. Thus, we finally obtain for the mean lateral force F_F :

$$\begin{aligned} F_F &= F^* + A \ln(v_0/v) - \left[\frac{\beta k_B T}{3} \mathcal{W}\left(\frac{3(F^* v_1^2)^{3/2}}{\beta k_B T v^3}\right) \right]^{2/3} \\ &= F^* + F_C - F_{SS} \end{aligned} \quad (3.26)$$

with

$$v_1 = \frac{2f_0\beta k_B T}{3k\sqrt{F^*}} \quad (3.27)$$

In Equ. 3.26, we replace the capillary force F_C by $A \ln(v_0/v)$. This last equation describes the phenomenology of F_C in terms of capillary bridges between the asperities of the tip and the surface [69] and will be studied more deeply in the next section. v_0 is a characteristic velocity of the system "tip - capillary bridges - surface". For a scanning velocity v higher than v_0 , no capillary bridges will have the time to form and the adhesion force due to these capillary bridges will vanish. For sufficiently low scanning velocities, the amount of capillary bridges should reach their maximum and the capillary force should become constant even for lower scanning velocities. The parameter A is related to the capillary bridges formed between the asperities of the surface and the AFM tip. It takes into account the applied normal force F_N , the relative humidity RH , the geometry and material of the system [69]. \mathcal{W} is the lambert-W function defined as $\mathcal{W}(x) \exp(\mathcal{W}(x)) = x$. v_1 has the meaning of an upper velocity

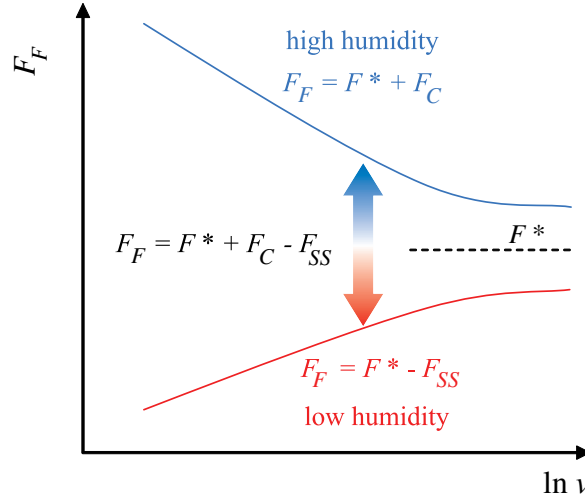


Figure 3.9: Illustration of the behavior of F_F versus $\ln v$. The transition from a positive to a negative slope of F_F vs. $\ln v$ is explained in terms of competition between F_C and F_{SS} . The action of F_C dominates at high humidity, but becomes negligible as the humidity decreases, which gives rise to the slope transition.

limit defined for the increasing sliding friction versus $\ln v$ [58, 65]. In the case of negligible solid-solid interactions F_{SS} , one finds the classic approximation of the behavior of the friction force versus $\ln v$: $F_F = \text{constant} + A \ln v$ [46, 62]. If F_C is negligible, one obtains again the relation developed by Riedo *et al.* in Ref. [58].

In Equ. 3.26, two different regimes are playing: F_C decreases with increasing the scanning velocity, whereas $F_{SS}(\ln v)$ increases. From the order of magnitude of the terms appearing in Equ 3.26, one observes that $F_C \gg F_{SS}$ for sufficiently high humidity. Then by reducing the relative humidity, the capillary force decreases progressively to become of the order of F_{SS} . The result is a competition between F_C , which adds to F^* , and F_{SS} , which is subtracted from F^* . From the competition between F_C and F_{SS} results the shape of the friction curve versus the natural logarithm of the scanning velocity: a positive slope for low humidity and negative slope for high humidity (See Fig. 3.9).

3.3.2 Experimental results on the effects of the sliding velocity on the nanofriction of hydrophilic surfaces

The theoretical model described in the previous section has been applied to our experimental data of the friction of a nanotip on a CrN surface. We will show the agreement of this model with both the increase and decrease of the friction force as function of the scanning velocity for different humidity levels. Furthermore, we highlight the appearance of "plateaux" of constant friction once a critical velocity is exceeded. Until now, this friction behavior was only observed for hydrophobic surfaces at sufficiently high sliding velocities [71]. The dependence of those plateaux on the normal load and relative humidity finds its explanation in our theoretical model.

The sample studied is a CrN film deposited at 600°C (HT-CrN) substrate temperature and having a lattice constant $a = 4.2 \text{ \AA}$ [73]. It is analog to samples already used in a

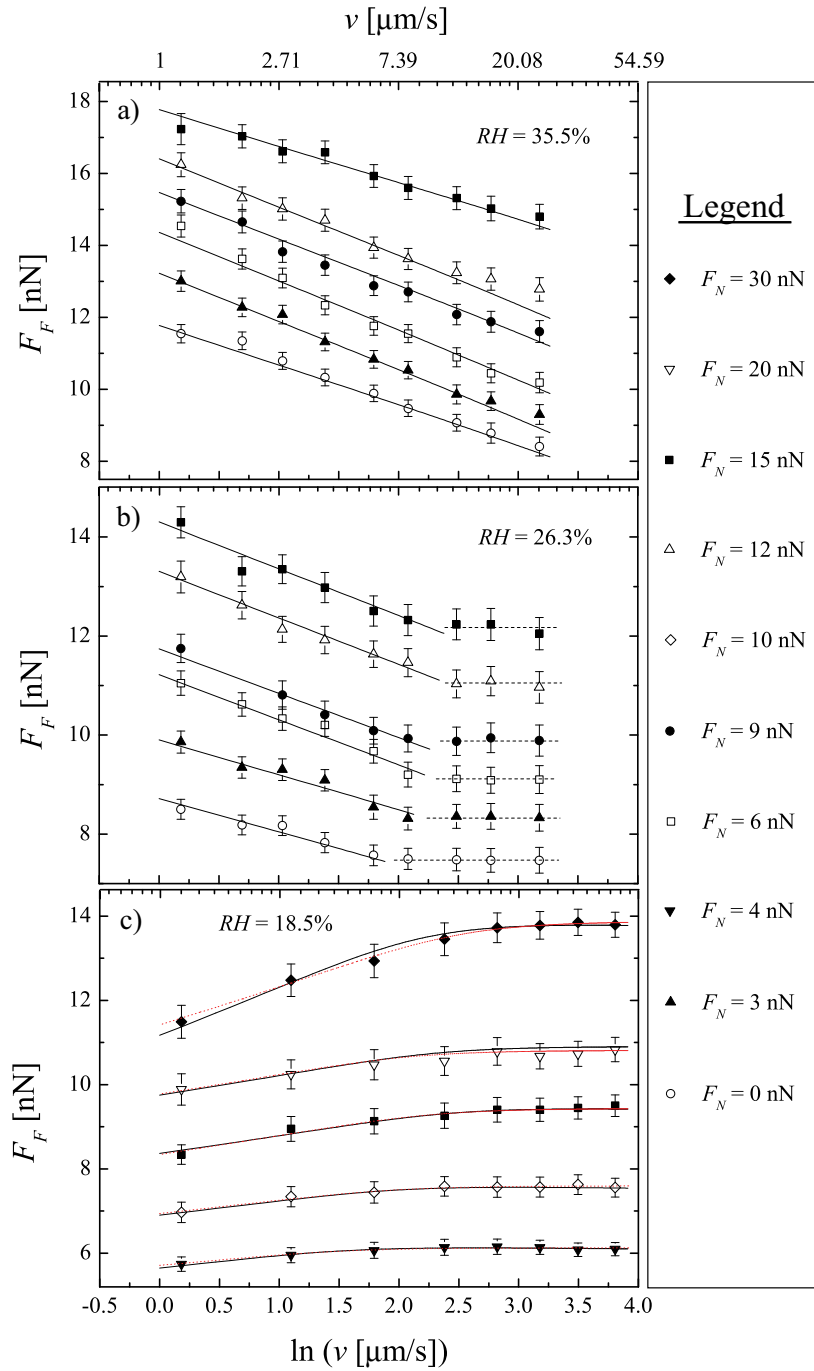


Figure 3.10: Friction force F_F as function of the natural logarithm of the scanning velocity $\ln v$ for three different levels of relative humidity: $RH = 35.5\%$, $RH = 26.3\%$ and $RH = 18.5\%$. The experimental data are fitted using Equ. 3.26 (solid lines). The dashed lines appearing for $RH = 26.3\%$ are only here to highlight the appearance of "plateaux" once a critical velocity is exceeded. Red dash-dotted lines of the data corresponding to $RH = 18.5\%$ are fit using the formula $F_F = F^* - F_{SS}$, where the capillary force has been neglected. Parameters extracted from the fits are reported in Tables 3.2 to 3.4.

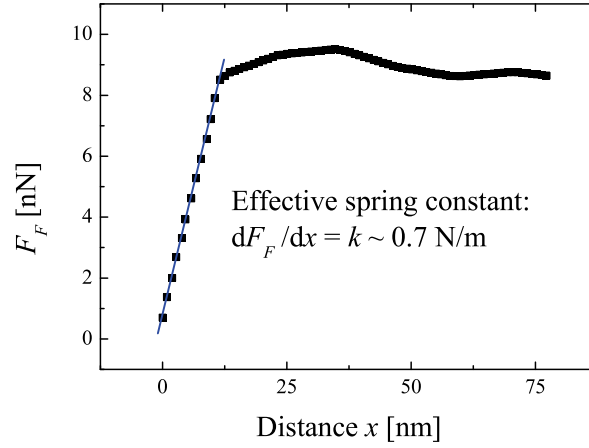


Figure 3.11: Part of a friction loop obtained by averaging the friction loops resulting from the scan of a CrN area of $1 \mu\text{m}^2$ with a normal load of 18 nN and for a low relative humidity ($RH \sim 18\%$). The variation of k over our range of experimental parameters was negligible and we consider $k = 0.7 \text{ N/m}$ as a mean value for the whole data. In our case, the variation of $F_F(x)$ during a single friction loop is mainly due to the surface roughness.

previous experiment on kinetics of capillary condensation [64]. The static water contact angle measured for this sample is $\theta_C = 35^\circ$. This value confirms its wettability behavior. We obtain a root mean square (RMS) surface roughness of 5.5 nm on $3 \mu\text{m}^2$, which was usually the typical scan size for data acquisition. Friction measurements were performed staying on the same area of the sample using an atomic force microscope (AutoprobeTM M5). The friction force F_F was defined as half the mean friction force difference given for the forward and backward directions of the friction loop. Friction forces and topography were acquired simultaneously for different velocities v at fixed size of the scanned area and for different levels of relative humidity RH ⁴. Varying the sliding velocity by changing the scan size at constant scan frequency yielded consistent results. We used commercial V-shaped silicon cantilevers characterized by a conical tip with a nominal radius of 10 nm, and a normal and lateral spring constant of the order of 0.4 N/m and 64 N/m respectively. We deduced from the slope of the friction force versus distance curves performed on the CrN sample an effective spring constant $k = 0.7 \text{ N/m}$. This value is obtained by averaging friction loops performed on small scanning areas and then, measuring dF_F/dx on the resulting initial slope (See Fig. 3.11). We defined the normal force as equal to zero ($F_N = 0$) at the point where the cantilever was not bent. The accuracy in relative change of the measured forces was guaranteed by using the same cantilever throughout each whole series of measurement. The experiment was done at room temperature ($\sim 24^\circ\text{C}$) in a tight box where the humidity was controlled through inlets for dry and water-saturated nitrogen.

Figures 3.10 to 3.13 present the experimental results on the variation of F_F as function of

⁴ We remind that the relative humidity RH is defined as the ratio between the equilibrium and the saturated vapor pressure of water, respectively P and P_S .

F_N [nN]	f_0 [kHz]	β [M N ^{1/2} /m]	A [nN]	v_0 [μ m/s]	F^* [nN]
15	30.8	1.80	1.19	19.8	14.8
12	29.8	0.93	1.46	21.3	12.3
9	30.8	0.82	1.37	19.3	11.6
6	29.7	0.26	1.4	19.4	10.3
3	29.6	0.72	1.44	19.4	9.2
0	29.7	0.6	1.19	19.9	8.4

Table 3.2: Parameters for $RH = 35.5\%$ extracted from fitting the experiment with Equ. 3.26.

F_N [nN]	f_0 [kHz]	β [M N ^{1/2} /m]	A [nN]	v_0 [μ m/s]	F^* [nN]
15	29.3	0.88	1.06	11.4	12.0
12	31.8	0.83	1.05	11.0	11.1
9	32.7	0.76	1.00	7.53	10.0
6	29.4	0.58	0.99	7.46	9.4
3	29.7	0.47	0.78	7.50	8.5
0	29.9	0.43	0.74	7.02	7.4

Table 3.3: Parameters for $RH = 26.3\%$ extracted from fitting the experiment with Equ. 3.26.

F_N [nN]	f_0 [kHz]	β [M N ^{1/2} /m]	A [pN]	v_0 [μ m/s]	F^* [nN]
30	1.8 (3.1)	28.2 (18.9)	58.3	20.9	13.8 (13.8)
20	5.0 (4.0)	6.8 (6.7)	46.4	2.4	10.9 (10.8)
15	5.8 (4.6)	6.6 (6.6)	29.4	2.4	9.5 (9.4)
10	4.4 (5.0)	4.8 (3.7)	36.3	0.3	7.7 (7.6)
4	3.3 (3.9)	4.0 (2.7)	23.9	0.2	6.2 (6.1)

Table 3.4: Parameters for $RH = 18.5\%$ extracted from fitting the experiment with Equ. 3.26. In parenthesis, the results obtained by fitting the data with $F_F = F^* - F_{SS}$ are shown for comparison.

$\ln v$ and RH . The experimental data are fitted using Equ. 3.26 (solid lines). The main results of the fits are reported in Tables 3.2 to 3.4. In our fitting procedure, we tried to keep f_0 close to a constant value to allow comparison between the other free parameters, namely, β , A , v_0 and F^* . The dashed lines shown in Fig. 3.10 for $RH = 26.3\%$ are only here to illustrate the plateaux, whereas the red dash-dotted lines appearing for $RH = 18.5\%$ correspond to fits where we neglected the capillary force, i.e. with $F_F = F^* - F_{SS}$.

The variation of the friction force as function of the logarithm of the scanning velocity for different normal loads and at three different levels of humidity ($RH = 35.5\%$, $RH = 26.3\%$

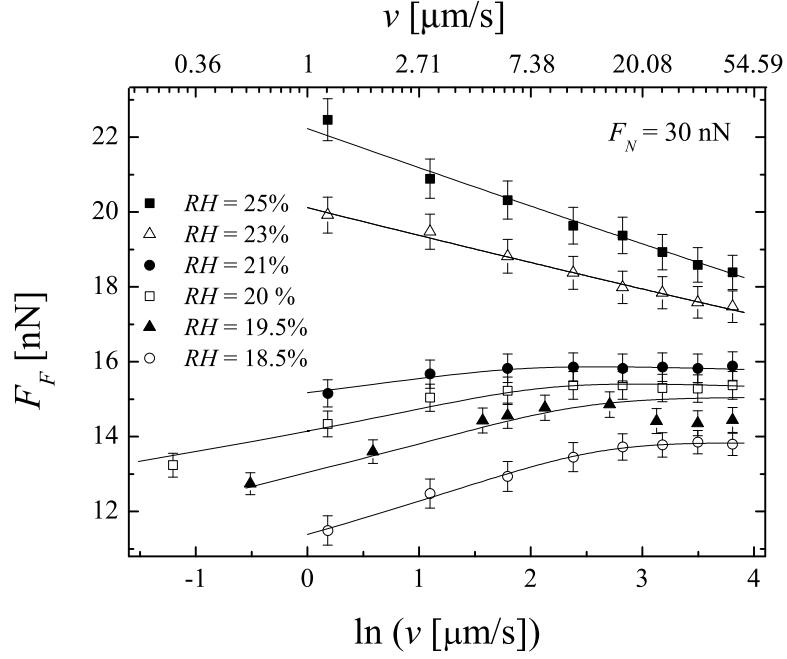


Figure 3.12: Friction force as function of the natural logarithm of the scanning velocity for a decreasing relative humidity surrounding the CrN surface and at a fixed applied normal force. The experimental data are fitted using Equ. 3.26.

and $RH = 18.5\%$) is presented in Fig. 3.10. For a relative humidity higher than 30%, we observe the linear decrease of F_F versus $\ln v$ as predicted by the theoretical model when F_{SS} is negligible in comparison to F_C . At sufficiently low humidity, this linear decrease is followed by an apparent plateau once the scanning velocity exceeds a limit value v_0 . This limit value of the velocity decreases gently with the normal force as shown in Fig. 3.10(b). Our theoretical model applied to the experimental data for $RH = 26.3\%$ gives rise to a limit value v_0 going from $11 \mu\text{m/s}$ for $F_N = 15 \text{ nN}$ to $7 \mu\text{m/s}$ for $F_N = 0 \text{ nN}$, whereas this limit value equals $20 \mu\text{m/s}$ for $RH = 35.5\%$, regardless of F_N (see Table 3.2 and 3.3). Finally, for a relative humidity below than 22%, the CrN behaves as a hydrophobic surface, showing a linear increase of F_F versus $\ln v$ until it reaches again a plateau. In this case, the capillary force is so weak that it can be neglected. This fact is highlighted by the values taken by the parameter A for the different levels of humidity. This parameter is directly related to the order of magnitude of the capillary force. It is effectively possible to separate the friction behavior in three different regimes: high humidity, middle humidity and low humidity. In our case, for $RH = 35.5\%$, A is almost constant as function of F_N , as well as v_0 . No special trends are noticed. This result can be interpreted in terms of number of capillary bridges between the tip and the surface. When the humidity is sufficiently high, the number of capillary bridges does not depend on the applied normal load. We are in a kind of saturation state and F_C reaches a maximum value. The slopes of F_F versus $\ln v$ remain quasi constant and the series of data for each load are only shifted due to the effect of the applied normal load on F^* . This effect has already been pointed out in Ref. [69] through the relation between F^* and E_0 , and is also illustrated here in the inset of Fig. 3.13 for $RH = 26\%$. Then, by reducing the humidity, the number of capillary bridges decreases

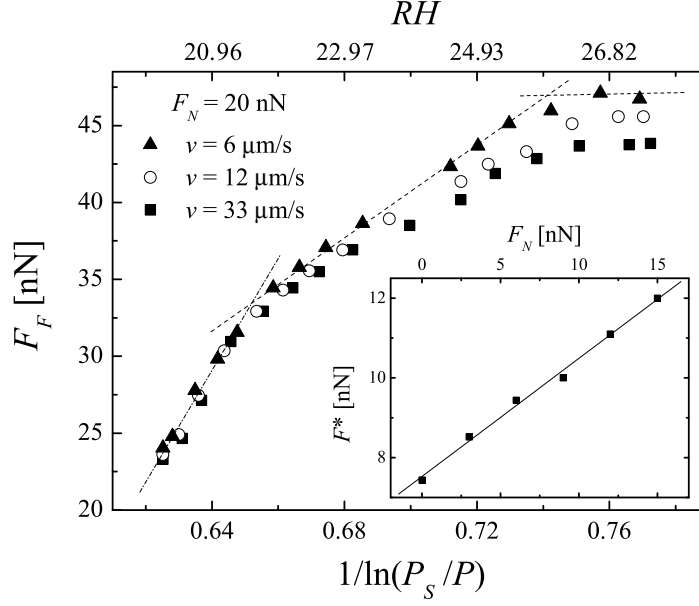


Figure 3.13: Friction force as function of $1/\ln(P_S/P)$ for three different scanning velocities and an applied normal force of 20 nN. The inset illustrates the linear dependence of F^* on F_N for $RH = 26\%$.

and becomes influenced by the normal load and the scanning velocity as shown through the parameters A and v_0 for $RH = 26\%$. At this point, the trend corresponds to a decrease of A and v_0 as the normal force, and with it, the number of capillary bridges, are reduced. Finally, for a low humidity level, the capillary force vanishes as pointed out by the parameter A that decreases from 10^{-9} nN for $RH = 35.5\%$ to 10^{-11} nN for $RH = 18.5\%$, whereas the parameter β takes larger values. At this low level of humidity, the solid-solid interaction dominates the capillary force, inducing the positive slope of F_F versus $\ln v$.

In Figure 3.12, F_F is plotted as function of the logarithm of the scanning velocity for a fixed normal force $F_N = 30$ nN and a relative humidity decreasing from 25% to 18.5%. The slope changes from a positive value (RH below 22%) to a negative one with increasing RH . This change of the slope is again highlighted in Fig. 3.13 for a normal force $F_N = 20$ nN. According to the relation $A \propto 1/\ln(RH^{-1})$ [69], F_F is plotted as function of $1/\ln(P_S/P)$ for three different scanning velocities, namely $33 \mu\text{m/s}$, $12 \mu\text{m/s}$ and $6 \mu\text{m/s}$. At a fixed value of $1/\ln(P_S/P)$, the difference between the curves corresponding to each scanning velocity represents the slope of F_F versus $\ln v$. From 22% of relative humidity, i.e. $1/\ln(P_S/P) = 0.66$, F_F takes the same value for the three scanning velocities. It corresponds to the appearance of a plateau in F_F versus $\ln v$. As shown in Fig. 3.13, the threshold of the plateau decreases gently by reducing the RH . Moreover, at fixed F_N and v , the three distinct regimes described before are highlighted: for $1/\ln(P_S/P) > 0.76$, F_F is almost constant, then, for $0.66 < 1/\ln(P_S/P) < 0.76$, F_F decreases linearly and finally, for $1/\ln(P_S/P) < 0.66$, F_F decreases still linearly, but with a change in the slope of $F_F(1/\ln(P_S/P))$, showing the end of the action of F_C .

Our fit function as presented in Equ. 3.26 is not restricted to a sinusoidal shape of the surface potential. It allows the comparison between the parameter $\beta \equiv \beta_{exp}$ obtained ex-

perimentally and the parameter β_{th} defined theoretically if we suppose a sinusoidal shape of the surface potential in our model. In this case, the parameter β_{th} is defined by the formula $\beta_{th} = 3\pi\sqrt{F^*}/(2\sqrt{2}a)$. From the fit of the data presented in Fig. 3.10, we obtain 0.99, 0.83 and 12.06 for the mean value of the ratio β_{exp}/β_{th} for the respective relative humidity $RH = 35.5\%$, $RH = 26.3\%$ and $RH = 18.5\%$. While β_{th} and β_{exp} are in good agreement in the case of high and middle levels of humidity, their respective values do not coincide anymore as RH decreases. Thus, the hypothesis of a sinusoidal surface potential is a good approximation only in the case of high and middle levels of humidity; otherwise, the theoretical model shows a discrepancy with the experimental data.

In conclusion, the application of the theoretical model developed in Section 3.3 to the experimental measurements of the friction of an AFM nanotip on a CrN surface allows to explain the transition from a positive to a negative slope of F_F versus $\ln v$. Moreover, the parameters extracted from the fits give an insight into the competition between the solid-solid force and the capillary force. In the next section, we develop more deeply the relations between the capillary force, the normal load and the scanning velocity.

3.4 Capillary effects

3.4.1 From water molecules to capillary bridges

Water represents about 70% of the earth surface as liquid and solid state and is also found in the atmosphere in the form of vapor. It is perhaps the most important molecule on earth, being a source of life and an integral part of the composition of biological bodies⁵. The chemical formula of water, also called dihydrogen monoxide, is H_2O : two hydrogen atoms bound to one oxygen atom form together an angle of 104.45° for a size of the order of the angstrom (See Fig. 3.14(a)). This peculiar geometry and the higher electronegativity of the oxygen compared to the hydrogen result in a polarity of the molecule. These charge differences cause water molecules to be attracted to each other through hydrogen bonding, but are also responsible for many other unusual properties of water, such as high melting and boiling points or its use as a universal solvent. In liquid water, the charges are balanced in all directions, but at the surface, the molecules line up in a kind of surface film layer where they are held together by hydrogen bonds. This cohesive force gives rise to the water surface tension treated in Chapter 1. It explains why it is more difficult to move an object through the surface of water than to move it when it is completely submersed⁶. Surface tension of water is exploited in nature by plants, but also by some insects having no wettable feet and walking on water, like the water strider (See Fig. 3.14(b)), which does not like detergent pollution in water as it reduces the surface tension. Knowing a little about surface tension may also be helpful for lost travellers who can make a compass by using some water and a magnetized needle.

⁵ The human body is for example made up of 50-80% of water.

⁶ The cohesive forces between the bulk water molecules are shared with all neighboring atoms. Those on the surface, having no neighboring atoms above, exhibit stronger attractive forces with their nearest neighbors on the surface.

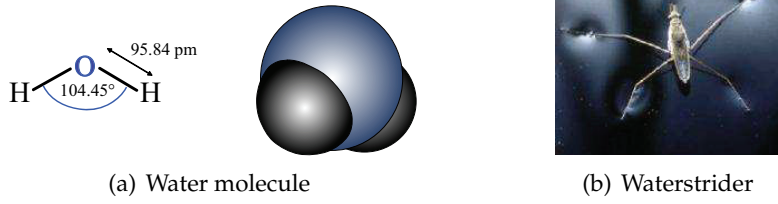


Figure 3.14: Schematic representation of a water molecule and illustration of the water surface tension thanks to a specialist of water walking, the waterstrider.

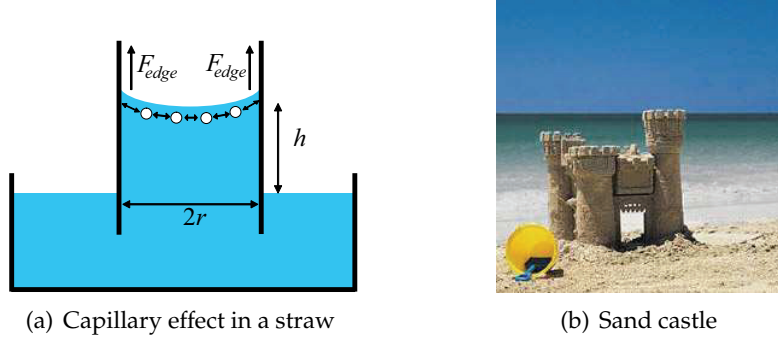


Figure 3.15: Illustration of the water capillaries in a straw and maintaining the cohesion of a sand castle.

The surface tension and the adhesion of water to a surface explain also why water rises in a thin straw. From a simple point of view and referring to Fig. 3.15(a), the adhesion of the water to the walls of the straw causes an upward force on the edge of the liquid surface, whereas surface tension acts to hold the molecules together. Thus, instead of having just the water climbing only at the edge of the straw, the whole surface of liquid follows and rises up until the force on the edge F_{edge} equals that one given by the mass of the raised water column, i.e. F_{water} , which can be written as

$$F_{edge} = 2\pi r\gamma = \rho g(\pi r^2 h) = F_{water} \quad (3.28)$$

where r is the radius of the cylindrical straw, γ the surface tension, ρ the water density and h the rising height. Capillarity occurs not only in macroscopic scales like in a straw, but also at the nanoscale. A well-known example is the sand castle effect [74, 75]. Interstitial liquid bridges hold the small sand grains together through capillary forces and increase the sand cohesion. The addition of small quantities of wetting liquid to a pile of such a granular media changes considerably its repose angle [74, 75] and it has been proven that the strength of the capillary bridges was predominantly controlled by the particle surface roughness [76].

For a long time, the capillary force was expressed by a simple equation finding its root in the work of Young, Laplace and Kelvin (See Section 1.2.6). This expression was almost exclusively based on geometrical aspects of the formation of a bridge between two smooth surfaces. This was not enough to explain experiments involving granular media and humidity. Indeed, experimental results showed that the capillary formation was time and hu-

midity dependent [64, 74–76], what explained for example why the stability of sand castles was increased when the wet sand was pressed into shape for a longer time. To take account of the experimental phenomenology, new models appeared that included the time and humidity dependence of the capillary force.

3.4.2 Thermally activated condensation of capillary bridges

Two solid surfaces brought into contact present an interface composed of interstices in which the humidity present in ambient air may condense to form a liquid bridge binding both surfaces. This phenomenon is known as capillary condensation and has drastic effects on granular media, modifying the friction and adhesion properties. One of the first models on the kinetics of capillary condensation was presented by Bocquet *et al.* in 1998 [76]. They studied the effect of waiting time on the angle of first avalanche of a granular system of small spherical glass beads contained in a rotating drum. They observed a logarithmic ageing of the maximum static angle. The ageing was not observed for beads with a diameter superior to 0.5 mm except at high humidity. They concluded that the humidity played a central role in the ageing of the avalanche angle and that it was related to the condensation of small liquid bridges between the beads. They developed a model based on the thermally activated nucleation of bridges to explain their results. This model serves as basis to explain, on the one hand, the kinetics of capillary condensation in nanoscopic sliding friction [64] and, on the other hand, our phenomenological model on the two-thirds power law dependence of the capillary force on the normal load in nanoscopic friction [69]. It is why we will briefly review the model proposed by the authors of Ref. [76].

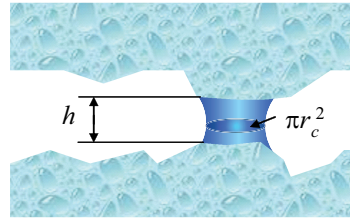


Figure 3.16: Schematic representation of a capillary bridge between two rough surfaces.

They consider two surfaces in contact with some interstices at their interface under an undersaturated vapor environment. At some places in the interstices where the distance between the bodies is small, capillary condensation should occur. For this, a threshold energy barrier ΔE has to be overcome. It corresponds to the free energy cost of condensing the capillary water of volume V from the undersaturated vapor phase. This energy is given by

$$\Delta E \approx k_B T \ln \left(\frac{P_S}{P} \right) \rho V \quad (3.29)$$

where k_B is the Boltzmann constant, T the temperature and ρ the liquid density. The relative humidity is given by the ratio of P over P_S that are respectively the vapor and saturated water pressure. Considering rough surfaces, the nucleation of a capillary occurs between asperities distant of a height h so that the nucleation volume becomes $V = h\pi r_c^2$, where r_c is

the radius of the capillary bridge cross section (See Fig. 3.16). Then, assuming an activation process, the time t needed to condense a bridge of height h is

$$t(h) = t_A \exp\left(\frac{\Delta E}{k_B T}\right) \quad (3.30)$$

where t_A is a microscopic time needed to condense one liquid layer⁷. After a given time t , only the bridges with an activation time inferior or equal to t have condensed. This leads to a maximum gap of height h_{max} for which a bridge had the time to grow:

$$h_{max}(t) = \frac{\ln(t/t_A)}{\ln(P_S/P)\pi r_c^2 \rho} \quad (3.31)$$

Finally, due to roughness (more precisely the height distribution), only a part of the contact area will be wetted. Thus, only a fraction $f(t)$ of the total number of liquid bridges is formed at a given time. This fraction $f(t)$ is proportional at first approximation to the number of activated bridges:

$$f(t) \approx h_{max}/\lambda = \frac{\ln(t/t_A)}{\lambda \ln(P_S/P)\pi r_c^2 \rho} \quad (3.32)$$

where λ is the typical width of distribution of distances between the surfaces. These last considerations lead to an adhesion force F_{adh} given by

$$F_{adh} = f(t)F_C \quad (3.33)$$

where F_C is the capillary force as defined in Section 1.2.6. Finally, the important observations following from the model developed by Bocquet *et al.* are its application restricted to rough surfaces, the ability of the bridges to form only in nanometer-scale interstices under ambient conditions and the logarithmic dependence of the resulting adhesion force on time and on humidity. These results have been recently confirmed again by D'Amour *et al.* [77].

3.4.3 2/3 power law dependence of the capillary force on the normal load

In this section, we propose a theoretical model⁸ that relates the dependence of the capillary force on the normal load via a 2/3 power law, as experienced in AFM measurements of the friction at different sliding velocities and levels of humidity. This study was motivated by the fact that usually AFM measurements are performed in ambient conditions in a non-zero relative humidity environment. The tip-surface contact forms then a potentially suitable geometry for the formation of thermally activated water bridges that modify the sliding properties. The resulting adhesion force depends on how much time t the tip faces the surface at a local position while scanning an area. For a contact area of diameter d , the residence time t is given by [64]

$$t = \frac{d}{v} \quad (3.34)$$

where v is the scanning velocity of the AFM cantilever. A decreasing scanning velocity results in an increase of the number of capillary bridges in the contact area and thus in an

⁷ t_A has been experimentally estimated to 25 μs in Ref. [64].

⁸ The theoretical model presented here has been the subject of the publication given in Ref. [69].

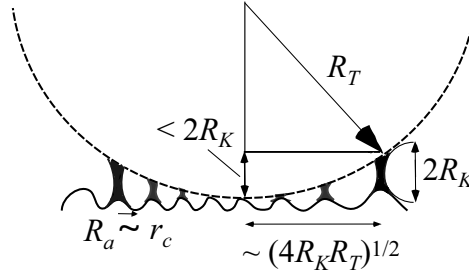


Figure 3.17: Illustration of the capillary bridges formed in the contact area between the sample and the AFM tip. Since $R_T \gg R_K$, the radius defining the area where the capillary can form, i.e. when the tip and the sample are closer than $2R_K$, is about $(4R_K R_T)^{1/2}$.

increase of the adhesion force. Thus, by considering the asperities for which a capillary has the time to form, the resulting number of capillaries N_c can be analytically estimated as a function of the sliding velocity v and the relative humidity P/P_S yielding to

$$N_c = \begin{cases} f(t)N_c^{tot} = \left(\frac{V_M}{\lambda \pi r_c^2} \right) \frac{\ln \frac{v_0}{v}}{\ln \frac{P_S}{P}} N_c^{tot} & : v_{min} < v < v_0, P < P_{max} \\ 0 & : v \geq v_0 \\ N_c^{tot} & : v \leq v_{min}, P \geq P_{max} \end{cases} \quad (3.35)$$

where V_M is the molecular volume of the liquid. $v_0 = d/t_A$, v_{min} and P_{max} are critical parameters. N_c^{tot} is the total number of asperities where the capillaries can form. Finally, using Equ. 1.11 in the case $D = 0$, we can approximate the total capillary force as the capillary force acting on each asperity times N_c :

$$F_C \cong 2\pi\gamma R_a (\cos(\theta_T) + \cos(\theta_S)) N_c \quad (3.36)$$

where θ_T and θ_S are the contact angles of the tip and the flat surface respectively and R_a is the average radius of the asperities. This analytical expression of the capillary force is in agreement with the experimental phenomenology showing how F_C increases with humidity and decreases with sliding velocity v .

The load dependence of F_C in Equ. 3.36 is hidden in the expression of N_c via the number of asperities that are able to generate the condensation of a capillary when the applied load F_N presses the surfaces together. As found by Kelvin, water condenses in interstices which are smaller than $2R_K$, R_K being the Kelvin radius defined in Equ. 1.9 [4, 76]. This means that the available surface where the capillaries can form is $A_{av} \approx 4\pi R_K R_T$, where R_T is the tip radius (See Fig. 3.17). N_c^{tot} can be written as the ratio between A_{av} and the area of one capillary πr_c^2 . The radius r_c has an intermediate value between R_K and R_a , however the surfaces investigated in our experiment have typically $R_a \approx 1$ nm and thus, at ambient conditions $R_K \approx R_a \approx r_c$. The deformation of the tip and the surface once in contact can be taken into account by writing, from geometrical considerations (See Fig. 3.18), $A_{av} \approx 4\pi R_K R_T (1 + \frac{\delta}{R_K})$, where δ is the indentation depth. Using the Hertz theory to estimate δ [17], we can write $A_{av} \approx 4\pi R_K R_T (1 + K F_N^{2/3})$ where

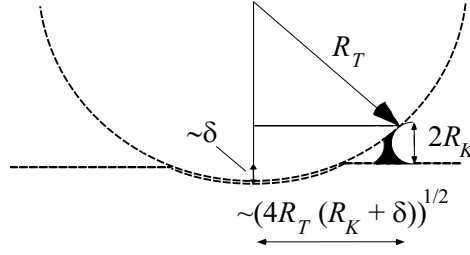


Figure 3.18: The new radius $(4R_T(R_K + \delta))^{1/2}$ defines the area where the capillary bridges can form when the tip penetrates in the surface for a depth δ .

$$K = \frac{1}{R_K} \left(\frac{9}{16R_T E^{*2}} \right)^{1/3} \quad (3.37)$$

with E^* being the reduced elastic modulus of the system (See Equ. 1.26). Finally, we obtain the following relationship for N_c^{tot} :

$$N_c^{tot} \cong \frac{A_{av}}{\pi r_c^2} \cong \frac{4R_K R_T (1 + K F_N^{2/3})}{R_a^2} \cong \frac{4R_T (1 + K F_N^{2/3})}{R_a} \quad (3.38)$$

Finally, using Equ. 3.35, 3.36 and 3.38, the expression obtained for the capillary force as a function of the normal load, humidity and velocity, is given by

$$F_C \cong 8\pi\gamma R_T \left(1 + K F_N^{2/3} \right) \left(\frac{V_M}{\lambda\pi r_c^2} \right) \frac{\ln \frac{v_0}{v}}{\ln \frac{P_S}{P}} \quad (3.39)$$

where we have considered $\theta_T \approx 90^\circ$ and $\theta_S \approx 0^\circ$, since these were the conditions during our measurements. In this equation we obtain the $2/3$ power law dependence of the capillary force on the load in agreement with our experimental results as presented in the next section.

3.4.4 Experimental results on capillary condensation

We present here our experimental results on the relation between the capillary force, the normal load, the relative humidity and the scanning velocity⁹. The experiments were performed on a standard glass sheet with an RMS roughness of 1 nm on a $1 \mu\text{m}^2$ surface. The capillary force has been investigated through friction force measurements at room temperature by means of an AFM (AutoProbeTM M5). For humidity control, the AFM was placed into a tight box with inlets for dry and water saturated nitrogen. We used V-shaped silicon cantilevers (Ultralevers type B) with normal and lateral spring constants of 0.4 and 50 N/m respectively, and silicon conical tips with nominal radius of curvature greater than 10 nm. The zero normal load, $F_N = 0$ nN, was defined at the point where the cantilever was not bent. Relative changes of the lateral forces were determined accurately by using the same cantilever throughout a series of experiments. The velocity dependence of friction was investigated in varying the scan frequency at fixed size. We verified that different scan sizes at

⁹ The experimental results presented in this section have been the subject of the publication given in Ref. [69].

constant frequency yielded consistent results. All the measurements at different loads were reversible, this means that we were always in the elastic regime.

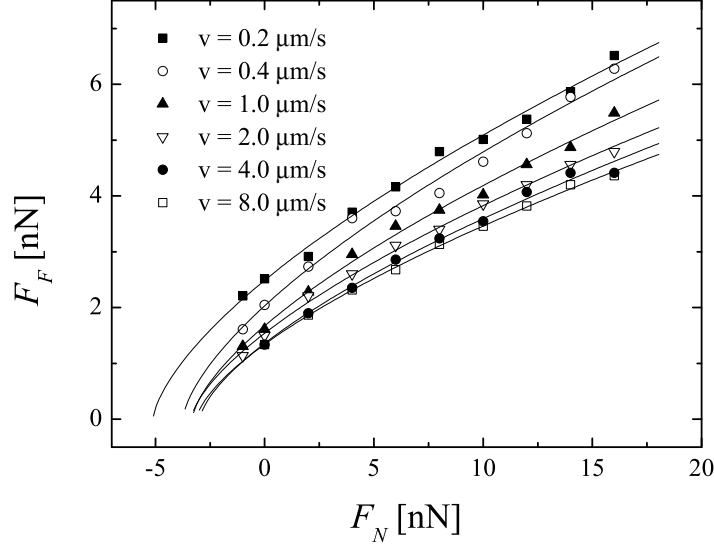


Figure 3.19: Friction force versus normal load for different sliding velocities at a relative humidity of 33%. The solid lines are fits by using Equ. 3.40.

The behavior of the friction force as a function of the normal load at different sliding velocities for a fixed humidity $P/P_S = 0.33$ is presented in Fig. 3.19. We observe that F_F increases with the normal load following a power law with an exponent significantly lower than 1. This is expected from continuum mechanics theory of contact deformation as defined in Section 1.3. The friction force is given by Equ. 3.5 in the case of elastic deformation, i.e. with $F_{def} = 0$. Thus, since in the elastic regime the friction force is proportional to the contact area, the power law dependence of the friction force on the normal load can be traced back to the load dependence of the contact area yielding

$$F_F \cong \mu_0(F_N + F_{adh})^{2/3} \cong \mu_0(F_N + F_C)^{2/3} \cong \mu_0(F_N + f_c \ln \frac{v_0}{v})^{2/3} \quad (3.40)$$

where μ_0 is a parameter with a meaning similar to the friction coefficient and F_{adh} is the adhesion force mainly composed of van der Waals solid-solid forces and capillary forces [78, 79]. According to Equ. 3.40, the value of F_N when $F_F = 0$ in Fig. 3.19 is the adhesion force. Since in our experiments the capillary forces are much greater than all the other adhesive forces, i.e. the adhesive force is lower than 1 nN for a relative humidity $P/P_S = 0.5$ [78, 79], we can write $F_{adh} \simeq F_C$. The fits of the data with the Equ. 3.40 are given in Fig. 3.19 showing a good agreement between theory and experiment.

Figure 3.20 shows that F_F and F_C decrease with $\ln v$. The same behavior for F_F at three different humidities is reported in Fig. 3.21. This figure shows that the slope of the F_F versus $\ln v$ curves decreases with decreasing humidity and is almost zero at very low humidities.

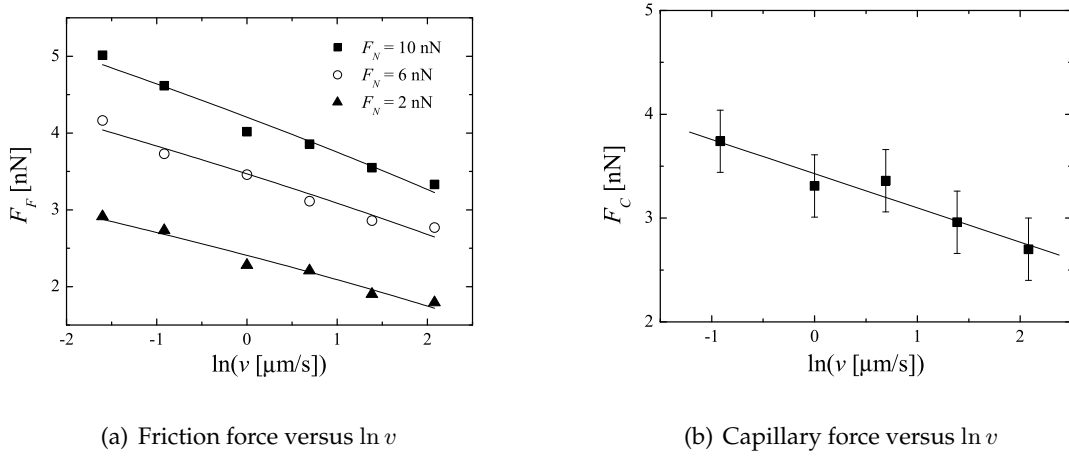


Figure 3.20: Behavior of the friction force as function of $\ln v$ at different loads, $F_N = 2, 6$ and 10 nN and plot of F_C , i.e. the value of F_N when $F_F = 0$, as a function of $\ln v$.

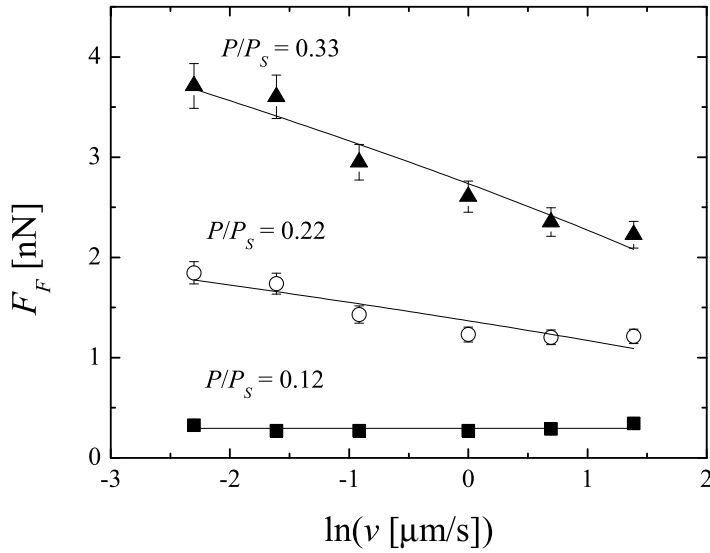


Figure 3.21: Friction force as a function of $\ln v$ for three different humidities, at $F_N = 4$ nN. The solid lines are fits with the relationship $F_F = (A - B \ln v)^{2/3}$, with A and B being free-fitting parameters.

We point out that on the same glass surface at even lower humidities and in ultra high vacuum or on an atomically flat mica surface in air, the friction increases with the velocity because of a thermally activated stick and slip process [58]. All these results are in perfect agreement with the study in Ref. [64] and with Equations 3.35 and 3.36 through Equ. 3.40. According to these findings and the above equations, we write:

$$F_F \cong \mu_0(F_N + F_C)^{2/3} \cong \mu_0 \left(F_N + f_c \ln \left(\frac{v_0}{v} \right) \right)^{2/3} \quad (3.41)$$

where f_c is a function of the humidity. Moreover, we note that the velocity and load dependence of friction shown in Fig. 3.19 highlight the increase of the slope of F_F versus F_N curves by decreasing the velocity, i.e. the slope of F_F versus $\ln v$ curves increases with increasing loads. This means that by increasing the sliding velocity we have not only a shift of the curves on the F_N -axis due to a decrease of F_C according to Equ. 3.36, but also a decrease of the slope. This effect can be explained with the increase of f_c with increasing loads.

The data in Fig. 3.19 can be plotted by using $\ln v$ as independent variable. The data of the friction force F_F versus $\ln(v)$ at different loads have been fitted with $F_F = \mu_0(F_N + f_c \ln(\frac{v_0}{v}))^{2/3}$. From this fitting procedure, we find the values of $\mu_0 f_c$ at different loads. By solving the equations for the intercepts at different loads we also obtain the value of $\ln v_0$ and μ_0 . The capillary force $F_C = f_c \ln(\frac{v_0}{v})$ is then plotted as a function of the normal load at different velocities as shown in Fig. 3.22. The resulting power law dependence on F_N for the capillary force is 0.7 ± 0.1 .

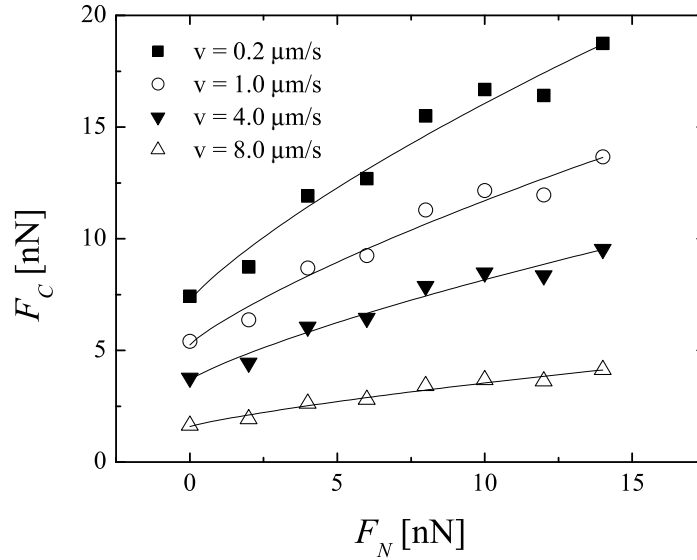


Figure 3.22: Capillary force as a function of normal load at different velocities. The solid lines are fits with the relationship $F_c = (A + BF_N)^{2/3}$, with A and B free-fitting parameters.

To compare more precisely the model established in the previous section with the experimental data, we can first rewrite F_F combining Eqs. 3.35 and 3.40, which leads to

$$F_F \cong \mu_0 \left(F_N + F_0 \left(1 + KF_N^{2/3} \right) \frac{\ln \left(\frac{v_0}{v} \right)}{\ln \left(\frac{P_S}{P} \right)} \right)^{2/3} \quad (3.42)$$

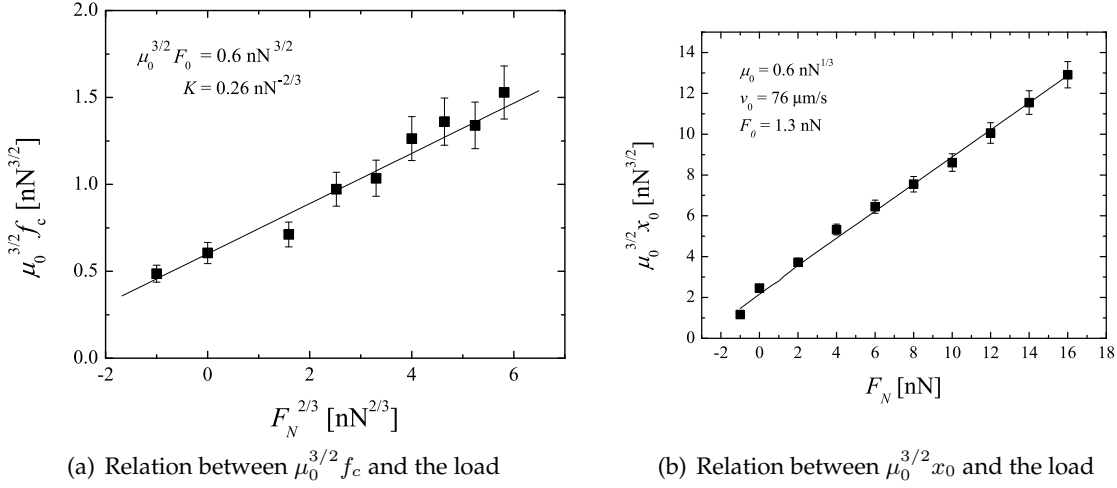


Figure 3.23: Load dependence of $\mu_0^{3/2} f_c$ and $\mu_0^{3/2} x_0$ obtained by fitting the data in Fig. 1 with the equation $F_F = \mu_0(x_0 + f_c \ln v)^{2/3}$.

with

$$F_0 = \frac{8\pi\gamma R_T V_M}{\lambda\pi r_c^2} \quad (3.43)$$

Then, to extract important information such as the values of K , v_0 and μ_0 in a more convenient way for the fitting procedures, the previous equations might be written as

$$F_F = \mu_0 (x_0 + f_c \ln(v[\mu m/s]))^{2/3} \quad (3.44)$$

with

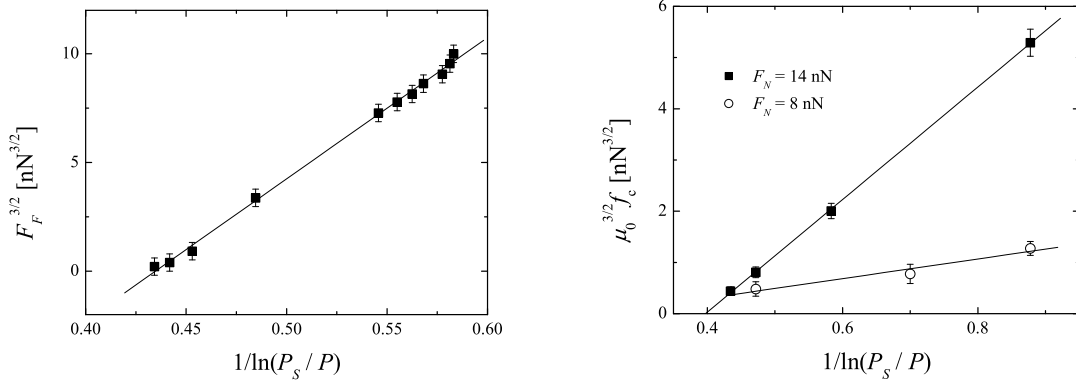
$$f_c = F_0 (1 + K F_N^{2/3}) \left(\ln \left(\frac{P}{P_S} \right) \right)^{-1} \quad (3.45)$$

and

$$x_0 = \left(F_N + F_0 \left(1 + K F_N^{2/3} \right) \frac{\ln(v_0)}{\ln \left(\frac{P_S}{P} \right)} \right) \quad (3.46)$$

The values of $\mu_0^{3/2} f_c$ and $\mu_0^{3/2} x_0$ as a function of the normal load are presented in Fig. 3.23. The linear increase of f_c with $F_N^{2/3}$ confirms the predictions of our model as it is rationalized in Equ. 3.45. At higher loads the number of asperities where the capillaries can form is larger, thus the phenomenon of capillary condensation plays a more important role leading to an increased slope of the $F_F(\ln v)$ curves.

By comparison of the experimental data in Fig. 3.23 with Eqs. 3.45 and 3.46, we can determine F_0 , K , v_0 and μ_0 . To fit $\mu_0^{3/2} f_c$ versus $F_N^{2/3}$, we use two free parameters: $\mu_0^{3/2} F_0$ and K . Whereas to fit $\mu_0^{3/2} x_0$ versus F_N we use as free fitting parameters F_0 and v_0 , because K and $\mu_0^{3/2} F_0$ are fixed to the values found in the previous fit. We obtain $F_0 = 1.3 \pm 0.4$ nN which has to be compared with Equ. 3.43. From this comparison, by taking $\lambda = 1$ nm and $r_c = 1$ nm, we calculate $R_T \approx 30$ nm, which is in agreement with our expectations for the tip used for those experiments. Furthermore, our fits give $K = 0.20 \pm 0.15$ nN $^{-2/3}$ which



(a) Relation between $F_F^{3/2}$ and the humidity for $F_N = 12$ nN and $v = 0.2$ $\mu\text{m/s}$ (b) Relation between $\mu_0^{3/2} f_c$ and the humidity for two different loads

Figure 3.24: Friction force and $\mu_0^{3/2} f_c$ as a function of the relative humidity for different normal loads. The linear dependence with the logarithm of the humidity is highlighted.

P/P_S	$(\mu_0^{3/2} f_c)_{th} [\text{nN}^{3/2}]$	$(\mu_0^{3/2} f_c)_{exp} [\text{nN}^{3/2}]$
0.12	0.6	0.5 ± 0.1
0.22	0.9	0.8 ± 0.1
0.33	1.3	1.3 ± 0.1

Table 3.5: Experimental and theoretical values of $\mu_0^{3/2} f_c$ for $F_N = 8$ nN.

is of the same order of magnitude of the value $0.02 \text{ nN}^{-2/3}$ coming from Equ. 3.37 with $E^* = 40 \text{ GPa}$, $R_K = 1 \text{ nm}$ and $R_T = 30 \text{ nm}$. Finally the fits give $v_0 = 76 \text{ } \mu\text{m/s}$ and $\mu_0 = 0.6 \pm 0.2 \text{ nN}^{1/3}$.

Finally, the humidity dependence of the friction force has been studied at different normal loads and velocities. At $v = 0.2 \text{ } \mu\text{m/s}$, in the range of relative humidities 4-20%, we show in Fig. 3.24(a) that F_F grows linearly with $1/\ln(P_S/P)$ as predicted by Equ. 3.39. Fig. 3.24(b) presents our measurements of $\mu_0^{3/2} f_c$ as a function of $1/\ln(P_S/P)$ at two loads, $F_N = 8$ and 14 nN . As predicted by Equ. 3.45, f_c increases linearly with $1/\ln(P_S/P)$, because at higher humidities more capillaries can form at the same sliding velocity. Furthermore, at higher normal loads, f_c increases more rapidly with humidity. Again, this is related to the increase of the efficiency of the capillary condensation process at higher normal loads and confirms the link between humidity and load as described in our model. In Table 3.4.4, we show the humidity dependence of $\mu_0^{3/2} f_c$ found directly from measurements of F_F versus $\ln v$ at different humidities and found from Equ. 3.45 using the values of μ_0 , F_0 and K previously obtained from the fit of the data in Fig. 3.19 ($P/P_S = 0.33$) with the equations of our model. The very good agreement between these values definitely proves the correctness of Equation 3.39 in describing the capillary force. Our experimental results have been experimentally strengthened in a recent study [80] on the nanoscopic contact between hy-

drophilic surfaces. They found that both the friction force and the contact radius decrease with the sliding velocity which is in agreement with our model. These decreases are due to the decrease of the adhesive force with the sliding velocity resulting from the disappearance of the capillary force.

3.5 Conclusion

In this chapter, we were interested in the friction phenomenon, an old subject of research that still remains topical due to its application in industry and everyday life. One of the important changes occurring in the field of the friction research has been the scale reduction of the studies, going from the macroscopic world to the atomic level. At these small scales, the balance between forces proportional to the surface and the volume is not the same as the one for macroscopic bulk material. The result is a divergence of the phenomenological behaviors depending on the size of the system.

To enlarge our knowledge on the friction at the nanometer scale, we studied the changes in the friction force for a nanoscopic AFM tip sliding on various samples, while exterior parameters, such as the scanning velocity, the applied normal load or the humidity varied. Emphasis was carried on the thermally activated phenomena occurring in the nanoscopic friction by the investigation of the friction dependence on the velocity. The main experimental results were the logarithmic dependence of the friction on both the scanning velocity and the relative humidity. For the first time, a transition from a positive to a negative slope of the friction force versus the logarithm of the sliding velocity has been observed for the very same tip-surface contact, by varying the relative humidity. We suggested a model based on the one-dimensional Tomlinson model to explain those behaviors. Finally, we proposed also a model for the condensation of capillary bridges in the interstices of the tip-surface contact. This model is based on the Hertz theory and on probabilities for the tip to jump from one equilibrium position to the next one while sliding on the surface.

The complexity of the friction phenomenon results in the difficulty of finding a fundamental model to explain its different behaviors. This complexity emerges from its universal nature, meaning the great variety of materials that are in relative motion the one against the other one. If an analytical comprehension of the frictional process is not possible, other apertures are given by the computer sciences. It is now possible to simulate the interactions between contacting bodies at the molecular level. Perhaps a complete comprehension of the friction is not yet possible, but in the actual climate of economy of energy, whatever could reduce the friction becomes relevant and might have non negligible consequences.

Chapter 4

Nanomechanics

This chapter deals with the continuum mechanics applied to small tubular structures in order to evaluate their elastic properties. The diversity and the fabulous potential of applications of the nanostructures is briefly reviewed by presenting some advances in nanotechnologies. Then, theoretical models based on continuum mechanics are developed to mimic the elastic behavior of tubular nanostructures. Finally, these models are applied to experimental data of AFM measurements of the elastic deformations of hard carbon nanotubes and soft tobacco mosaic viruses. Radial Young moduli as function of the carbon nanotube diameter and a mean value for the bending Young modulus of the tobacco mosaic viruses are by this way experimentally estimated.

"There is Plenty of Room at the Bottom" was entitled a famous talk given by Richard P. Feynman in 1959 at the annual meeting of the American Physical Society [81]. The subject was the atomic level and its enormous potential of applications. At this time, it was still difficult to perceive the extent of the technological possibilities residing in the small scales of the matter. Fifty years later, the science and technology of the smallness are present in every fields of research and are popularly referred to as the nanotechnologies. Ideas raised in 1959 during Feynman's talk, like the one of swallowing a mechanical surgeon inside the blood vessel in order to look around in the human body, become nowadays accessible. We are able to create special nanoparticles that detect, identify and quantify proteins target [82] that are a sign of cancer or other diseases. Bound to medical imagery, such techniques allow to localize these nanoparticles in the human body and to make an early diagnosis of the disease, which may result in a rapid recovery. Thus the first concepts present in the minds in the middle of the last century have grown and are now under intensive investigations, like the bottom-up approach of atomic scale fabrication, contrary to the usual top-down approach [83]¹. The impact of the nanotechnologies on the everyday life issues is not only restricted to the application of the scientific discoveries, but also concerns the exploration of the fundamental processes and interactions that take place in the matter at the atomic level. Nanomaterials are perfect representations of one-, two-, or three-

¹ The bottom-up approach is the self-assembly of machines from basic chemical building blocks, which is considered to be an ideal through which nanotechnology will ultimately be implemented. The top-down approach is the assembly by manipulating components with much larger devices, which is more readily achievable using the current technology.

dimensional objects in their simplest forms. It becomes then possible to compare their real behavior when varying parameters such as stresses, electric or magnetic fields, with precise numerical simulations based on the actual laws of physics. This kind of comparisons between experiments and theory on low dimension objects is helpful to better understand the interactions at the atomic scale. Thus, nanomaterials represent one of the most rapidly expanding and challenging fields of research that crosses many borders between areas of natural sciences and physics.

This chapter brings up the question related to the behavior of nanometer sized structures under stress and strain compared to our knowledge for the same geometries at larger scale. The first part of the chapter introduces the concepts of nanomaterials and nanostructures by few examples. Then, the second part deals with the study of two typical cases of cylindrical nano-objects under normal stress: a non-biological nanostructure called the multiwalled carbon nanotube (CNT), and an organic nano-rod, namely the tobacco mosaic virus (TMV).

4.1 Introduction to nanostructured materials

Nanostructures usually refer to structurized devices with a size of few nanometers to several hundreds of nanometers. One finds such structures in the nature where they are an integral part of biological systems (See Fig. 4.1), e.g. cell components or viruses, but also in non-organic items like extremely small sand grains or nanometric droplets of water. What propelled the nanostructures among the major fields of research and, at the same time, gave birth to the nanotechnologies, is the faculty of the researchers to tune, use and create new or existent nanostructures for technological applications and academic research, motivated by the fact that materials with nanoscale dimensions display physical properties (e.g. electronic, photonic or magnetic properties) different from those observed by their respective bulk materials. We present now few inorganic and organic/biologic nanostructures to highlight the high diversity and the abilities of these nano-objects.

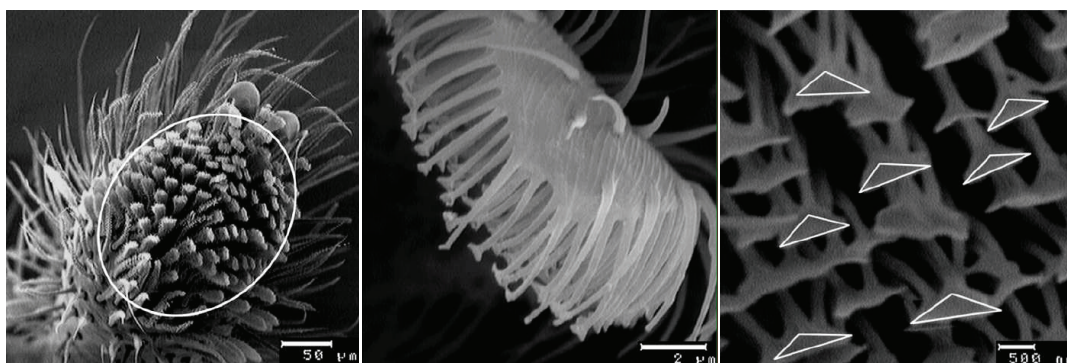


Figure 4.1: Example of nanostructured material found in the living nature. These pictures are SEM enlargements of the foot of the jumping spider *E. arcuata* (From Ref. [84]).

4.1.1 Inorganic nanostructures

A well-known group of inorganic nanostructures is the fullerenes. They are part of the allotropes of the carbon, one of the most important elements in nature. They were discovered by chance in 1985 by Kroto, Curl and Smalley, who were awarded the Nobel prize in Chemistry in 1996 for this discovery of a new class of carbon compounds [85]. Until 1985, the basic crystalline known forms of the carbon were the diamond, the graphite and the amorphous carbon. The fullerenes introduced new stable carbon structures in the form of hollow spheres (called buckyballs or buckminsterfullerene²) [85], onion-like graphitic sphere [86], tubes (called carbon nanotubes) [87] or ellipsoids (See Fig. 4.2). The structure of these nanomaterials is generally quite similar to the graphite. They find their applications, in particular for the case of the nanotube, in a wide range of techniques such as components of nanoelectronic devices like interconnects or field-effect transistors, and are also good components for mechanically reinforced composite materials and nanometer sized sensors [88–94].

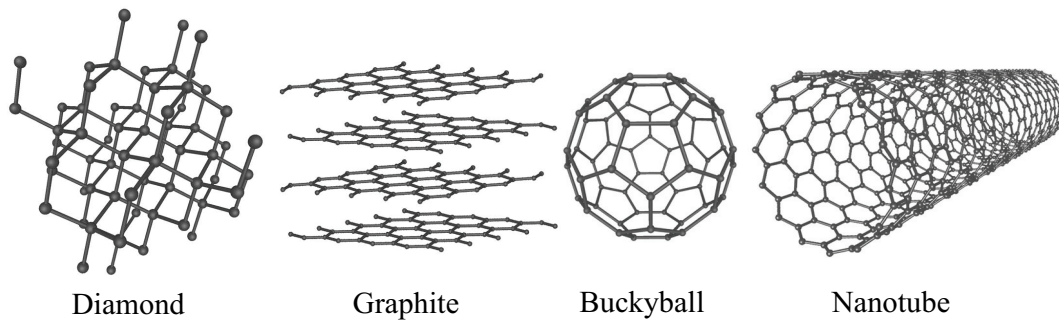


Figure 4.2: Illustration of the main carbon allotropes.

The potential of applications of the nanotubes led to the development of other kinds of small cylindrical shaped nano-objects: the nanowires (also called nanorods). These nano-objects, essentially based on metallic elements, are wirelike nanomaterials, such as carbides [95], nitrides [96], oxides [97–99], having as common characteristic a cylindrical symmetric cross-section. The extensive interest in such nano-objects is due to their great potential of addressing some basic issues about dimensionality and space-confined transport phenomena [98], as well as future industrial applications [100–102].

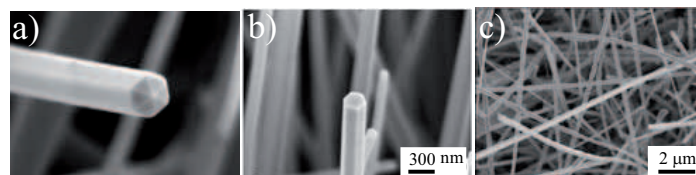


Figure 4.3: Example of nanowires: (a) and (b) are hexagon and pentagon shaped ZnO nanowires, whereas (c) presents GaN nanowires.

Besides the tubular nanostructures, another interesting two-dimensional structure is the

² The name "buckminsterfullerene" - C_{60} - comes from Richard Buckminster Fuller, an architect who erected the world's first geodesic dome. By analogy, the name "buckminsterfullerene" was thought appropriate.

nanobelt [103]. This nanostructure has a rectangular cross section and looks like a ribbon. Nanobelts are made of different semiconducting oxides, like zinc or tin, and are synthesized by evaporating metal oxide powders at high temperatures. One of their distinctive features is to be an ideal system for understanding piezoelectric effect and spontaneous polarization induced ferroelectric effect at the nanoscale [104]. Moreover, it is possible to obtain nanobelts in the form of rings or springs (See Fig. 4.4), which can work as mechanical nanosensors.

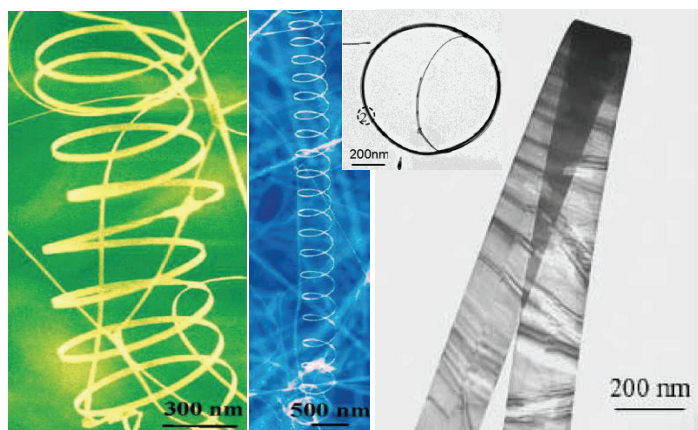


Figure 4.4: Nanobelts in the form of springs, rings and ribbon from Ref. [104].

Finally, numerous inorganic nanostructures show potential applications as one-dimensional nanoscale sensors, transducers, resonators or lasers, which is really promising since the properties related to low dimensions are more important than the size [105]. Moreover, the functionalization [106, 107] or the use as template [108] of such versatile objects may enlarge their domains of application. At the end, we better understand the strong interest of the research for so small objects that hide an enormous potential of fundamental and technological developments.

4.1.2 Organic nanostructures

The organic nanostructures are chemical compounds consisting primarily of carbon and hydrogen. Compared to inorganic nanostructures, these organic structures keep the attention of researchers due to their extreme flexibility in being tailored to meet the needs of particular applications and also due to their great potential for coating and molding [109–112]. Another interesting feature for industrial applications is their low production cost. They are effectively materials that are, for example, easily integrated with conventional inorganic nanostructures like in semiconductor devices and in addition, they provide supplementary functionalities to existing photonic circuits and components. Nanostructured organic thin films are for example used as organic light emitting devices (OLEDs) [113, 114] or also as organic thin film transistors [115]. Beside this "planar" use of organic structures, three-dimensional specimens provide templates for the synthesis of inorganic structures. These templates are for example protein cages [116, 117], viroid capsules [118], multicellular superstructures [119, 120], biolipid cylinders [121]. Thus, the use of organic molecules

in the development of inorganic material synthesis provides an alternative way to conventional synthetic strategies for the direct deposition, assembly, and patterning of inorganic nanoparticles and microstructures. An example of organic-inorganic application is shown in Fig. 4.21 with the use of the tobacco mosaic virus as template for metallization.

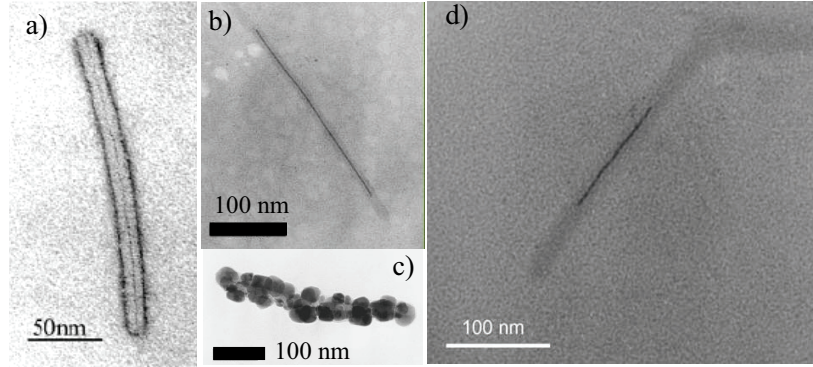


Figure 4.5: TEM images of the tobacco mosaic virus from Ref. [122, 123]. This virus has a cylindrical shape with an inner channel at its center. Its exterior shape and the central channel appear dark in picture (a). Template uses of the virus are illustrated in pictures (b)-(d): (b) and (d) are TEM images of a single virion containing a nickel, respectively a copper, wire inside its central channel; (c) is a TEM image of the virus metallized with cobalt.

4.2 Mechanics of nanostructures

The use of the nanostructures in technical applications such as nanosensors, nanometer-scale devices or for composite bulk materials requires the knowledge of their mechanical properties. Unfortunately, the properties of a material at the nanoscale diverge strongly from its properties at the macroscale. One of the reasons is the presence of defects in the macroscopic bodies. The mechanical properties of a macroscopic object, such as the Young modulus, are often far away from the theoretical values obtained by extrapolating from the atomic bond strength up to the macroscopic scales [124]. At the opposite, nanostructures are special cases for which the number of defects decreases so much that the structures approach ideal cases of perfect bodies. It remains then challenging to manipulate such nano-objects and measure experimentally their mechanical properties from both the fundamental and the application point of view.

The nanoscopic techniques used to test the nano-objects are often inspired by techniques used in the macroscopic world, with of course some precautions. Since the work of Yakobson *et al.* [125], who first showed that the peculiar behavior of CNTs can be well described by a continuum model, the use of continuum mechanics concepts applied to nano-objects has become a common practice. The most classical approach for the continuum modelling of nanostructures is thus to adopt a standard continuum theory like the linear elasticity, and adjust the material parameters to the data available for the bulk material [126]. From a simple point of view, a continuum theory based on linear elasticity, such as Hooke's law, rests on a parabolic approximation of the potential function of a system around its equilibrium

position. This basic idea is then also valuable in the case of nanostructures characterized by a smooth interatomic potential around their equilibrium position.

In this section, we present the two methods and related theories used for measuring the mechanical properties of the stiff CNTs and the soft TMVs. Both methods rely on atomic force microscopy. The AFM technique has already been used to characterize numerous organic and inorganic nanostructures. Among the inorganic nanostructures, a pronounced interest was shown for tubular nanostructures and long thin structures, such as CNTs, ropes of CNTs, nanobelts [127] and nanowires [128–132], which have an adequate symmetry and shape for experimental manipulations and theoretical calculations. The faculty of the AFM to work in different kinds of surrounding environments, like in liquids, has also led to its common use for probing biological samples, among which we find the T4 bacteriophages on silicon substrates [133], pox viruses and living cells [134], microtubules [135], and finally, the nanoindentation of viral capsids³ to determine how the strength and elasticity depend on the capsid structure [136].

Thus, the versatility and easy use of the AFM make it the ideal tool to test materials at the nanoscale under different working environments [137]. Another interesting alternative method to the AFM is based on nanostructures resonance using TEM. It has been used to characterize the elasticity of CNTs and nanowires [138, 139], and also nanobelts [140–142]. In each case, the obtained values agreed with the AFM results. Unfortunately, it is sometimes subject to large errors bars (20–60%) [138] and it cannot be applied in a way as general as the AFM techniques. It needs effectively special preparation of the nano-objects for the vacuum and it tests almost only the bending elastic property of long thin structures.

4.2.1 The modulated nanoindentation AFM method

The modulated nanoindentation method is based on the FMM method described previously in Chapter 2. We used this technique to determine the radial elasticity of CNTs. It consists of indenting an AFM tip in a sample up to a fixed distance while small oscillations are applied to the sample. One distinguishes normal modulated nanoindentation from shear (or lateral) modulated nanoindentation. In the first case, oscillations and indentation are colinear, normal to the surface of the sample, whereas in the second case, they are tangential to the sample surface. From a theoretical point of view, normal and lateral modulated nanoindentations are very similar. Therefore, we will treat especially in the following the case of the normal modulated nanoindentation, while the case of the lateral modulated nanoindentation is easily deducted from the theoretical formulas obtained here. The example of CNTs adsorbed on a silicon oxide substrate is taken as illustration of the method.

In this technique, the amplitude of the oscillations is chosen very small, close to 1 Å, in order to remain in the sticking and elastic regime of the tip interacting with the nano-object surface. In this amplitude range and experimental geometry, the normal force F_N required to move vertically the support of the nano-object (e.g. the substrate of adsorbed CNTs) by a distance D with respect to the cantilever support coincides with the force needed to elastically stretch two springs in series [30, 72]: the cantilever, with stiffness k_N , and the tip-sample contact, with stiffness k_{cont} . If D is the total normal displacement of the nano-object support, i.e., D is equal to cantilever bending plus tip and nano-object normal deformation,

³ The interest in the capsids is that they contain highly stressed DNA genomes and are capable of withstanding internal pressures of tens of atmospheres without rupturing.

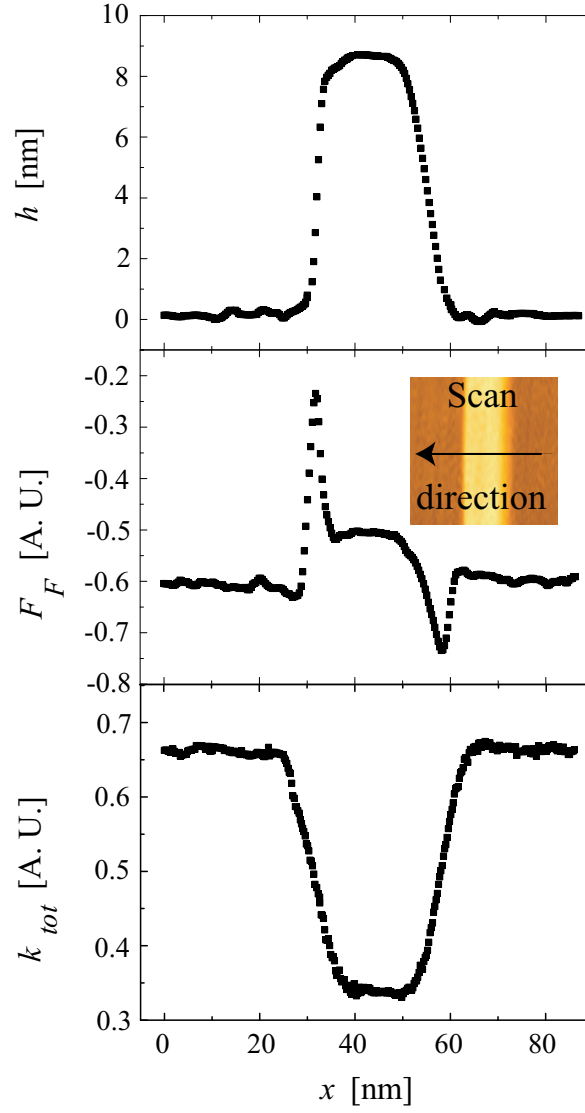


Figure 4.6: Illustration of the normal modulated nanoindentation technique on a multiwalled CNT adsorbed on a silicon oxide surface. This technique allows to record simultaneously the topography h , the friction force F_F , and the total stiffness of the system as function of the AFM tip displacement x .

and F_N is the total normal force, then this configuration allows the measurement of the total stiffness k_{tot} at each load, defined by the relation:

$$\frac{dF_N}{dD} = k_{tot} = \left(\frac{1}{k_N} + \frac{1}{k_{cont}} \right)^{-1} \quad (4.1)$$

Since k_N is known⁴, a measurement of dF_N/dD at different normal loads leads to the value of k_{cont} as a function of F_N . For this, a lock-in amplifier is used to vertically modu-

⁴ In the case of lateral modulated nanoindentation, it would be k_L and the displacement D is parallel to the nano-object surface.

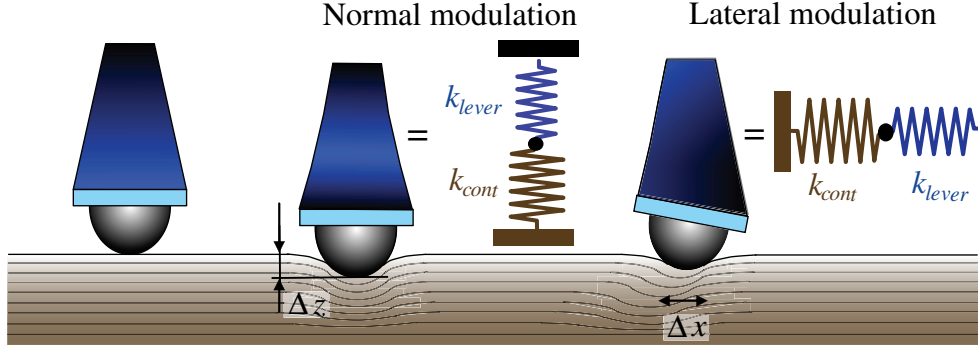


Figure 4.7: Sketch of the normal and lateral surface stiffness measurement while indenting a surface. The total stiffness is represented by two springs in series, k_{lever} and k_{cont} being respectively the elastic constants of the tip-cantilever and the probed surface.

late the nano-object support, dD , and measure dF_N . Figure 4.6 illustrates the experimental results of the normal modulated nanoindentation method applied to a CNT. It gives access simultaneously to the topography, the friction force and the total stiffness of the system while scanning the surface.

We can extract then the related Young modulus E from k_{cont} versus F_N measurements by modelling the contact between the AFM tip and the nano-object, here a CNT, with the Hertz model [132, 143, 144] described in Chapter 1. We underline that the extracted E is therefore the linear elasticity of the object under a stress normal to its surface. Thus, under the assumptions of standard elasticity theory, the Hertz model gives the dependence of the indentation distance δ_z versus the normal force F_N between two elastic solids in contact [10]. Although very sophisticated extensions of this model were developed to include the effect of the adhesion at low external forces [14], in the context of this work, it suffices to use the first level approximation, consisting of an additive correction of the normal force F_N (See Section 1.3.2). We consider the contact between a sphere and a cylinder (corresponding to the tip and the CNT) of respective radii R_T and R_{cyl} , and we include the adhesive force F_{adh} , which is experimentally determined. From the Equations 1.31, 1.32, 1.33 and the Hertz theory, we have:

$$k_{cont} = \frac{1}{C_z} = \beta \left(\frac{R(F_N + F_{adh})}{\tilde{K}^2} \right)^{1/3} \quad (4.2)$$

with

$$\frac{1}{R} = \frac{1}{R_T} + \frac{1}{2R_{cyl}} \quad (4.3)$$

$$\tilde{K} = \frac{3}{4} \left(\frac{1 - \nu_1^2}{E_1} + \frac{1 - \nu_2^2}{E_2} \right) \quad (4.4)$$

$$\beta = (\pi/2k)^{2/3} \cdot \frac{[E(\sqrt{1 - k^2})]^{1/3}}{K(\sqrt{1 - k^2})} \quad (4.5)$$

where ν_1 , ν_2 and E_1 , E_2 are respectively the Poisson ratios and radial Young moduli of the sphere and the cylinder. For convenience, we put in β the parameters related to the

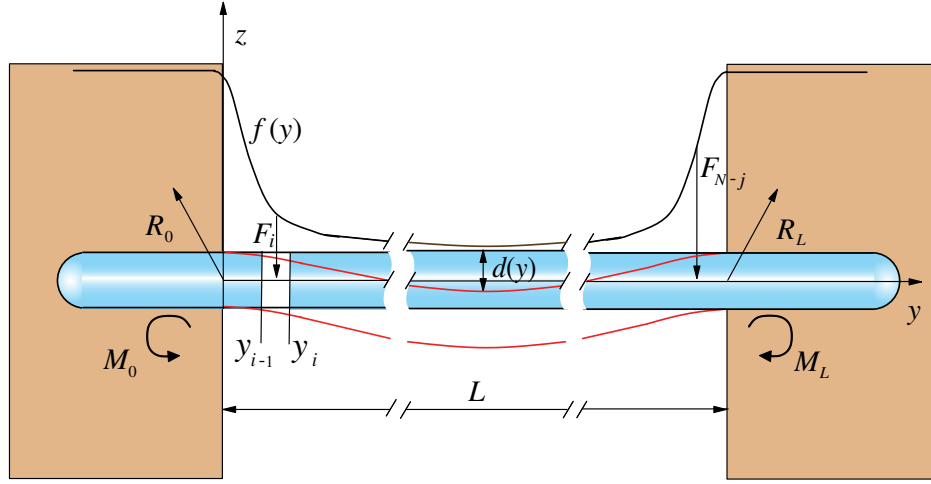


Figure 4.8: Model of a clamped TMV under discrete forces represented by the force gradient $f(y)$.

geometry of the contact area. In the case of lateral modulated nanoindentation, C_z has to be replaced by C_x or C_y given by Equations 1.34 and 1.35. Thus, by fitting k_{cont} versus F_N with Equ. 4.2, we obtain the radial Young modulus $E_2 = E_{rad}$ of the cylindrical nanostructure, as it is the only free fit parameter⁵.

4.2.2 Classical elastic beam in the nanoworld

Another interesting method that gives access to the mechanical properties of high aspect ratio nanostructures is based on the classical elastic beam. Referring to Figure 4.8, it consists in measuring the normal deflection $d(y)$ of a suspended nanobeam under the assumption of clamped beam. This method has already been used to measure the bending Young modulus of CNTs [129, 145, 146] and microtubules [135] submitted to a normal force F_N loading the middle of the suspended length. In our case, we will not be restricted to a single normal force F_N applied to the middle of the beam, but we will consider a discrete gradient $f(y)$ of forces F_i applied along the whole length of the beam. Moreover, the geometric configuration of the problem leads to choose the case of a symmetric gradient of force $f(y)$ relatively to the center of mass of the beam. It represents for example the action of the vdW forces between the nanobeam and its surrounding environment.

We consider now a beam with its long axis along y and of suspended length L , as shown in Fig. 4.8. The discrete division $dy = y_i - y_{i-1}$ of the beam along the y -axis is given by the equation $dy = (L - 2h)/N$ where N is a positive entire multiple of 2, representing the number of divisions of the TMV and chosen so that $dy \cong 0.4$ nm. The parameter h takes into account the RMS roughness of the surface on which the nanobeam lies. Each force F_i ($i = 1, \dots, N$) composing the discrete gradient $f(y)$ is directed along z , perpendicularly to the y -axis. As the loading forces F_i are symmetric compared with the midpoint of the beam,

⁵ For unknown Poisson ratios, it is necessary to fix it close to the mean value $\nu_2 = 0.3$ admitted for common materials.

the reaction forces R_y and moments M_y acting in $y = 0$ and $y = L$ are equal: $R_0 = R_L$ and $M_0 = M_L$. Moreover, it results from Newton's equations projected along the z -axis at the static equilibrium that $R_{0,z} = R_{L,z} = \frac{1}{2} \sum_{i=1}^N F_i$, where we considered that the forces F_i are negative.

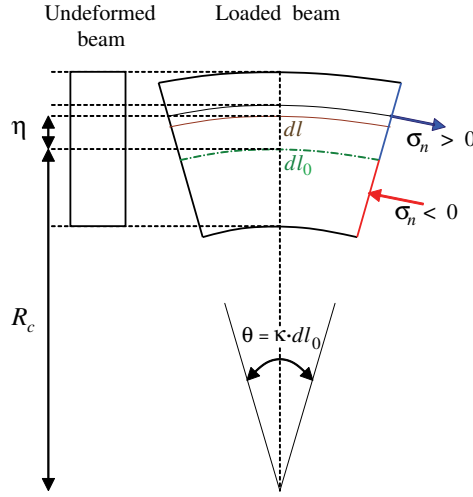


Figure 4.9: Representation of the stress-strain on a loaded beam.

According to the beam theory, the upper and lower part of the beam will be alternatively in tension and in compression, submitted to a stress σ_n . While the lower part of the beam is in compression ($\sigma_n < 0$), the upper part is in tension ($\sigma_n > 0$) and vis versa (See Fig. 4.9). Inside the beam, there is a surface that does not change in length, called the neutral surface of the beam and represented in Fig. 4.9 by dl_0 . It is the line of zero normal strain. For a beam made of a material that obeys the Hooke's law, this surface will pass through the middle of the beam. Referring to Fig. 4.9 and taking the origin of the η -coordinate axis at the neutral surface, the stress distribution is given by

$$\begin{aligned} \sigma_n &= E \cdot \varepsilon_n = E \cdot \frac{dl_0 - dl}{dl_0} \\ &= E \cdot \frac{(R_c + \eta)\theta - R_c\theta}{R_c\theta} = E \frac{\eta}{R_c} \end{aligned} \quad (4.6)$$

where ε_n is the normal strain distribution, R_c is the radius of curvature of the neutral surface and E is the bending Young modulus of the beam. Then, the bending moments M due to the stress acting on a small beam section positioned arbitrarily in $y = a$ is given by [147, 148]

$$M = \int_{section} \eta \sigma_n dS = \frac{E}{R_c} \int_{section} \eta^2 dS = \frac{EI}{R_c} = \kappa EI \quad (4.7)$$

where $\kappa = 1/R_c$ is the beam curvature and I is the inertial momentum of the section of the beam along its long axis. In the case of a cylindrical beam of diameter D , we have $I = D^4/64$. This total bending moment is also equal to the sum of the bending moments due to the forces acting on the beam for $y > a$. Applying these last considerations in our case, we have for $y_{i-1} + dy/2 \geq a$

$$\frac{EI}{R_c} = \sum_i F_i \cdot (y_{i-1} + dy/2 - a) - M_L + R_L \cdot (L - a) \quad (4.8)$$

For small deformations, the deflection $d(y)$ of the beam relatively to its non deformed position is related to the curvature of the neutral surface via simple geometric considerations as described in Ref. [147, 148]. At the first order, the relationship between κ and $d(y)$ becomes

$$\kappa = \frac{1}{R_c} = \frac{d^2 d(y)}{dy^2} \quad (4.9)$$

Finally, by combining Equ. 4.8 and Equ. 4.9, we obtain for $y_{i-1} + dy/2 \geq y = a$

$$EI \cdot \frac{d^2 d(y)}{dy^2} = \sum_i F_i \cdot (y_{i-1} + dy/2 - y) - M_L + R_L \cdot (L - y) \quad (4.10)$$

The double integration of this last equation versus y under the boundary conditions of clamped beam and continuity gives rise to the suspension depth $d(y)$ for $0 < y < L$. The maximum suspension depth is then found at the middle of the nanobeam, corresponding to $d(L/2)$. This last formula gives a direct access to the bending Young modulus E from experimental measurements of the suspended beam geometry once the forces acting on the beam have been determined.

4.3 The mutliwalled carbon nanotube

Since their first reported observation [87], carbon nanotubes have been the subject of numerous researches. The investigations on their mechanical, electrical and thermal properties [145, 149–155] have attracted great scientific and also technological interest. Indeed, their exceptional properties offer tremendous opportunities for the development of new devices and materials going from nanotube reinforced composite materials to nanotube transistors. The first part of this section provides a concise review of the main characteristics of the CNTs, while the second part focuses more deeply on their mechanical properties to finally present our experimental results on the radial Young modulus of multiwalled CNTs.

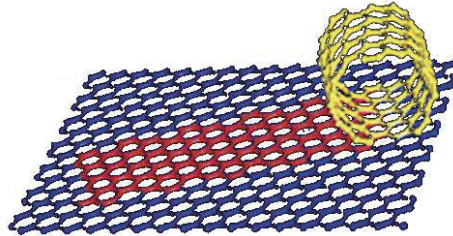


Figure 4.10: Each layer forming a CNT is analog to a graphene sheet wrapped seamlessly onto itself.

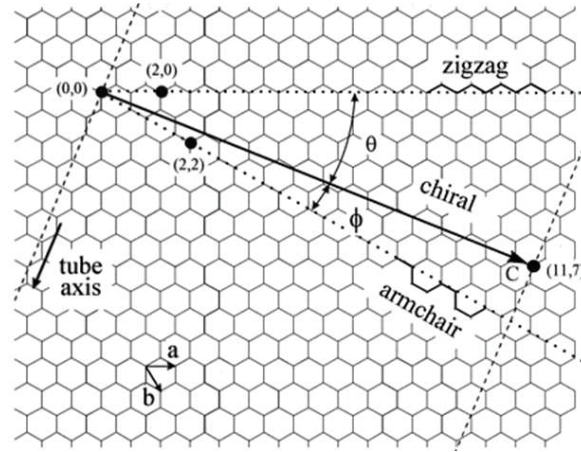


Figure 4.11: Carbon nanotubes can be thought as rolled-up sheets of graphene plane characterized by the unit lattice vectors (a, b) . An armchair tube is the tube rolled-up along the direction $((0,0),(2,2))$ and the zig-zag shape is obtained by rolling-up the graphene sheet along the direction $((0,0),(2,0))$. In between, the tubes characterized by the angles θ or ϕ are called chiral tubes. We distinguish single-walled carbon nanotubes consisting in only one single sheet of graphene, and multi-walled carbon nanotubes which contain several graphene layers forming a tube with coaxially stacked cylinders.

4.3.1 Description and characteristics

Multiwalled carbon nanotubes (MWCNTs) are part of the fullerenes. They were discovered by S. Iijima in 1991 [87]. As presented in Fig. 4.10, they consist of graphene sheets wrapped seamlessly onto themselves forming a tube of concentric shells with an outer diameter ranging from 1 to 50 nm for lengths up to several micrometers [156]. It is also possible to have CNTs of only one shell. They are called single-walled CNTs (SWCNTs). The inter-shell spacing can range from 0.34 to 0.39 nm, increasing with decreasing diameter and having an asymptotic value of 0.344 nm for tube diameters of roughly 10 nm [157]. This variation in the interlayer spacing is attributed to the change in shell curvatures. Note that the obtained asymptotic value is close to the interlayer spacing of graphite⁶, which is 0.335 nm, but is better described in terms of turbostratic graphite [157].

4.3.2 CNTs chirality

There are different manners to form a cylinder with a sheet of graphene, resulting finally in one concentric layer of a CNT. If the plane is rolled up along one of the symmetry axis of the graphite, it gives either a zig-zag tube or an armchair tube (See Fig. 4.11). It is also possible to roll up the sheet in a direction that differs from a symmetry axis. The obtained CNT is then called a chiral nanotube. In general, the whole family of nanotubes is classified as zigzag, armchair, and chiral nanotubes of different diameters and with tube extremities that may be open or closed. The chirality of the CNTs influences its properties. For example, depending on the chirality, the tube is either metallic or semiconductive⁷. It influences also

⁶ The graphite might be seen as a layered structure of graphene sheets with an interlayer distance in the c -direction being on average about 0.344 nm. Higher values in this direction appear in the so-called turbostratic graphite leading to uncorrelated graphene layers.

⁷ More details on CNT conductivity are given in Ref. [149, 158].

its mechanical properties [159], but unfortunately, it is not obvious to determine the chirality of a tube that is experimentally tested under mechanical stress. The fact is that CNTs are generally produced in a wide distribution of tube diameters and chiralities without real experimental control on it. Furthermore, MWCNTs may exhibit different chiralities for their constituting shells. Therefore only atomic resolution SEM, TEM and diffraction patterns allow to determine the CNT chirality.

4.3.3 Synthesis of CNTs

We present briefly here the three main procedures used to synthesize CNTs. They are the *chemical vapor deposition* (CVD), the *arc discharge* (AD) method and the *laser ablation* (LA) method. The quantity, the quality and the characteristics of the tubes obtained with these different methods vary slightly. The CVD technique is the more flexible method, producing a high quantity of CNTs, but sometimes with a non negligible amount of defects. The AD method generates a mixture of fullerenes which requires different procedures of purification to differentiate the CNTs. The LA method produces high quality CNTs, but in very small quantities.

CVD

As indicated by its name, the CVD is based on chemical vapor deposition [160, 161]. It consists in chemical reactions that take place in a tube furnace and transform gaseous molecules of hydrocarbon flowing into the tube into solid material on the surface of a substrate prepared with a layer of catalyst particles of transition metal (See Fig. 4.12). The control of temperature, gas parameters (species, flow and pressure), catalyst material (diameter of the particles and species) and dispersion (patterning) on the support material, offers a great variety of tube growth. It allows for example to produce nanoscale structures with integrated CNTs thanks to the surface patterning by microcontact printing with the transition metal catalysts.

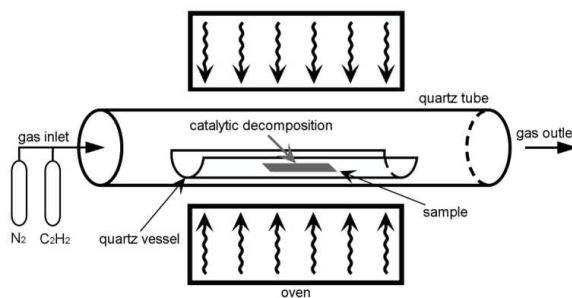


Figure 4.12: Illustration of one of the CNTs growth techniques: the CVD method. Chemical reactions transform the gaseous molecules into the CNT solid material. The decomposition of the gas ($C_2H_2 \rightarrow C_2 + H_2$ in the case of acetylene) and the nanotube growth are activated by the catalyst, which usually is iron, cobalt or nickel. The oven is typically working at temperature of $\sim 700^\circ\text{C}$. On one end of the tube, the gases are introduced and at the other end, they are pumped out by a vacuum pump.

AD method

The arc discharge method was initially used for producing C_{60} fullerenes and then to manufacture CNTs [162]. It is based on the cooling of carbon plasma generated by an electric arc discharge between two graphite rods (electrodes). The carbon is evaporated by a plasma of inert gas in a confined environment in which are placed the two electrodes. The gases are usually helium, argon or hydrogen at pressure from 50 to 900 mbar. Due to the high current density between the electrodes, and thus, high temperature, the rods gently evaporate, while the distance between them is kept constant [163]. At the end, upon cooling, a soot containing the fullerenes is collected on the cathode.

LA method

The laser ablation method consists in intense laser pulses that are used to ablate a carbon target placed in a furnace heated at 1200°C [164]. Then, during the laser ablation process, a flow of inert gas passing inside the furnace carries the produced CNTs that are collected on a cold collector. This method produces a majority of CNT bundles.

4.3.4 CNTs properties

Mechanical properties

The tubular structure of CNTs takes advantage of the high basal-plane elastic modulus of graphite resulting from the strong in plane covalent C–C bond. The strength of this bond gives rise to an extraordinary axial stiffness, as pointed out by several experimental [128–130, 139, 145, 146] and theoretical [154, 155, 165] studies, finding values for the axial Young modulus of about 1 TPa⁸. In graphite, the C'_{11} in plane elastic constant is 1.06 TPa, while the perpendicular elastic constant C_{33} is only 0.036 TPa [154]. Similarly, the radial Young modulus of CNTs is expected to be much smaller than the axial one. Evidence for the softness of CNTs in the radial direction has been reported in experiments under hydrostatic pressure [166], where a critical pressure of only 2 GPa has lead to the collapse of SWCNTs with a radius of 0.7 nm. Finally, another remarkable property is their faculty to recover their original shape after repeated large bendings [132, 152, 167, 168]. Simulations confirm the elastic and reversible character of the deformations and indicate also a decrease of the dependence of the stiffness on the number of layers with the increase of the nanotube radius [155, 169].

Other properties

Besides its mechanical capacities to resist to strain and stress, CNTs present interesting conductive and chemical properties. Depending on the chirality, CNTs are metallic or semi-conductive. This faculty combined with their small size promises them to future applications as building blocks in nanoelectronic devices [150, 153]. In particular, SWCNTs exhibit one-dimensional carrier transport which implies a reduced phase space for scattering of the carriers and opens up the possibility of ballistic transport [149]. They are also an ideal

⁸ Most of the experiments on the mechanics of CNTs probed its axial stiffness through its bending and only few studies measured its tensile and radial properties. A non exhaustive list of the main experiments and results on CNT mechanics is given in Appendix A.

material for the study of low-dimensional phonon physics, and for thermal management, both on the macro- and the micro-scale. They are in fact revealed as an excellent filler for making high-thermal-conductivity composites [151]. In addition to their properties of electrical and thermal conductivity [152], CNTs exhibit a chemical reactivity higher than the graphene sheet due to the shell curvature. Thus, its more reactive zones are in fact the end caps, whereas the sidewalls are a little less reactive [170–172].

4.4 Experimental results on radial elasticity of CNTs

While many studies probed the axial stiffness of CNTs, our quantitative understanding of their radial elasticity is so far based on studies performed on only one tube, with an unknown number of layers, and using deformations up to the non-linear regime [132, 144, 169, 173]. Nevertheless, achieving a fundamental understanding of the radial deformability of CNTs is important for applying them in nanoelectromechanical and nanoelectronic systems. It has been shown, for example, that the radial deformation of CNTs may strongly affect their electrical properties [143, 150, 174–176].

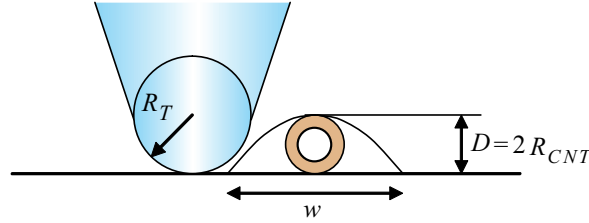


Figure 4.13: Illustration of the convolution of the AFM tip of radius R_T with a tube of height D giving rise to an apparent width w .

In this section, we present quantitative measurements⁹ of the radial elasticity of 39 multiwalled CNTs with external radii ranging from 0.2 to 12 nm and having a constant ratio of external to internal radii. We underline that the CNT with the external radius $R_{ext} = 0.2$ nm is most likely a single-walled CNT. In principle, the simplest way to measure the radial elasticity of CNTs would be to indent an AFM tip into a nanotube adsorbed at a surface and to measure force versus indentation curves. However, in practice such measurements are very challenging since in order to stay in the linear elastic regime, one has to measure forces of a few nanonewtons versus displacements of a few Å. Some authors have proposed an alternative AFM based method to investigate the radial elasticity of CNTs [132]. While scanning the tip across the sample the authors vertically vibrate the cantilever in non-contact or tapping mode with amplitudes in the range of several hundreds of Å and with the turning point situated a few Å above the sample. Due to the large amplitudes, a considerable fraction of the signal arises from the van der Waals forces acting between the tip and the tube, and only a small part comes from the elastic properties of the tube. Therefore in these experiments, in order to extract quantitative results on the radial deformation of a CNT, it is necessary to evaluate the van der Waals forces taking the cantilever, tip and sample geometry into account, which is far from trivial [178]. Here we propose to use the normal

⁹ The experimental results presented in this section have been the subject of the publication given in Ref. [177].

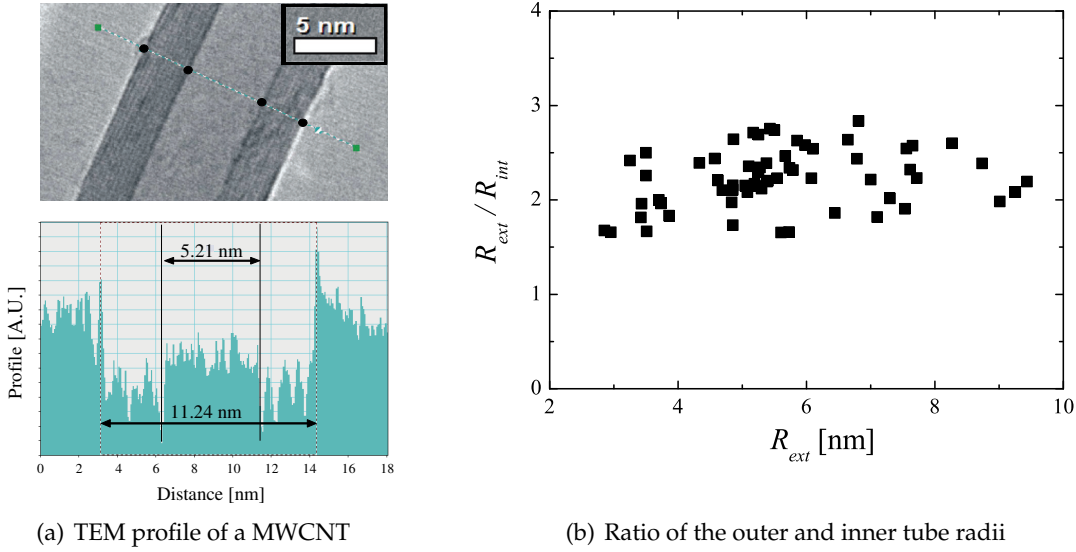


Figure 4.14: Ratio of external to internal radii of MWCNTs as obtained by TEM measurements. Picture (a) presents the TEM image of a MWCNT (top) for which the profile is measured (bottom) to determine the ratio between its internal and external radii. The final result for 62 CNTs is presented in (b) with an average $R_{ext}/R_{int} = 2.2$.

modulated nanoindentation method described in Section 4.2.1 to measure the radial elasticity of CNTs adsorbed on a flat surface.

4.4.1 Experimental details

The multiwalled CNTs were produced by chemical vapor deposition using acetylene as carbon feedstock [179]. Our CVD production method generates CNTs with an external to internal radii ratio $R_{ext}/R_{int} = 2.2 \pm 0.2$, as obtained from a large number of measurements with TEM and illustrated in Fig. 4.14. The morphology and the mechanical properties of CNTs have been measured with an AFM operating in contact mode in ambient conditions and equipped with commercial SiN cantilevers with tip radius of typically 35 nm. Normal cantilever spring constants, k_N , have been carefully calibrated and typical values were about 46 N/m. For each CNT, the tip radius has been explicitly determined in two ways. First, referring to Fig. 4.13, by using the equation $R_T = w^2/(16R_{CNT})$, where R_{CNT} is the tube radius inferred from its apparent height and w its apparent width. Second, by imaging the tip with a scanning electron microscope. Both methods yielded consistent results.

In order to image the CNTs, a drop of an alcohol suspension containing the CNTs is deposited onto a silicon surface and the solvent is allowed to evaporate at room temperature. In this way, the CNTs are adsorbed on the Si substrate with their principal axis parallel to it. At the end, we obtain a kind of "carpet" of scattered CNTs as illustrated in Fig. 4.15. The greatest concentration of CNTs is found at the edges of the substrate showing sometimes some aggregations. Around the piles of CNTs and in the direction of the center of the substrate, isolated CNTs are properly lying on the substrate leading to possible measurements

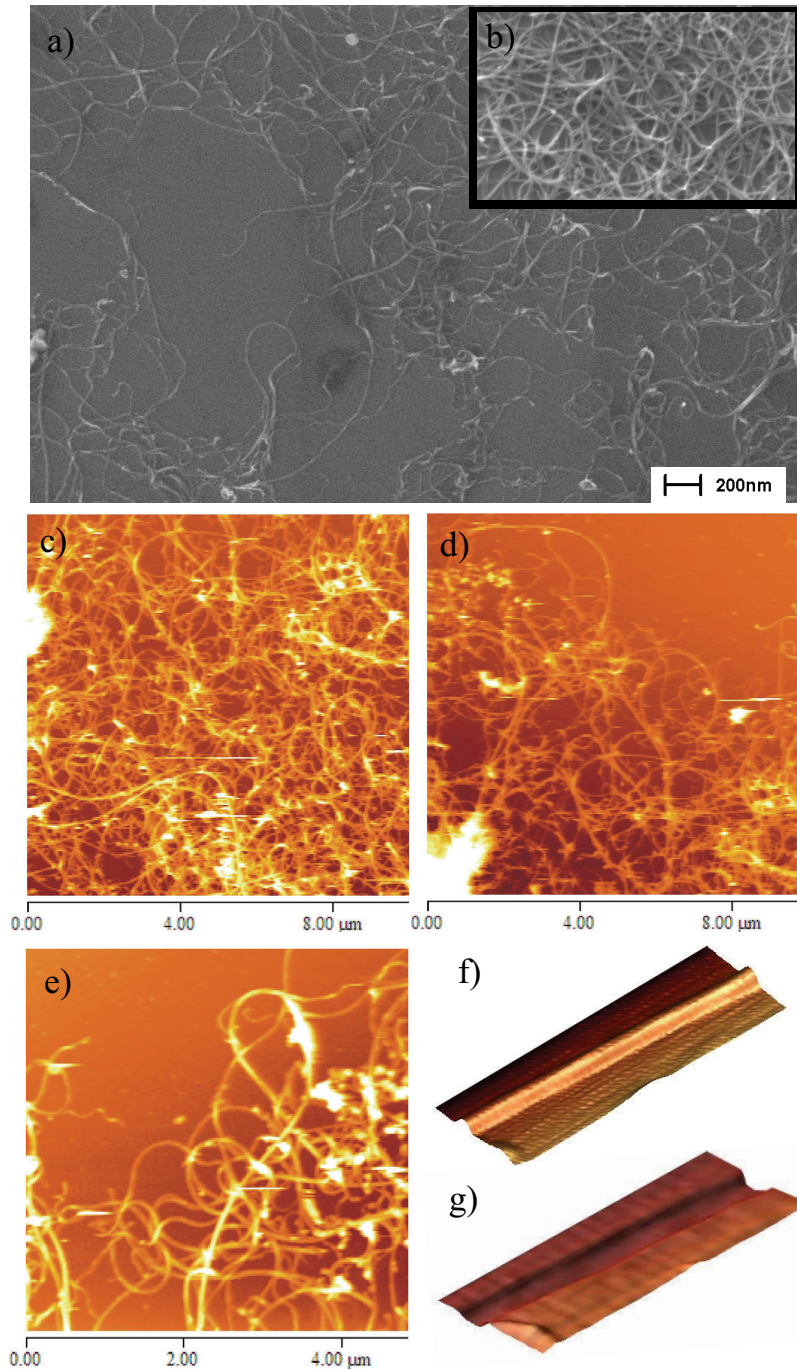


Figure 4.15: Images of the adsorbed CNTs on the silicon oxide surface. Pictures (a) and (b) are SEM images of the tubes, respectively far away and close to the substrate edges. Pictures (c) to (f) are contact mode AFM images of the CNTs under an applied normal force $F_N = 2$ nN. It is always possible to find isolated straight tubes lying properly on the surface as presented in (f) and to perform on it normal modulated nanoindentation leading to an image of the total stiffness of the sample as shown in picture (g). The CNT presented in (f) has a length of 500 nm for 10.5 nm height.

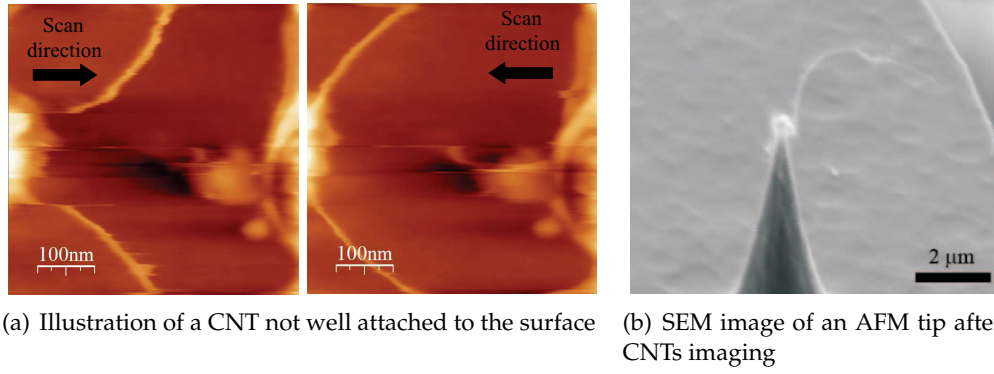


Figure 4.16: Illustration of the problems arising from CNTs imaging. On the left, trace and retrace of the topographical AFM signal of a CNT that bends in the direction of scan. On the right, SEM image of the AFM tip after imaging CNTs. CNTs ropes or isolated CNTs are attached to the tip, disrupting the measurements.

of their elasticity. Thus, the quest of the ideal CNT begins by imaging the center of the substrate where there are generally no CNTs and then, gently move towards the edges. By this way, one avoids to perform large scans over the areas covered with numerous CNTs that may be not well attached to the surface. In fact, CNTs that have not their long axis lying completely on the surface are generally not enough stable to perform modulated nanoindentation, but above all they can adhere to the AFM tip leading to bad topographical and contact stiffness signals (See Fig. 4.16).

Once an adequate straight CNT is found, then begins the process of focusing on the tube by decreasing the scan size until the AFM tip scans only the top of the CNT. Scanning a too large area while performing the data acquisition leads to the jump out-of-contact of the AFM tip since the series of measurements includes increasing and decreasing normal loads. In fact, any abrupt change in the topography, like climbing the CNT, may signify the loss of the contact between the AFM tip and the surface when the normal load reaches low values. Finally, if the system AFM tip-CNT is stable enough, i.e. good adhesion of the tube to the surface and negligible piezo drift, then the normal modulated nanoindentation method may be applied. We chose $dD = 1.3 \text{ \AA}$ and a frequency of 1.8967 kHz as parameters for the vertical modulation of the sample. Note that in our method, the tip deformations can be neglected due to the large difference in stiffness, one exception being presumably the smallest tube.

4.4.2 Molecular dynamics simulations

To mimic the experiments, molecular dynamics (MD) simulations with empirical C–C potentials have also been performed by modelling the AFM tip as a rigid continuous sphere and the CNT by atoms interacting through an empirical potential (See Fig. 4.17). For this, forces between carbon atoms are derived from a two-body pair energy plus a three-body angular penalty for the covalent energy (intra-layer energy), as developed by N. A. Marks [180], and from a truncated Lennard-Jones potential for the inter-layer energy, as applied by J. P. Lu [154]. The free potential parameters are fitted on the bulk graphite elastic constants, C_{11} , C_{12} and C_{33} , the cohesive energy, and the two lattice constants. CNTs are built with

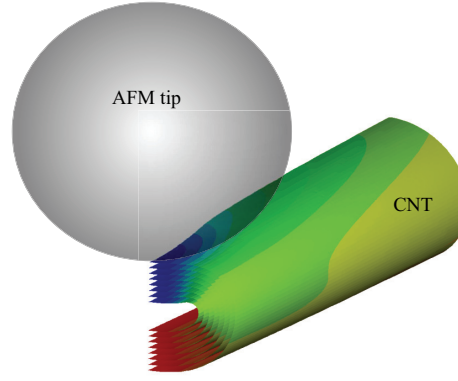


Figure 4.17: Simulation of the indentation of a MWCNT by a rigid sphere representing the AFM tip.

graphene sheets spaced by an inter-wall distance as close as possible to the graphite inter-layer distance, the chirality being a free parameter. Subsequently, the CNTs are compressed between the rigid sphere and a rigid plane using short range purely repulsive potentials for both interactions. The two ends of the CNTs are frozen. The CNT length and the sphere radius are respectively fixed to 20 and 12 nm. In all cases studied, the largest diameter of the contact area is smaller than 1.4 nm. Technically, the sphere is slowly moved against the CNT, while the kinetic energy is periodically removed. Expressed in the usual MD units (m.a.u., eV and Å), the time step is 0.4 and the sphere velocity is equal or lower than $2 \cdot 10^{-5}$ Å per time step.

4.4.3 Results and discussion

According to Equ. 4.1, the measurement of dF_N/dD at different normal loads leads to the value of k_{cont} as a function of F_N since k_N is known. Figure 4.18 shows the results of the measurement of $k_{cont}(F_N)$ for a multiwalled CNT with an external radius of 3 nm. $F_N = 0$ nN corresponds to the cantilever being unbent. The fact that tip and sample remain in contact at negative external loads indicates the presence of an adhesive force.

By integrating the equation $dF_N = k_{cont} \cdot dz$, where z is the indentation of the tip in the CNT, we obtain F_N versus the indentation z from the experimental curves $k_{cont}(F_N)$. The result is shown in Fig. 4.19(a) for CNT radii from 0.2 to 5.25 nm. If we call $F_N(z)/z$ the radial stiffness of the CNT, Fig. 4.19(a) indicates that the radial stiffness increases when the tube radius is decreasing for any value of z in the range explored by the experiment. Figure 4.19(b) presents the normal force versus the indentation distance obtained by the MD simulations and with R_{ext}/R_{int} kept close to the experimental value for CNTs with 2 to 6 layers. The respective CNT external radii are 0.61, 1.22, 1.82, 2.43, and 3.65 nm, while the ratios between external and internal radius is kept constant and equal to 2.2. In agreement with experiment, the nanotube radial stiffness also increases when its radius decreases, and, again in agreement, this effect is less pronounced for larger CNT radii. Compared to the results of Fig. 4.19(a), normal forces at equivalent indentation distances are typically one order of magnitude lower in the simulation. This is mainly attributed to the fact that the tip radius in the experiment is a factor of two larger than the sphere radius in the simulations.

The Hertz model predicts a $3/2$ power law dependence of F_N on z , which we indeed ob-

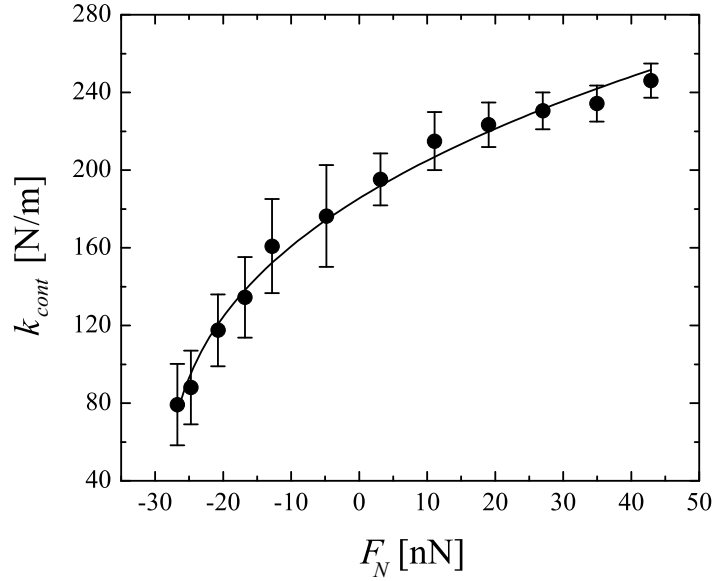


Figure 4.18: Experimental normal contact stiffness versus normal indentation force F_N for a 3 nm tube radius. Errors presented here are due to mean errors on the detection signal dF_N , taking into account the uncertainty on the cantilever stiffness. Experimental data are fitted with Equ. 4.1 and 4.2.

serve in our experiments (See Fig. 4.19(a)). From the calculations, we find the $3/2$ power law for filled CNTs, while there are deviations from $F_N \propto z^{3/2}$ for hollow CNTs with the cross sections used in experiment ($R_{ext}/R_{int} = 2.2$, see Fig. 4.19(b)). We attribute the deviations to the fact that the calculations have been performed for technical reasons with a smaller tip radius than the one in the experiment. This suggests that our experiment is just at the limit where the Hertz model might be applied, whereas the size of the contact in the simulations falls below this limit.

k_{cont} versus F_N (as in Fig. 4.18) is then fitted with Equ. 4.2, the Young modulus $E_2 = E_{rad}$ being the only free fit parameter for each CNT. The elastic constants of the SiN tip are $\nu_1 = 0.27$ and $E_1 = 155$ GPa [181]. The Poisson ratio of the CNT is taken as $\nu_2 = 0.28$, a mean value of common materials. Obviously, any reasonable errors on ν_2 would have only a minor impact on the extracted E_{rad} and even less so on the variation of the modulus with the CNT radius. The obtained values of E_{rad} as a function of the CNTs external radius are reported in Fig. 4.20. The radial Young modulus, as previously observed for the radial stiffness, increases when decreasing the CNT radius. More precisely, E_{rad} increases sharply for R_{ext} smaller than 4 nm while it is almost constant and equal to about 30 ± 10 GPa for R_{ext} between 4 and 12 nm. This last value is, within the experimental error, equal to the Young modulus of graphite along its C-axis, $E_{graphite} = 36$ GPa [182]. For the CNTs studied in this work, R_{ext} is proportional to R_{int} , and both are proportional to the number of layers since the distance between layers is approximately constant [154]. Thinking to the elastic energy necessary to roll up a plane, we could deduce that the radial rigidity and hence E_{rad} of a CNT should increase by increasing the number of layers and by decreasing the internal radius. This is confirmed by measurements of radial deformations of CNTs due to van der Waals forces between the tube and the substrate [90, 183]. In both studies, the radial deformation increases with the radius for single-walled CNT and decreases with

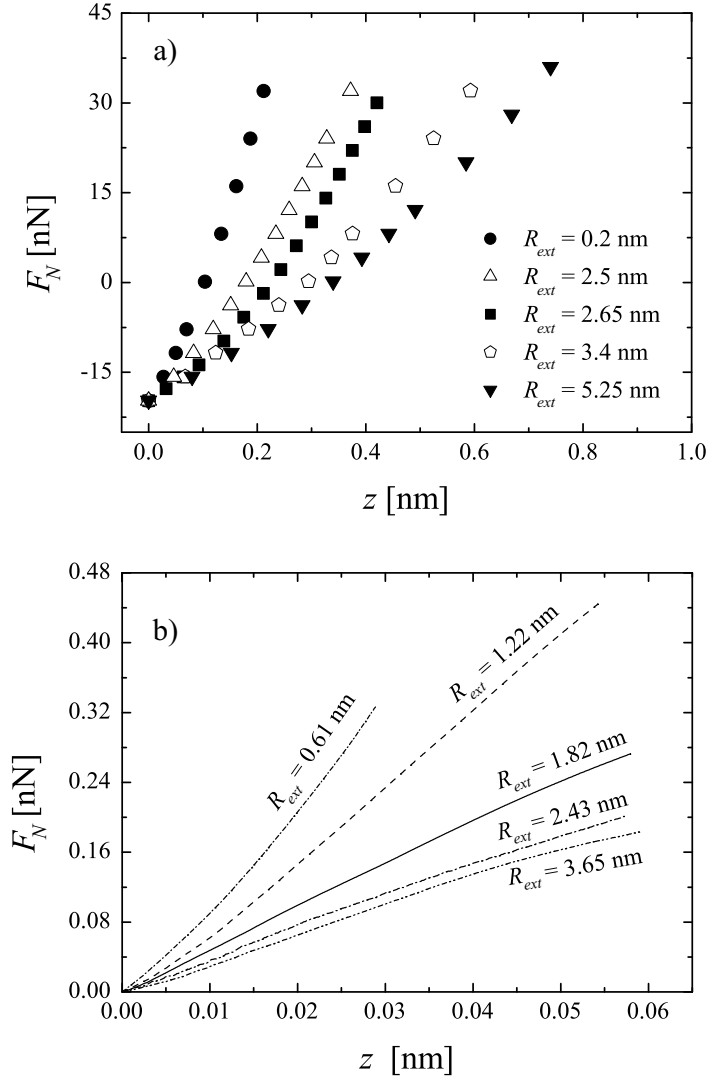


Figure 4.19: (a) Normal force as a function of indentation for CNTs of different radii, obtained by the integration of experimental $1/k_{cont}$ versus F_N curves using the trapeze method. (b) Theoretical normal force as function of indentation for CNTs of different radii (different numbers of layers), obtained by MD simulations of the indentation of a rigid sphere in a CNT.

the number of layers. Our experiments show that for small R_{int} , E_{rad} increases sharply by decreasing R_{int} ; we conclude that in this size range, the radial rigidity is controlled by the magnitude of R_{int} , whereas the number of layers plays a minor role. This result is in agreement with a previous theoretical study [154] that shows that the elastic properties of a CNT with $R_{int} = 0.34$ nm do not change by increasing the number of layers as long as the interlayer distance is fixed to 0.34 nm, i.e. the distance between planes in graphite. A similar finding is also obtained in the simulations of Ref. [90] where the radial deformation of a single-walled CNT is the same of a multi-walled CNT when the radius of the first one is equal to R_{int} of the second one. For large R_{int} , our experiments show that E_{rad} is almost constant. This could mean that the effect due to the increase of R_{int} is counter balanced

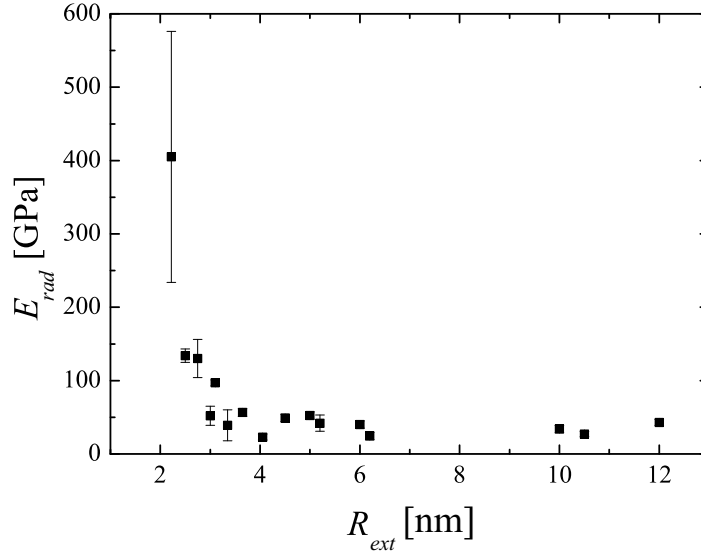


Figure 4.20: Experimental values of the radial Young modulus of CNTs as a function of R_{ext} as obtained from normal modulation experiments. Error bars correspond to mean errors on tubes of the same diameter. Errors due to the fit of k_{cont} versus F_N are included in the symbol size.

by the increase of the number of layers, up to the point at which CNT's properties reach asymptotically those of graphite. We believe that the behavior shown in Fig. 4.20 is not restricted to CNT with $R_{ext}/R_{int} = 2$, but it is expected for other ratios larger than 1 since the asymptotic value corresponds to the Young modulus of graphite.

The radial stiffness of multiwalled CNTs has been investigated experimentally by Yu *et al.* [132] and by Shen *et al.* [144]. In both cases, one CNT with an unknown number of layers is compressed, the maximum indentation distance being larger than 40% of the initial diameter. In Ref. [132], the force versus indentation distance curves are obtained through a model of the tip-CNT van der Waals forces. By interpreting these curves with the Hertz model they find, for a CNT with a diameter of 8 nm, a radial Young modulus between 0.3 and 4 GPa, which is roughly 1 order of magnitude lower than our results for CNTs of similar diameters. This discrepancy can be ascribed to a difference in the number of graphene layers forming the CNT, which is plausible since the CNT preparation techniques are different. The radial elastic modulus of CNTs obtained in Ref. [144], where the tubes are deformed up to the non-linear regime, is hardly comparable to our findings since its definition differs notably from the one exposed above.

In summary, we measured the radial stiffness and Young modulus of carbon nanotubes. They steeply decline with increasing radii, until the Young modulus takes on an asymptotic value of 30 ± 10 GPa for CNTs with $R_{ext} > 5$ nm. The experiments were performed with normal modulated nanoindentation on a statistically significant amount of CNTs with well defined external to internal radii. This trend is very well reproduced by force-indentation curves obtained by molecular dynamic simulations.

4.5 The tobacco mosaic virus

An interesting field of research in biotechnology concerns the biomolecules. Compared to other nanometer scale objects, biological molecules have generally the advantage to be entities easily reproducible, modifiable and functionalizable [110–112]. Their potential of being integrated to nanodevices or their use as nanotemplates have already kept the attention of researchers, using for example viruses as templates for producing nanowires [122]. Such promises in future nano-technological developments require a precise comprehension of the interaction between the biomolecules and other organic or non-organic structures. An ideal candidate to study these interactions is the tobacco mosaic virus.

The TMV is a well-known molecular system, which has interested virologists since the end of the 19th century, leading to the birth of the virology. This virus infects plants causing characteristic yellow-green patterns at the leaves and hindering the growth. Its availability and the fact that its genome has been completely characterized make it almost "the" ideal candidate for the study of the interactions between organic and non-organic surfaces [111], including its functionalization and its use as template. Moreover, this virus is only specialized for specific hosts like tobacco or tomato and does not infect mammals [184]. Thus, the safety measures that have to be taken in a laboratory are not too restricting compared to the precautions needed for other highly infective mammal diseases.

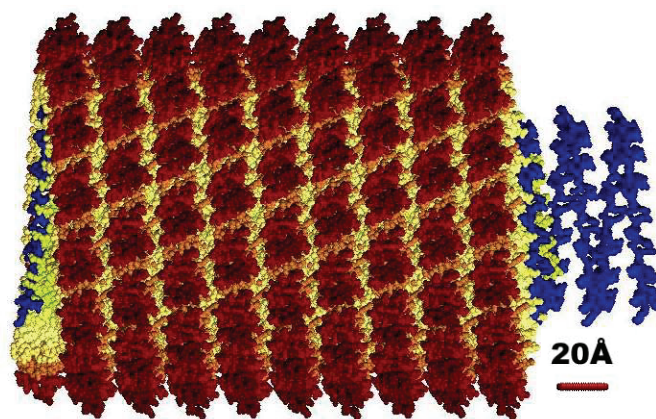


Figure 4.21: Part of a TMV. The RNA is represented in blue, embedded in the proteins forming the TMV shell (From Ref. [185]).

4.5.1 Description and characteristics

The TMV is a rigid rod-shaped virus of 300 nm of length for 18 nm of diameter, with a central channel diameter of 4 nm [186, 187]. It is composed of 2132 identical proteins bound to a helical single-strand of ribonucleic acid (RNA) [188]. Each protein has a molecular mass of 17.5 kDa and the helix formed by the RNA has a diameter of 8 nm with 16.3 protein units building up one turn for a total of 131 turns [189, 190]. Thus, the mass of one TMV is approximately $6.23 \cdot 10^{-20}$ kg. 95% of its mass comes from the proteins and about 5% is due to the RNA. The outer shell of the TMV is hydrophilic, whereas the inner shell is hydrophobic. Moreover, the electrostatic charges on the surface of the outer shell and in

the inner cavity depend on the pH surrounding the TMV. In fact, the amino acids of the TMV shell have different isoelectric points and thus, local charges are not identical everywhere in the virus for a given pH. However, it has been found that the global isoelectric point of the whole TMV is at pH 3.5 [191]. Below this value, the outer shell of the TMV is predominantly positively charged, whereas for pH higher than 3.5, the TMV outer shell becomes negative. In some pH, the outer and inner surfaces of the TMV can have opposite charges. The virus does not support high acidity ($\text{pH} < 2.8 - 3$ [189, 192]) and basicity ($\text{pH} > 10.5$ [192]), which cause the dissociation of the TMV particles leading to a separation of the RNA and the proteins. Nevertheless, the TMV presents a higher tolerance to pH variations than other viruses. Moreover, its chemical stability against solvents has also been proven. Indeed no structural changes were observed when adding to a water suspension of dry TMVs the following solvents: 2-propanol, tetrahydrofuran (THF) up to 30%, acetone, or DMSO (dimethylsulfoxide) up to 70% [123, 193]. Besides this chemical stability, the TMV supports also temperatures up to 80-90°C without decomposition or denaturation of the virion, and can survive frozen for years and infect again plants once unfrozen.

4.5.2 Possible applications

TMVs of a same type present exactly the same size and morphology, which becomes very interesting for their use as template for producing inorganic nanostructures. In addition, the TMVs tend to self-assemble end-to-end along their long axis or side-by-side depending on the experimental conditions of use. This feature has been attributed to the complementary electrostatics and hydrophobic interactions between the ends of the helical structure and the sides of the virion [194, 195], and might be a good way to create defined structures at solid surfaces. Thus, all these characteristics, well-defined structure, versatility and stability, make the TMV an ideal candidate for biotechnological applications. It has effectively already shown its ability to be used as template for chemical reactions resulting in metal-organic nanostructures (See Fig. 4.21). Shenton *et al.* [194] fabricated a whole range of hybrid nanotubular organic-inorganic composites by coating the outer surface of the TMV with inorganic nanoparticles and microstructures. Dujardin *et al.* [196] grew inorganic particles not only on the outer surface of the TMV, but also inside its hollow channel. It was thus possible to diffuse ions through the central channel during the mineralization process of the virus. This idea has been carried on by the authors of Ref. [122, 123] who used the central channel of the TMV for producing copper nanowires of 3 nm diameter and up to 150 nm in length by electroless deposition.

4.5.3 Experiments on TMV mechanics

While a lot of work has been done by modifying or using its chemical properties, few studies have tested its mechanical behavior when adsorbed on a surface. This knowledge on the TMV mechanical properties is important for the characterization of virus-based nano-templates, for in-situ control of nanostructure self-assembly, with the future aim to create nanostructurized conductive circuits [197–199]. A previous work on TMV mechanical properties reported that the diameter of TMVs adsorbed on an inorganic surface was probably related to the strength of the adhesion, explaining in that way the various diameter measurements of TMVs adsorbed on flat surfaces [123]. Another study based on the manipula-

tion of an individual TMV on a graphite surface gave rise indirectly to a first approximation of 1 GPa for its bending Young modulus [200]. For this estimation, TMVs were adsorbed on an atomically flat graphite surface. Then, using atomic force microscopy, the middle of the TMV was gently pushed from the side, tangentially to the substrate plane, to make it bend. Theoretically, three results are possible. First, if we suppose TMV internal forces stronger than the adhesion forces, then, by pushing the TMV, you will translate the whole TMV over the surface while it keeps its straight shape. On the contrary, and as a second result, if the adhesion forces predominate over the internal forces, then, by pushing it, you will either destroy the TMV or make it bend unelastically. Finally, the third possible result is related to the case where the adhesion forces are of the same order of magnitude as internal forces. By pushing the TMV at its middle, you will first make it bend elastically without any displacements of its ends, and then, if you continue to push it, you will translate the whole TMV while keeping a constant bending. When removing the action of pushing, the TMV should take at equilibrium a constant bending value. Nevertheless, in the previous work on manipulation of TMVs, the authors observed strong (up to 90°) and weak bendings of the TMVs for the same kind of manipulation and by supposing a flexural rigidity comparable to the substrate adhesion. Thus it was difficult to know if the elastic regime of the deformation was respected in each manipulation.

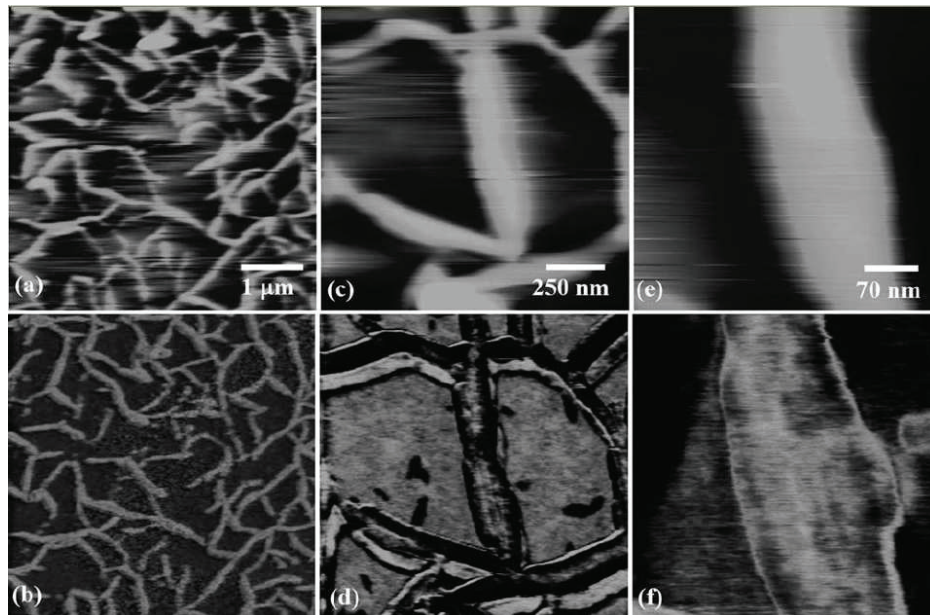


Figure 4.22: Images obtained by the authors of Ref. [201]: (a), (c) and (e) are surface topography of the adsorbed TMVs on the mica, whereas (b), (d) and (f) are the corresponding piezoresponse images.

Finally, a more recent study used a flexoelectrical method to measure a radial Young modulus of 1 GPa for a TMV lying on a mica disk [201]. The method is based on electromechanical coupling in TMVs, i.e. the linear coupling between the electric field and the strain applied to the virion. Such behavior is for example found for the cellular membranes, in which regions with smaller radius of curvature have higher dipole moments and hence stronger electromechanical response. The authors of Ref. [201] used an AFM working in

piezoresponse force microscopy (PFM) mode¹⁰ with an AFM tip radius of 80 nm to measure the piezoelectric/flexoelectric response of a continuous network of viral particles. The interpretation of the available information of the observed PFM contrast in terms of intrinsic electromechanical response of the material is not possible (See Fig. 4.22). Indeed, the use of relatively soft cantilevers and high PFM driving frequencies can give rise to a crosstalk between the topography and the PFM signal. In addition, the variations in the elastic properties between the virus and the substrate may disturb the measurement of the variations in the magnitude of the electrostatically driven tip oscillations. Finally, the theoretical model allowing the extraction of the Young modulus from PFM measurements relies on many unknown parameters that have to be approximated, leading to a rough estimation of the TMV Young modulus.

4.6 Experimental results on longitudinal elasticity of TMVs

In this section, we present quantitative measurements on TMV mechanics. We highlight the influence of the adhesion force on the shape of TMVs adsorbed on an inorganic surface, and then, by using a mechanical model of beam based on van der Waals forces, we evaluate the bending Young modulus from a sample of 16 TMVs lying above a hole on a porous polyimide (PI) membrane.

4.6.1 Experimental details

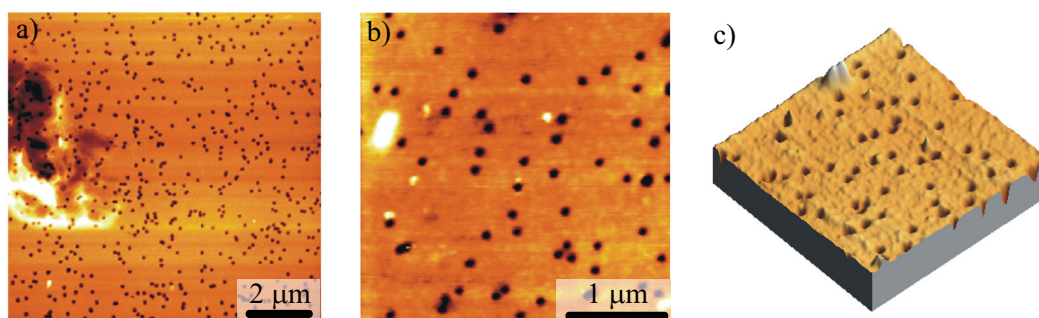


Figure 4.23: NCM AFM images of the ion beam track-etched porous polyimide membranes with pore width tuned by treatment with hot NaOH/H₂O. Pictures (a) and (b) illustrate the repartition of the pores over the surface, while (c) is a three-dimensional view of the latter.

We used ion beam track-etched porous polyimide membranes with pore width tuned by treatment with hot NaOH/H₂O as substrates¹¹. Figure 4.23 illustrates the pores density

¹⁰ A conductive AFM tip is used as top electrode and is brought into contact with the surface, while a voltage is applied between the scanning AFM tip and the surface. This method works well with ferroelectric thin films to differentiate the polarization domains. Indeed, the electric field generated in the sample causes the domains with the polarization parallel to the field to extend and the domains with opposite polarization to contract, while shear strain appears for the domains with a polarization vector perpendicular to the applied electric field. Then, the piezoelectric deformation is recorded via the torsion or bending of the cantilever.

¹¹ Best results were obtained by plunging the substrate in a suspension 6 M NaOH at 55°C for 2.5 minutes. Then the substrate was rinsed with pure water.

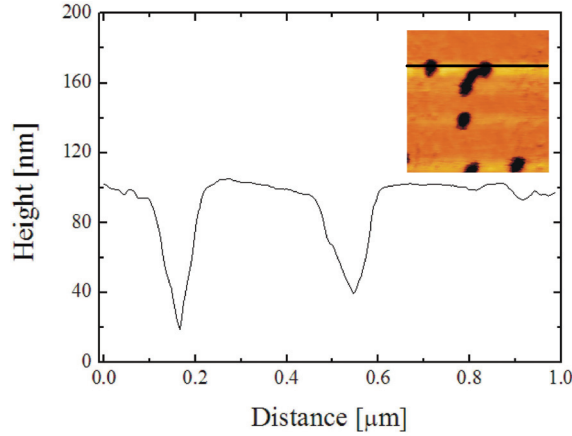


Figure 4.24: Profile of the topography obtained by NCM AFM along the straight line shown in the image of the inset.

and morphology obtained with this method. The pores diameter measures between 50 nm and 250 nm for depth variations between 15 nm and 80 nm as shown in Fig. 4.24. Due to the AFM tip-pore convolution, these dimensions are virtual measurements of the real pore geometry. Just before adsorbing the TMVs on the surface, the membrane was cleaned with oxygen plasma. Then we used 0.1 mg/ml of TMV suspension in water obtained from virus isolation of infected leaves of *Nicotiana tabacum* cv. Samsun nn plants with TMV *vulgare*¹². Solutions were sometimes mixed with acetone just before deposition on the surface to shorten the evaporation time. The water/acetone ratios were 1/3 or 2/3. No relevant changes were noticed by imaging TMVs coming from a water solution or a mixture of water/acetone. A droplet of the solution was deposited on the PI membrane until complete evaporation. Non-contact mode AFM¹³ was then used under ambient conditions to image the TMVs adsorbed on the surface. The AFM tip radius R_T was evaluated by considering simple geometric relations between the diameter D of the TMV and its apparent width w : $R_T = w^2/8D$ (See Fig. 4.13). Using this formula, we obtained a typical tip radius of 20 nm.

After the deposition of the TMV suspension, we obtained a non homogeneous repartition of the viruses over the surface, going from isolated TMV to aggregates of various sizes as illustrated in Fig. 4.25. We measured TMVs longer and also shorter than 300 nm, indicating their propensity for attaching each other head-to-tail or side-by-side and also a possible fragmentation of the TMVs during the procedure of deposition (See Fig. 4.25(c)). It was not possible to find by AFM the exact location of the bond for head-to-tail attraction. Such observations have already been reported in previous works on TMVs [112, 200, 202] and, as consequence, we have to keep in mind a probable presence of defects or locally weakened inter-subunit bonding in some proteins of the well-shaped TMVs. Nevertheless, we imaged

¹² *Nicotiana tabacum* cv. Samsun nn plants were mechanically infected using a TMV plasmid-DNA. 4 weeks post inoculation, systematically infected leaves were harvested and stored at -20°C. The TMV particles were isolated using centrifugation in CsCl or sucrose gradients, yielding to 10 mg/ml TMV suspensions in water which were stored at 4°C. In some cases, the water was replaced by Na-K-phosphate buffer (pH 7) prepared from 10 mM Na₂HPO₄ + 10 mM KH₂PO₄. More details on TMV suspension preparation and TMVs binding to inorganic surfaces are given in Ref. [123].

¹³ Autoprobe CP2, M5 and Molecular Imaging AFM have been used to image the adsorbed TMVs.

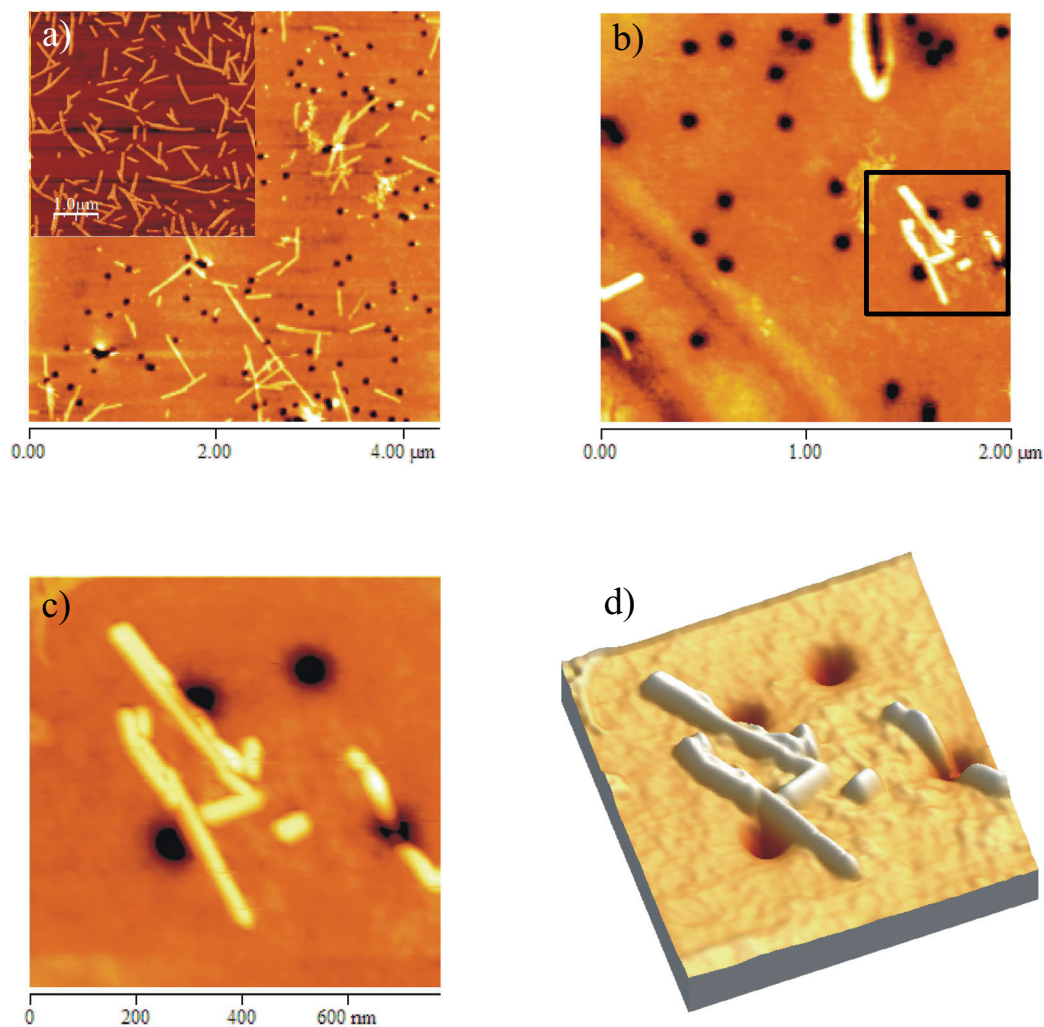


Figure 4.25: NCM AFM images of TMVs adsorbed on the PI membrane. The inset in picture (a) shows TMVs adsorbed on a silicon oxide surface. Image (c) was obtained by zooming in the area surrounded by a square in (b). Picture (d) presents a three-dimensional view of (c).

many TMVs having the correct dimension of 300 nm length.

4.6.2 Results and discussion

The first idea to study the mechanical properties of TMVs was to find TMVs hanging like beams over some pores of the porous surface and to apply a normal load at the middle of the TMV beam using the AFM tip. Unfortunately, this kind of experiment was not possible with the TMVs, although the method has been successfully applied to other organic tubular structures such as microtubules [135]. Indeed, applying a normal load to the tubular structure of the TMV while hanging over a pore either deforms it unelastically, either breaks it. This fragility of the TMV is illustrated in Fig. 4.26 for a TMV lying on a flat surface. Furthermore, imaging TMVs in contact mode while decreasing the normal force leads to the jump out-of-contact of the tip before obtaining precise and stable images of the virus. Thus, it

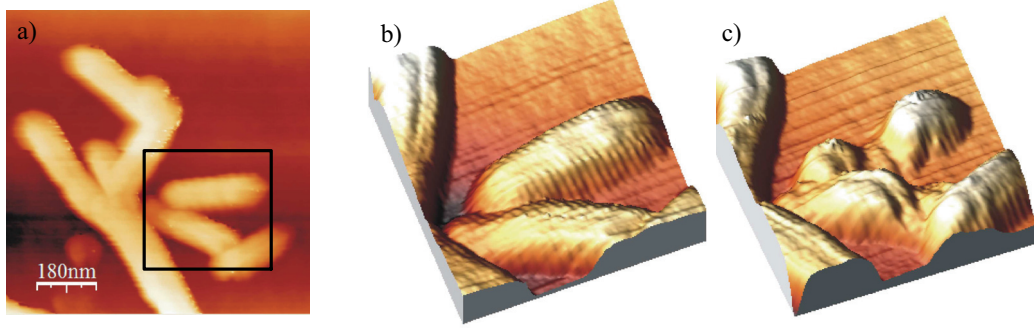


Figure 4.26: NCM AFM images of TMVs adsorbed on the PI membrane. Images (b) and (c) are enlargements of the area surrounded by a square in image (a). In the image (b) we observe a well shaped TMV lying on the surface. The same TMV presented in image (c) shows a plastic deformation resulting from the contact of the AFM tip with the middle of the TMV.

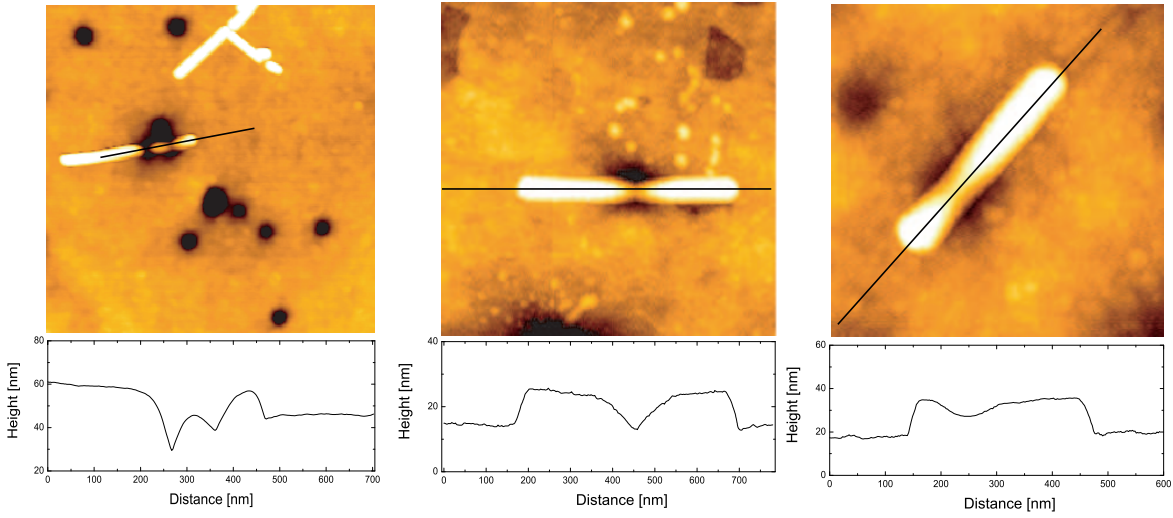


Figure 4.27: Images of TMVs lying on the porous polyimide membrane and corresponding height profile for the selected TMVs.

was really difficult to find the frontier between elastic and plastic deformation of the TMV, and, as major consequence, contact mode AFM was not reliable to measure the mechanical properties of hanging TMVs.

The second idea was to image the TMVs using NCM AFM, to measure their deflections and finally to use the continuum mechanical model presented in Section 4.2.2 to extract their bending Young modulus. This theoretical model needs an evaluation of the forces loading the TMV. For this, we considered a discrete gradient of normal forces due to van der Waals attractions between the TMV and the walls of the pore. In this model, the forces arising from the gravity are neglected since the order of magnitude of the gravity force acting on the middle of a suspended TMV is 10^{-19} N, whereas forces due to vdW attractions are of the order of 10^{-13} N.

Depending on the diameter of the pores, the bridge formed by the TMV adopts different

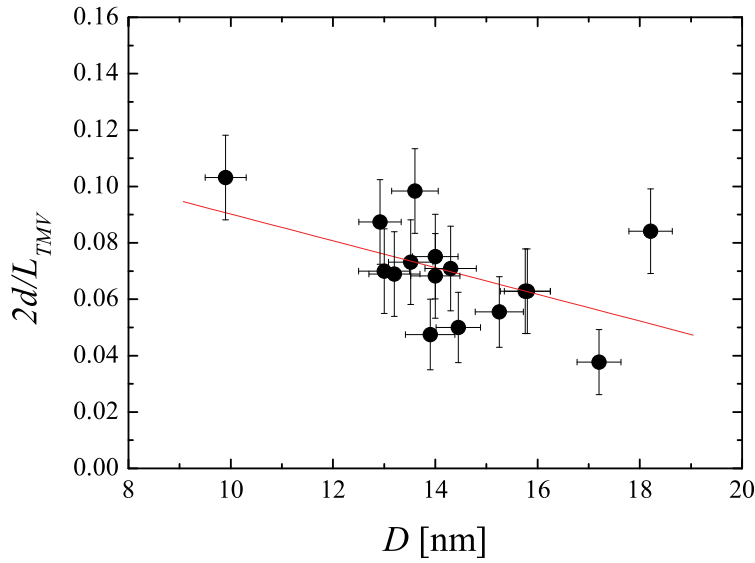


Figure 4.28: TMV diameters in function of $2d/L_{TMV}$ with the outgoing tendency highlighted by the linear fit (straight line).

configurations as illustrated in Fig. 4.27. For holes with a diameter approximately inferior to 140 nm, the TMV hangs like a rope characterized by a convex shape of bending. For holes between 140 nm and 200 nm, the bridge formed by the TMV corresponds to two concave parts joined in the middle. And finally, for bigger holes, the TMV is usually broken and attached to the wall of the well. This kind of behavior indicates either a really strong adhesion of the TMV to the PI substrate and/or a great fragility of the tubular structure of the virus. These observations are in agreement with previous experimental studies on TMV imaging with contact mode AFM [123].

The mean value of the TMV diameters for our selected bridges was 14 nm, with 10 nm for the smallest tube and 18.2 nm for the biggest one. Figure 4.28 shows a correlation between the tube diameter D and its bending properties given by the ratio of $d(y = L/2)$, the maximum suspension depth, and $L/2$, half the bending length of the TMV. The outgoing tendency is that tubes with a small radius are the more flexible in bending. If we suppose that the loading force, mainly due to vdW forces, is sufficiently homogeneous over the whole surface, this result would highlight a discrepancy for the tube rigidities while submitted to a load that is almost constant over the whole sample of pores. However, it seems that the adhesion of the TMV to the surface do play a more important role. It is found in the literature that TMV diameters vary from 9 to 23 nm depending on which surface the TMVs are adsorbed [123, 200, 203–207]. Thus, the direct interaction of the TMV with the surface may modify the cylindrical shape of the TMV, explaining why TMVs with diameters of 18 nm are generally easy to slide on the surface using contact mode AFM, whereas TMVs with small diameters are destroyed before any displacement due to a stronger adhesion. In our case, the interaction between the TMV and the surface is highlighted by the measurements

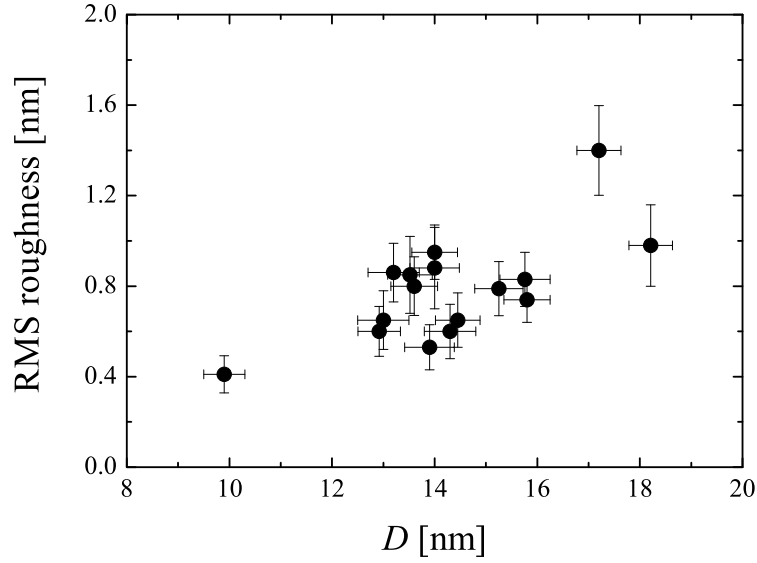


Figure 4.29: Relation between the TMV diameters and the surface roughness measured in the close proximity of the tube.

of the surface roughness versus the tube diameter as shown in Fig. 4.29. TMVs adsorbed on flat areas of the PI membrane are submitted to stronger vdW forces than TMVs lying on rough areas. As result, the TMV adsorbed on a flat surface has a smaller diameter and a larger bending than TMVs adsorbed on rough surfaces. In our estimation of the bending Young modulus, the roughness surrounding each TMV has been measured and serves as input value in the theoretical model through the parameter h as explained in Section 4.2.2.

We chose a sample of 16 TMVs lying at different locations on the PI membrane so that the final value obtained for the Young modulus corresponds to a mean value of the TMV elastic properties. Once the geometry of the suspended TMV has been measured, it is then necessary to estimate the loading gradient of vdW forces acting on the beam.

Evaluation of the vdW forces

We calculated the vdW forces acting between the TMV and the polyimide substrate using a microscopic approach. We represented the TMV as a cylinder of molecular density ρ_A and the pore of the polyimide membrane as two semi-infinite flat surfaces of molecular density ρ_B , having the same height and separated by a gap as illustrated in Fig. 4.30. In this configuration, the pores have steep walls perpendicular to the horizontal surface of the membrane. We worked under the classical assumptions of additivity of the interaction forces, continuous medium and constant material properties. As told before, we neglected the gravity force that does not enter into consideration at this scale and we admitted a perfect symmetry of our system. The potential energy arising from the interaction of a molecule A of the TMV with a molecule B of the membrane is commonly given by [2]

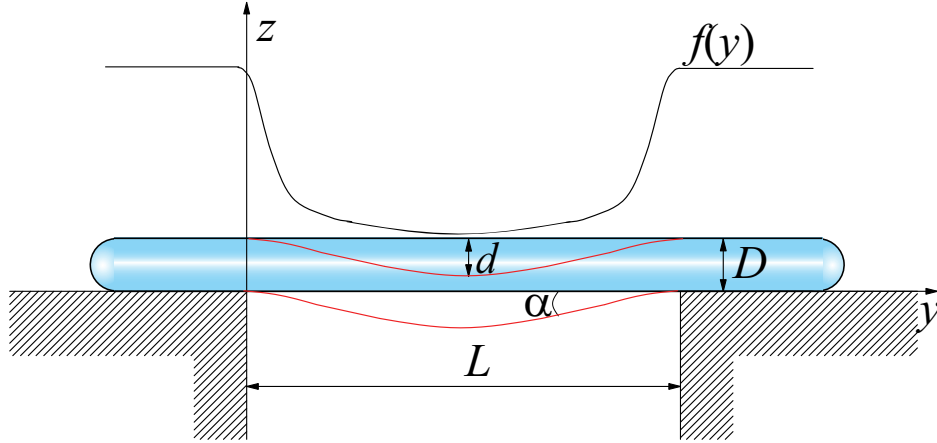


Figure 4.30: Model of a TMV lying over a pore schematically represented by two semi-infinite corners. The action of the vdW forces on the TMV median line along the z direction is represented by the gradient of force $f(y)$.

$$W_{AB}(r) = \frac{-C_{AB}}{r^6} \quad (4.11)$$

where r is the intermolecular separation, C_{AB} is related to the contributions of the dipole-dipole interactions due to Keesom, Debye and London forces, and finally, the minus sign refers to an attractive force.

The first step is to determine the van der Waals energy between one molecule A of the TMV and all the molecules B forming the volume of one of the semi-infinite corners of the gap (See Fig. 4.31). Practically, this is done via an integration of the molecular density ρ_B over the entire volume V of the semi-infinite corner. The expression we obtained for the energy $W_{A-corner}$ depends only on y and z , due to the symmetry of the problem:

$$\begin{aligned} W_{A-corner}(y, z) &= -C_{AB} \cdot \int_{t=-\infty}^{\infty} \int_{u=-\infty}^0 \int_{v=-\infty}^0 \frac{\rho_B dV}{(r'(x-t, y-u, z-v))^3} \\ &= \left(-\frac{\pi}{12y^3} - \frac{\pi}{12z^3} + \frac{\pi y}{12z^3 \sqrt{y^2 + z^2}} \right. \\ &\quad \left. + \frac{\pi}{24yz \sqrt{y^2 + z^2}} + \frac{\pi z}{12y^3 \sqrt{y^2 + z^2}} \right) C_{AB} \rho_B \end{aligned} \quad (4.12)$$

where $r'(x-t, y-u, z-v)$ is the distance between the molecule A of the TMV and a molecule B in the semi-infinite corner with the respective cartesian coordinates (x, y, z) and (t, u, v) . $dV = dt du dv$ is the infinitesimal volume of integration. The second step concerns the estimation of the vdW forces acting on the entire volume of the TMV. The negative derivative of the energy $W_{A-corner}$ versus y and z (Equ. 4.12) gives the forces dF_y and dF_z , exerted by the whole corner on a molecule A of the TMV. From now, we will consider only the infinitesimal force dF_z that is interesting in measuring the bending behavior of the TMV. Using the symmetry of our problem, the total vdW force dF_z acting along z on one molecule of the TMV is given by

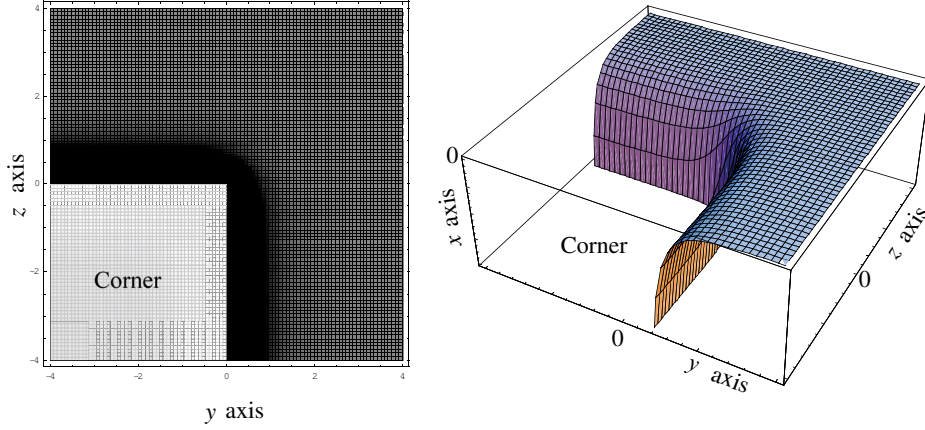


Figure 4.31: Schematic representation of the density plot (left image) and three-dimensional plot (right image) of the vdW energy between one molecule A of the TMV and all the molecules B forming the volume of one of the semi-infinite corners of the gap.

$$dF_Z(y) = dF_z(y) + dF_z(L - y) \quad (4.13)$$

where $dF_z(L - y)$ is the contribution of the second corner. Due to these infinitesimal forces, the TMV is bending at equilibrium according an angle α as shown in Fig. 4.30. Using cylindrical coordinates, we estimated the discrete force $F_Z(y)$ acting on the mass center of TMV sections positioned in y and of thickness dy by integrating dF_Z on each molecule of the sections. dy was chosen equal to 4 Å. Taking smaller values for dy induced negligible changes (inferior to 0.3%) on the final estimation of the bending Young modulus of the TMV. By this way, we obtained a discrete gradient $f(y)$ of forces F_i acting on the center of the TMV sections and that becomes continue in the limit of $dy \rightarrow 0$, as schematically illustrated in Fig. 4.30. The critical case where $y \rightarrow 0$ was avoided by taking into account the RMS surface roughness h measured experimentally at the edge of the corners for each TMV. Practically, the discrete division and the integration was done for $h < y < L - h$ by steps dy , with a RMS roughness varying between 0.4 – 1.4 nm. Following this procedure, we obtained a discrete representation of mean vdW forces F_i acting on the center of mass of the TMV sections (See Fig. 4.8) and proportional to the quantity $\rho_A \rho_B C_{AB}$ that is a characteristic of the matter in presence:

$$\begin{aligned} f(y) &= F_Z(y_{i-1} + \frac{dy}{2}) = F_i \quad \text{for } y_{i-1} \leq y < y_i \text{ and with} \\ y_0 &= h; \\ y_i &= y_{i-1} + dy; \\ F_i &\propto \rho_A \rho_B C_{AB}; \end{aligned} \quad (4.14)$$

Thus, we have obtained an analytical expression of the gradient of forces characterizing the action of the corner on the TMV. We have still to determine the quantity $\rho_A \rho_B C_{AB}$. For this, we considered a TMV lying on a flat part of the polyimide membrane and we deduced $\rho_A \rho_B C_{AB}$ from measuring experimentally its adhesion force corresponding to the total vdW

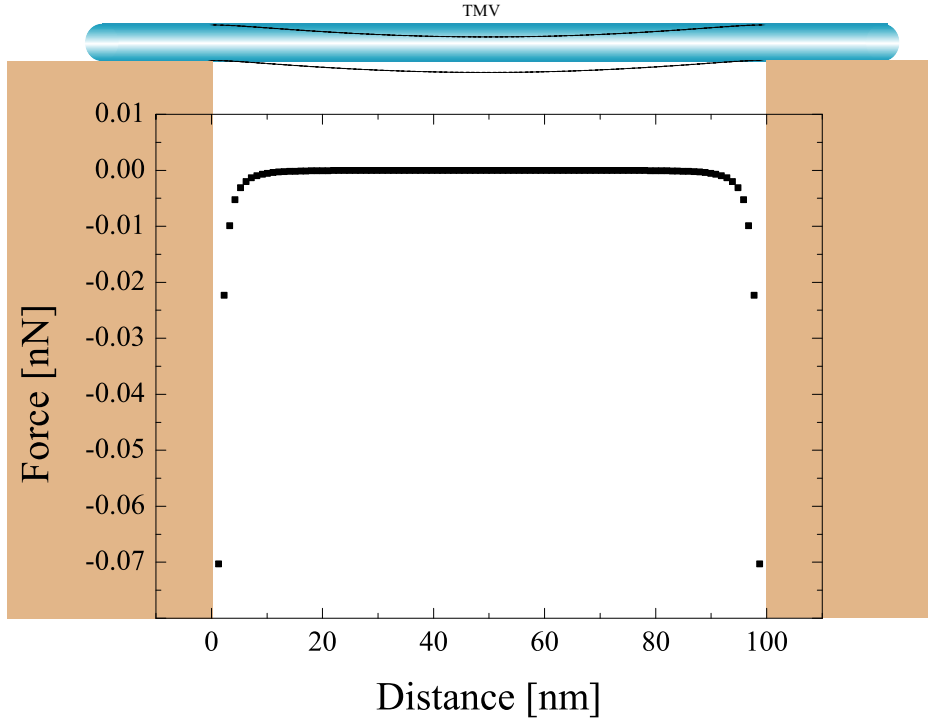


Figure 4.32: Gradient of vdW forces acting on a TMV hanging over a hole as schematically represented in the top image. This gradient of forces has been obtained by solving the TMV nanobeam problem taking into account vdW forces. The input parameters necessary to solve this problem are the suspended length (100.3 nm), the deflection at the middle of the TMV ($d(L/2) = 3.2$ nm), the tube diameter (14.5 nm) and the surface roughness (0.8 nm). The dashed lines represented in the top TMV image are the deflection versus distance of the TMV beam as obtained with our model.

forces evaluated with a theoretical model analogous to the previous one. The total energy $W_{A-flat\ surface}$ due to the vdW forces acting on a molecule A of the TMV is given in this case by letting u aim to plus infinity in Equ. 4.12, and the force $F_{A-flat\ surface}$ is then derived from the energy. We obtain:

$$W_{A-flat\ surface}(z) = -\frac{\pi\rho_B C_{AB}}{6z^3} \quad (4.15)$$

and

$$F_{A-flat\ surface}(z) = -\frac{\pi\rho_B C_{AB}}{2z^4} \quad (4.16)$$

Again, the integration of $F_{A-flat\ surface}$ over the whole molecules of the TMV leads to a total force $F_{TMV-flat\ surface}$ acting along z at the centre of mass of the TMV. This force corresponds to the adhesion force of the TMV to the PI membrane, and, like the discrete forces calculated in the case of the corner, it depends on the quantity $\rho_A\rho_B C_{AB}$. An important parameter in the theoretical evaluation of the vdW force for the TMV lying on the flat surface is the distance of integration h_{ts} between the bottom of the TMV and the surface. We choose $h_{ts} = h$, the RMS surface roughness measured around the TMV to be consistent with the mathematical development described before.

Then, we characterized experimentally the order of magnitude of the adhesion force of the TMV to the flat surface by using contact mode AFM in ambient conditions (with low humidity environment to avoid capillary effects). We consider a typical TMV of 14 nm diameter, which means that its section forms an ellipse of major and minor axes a and b with respective dimensions $a = 10.8$ nm and $b = 7$ nm. The a -axis is parallel to the surface as illustrated in Fig. 4.33. We estimated the contact area of the TMV with the surface by considering the points of the elliptic section that are close to the surface (within ~ 1 nm) and for which the interaction with the surface results in the adhesion force. This gives rise to a contact width $w \sim 11$ nm. Note that the surface roughness will give rise to a real contact area with a corresponding width smaller than 11 nm.

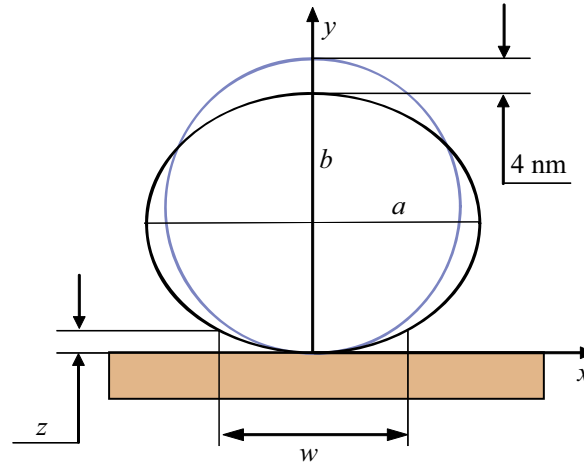


Figure 4.33: Approximation of the contact area between the TMV and the surface by considering an elliptic TMV section. The circle corresponds to the natural shape of the TMV with a diameter of 18 nm. The ellipse is the probable shape of the TMV submitted to strong adhesion forces. From geometric considerations, for $z = 1$ nm, the contact width w equals ~ 11 nm.

Using an AFM mounted with low normal spring constant cantilevers, we measured at which friction force it was possible to move a TMV or parts of TMV over the surface. In this work, we will suppose that the measured friction force used to move a TMV is close to the real adhesion force of the TMV to the surface, or have at least the same order of magnitude. We measured friction forces F_F in the range of 5 nN for a contact area of typically 100 nm^2 , which is consistent with adhesion force measurements between proteins and organic surfaces in other AFM experiments [208–210]. It has to be noticed that the TMV often disappeared from the surface while imaging (it probably stuck to the tip) even for extremely low normal forces (less than 1 nN for a pull-off force at 0 nN), and other times, the TMV was partially destroyed by the tip before any displacement, showing a stronger adhesion. The adhesion force was obviously not a constant value for all TMVs and our friction force, estimated to $f_f = 0.5$ nN per unit length l_{TMV} [nm] of TMV, is an intermediate value between weak and strong adhesion. Unfortunately, this rough estimation is a critical parameter in the determination of the final bending Young modulus. Finally, the equality between the vdW forces integrated over the volume V_{TMV} of the TMV and the experimental measurement of the adhesion force through the friction force F_F leads to:

$$F_{TMV-flat surface} = - \int_{V_{TMV}} \frac{\pi \rho_A \rho_B C_{AB}}{2z^4} dV = f_f l_{TMV} \quad (4.17)$$

The only unknown in Equ. 4.17 is the quantity $\rho_A \rho_B C_{AB} = A_H/\pi^2$, where A_H is the Hamacker constant. By this method, the order of magnitude of the Hamacker constant of our system has been evaluated to 10^{-20} J that is in agreement with the value of common materials [4, 211–216]. Thus, friction measurements served as "calibration method" to evaluate the vdW forces F_i acting between the TMV and the surface. Figure 4.32 illustrates a force gradient $f(y)$ obtained by this method for a system with the following characteristics: a suspended length of 100.3 nm, a deflection $d(L/2) = 3.2$ nm, a tube diameter of 14.5 nm and a surface roughness of 0.8 nm.

Bending Young's modulus of TMVs

Combining the mechanical model of beam described in Section 4.8 with the experimental evaluation of the forces F_i by means of friction measurements of the adhesion force of the TMV to the PI membrane, it has been possible to evaluate the bending Young modulus of a selection of 16 well shaped TMVs hanging like ropes over the PI holes. We measured for each tube the suspended depth $d(L/2)$, the length L , the diameter D and the RMS roughness h of the surface surrounding the tube. The problem was solved numerically as the mathematical expression cannot be integrated analytically. We obtained finally a Young modulus equals to 3.1 ± 0.1 MPa characterizing the bending property of the TMV for a standard deviation of 0.56 MPa. The small error on the Young modulus value indicates a similar elastic behavior for all the TMVs once the roughness and the tubes diameter have been taken into consideration in the model. On the other hand, the effect of a bad evaluation of the adhesion force through friction measurements is not considered in the error. Its effect would be a shift of the result to higher values if the adhesion force has been underestimated.

Comparable values of Young modulus have been found on experiments on soft biological materials. In a similar experiment, Murein sacculi from *Escherichia coli* K-12 have been suspended over a narrow groove and an AFM tip has been used to mechanically and elastically bend it [217]. Elastic moduli of 25 MPa were measured in the hydrated state, in agreement with theoretical calculations. Another work on the green alga *Enteromorpha* measured a Young modulus of 0.5 MPa for its adhesive glycoprotein [218] and a study on the local elasticity of microbial cells measured Young modulus values of 0.6 MPa for the mother cell surface and 6.1 MPa for the bud scar [219]. Those works based on AFM measurements confirm the order of magnitude of 10^6 Pa found for the rigidity of soft biological matter. Biological materials present of course also higher rigidities, and values of Young modulus are spread out from 10^6 Pa to 10^{10} Pa highlighting the great variety of structures and forms of our environment [220].

In summary, we used non-contact mode AFM in air to image TMVs adsorbed on a porous polyimide membrane. We highlight the behavior of soft biological material of these viruses by characterizing their rigidity. We used a clamped-beam mechanical model to extract the Young modulus of TMVs suspended like ropes over the pores of the membrane. We found a mean value of 3.1 MPa for their bending Young modulus, a value in agreement with other experiments on soft biological material.

4.7 Conclusion

The nanotechnology has the potential to transform technological domains such as electronics, micro mechanics or medicine by offering new functional materials and structures with unique properties. Nanometer sized objects reveal indeed physical and chemical properties that differ largely from the behavior of the bulk material. The exploitation of such low dimension objects and structures in technological applications requires an accurate understanding of their behaviors under various physical and chemical environments [221].

In this last chapter, small tubular structures have been elastically stressed to measure quantitatively their resistance against deformation in a particular direction, i.e. their Young modulus. By means of a normal modulated nanoindentation method based on atomic force microscopy, we found a radial Young modulus strongly decreasing with increasing radius and reaching an asymptotic value of 30 ± 10 GPa for multiwalled carbon nanotubes. At the opposite, the tobacco mosaic virus, that is very similar in shape and size to the carbon nanotubes, showed an extreme softness under bending, giving rise to a bending Young modulus of 3.1 ± 0.1 MPa. For both tubular structures, mechanical models based on continuum mechanics were used to extract the value of Young modulus from experimental data of tube deformation. Thus, the extremely stiff carbon nanotube and the very soft tobacco mosaic virus have bending moduli that differ from a factor 10^6 , since the order of magnitude of the bending Young modulus of CNTs is the TPa. This difference illustrates the great variety of properties that may be found in the nanoworld for similar structures and, by the same way, their large field of applications.

General conclusions

THE SUBJECT of this thesis was directly related to phenomena occurring at the nanometer scale, where atomic interactions are non-negligible. It was divided in two main parts. The first part dealt with the sliding friction of a nanoscopic AFM tip on hydrophilic surfaces, whereas the second part was related to the deformation of hard and then soft hollow cylinders that are respectively the multiwalled carbon nanotubes and the tobacco mosaic viruses.

For the first part, the sliding friction of an AFM tip on a CrN surface was studied as function of the scanning velocity for different applied normal loads and relative humidity levels. We observed a logarithmic dependence of the friction force on the scanning velocity. The transition from a positive to a negative slope of the friction force versus the logarithm of the scanning velocity was highlighted by varying the relative humidity of the surrounding environment of the AFM tip-surface system. A theoretical model, based on Tomlinson theory and including the effect of the capillary forces, was developed to explain our experimental observations. This model describes the friction as a phenomenon where two distinct regimes are playing depending on the humidity level: at high relative humidity, the capillary forces dominate, whereas at low relative humidity, solid-solid forces govern the friction behavior. From the competition between the solid-solid forces and the capillary forces results the dependence of the friction force on the scanning velocity, or, in other words, its temporal dependence. The condensation of capillary bridges in the interstices of the tip-surface contact has also been investigated by means of AFM friction studies on rough glass surfaces. We found a two-thirds power law dependence of the capillary force as function of the normal load. We traced back this behavior to the load induced change of the tip-surface contact area, which determines the number of asperities where the capillary bridges can form. An analytical relationship was derived from Hertz theory and fully explains the observed interplay between humidity, velocity, and normal load in nanoscopic friction.

For the second part, the behavior of multiwalled carbon nanotubes and tobacco mosaic viruses under some constraints has been studied. These structures were elastically stressed to measure quantitatively their resistance against deformation in a particular direction, i.e. their Young modulus. Carbon nanotubes were adsorbed on a silicon oxide surface and then imaged with an AFM. The experiments were performed with modulated nanoindentation and on a statistically significant amount of CNTs with well-defined external to internal radii. Using a theoretical model based on Hertz theory, we found a radial Young modulus strongly decreasing with increasing tube radius and reaching an asymptotic value of 30 ± 10 GPa. This trend was very well reproduced by MD simulations.

While similar in shape and size, the tobacco mosaic virus showed an elastic behavior at the opposite of the carbon nanotubes. The viruses were adsorbed on a porous polyimide membrane and imaged by means of AFM in non-contact mode. Viruses hanging like ropes over some pores highlighted the softness of these tubes. A theoretical model based, on the one hand, on the experimental measurement of the adhesion of the viruses to the surface, and, on the other hand, on the continuum mechanics of clamped beam, has been developed to extract their bending Young modulus from measurements of their depth suspension. We obtained a bending Young modulus of 3.1 ± 0.1 MPa in agreement with other studies on soft biological structures.

The difference in elastic properties of similar tubular structures like the tobacco mosaic virus and the carbon nanotube highlights the great diversity of the properties of the nanostructures. It is thus necessary to enlarge our knowledge on their properties and to understand their behaviors under various surrounding environments if we want to optimize their applications. In fact, we are now just at the beginning of the possible applications of the nanotechnologies to everyday life. The promises of advances across electronics, medicine, communications, genomics, and robotics, seem innumerable, but all the techniques leading to a concrete application of the new technologies of the infinitely small are still not under complete control. For many fields of the nanotechnologies, we are more observers than actors, still being surprised by the ability of the nature in synthesizing fine and elegant nanostructures in ambient temperature, while we have to use high pressure and/or high temperature. Nevertheless, the tendency is gently changing. The future developments at an industrial level of nano-objects with specific physical and chemical properties chosen in function of their applications will probably have a strong economical and social impact on the human being, notably for diseases treatments where nanotechnologies already afford novel techniques such as the intracellular imaging through attachment of quantum dots or synthetic chromophores to selected molecules [222].

Although wide benefits emerge from the nanotechnologies, we have also to keep in mind that the toxicology of many nanomaterials has not yet been fully evaluated. An example is the use of DNA for the size separation of carbon nanotubes. The DNA strand just wraps around the carbon nanotube when its diameter has the right value. Such a purpose is excellent for the size separation of carbon nanotubes, but in return, it may result in some concerns over the consequences of carbon nanotubes entering the human body [222]. Thus, while nanotechnology promises many solutions related to health care or energy saving based for example on low weight high strength materials, it remains important to develop at the same time the knowledge of their impact on our environment and for this, it is important to characterize as accurately as possible each nanomaterial.

Appendix A

CNTs elasticity: an overview

- * Treacy *et al.* [138] estimated the bending Young modulus of isolated MWCNTs by measuring their thermal vibrations using TEM. They obtained an average Young modulus of 1.8 TPa with a decreasing value for decreasing tube diameter.
- * Falvo *et al.* [167] demonstrated the extraordinary strength of CNTs by observing reversible, periodic buckling of CNTs under large strains. Their results were confirmed by continuum mechanics.
- * Wong *et al.* [128] measured the mechanical properties of one end clamped MWCNTs and silicon carbides nanorods. The MWCNTs were about two times as stiff as the nanorods and they found a mean value of 1.3 TPa for their bending modulus .
- * Krishnan *et al.* [223] determined the bending Young modulus of freestanding SWCNTs by observing their room-temperature resonance in a TEM. They found an average value of 1.25 TPa demonstrating that CNTs have both high modulus and high strength, which makes them superior to conventional carbon fibers that have only either high modulus or high strength.
- * Walters *et al.* [129] tested with an AFM in lateral force mode the elastic strain of suspended single-walled CNT ropes. The ropes were pinned beneath metal pads on an oxidized silicon surface and then released by wet etching. They obtained a tensile strength of 45 GPa for the ropes at the maximum strain, assuming a value of 1.2 TPa for the SWCNTs.
- * Salvétat *et al.* [130, 145, 146] measured the Young modulus of SWCNT ropes and MWNTs in a series of experiments where the tubes were adsorbed on a porous surface leading to the configuration of clamped beam. They obtained a bending Young modulus of 1 TPa for the ropes (1 GPa for their shear modulus) with a decreasing Young modulus for decreasing rope diameter and 10-50 GPa for disordered MWCNTs, whereas 810 GPa were found for structurally ordered MWCNTs.
- * Poncharal *et al.* [139] determined also the bending Young modulus of freestanding MW-CNTs. The nanotubes were directly excited using an AC electric field and vibrations were observed using a TEM. They found that nanotubes with diameters below 10 nm show a typical stiffness value of 1 TPa, while it dropped to 100 GPa for larger tube diameters.
- * Yu *et al.* [131] tested the tensile strength of individual MWCNTs. The MWCNTs were mounted between two opposing AFM tips and attached at both ends by electron beam

deposition. Using high-magnification SEM and AFM principles, they measured the tensile-loading properties of their system and deducted Young moduli of 19 MWCNTs. The obtained value for the Young modulus of the outermost layer varied from 270 to 950 GPa. The same kind of experiment was done with SWCNTs ropes in agreement with previous results [224].

List of Figures

1.1	Ideal and real crystal	4
1.2	Coulomb and Keesom interactions	7
1.3	Contact Angle	9
1.4	Capillary bridge	10
1.5	Capillary geometry	11
1.6	Stress field on a body	12
1.7	Transverse isotropic solid	14
1.8	Hertz model	15
1.9	Contact theory	19
1.10	Contact models	20
2.1	AFM working principle	25
2.2	Cantilever shapes	26
2.3	Torsion and bending in AFM	27
2.4	Force-distance curve	28
2.5	Change in the resonance frequency for NC-AFM	30
2.6	FMM technique	31
2.7	Lateral force principle	31
2.8	Friction loop principle	32
2.9	Forces experienced by a AFM tip	33
2.10	Cantilever geometry	34
2.11	Tip-surface convolution	36
2.12	Tip shape characterization	37
2.13	Scanner artifacts	38
2.14	Calibration grating	38
2.15	Normal bending	39
2.16	Torsion of the cantilever	40
2.17	Lateral sensitivity calibration	41
2.18	FEM method	43
2.19	Influence of the laser position on the calibration	44
2.20	Electron beam interactions with the surface	46
2.21	TEM and SEM principles	47
2.22	Static and dynamic behavior of a droplet	48
2.23	Experimental contact angle	49

3.1	Micro asperities	53
3.2	Stick-slip phenomenon	56
3.3	Tomlinson geometry	57
3.4	Tomlinson model	58
3.5	Superlubricity on graphite	60
3.6	Superlubricity and modulation of the tip-surface sample	61
3.7	Forces acting on the AFM tip	65
3.8	Modified Tomlinson model	66
3.9	Illustration of the theoretical model of F_F versus $\ln v$	69
3.10	F_F versus $\ln v$ for different RH and F_N	70
3.11	Deduction of the effective spring constant k from friction loops	71
3.12	Transition from decreasing to increasing friction	73
3.13	Changes in friction slope	74
3.14	Water molecule and properties	76
3.15	Capillary forces and sand castle	76
3.16	Capillary bridge geometry	77
3.17	Capillary water bridges and Kelvin radius	79
3.18	Contact area for capillary water bridges	80
3.19	F_F versus F_N at different scanning velocities	81
3.20	Friction dependence on F_C and $\ln v$	82
3.21	F_F versus $\ln v$	82
3.22	F_C versus F_N : 2/3 power law dependence	83
3.23	Extraction of friction fitting parameters	84
3.24	Validation of the theoretical model	85
4.1	Biological nanostructure	88
4.2	Example of fullerenes	89
4.3	Example of nanowires	89
4.4	Nanobelts under different geometries	90
4.5	TMV used as template	91
4.6	Normal modulated nanoindentation	93
4.7	Normal and lateral modulation	94
4.8	Representation of a clamped TMV.	95
4.9	Representation of the stress-strain on a beam.	96
4.10	CNT as wrapped graphene sheet	97
4.11	CNT chirality	98
4.12	CVD method	99
4.13	Tip-tube convolution	101
4.14	External to internal CNT radii	102
4.15	CNT morphology	103
4.16	Problems arising from CNT imaging	104
4.17	MD simulation of indenting a CNT with a sphere	105
4.18	k_{cont} versus F_N	106
4.19	F_N versus the indentation distance z	107
4.20	E_{rad} versus CNT external radius	108
4.21	TMV structure	109

4.22	TMV imaging using a PFM technique	111
4.23	Porous polyimide surfaces	112
4.24	Pores morphology	113
4.25	TMVs adsorbed on the polyimide membrane	114
4.26	TMV plastic deformation	115
4.27	Bending shape of TMVs	115
4.28	TMV diameter versus bending geometry.	116
4.29	TMV diameter versus surface roughness.	117
4.30	Theoretical representation of a TMV over a pore	118
4.31	VdW energy around the edge of a hole of the porous membrane	119
4.32	Discrete vdW gradient of forces acting on a TMV	120
4.33	Elliptic shape of the TMV	121

List of Tables

1.1	Type of surface forces	11
1.2	Hertz theory	18
3.1	Overview of the dependence of F_F on the scanning velocity v	63
3.2	Value of the fitting parameters for $RH = 35.5\%$	72
3.3	Value of the fitting parameters for $RH = 26.3\%$	72
3.4	Value of the fitting parameters for $RH = 18.5\%$	72
3.5	$\mu_0^{3/2} f_c$ for $F_N = 8$ nN	85

Bibliography

- [1] B. P. Straughan, S. Walker, A. V. Golton, and J. K. Burdett, *Spectroscopy* (Chapman and Hall, 1976).
- [2] G. C. Maitland, *Intermolecular Forces: Their Origin and Determination* (Oxford: Clarendon Press, 1987).
- [3] T. Young, Philos. Trans. R. Soc. London **95**, 65 (1805).
- [4] J. Israelachvili, *Intermolecular and Surface Forces* (Academic Press: San Diego, 1997).
- [5] H.-J. Butt, K. Graf, and M. Kappl, *Physics and Chemistry of Interfaces* (Wiley-VCH, 2003).
- [6] H. Hertz, J. fuer reine und angewandte Mathematik **92**, 156 (1881).
- [7] W. M. Lai, D. Rubin, and E. Krempf, *Introduction to Continuum Mechanics* (Butterworth-Heinemann, 1999).
- [8] M. Kwon and E. Spacone, Computers and Structures **80**, 199 (2002).
- [9] E. Saether, S. J. V. Frankland, and R. B. Pipes, Composites Science and Technology **63**, 1543 (2003).
- [10] A. P. Boresi and O. M. Sidebottom, *Advanced Mechanics of Materials* (John Wiley & Sons, 5th Ed., 1993).
- [11] K. L. Johnson, K. Kendall, and A. D. Roberts, Proc. Royal Soc. London **A324**, 301 (1971).
- [12] W. D. Harkins, P Natl Acad Sci USA **5**, 562 (1919).
- [13] B. Derjaguin, Kolloid-Zeits. **69**, 155 (1934).
- [14] B. Bhushan, *Handbook of Micro/NanoTribology* (CRC Press, 2nd Ed., 1999).
- [15] N. A. Burnham, R. J. Colton, and H. M. Pollock, Nanotechnology **4**, 64 (1993).
- [16] D. Maugis, J. Colloid. Interf. Sci. **150**, 243 (1992).
- [17] K. L. Johnson, *Contact Mechanics* (University Press: Cambridge, 1987).
- [18] R. D. Mindlin, Journal of Applied Mechanics-Transactions of the ASME **16**, 259 (1949).

- [19] J. M. Sancho, A. M. Lacasta, K. Lindenberg, I. M. Sokolov, and A. H. Romero, *Phys. Rev. Lett.* **92**, 250601 (2004).
- [20] K. Lindenberg, A. M. Lacasta, J. M. Sancho, and A. H. Romero, *AIP Conf. Proc.* **800**, 50 (2005).
- [21] G. Binnig and H. Rohrer, *Helv. Phys. Acta* **55**, 726 (1982).
- [22] G. Binnig, H. Rohrer, C. Gerber, and E. Weibel, *Physica* **109&110B**, 2075 (1982).
- [23] S. M. Hues, R. J. Colton, E. Meyer, and H. J. Guntherodt, *MRS Bulletin* **18**, 41 (1993).
- [24] P. Maivald, H. J. Butt, S. A. C. Gould, C. B. Prater, B. Drake, J. A. Gurley, V. B. Elings, and P. K. Hansma, *Nanotechnology* **2**, 103 (1991).
- [25] J. M. Neumeister and W. A. Ducker, *Rev. Sci. Instrum.* **65**, 2527 (1994).
- [26] T. J. Senden and W. A. Ducker, *Langmuir* **10**, 1003 (1994).
- [27] U. D. Schwarz, P. Köster, and R. Wiesendanger, *Rev. Sci. Instrum.* **67**, 2560 (1996).
- [28] J. P. Cleveland, S. Manne, D. Bocek, and P. K. Hansma, *Rev. Sci. Instrum.* **64**, 403 (1993).
- [29] S. Fujisawa, E. Kishi, Y. Sugawara, and S. Morita, *Appl. Phys. Lett.* **66**, 526 (1995).
- [30] R. W. Carpick, D. F. Ogletree, and M. Salmeron, *Appl. Phys. Lett.* **70**, 1548 (1997).
- [31] O. Piétrement, J. L. Beaudoin, and M. Troyon, *Trib. Lett.* **7**, 213 (1999).
- [32] D. F. Ogletree, R. W. Carpick, and M. Salmeron, *Rev. Sci. Instrum.* **67**, 3298 (1996).
- [33] G. Bogdanovic, A. Meurk, and M. W. Rutland, *Colloid Surface B* **19**, 397 (2000).
- [34] A. Feiler, P. Attard, and I. Larson, *Rev. Sci. Instrum.* **71**, 2746 (2000).
- [35] E. Liu, B. Blanpain, and J. P. Celis, *Wear* **192**, 141 (1996).
- [36] J. K. Spelt, Y. Rotenberg, D. R. Absolom, and A. W. Neumann, *Colloids and Surfaces* **24**, 127 (1987).
- [37] F. K. Skinner, Y. Rotenberg, and A. W. Neumann, *Journal of Colloid and Interface Science* **130**, 25 (1989).
- [38] R. L. Hoffman, *Journal of colloid and interface science* **50**, 228 (1975).
- [39] J. Gao, W. D. Luedtke, D. Gourdon, M. Ruths, J. N. Israelachvili, and U. Landman, *J. Phys. Chem. B* **108**, 3410 (2004).
- [40] J. Leslie, *An Experimental Inquiry Into The Nature and Propagation of Heat* (Bell & Bradfute, 1804).
- [41] F. P. Bowden, A. J. W. Moore, and D. Tabor, *J. of Appl. Phys.* **14**, 80 (1943).
- [42] F. P. Bowden and D. Tabor, *Brit. J. Appl. Phys.* **17**, 1524 (1966).

- [43] J. A. Greenwood, *Fundamentals of friction* (Kluwer: Dordrecht, 1992).
- [44] M. Enachescu, R. J. A. van den Oetelaar, R. W. Carpick, D. F. Ogletree, C. F. J. Flipse, and M. Salmeron, *Tribology Letters* **7**, 73 (1999).
- [45] B. N. J. Persson, *Phys. Rev. Lett.* **87**, 116101 (2001).
- [46] B. Persson, *Sliding Friction: Physical Principles and Applications* (Springer: Berlin, 2000).
- [47] A. Socoliuc, R. Bennewitz, E. Gnecco, and E. Meyer, *Phys. Rev. Lett.* **92**, 134301 (2004).
- [48] E. Gnecco, R. Bennewitz, T. Gyalog, C. Loppacher, M. Bammerlin, E. Meyer, and H.-J. Güntherodt, *Phys. Rev. Lett.* **84**, 1172 (2000).
- [49] G. A. Tomlinson, *Philos. Mag.* **7**, 905 (1929).
- [50] M. Weiss and F. J. Elmer, *Phys. Rev. B* **53**, 7539 (1996).
- [51] M. Hirano, *Surf. Sci. Rep.* **60**, 159 (2006).
- [52] C. Fusco and A. Fasolino, *Phys. Rev. B* **71**, 045413 (2005).
- [53] N. Sasaki, M. Kobayashi, and M. Tsukada, *Phys. Rev. B* **54**, 2138 (1996).
- [54] M. Hirano and K. Shinjo, *Phys. Rev. B* **41**, 11837 (1990).
- [55] M. Dienwiebel, G. S. Verhoeven, N. Pradeep, J. W. M. Frenken, J. A. Heimberg, and H. W. Zandbergen, *Phys. Rev. Lett.* **92**, 126101 (2004).
- [56] M. Dienwiebel, N. Pradeep, G. S. Verhoeven, H. W. Zandbergen, and J. W. M. Frenken, *Surf. Sci.* **576**, 197 (2005).
- [57] S. Y. Krylov, K. B. Jinesh, H. Valk, M. Dienwiebel, and J. W. M. Frenken, *Phys. Rev. E* **71**, 065101 (2005).
- [58] E. Riedo, E. Gnecco, R. Bennewitz, E. Meyer, and H. Brune, *Phys. Rev. Lett.* **91**, 0845021 (2003).
- [59] A. Socoliuc, E. Gnecco, Maier, Pfeiffer, A. Baratoff, R. Bennewitz, and E. Meyer¹, *Science* **313**, 207 (2006).
- [60] C. M. Mate, G. M. McClelland, R. Erlandsson, and S. Chiang, *Phys. Rev. Lett.* **59**, 1942 (1987).
- [61] O. Zwörner, H. Hölscher, U. D. Schwarz, and R. Wiesendanger, *Appl. Phys. A* **66**, 263 (1998).
- [62] T. Bouhacina, J. P. Aimé, S. Gauthier, D. Michel, and V. Heroguez, *Phys. Rev. B* **56**, 7694 (1997).
- [63] E. Riedo and E. Gnecco, *Nanotech.* **15**, S288 (2004).
- [64] E. Riedo, F. Lévy, and H. Brune, *Phys. Rev. Lett.* **88**, 185505 (2002).

- [65] Y. Sang, M. Dubé, and M. Grant, *Phys. Rev. Lett.* **87**, 1743011 (2001).
- [66] D. Gourdon, N. A. Burnham, A. Kulik, E. Dupas, F. Oulevey, G. Gremaud, D. Stamou, M. Liley, Z. Dienes, H. Vogel, et al., *Trib. Lett.* **3**, 317 (1997).
- [67] R. Prioli, A. M. F. Rivas, F. L. F. Jr., and A. O. Caride, *Appl. Phys. A* **76**, 565 (2003).
- [68] A. Opitz, S. I.-U. Ahmed, M. Scherge, and J. A. Schaefer, *Trib. Lett.* **20**, 229 (2005).
- [69] E. Riedo, I. Palaci, C. Boragno, and H. Brune, *J. Phys. Chem. B* **108**, 5324 (2004).
- [70] J. Chen, I. Ratera, J. Y. Park, and M. Salmeron, *Phys. Rev. Lett.* **96**, 2361021 (2006).
- [71] P. Reimann and M. Evstigneev, *New J. of Phys.* **7**, 25 (2005).
- [72] M. A. Lantz, S. J. O'Shea, M. E. Welland, and K. L. Johnson, *Phys. Rev. B* **55**, 10776 (1997).
- [73] P. M. Fabis, R. A. Cooke, and S. McDonough, *J. Vac. Sci. Technol. A* **8**, 3819 (1990).
- [74] D. J. Hornbaker, R. Albert, I. Albert, A.-L. Barabási, and P. Schiffer, *Nature* **387**, 765 (1997).
- [75] T. C. Halsey and A. J. Levine, *Phys. Rev. Lett.* **80**, 3141 (1998).
- [76] L. Bocquet, E. Charlaix, S. Ciliberto, and J. Crassous, *Nature* **396**, 735 (1998).
- [77] J. N. D'Amour, J. J. R. Stalgren, K. K. Kanazawa, C. W. Frank, M. Rodahl, and D. Johannsmann, *Phys. Rev. Lett.* **96**, 058301 (2006).
- [78] A. Fogden and L. R. White, *J. Colloid Interface Sci.* **138**, 414 (1990).
- [79] S. Kim, H. K. Christenson, and J. E. Curry, *J. Phys. Chem. B* **107**, 3774 (2003).
- [80] P.-E. Mazeran, *Mat. Sci. Eng. C* **26**, 751 (2006).
- [81] R. P. Feynman, *Engineering and Science Magazine of Cal. Inst. of Tech.* **23**, 22 (1960).
- [82] C.-C. You, O. R. Miranda, B. Gider, P. S. Ghosh, I.-B. Kim, B. Erdogan, S. A. Krovi, U. H. F. Bunz, and V. M. Rotello, *Nat. Nanotech.* **2**, 318 (2007).
- [83] J. V. Barth, G. Costantini, and K. Kern, *Nature* **437**, 671 (2005).
- [84] A. B. Kesel, A. Martin, and T. Seidl, *Smart Mater. Struct.* **13**, 512 (2004).
- [85] H. W. Kroto, J. R. Heath, S. C. O'Brien, R. F. Curl, and R. E. Smalley, *Nature* **318**, 162 (1985).
- [86] D. Ugarte, *Nature* **359**, 707 (1992).
- [87] S. Iijima, *Nature* **354**, 56 (1991).
- [88] R. Saito, G. Dresselhaus, and M. S. Dresselhaus, *Phys. Rev. B* **53**, 2044 (1996).

- [89] M. S. Dresselhaus, G. Dresselhaus, A. M. Rao, and P. C. Eklund, *Synthetic Met.* **78**, 313 (1996).
- [90] T. Hertel, R. E. Walkup, and P. Avouris, *Phys. Rev. B* **58**, 13870 (1998).
- [91] A. Kis, K. Jensen, S. Aloni, W. Mickelson, and A. Zettl, *Phys. Rev. Lett.* **97**, 025501 (2006).
- [92] B. Lukic, J. W. Seo, E. Couteau, K. Lee, S. Gradecak, R. Berkecz, K. Hernadi, S. Delpeux, T. Cacciaguerra, F. Béguin, et al., *Appl. Phys. A-Mater.* **80**, 695 (2005).
- [93] S. Paulson, M. R. Falvo, N. Snider, A. Helser, T. Hudson, A. Seeger, R. M. Taylor, R. Superfine, and S. Washburn, *Appl. Phys. Lett.* **75**, 2936 (1999).
- [94] E. T. Thostenson and T.-W. Chou, *J. Phys. D: Appl. Phys.* **36**, 573 (2003).
- [95] H. Dai, E. W. Wong, Y. Z. Lu, S. Fan, and C. M. Lieber, *Nature* **375**, 769 (1995).
- [96] W. Q. Han, S. S. Fan, Q. Q. Li, B. L. Gu, X. B. Zhang, and D. P. Yu, *Appl. Phys. Lett.* **71**, 2271 (1997).
- [97] P. D. Yang and C. M. Lieber, *J. Mat. Res.* **12**, 2981 (1997).
- [98] J. L. Liu, Y. Lu, Y. Shi, S. L. Gu, R. L. Jiang, F. Wang, and Y. D. Zheng, *Appl. Phys. A* **66**, 539 (1998).
- [99] Y. Li, G. S. Cheng, and L. D. Zhang, *J. Mat. Res.* **15**, 2305 (2000).
- [100] C. Dekker, *Phys. Today* **52**, 22 (1999).
- [101] X. Duan, Y. Huang, R. Agarwal, and C. M. Lieber, *Nature* **421**, 241 (2003).
- [102] M. Willander, O. Nur, Y. E. Lozovik, S. M. Al-Hilli, Z. Chiragwandi, Q.-H. Hu, Q. X. Zhao, and P. Klason, *Microelectr. J.* **36**, 940 (2005).
- [103] Z. W. Pan, Z. R. Dai, and Z. L. Wang, *Science* **291**, 1947 (2001).
- [104] X. Y. Kong and Z. L. Wang, *Nano Lett.* **3**, 1625 (2003).
- [105] J. Riu, A. Maroto, and F. X. Rius, *Talanta* **69**, 288 (2006).
- [106] J. I. Paredes and M. Burghard, *Langmuir* **20**, 5149 (2004).
- [107] K. Balasubramanian and M. Burghard, *Small* **1**, 180 (2005).
- [108] S. J. Son, X. Bai, A. Nan, H. Ghandehari, and S. B. Lee, *J. Control. Release* **114**, 143 (2006).
- [109] M. Reches and E. Gazit, *Nat. Nanotech.* **1**, 195 (2006).
- [110] Y. Zhou, *Current Nanoscience* **2**, 123 (2006).
- [111] A. M. Bittner, *Naturwissenschaften* **92**, 51 (2005).

- [112] M. Knez, A. Kadri, C. Wege, U. Glösel, H. Jeske, and K. Nielsch, *Nano Lett.* **6**, 1172 (2006).
- [113] B. W. D'Andrade, M. A. Baldo, C. Adachi, J. Brooks, M. E. Thompson, and S. R. Forrest, *Appl. Phys. Lett.* **79**, 1045 (2001).
- [114] V. Bulovic, P. E. Burrows, and S. R. Forrest, *Semiconductors and Semimetals* **64**, 255 (2000).
- [115] A. Dodabalapur, H. E. Katz, L. Torsi, and R. C. Haddon, *Science* **269**, 1560 (1995).
- [116] K. K. W. Wong, T. Douglas, S. Gider, D. D. Awschalom, and S. Mann, *Chem. Mater.* **10**, 279 (1998).
- [117] K. K. W. Wong and S. Mann, *Adv. Mater.* **8**, 928 (1996).
- [118] T. Douglas and M. Young, *Nature* **393**, 152 (1998).
- [119] S. A. Davis, S. L. Burkett, N. H. Mendelson, and S. Mann, *Nature* **385**, 420 (1997).
- [120] M. Mertig, R. Wahl, M. Lehmann, P. Simon, and W. Pompe, *Eur. Phys. J. D* **16**, 317 (2001).
- [121] D. D. Archibald and S. Mann, *Nature* **364**, 430 (1993).
- [122] S. Balci, A. M. Bittner, K. Hahn, C. Scheu, M. Knez, A. Kadri, C. Wege, H. Jeske, and K. Kern, *Electrochimica Acta* **51**, 6251 (2006).
- [123] M. Knez, M. P. Sumser, A. M. Bittner, C. Wege, H. Jeske, D. M. P. Hoffmann, K. Kuhnke, and K. Kern, *Langmuir* **20**, 441 (2004).
- [124] A. Kelly and N. H. Macmillan, *Strong solids* (Oxford : Clarendon Press, 1986).
- [125] B. I. Yakobson, C. J. Brabec, and J. Bernholc, *Phys. Rev. Lett.* **76**, 2511 (1996).
- [126] M. Arroyo and T. Belytschko, *Meccanica* **40**, 455 (2005).
- [127] G. Y. Jing, H. Ji, W. Y. Yang, J. Xu, and D. P. Yu, *Appl. Phys. A* **82**, 475 (2006).
- [128] E. W. Wong, P. E. Sheehan, and C. M. Lieber, *Science* **277**, 1971 (1997).
- [129] D. A. Walters, L. M. Ericson, M. J. Casavant, J. Liu, D. T. Colbert, K. A. Smith, and R. E. Smalley, *Appl. Phys. Lett.* **74**, 3803 (1999).
- [130] J. P. Salvetat, J.-M. Bonard, N. H. Thomson, A. J. Kulik, L. Forró, W. Benoit, and L. Zuppiroli, *Appl. Phys. A* **69**, 255 (1999).
- [131] M.-F. Yu, O. Lourie, M. J. Dyer, K. Moloni, T. F. Kelly, and R. S. Ruoff, *Science* **287**, 637 (2000).
- [132] M. F. Yu, T. Kowalewski, and R. S. Ruoff, *Phys. Rev. Lett.* **85**, 1456 (2000).
- [133] W. Kolbe, D. Ogletree, and M. Salmeron, *Ultramicroscopy* **42-44**, 1113 (1991).

- [134] F. M. Ohnesorge, J. K. H. Horber, W. Haberle, C.-P. Czerny, D. P. E. Smith, and G. Bin-nig, *Biophys. J* **73**, 2183 (1997).
- [135] A. Kis, S. Kasas, B. Babic, A. J. Kulik, W. Benoît, G. A. Briggs, C. Schoenenberger, S. Catsicas, and L. Forró, *Phys. Rev. Lett.* **89**, 248101 (2002).
- [136] J. P. Michel, I. L. Ivanovska, M. M. Gibbons, W. S. Klug, C. M. Knobler, G. J. L. Wuite, and C. F. Schmidt, *P. Natl. Acad. Sci. USA* **103**, 6184 (2006).
- [137] N. C. Santos and M. A. R. B. Castanho, *Biophys. Chem.* **107**, 133 (2004).
- [138] M. M. J. Treacy, T. W. Ebbesen, and J. M. Gibson, *Nature* **381**, 678 (1996).
- [139] P. Poncharal, Z. L. Wang, D. Urgarte, and W. A. de Heer, *Science* **283**, 1513 (1999).
- [140] Z. L. Wang, R. P. Gao, P. Poncharal, W. A. de Heer, Z. W. Pan, Z. R. Dai, and Z. W. Pan, *Mat. Sci. Eng. C-Bio. S.* **16**, 3 (2001).
- [141] Z. L. Wang, R. P. Gao, Z. W. Pan, and Z. R. Dai, *Adv. Eng. Mat.* **3**, 657 (2001).
- [142] Z. L. Wang, *Adv. Mater.* **15**, 1 (2003).
- [143] C. Gómez-Navarro, P. J. de Pablo, and J. Gómez-Herrero, *Advanced Material* **16**, 549 (2004).
- [144] W. Shen, B. Jiang, B. S. Han, and S. s Xie, *Phys. Rev. Lett.* **84**, 3634 (2000).
- [145] J. P. Salvetat, G. A. D. Briggs, J. M. Bonard, R. W. Bacsá, A. J. Kulik, T. Stockli, N. A. Burnham, and L. Forró, *Phys. Rev. Lett.* **82**, 944 (1999).
- [146] J. P. Salvetat, A. J. Kulik, J.-M. Bonard, G. A. D. Briggs, T. Stockli, K. Metenier, S. Bon-namy, F. Beguin, N. A. Burnham, and L. Forro, *Adv. Mat.* **11**, 161 (1999).
- [147] P. Bhatt, *Structures* (Longman, 1999).
- [148] W. A. Jalil, *Calcul pratique des structures* (Eyrolles, 1977).
- [149] P. Avouris, J. Appenzeller, R. Martel, and S. J. Wind, *Proc. IEEE* **91**, 1772 (2003).
- [150] R. Martel, T. Schmidt, H. R. Shea, T. Hertel, and P. Avouris, *Appl. Phys. Lett.* **73**, 2447 (1998).
- [151] J. Hone, M. C. Llaguno, M. J. Biercuk, A. T. Johnson, B. Batlogg, Z. Benes, and J. E. Fischer, *Appl. Phys. A* **74**, 339 (2002).
- [152] E. T. Thostenson, Z. Ren, and T. W. Chou, *Compos. Sci. Technol.* **61**, 1899 (2001).
- [153] L. Roschier, R. Tarkiainen, M. Ahlskog, M. Paalanen, and P. Hakonen, *Microelectron. Eng.* **61-62**, 687 (2002).
- [154] J. P. Lu, *Phys. Rev. Lett.* **79**, 1297 (1997).
- [155] V. N. Popov and V. E. V. Doren, *Phys. Rev. B* **61**, 3078 (2000).

- [156] H. W. Zhu, C. L. Xu, D. H. Wu, B. Q. Wei, R. Vajtai, and P. M. Ajayan, *Science* **296**, 884 (2002).
- [157] C.-H. Kiang, M. Endo, P. M. Ajayan, G. Dresselhaus, and M. S. Dresselhaus, *Phys. Rev. Lett.* **81**, 1869 (1998).
- [158] K. Tanaka, T. Yamabe, and K. Fukui, *The science and Technology of Carbon Nanotubes* (Elsevier Science, 1999).
- [159] M. B. Nardelli, B. I. Yakobson, and J. Bernholc, *Phys. Rev. B* **57**, R4277 (1998).
- [160] V. Ivanov, J. B. Nagy, P. Lambin, A. Lucas, X. B. Zhang, X. M. Zhang, D. Bernaerts, G. V. Tendeloo, S. Amelinckx, and J. V. Landuyt, *Chem. Phys. Lett.* **223**, 329 (1994).
- [161] S. Fan, M. G. Chapline, N. R. Franklin, T. W. Tombler, A. M. Cassel, and H. Dai, *Science* **283**, 512 (1999).
- [162] W. Kratschmer, L. D. Lamb, K. Fostiropoulos, and D. R. Huffman, *Nature* **347**, 354 (1990).
- [163] T. W. Ebbesen and P. M. Ajayan, *Nature* **358**, 220 (1992).
- [164] A. Thess, R. Lee, P. Nikolaev, H. Dai, P. Petit, J. Robert, C. Xu, Y. H. Lee, S. G. Kim, A. G. Rinzler, et al., *Science* **273**, 483 (1996).
- [165] Y. Xia, M. W. Zhao, Y. C. Ma, M. J. Ying, X. D. Liu, P. J. Liu, and L. M. Mei, *Phys. Rev. B* **65**, 155415 (2002).
- [166] J. A. Elliot, J. K. W. Sandler, A. H. Windle, R. J. Young, and M. S. P. Shaffer, *Phys. Rev. Lett.* **92**, 095501 (2004).
- [167] M. R. Falvo, G. J. Clary, R. M. Taylor, V. Chi, F. P. B. Jr, S. Washburn, and R. Superfine, *Nature* **389**, 582 (1997).
- [168] M. R. Falvo, G. J. Clary, A. Helser, S. Paulson, R. M. Taylor, V. Chi, J. F. P. Brooks, S. Washburn, and R. Superfine, *Microsc. And Microanal.* **4**, 504 (1998).
- [169] V. Lordi and N. Yao, *J. Chem. Phys.* **109**, 2509 (1998).
- [170] T. W. Ebbesen, *Accounts Chem. Res.* **31**, 558 (1998).
- [171] S. Niyogi, M. A. Hamon, H. Hu, B. Zao, P. Bhowmik, R. Sen, M. E. Itkis, and R. C. Haddon, *Accounts Chem. Res.* **35**, 1105 (2002).
- [172] M. S. Dresselhaus, G. Dresselhaus, and P. Avouris, *Carbon Nanotubes: Synthesis, Structure, Properties, and Applications* (Springer, 2001).
- [173] L. Shen and J. Li, *Phys. Rev. B* **69**, 045414 (2004).
- [174] E. D. Minot, Y. Yaish, V. Sazonova, J.-Y. Park, M. Brink, and P. L. McEuen, *Phys. Rev. Lett.* **90**, 156401 (2003).
- [175] S. Dag, O. Gulseren, S. Ciraci, and T. Yildirim, *Appl. Phys. Lett.* **83**, 3180 (2003).

- [176] P. Avouris, T. Hertel, R. Martel, T. Schmidt, H. R. Shea, and R. E. Walkup, *Appl. Surf. Sci.* **141**, 201 (1999).
- [177] I. Palaci, S. Fedrigo, H. Brune, C. Klinke, M. Chen, and E. Riedo, *Phys. Rev. Lett.* **94**, 1755021 (2005).
- [178] O. Piétrement and M. Troyon, *Trib. Lett.* **9**, 77 (2000).
- [179] C. Klinke, J. M. Bonard, and K. Kern, *Surf. Sci.* **492**, 195 (2001).
- [180] N. A. Marks, *Phys. Rev. B* **63**, 035401 (2000).
- [181] R. W. Carpick, M. Enachescu, D. F. Ogletree, and M. Salmeron, *Mat. Res. Soc. Symp. Proc.* **539**, 93 (1999).
- [182] B. T. Kelly, *Physics of Graphite* (Applied Science Publisher, London, 1981).
- [183] M. H. Park, J. W. Jang, and C. E. Lee, *Appl. Phys. Lett.* **86**, 023110 (2005).
- [184] T. Schwarz, F. Schmidt, and E. Proll, *Naturwissenschaften* **53**, 485 (1966).
- [185] C. M. Fauquet, M. A. Mayo, J. Maniloff, U. Desselberger, and L. A. Ball, *Virus Taxonomy: Eighth Report of the International Committee on Taxonomy of Viruses* (Elsevier Academic Press, 2005).
- [186] A. Klug, *Philos. Trans. R. Soc. Lond. B* **354**, 531 (1999).
- [187] G. Stubbs, *Philos. Trans. R. Soc. Lond. B* **354**, 551 (1999).
- [188] J. D. Watson, *Biochim. Biophys. Acta* **13**, 10 (1954).
- [189] P. J. G. Butler, *J. Gen. Virol.* **65**, 253 (1984).
- [190] J. I. Harris and C. A. Knight, *Nature* **170**, 613 (1952).
- [191] M. Deggelmann, C. Graf, M. Hagenbuchle, U. Hoss, C. Johner, H. Kramer, C. Martin, and R. Weber, *J. Phys. Chem.* **98**, 364 (1994).
- [192] C. W. Choi, S. H. Park, J. K. Choi, K. H. Ryu, and W. M. Park, *Acta Virol.* **44**, 145 (2000, 44, 2000).
- [193] A. Nicolaieff and G. Lebeurier, *Mol. Gen. Genet.* **171**, 327 (1979).
- [194] W. Shenton, T. Douglas, M. Young, G. Stubbs, and S. Mann, *Adv. Mater.* **11**, 253 (1999).
- [195] S. Lu, G. Stubbs, and J. N. Culver, *Virology* **225**, 11 (1996).
- [196] E. Dujardin, C. Peet, G. Stubbs, J. N. Culver, and S. Mann, *Nano Lett.* **3**, 413 (2003).
- [197] Z. Niu, M. Bruckman, V. S. Kotakadi, J. He, T. Emrick, T. P. Russell, L. Yang, and Q. Wang, *Chem. Commun.* **28**, 3019 (2006).
- [198] A. A. Balandin and V. A. Fonoberov, *J. Biomed. Nanotech.* **1**, 90 (2005).

- [199] V. A. Fonoberov and A. A. Balandin, *Phys. Stat. Sol (b)* **12**, R67 (2004).
- [200] M. R. Falvo, S. Washburn, R. Superfine, M. Finch, F. P. Brooks, V. Chi, and R. M. Taylor, *Biophys. J.* **72**, 1396 (1997).
- [201] S. V. Kalinin, S. Jesse, W. Liu, and A. A. Balandin, *Appl. Phys. Lett.* **88**, 153902 (2006).
- [202] E. V. Dubrovin, M. N. Kirikova, V. K. Novikov, Y. F. Drygin, and I. V. Yaminsky, *Colloid Journal* **66**, 673 (2004).
- [203] Y. F. Drygin, O. A. Bordunova, M. O. Gallyamov, and I. V. Yaminsky, *FEBS Letters* **425**, 217 (1998).
- [204] F. Zenhausern, M. Adrian, R. Emch, M. Taborrelli, M. Jobin, and P. Descouts, *Ultramicroscopy* **42-44**, 1168 (1992).
- [205] F. Zenhausern, M. Adrian, B. ten Heggeler-Bordier, F. Ardizzoni, and P. Descouts, *J. Appl. Phys.* **73**, 7232 (1993).
- [206] K. Wadu-Mesthrige, B. Pati, W. M. McClain, and G.-Y. Liu, *Langmuir* **12**, 3511 (1996).
- [207] J. Vesenka, S. Manne, R. Giberson, T. Marsh, and E. Henderson, *Biophys. J.* **65**, 992 (1993).
- [208] S. O. Vansteenkiste, S. I. Corneillie, E. H. Schacht, X. Chen, M. C. Davies, M. Moens, and L. V. Vaeck, *Langmuir* **16**, 3330 (2000).
- [209] S. Kidoaki and T. Matsuda, *Langmuir* **15**, 7639 (1999).
- [210] L. C. Xu and B. E. Logan, *Langmuir* **22**, 4720 (2006).
- [211] L. Bergstroem, *Adv. in Colloid .Interfac.* **70**, 125 (1997).
- [212] C. J. Drummond and D. Y. C. Chan, *Langmuir* **13**, 3890 (1997).
- [213] C. J. Drummond and D. Y. C. Chan, *Langmuir* **12**, 3356 (1996).
- [214] C. J. Drummond, G. Georgaklis, and D. Y. C. Chan, *Langmuir* **12**, 2617 (1996).
- [215] H. D. Ackler, R. H. French, and Y. M. Chiang, *Journal of Colloid and Interface Science* **179**, 460 (1996).
- [216] V. A. Parsegian and G. H. Weiss, *Journal of Colloid and Interface Science* **81**, 285 (1981).
- [217] X. Yao, M. Jericho, D. Pink, and T. Beveridge, *J. Bacteriol.* **181**, 6865 (1999).
- [218] J. A. Callow, S. A. Crawford, M. J. Higgins, P. Mulvaney, and R. Wetherbee, *Planta* **211**, 641 (2000).
- [219] A. Touhami, B. Nysten, and Y. F. Dufrene, *Langmuir* **19**, 4539 (2003).
- [220] A. V. Bolshakova, O. I. Kiselyova, and I. V. Yaminsky, *Biotechnol. Prog.* **20**, 1615 (2004).

-
- [221] B. Ji and H. Gao, *J. Mech. Phys. Solids* **52**, 1963 (2004).
- [222] S. Sahoo, S. Parveen, and J. Panda, *Nanomedicine: Nanotechnology, Biology, and Medicine* **3**, 20 (2007).
- [223] A. Krishnan, E. Dujardin, T. W. Ebbesen, P. N. Yianilos, and M. M. J. Treacy, *Phys. Rev. B* **58**, 14013 (1998).
- [224] M.-F. Yu, B. S. Files, S. Arepalli, and R. S. Ruoff, *Phys. Rev. Lett.* **84**, 5552 (2000).

ACKNOWLEDGEMENTS

A thesis work is not conceivable without the support of many people. I would like to express to everyone who contributed to this thesis my sincere gratitude.

I would like to thank especially Harald Brune, my supervisor, for his many suggestions and constant support during this research. His advice were always helpful.

I am also thankful to Elisa Riedo for her guidance through the early years of my thesis and for her welcome during my stay at the Georgia Institute of Technology in Atlanta.

I like to thank Klaus Kern for giving me the opportunity of working few months at the Max-Planck Institute in Stuttgart and for his enthusiastic support.

Many thanks also go to Alexander Bittner for teaching me some bases on working in a chemical lab with viruses and for his creative ideas.

The technical expertise of Andrzej Kulik, as well as helpful discussions helped me in saving the life of the old AFM M5.

Finally, I would like to thank Christian Klinke, Stephan Fedrigo, Robert Szoszkiewicz, who expressed their interest in my work and supplied me with many useful references and discussions.

CURRICULUM VITAE

PALACI ISMAËL

Nationality : Swiss

ismael.palaci@epfl.ch

Age: 29

Single

Fields of interest: surface sciences and bulk material properties.

Experience

- 2003-2007 : - PhD thesis on the subject of the nanotribology. The research work was partially performed at the EPFL, the Georgia Institute of Technology (7 months, Atlanta, USA) and the Max-Planck Institute (3 months, Stuttgart, D), using methods such as continuum mechanics, engineering simulations and atomic force microscopy.
- Teaching assistant for the course of General Physics for material and computer scientists at the EPFL.
- 2002-2003 : - Study of the effect of the capillary condensation on the friction force and impact of the relative humidity on adhesion: 5 months practical training in the framework of the master degree in physics at the EPFL.
- 1999 : - Design and development of a flowmeter using indirect confocal optics and Doppler effect to measure the blood flow in the optic nerve: 3 months practical training at the Research Institute in Ophtalmology (Sion, CH).

Languages : French: mother tongue German: scholar knowledge
English: fluent Italian and Spanish: basics

Computer skills : Microsoft Environment, programming (Fortran), Maple, Mathematica, Matlab, engineering simulations (ANSYS)

Publications : - The 2/3 Power Law Dependence of Capillary Force on Normal Load in Nanoscopic Friction (J. Phys. Chem. B **108**, 5324 (2004)).
- Radial Elasticity of Multiwalled Carbon Nanotubes (Phys. Rev. Lett. **94**, 175502 (2005)).
- Effects of Sliding Velocity on Nanofriction for a CrN Hydrophilic Surface (In preparation).
- Mechanical properties of the tobacco mosaic virus (In preparation).

Hobbies : MTB, trekking, basket ball, swimming, badminton, photography